

TECHNISCHE UNIVERSITÄT MÜNCHEN

TUM School of Engineering and Design

**A Multipurpose Euler-Lagrange Framework for the
Numerical Simulation of Particle and Dispersed
Flow Problems**

Georg Hammerl

Vollständiger Abdruck der von der TUM School of Engineering and Design der Technischen Universität München zur Erlangung des akademischen Grades eines

Doktors der Ingenieurwissenschaften (Dr.-Ing.)

genehmigten Dissertation.

Vorsitzender: Prof. Dr.-Ing. Harald Klein

Prüfer der Dissertation:

1. Prof. Dr.-Ing. Wolfgang A. Wall
2. Ass. Prof. Dr. Martin Kronbichler

Die Dissertation wurde am 19.07.2021 bei der Technischen Universität München eingereicht und durch die TUM School of Engineering and Design am 14.02.2022 angenommen.

Abstract

Particle problems and fluid-particle coupled problems exist in nature as well as in many industrial applications. Usually, the complexity in pure particle problems lies in the huge number of particles involved when e.g. considering transport processes of gravel or grain. The interaction of particles with fluid is of particular interest in the chemical industry in mixing processes. Many biological applications feature particulate flows as well, e.g. when it comes to drug delivery in the human body. In this thesis, particles are considered as small physical objects which are of spherical shape. Each object is modeled as a single particle which interacts with other particles, with walls and also with fluid flow.

In this thesis, a general framework is developed which enables the investigation of pure particle problems as well as fluid-particle coupled problems. For pure particle problems, the focus is on the parallel performance of the proposed approach. On this basis, a flexible multipurpose Euler-Lagrange framework has been developed in this work. Therein, the particles are accounted for in a Lagrangian frame whereas the fluid is treated in an Eulerian frame. The fluid is modeled via the volume averaged Navier-Stokes equations, which are derived for the first time within a variational multiscale finite element method in which the dispersed phase fraction is accounted for in the continuity equation. Proper modeling of the interaction between both fields is of paramount importance. In order to properly account for the volume displaced by the particles in the fluid, special attention is given to the computation of the dispersed phase fraction. Due to the point-like modeled particles, polynomial filtering functions are applied at the particle positions in order to compute the displaced volume in the fluid. The emerging volume integrals are transformed to line integrals by applying the divergence theorem twice. This enables an efficient analytical integration of the resulting line integrals. The coupling between particles and fluid is improved by a strong coupling scheme based on Aitken's Δ^2 method, which is the first time applied in an Euler-Lagrange framework. Convergence can be accelerated, or achieved at all, which is of particular importance when a variable radius evolution of the particles is considered. The Rayleigh-Plesset equation is included in the developed framework to evolve the particle radius dependent on the ambient conditions. Due to the highly nonlinear character of this ordinary differential equation, a subcycling procedure is applied which allows for time step size adaptations leading to an efficient time integration of the radius evolution. The time step size of the fluid can be chosen larger because the implicit time integration poses less restrictions on the admissible time step size.

Finally, the developed multipurpose framework is applied to several test cases featuring increasing complexity. The pure particle algorithm is validated with a simple outflow problem and parallel performance is assessed using a mixing problem. The fluid-particle coupled test cases include particle numbers between 2500 and a Taylor-Green vortex example with approximately 0.5 million particles. In a fluidized bed application, different flow patterns can be identified including regions with dense particle packing. Next, the strong coupling scheme is applied to flow around a NACA 0015 hydrofoil featuring particles with a variable radius governed by the Rayleigh-Plesset equation. Finally, it is shown that the developed framework can cope with complex fluid domains as they occur e.g. in biological applications when particulate flow into a human lung is investigated. A comparison of the drug delivery during a breathing cycle in a healthy and a pathological lung is performed.

Zusammenfassung

Partikelprobleme und fluid-partikel-gekoppelte Anwendungen treten in der Natur, wie auch in industriellen Fragestellungen auf. Üblicherweise liegt die Schwierigkeit von reinen Partikelproblemen in der großen Zahl an beteiligten Partikeln, wie beispielsweise bei Schüttvorgängen von Kies oder Getreide. Die Interaktion von Partikeln mit Fluiden ist für die chemische Industrie bei Mischvorgängen von besonderem Interesse. Außerdem finden sich in vielen biologischen Anwendungen partikelbehaftete Strömungen, wie beispielsweise bei der Verteilung von Medikamenten im menschlichen Körper. In dieser Arbeit werden Partikel als kleine physikalische Objekte gesehen, die in erster Näherung kugelförmig sind. Jedes Objekt wird als einzelnes Partikel modelliert, das mit anderen Partikeln, mit Wänden oder auch mit Strömungen interagieren kann.

In dieser Arbeit ist ein allgemeines Framework entwickelt worden, das die Untersuchung reiner Partikelprobleme, wie auch von fluid-partikel-gekoppelten Problemen ermöglicht. Der Fokus der reinen Partikelprobleme liegt bei der parallelen Leistungsfähigkeit des vorgeschlagenen Ansatzes. Darauf aufbauend wurde im Rahmen dieser Arbeit ein flexibles vielzweck Euler-Lagrange Framework entwickelt. Darin werden die Partikel in einer Lagrangen Betrachtung und das Fluid in einer Eulerschen Betrachtung berücksichtigt. Das Fluid wird mittels der volumengemittelten Navier-Stokes Gleichungen modelliert, welche erstmalig in einer variationellen Mehrskalen Finite Element Methode hergeleitet werden, in der der Anteil disperser Phase in der Kontinuitätsgleichung berücksichtigt wird. Eine gute Modellierung der Interaktion zwischen den Feldern ist von großer Bedeutung. Um das von den Partikeln verdrängte Volumen im Fluid korrekt zu berücksichtigen, wird besonderes Augenmerk auf die Berechnung des Partikelanteils gelegt. Aufgrund der punktförmigen Modellierung der Partikel werden polynomiale Filterfunktionen an den Partikelpositionen angebracht, um das verdrängte Volumen im Fluid ermitteln zu können. Die auftretenden Volumenintegrale werden dabei durch zweimalige Anwendung des Divergenztheorems zu Linienintegralen heruntergebrochen, was schließlich eine effiziente analytische Integration der resultierenden Linienintegrale ermöglicht. Die Kopplung zwischen Partikeln und Fluid wird durch ein starkes Kopplungsschema verbessert, das erstmalig auf Aitkens Δ^2 Verfahren innerhalb eines Euler-Lagrangeansatzes basiert. Die Konvergenz kann beschleunigt werden, was von besonderer Bedeutung ist, wenn ein zeitlich variabler Radius der Partikel berücksichtigt wird. Es wird die Rayleigh-Plessetgleichung verwendet um den Radiusverlauf, abhängig von den Umgebungsbedingungen, voranzuschreiten. Aufgrund des hochgradig nichtlinearen Charakters dieser gewöhnlichen Differentialgleichung wird ein Verfahren mit Unteriterationen angewendet, welches Zeitschrittweitenanpassungen ermöglicht, was eine effiziente Zeitintegration der Radiusänderungen ermöglicht. Die Zeitschrittweite des Fluids kann größer gewählt werden, da das implizite Zeitintegrationsschema geringere Einschränkungen an die zulässige Zeitschrittweite hat.

Schließlich wird das vielseitig einsetzbare Framework angewendet auf Testfälle mit ansteigendem Schwierigkeitsgrad. Der reine Partikelalgorithmus wird mittels eines einfachen Ausflussproblems validiert und die parallele Leistungsfähigkeit wird anhand eines Mischvorgangs untersucht. Die fluid-partikel-gekoppelten Testfälle enthalten ein Taylor-Green Wirbelbeispiel mit etwa einer halben Million Partikeln. Des Weiteren können in einer Wirbelschichtanwendung verschiedene Strömungsmuster identifiziert werden, einschließlich von Gebieten mit dichten Partikelpackungen. Als nächstes wird das starke Kopplungsschema auf die Umströmung eines NACA 0015 Profils angewendet, bei dem Partikel mit einem variablen Radius basierend auf der Rayleigh-

Plessetgleichung berücksichtigt werden. Schlussendlich wird gezeigt, dass das entwickelte Framework in der Lage ist, komplexe Fluidgebiete, wie sie beispielsweise in biologischen Anwendungen bei partikelbehafteter Strömung in die menschliche Lunge auftreten, zu berücksichtigen. Ein Vergleich der Medikamentenverteilung während eines Atemzyklus in einer gesunden und einer pathologischen Lunge wird durchgeführt.

Danksagung

Ich bedanke mich ganz herzlich bei meinem Doktorvater Prof. Wolfgang A. Wall für die Möglichkeit an seinem Lehrstuhl promovieren zu dürfen. Sein entgegengebrachtes Vertrauen und die mir gewährte Freiheit in meinen Entscheidungen habe ich sehr geschätzt. Die enorme Freiheit hat nicht immer dazu geführt, einen gerichteten Weg zu beschreiten, jedoch hat mich jeder dieser Umwege wissenschaftlich und persönlich weitergebracht. Ich habe die Zeit an diesem mit fachlich, wie menschlich, hochkarätig besetzten Lehrstuhl sehr genossen.

Es hat mich sehr gefreut, dass Prof. Martin Kronbichler den Mitbericht meiner Arbeit übernommen hat. Bereits während meiner Zeit am Lehrstuhl konnte ich von seinem tiefen Wissen der Fluidgleichungen und seinen Programmierkenntnissen lernen. Beim Vorsitzenden der Prüfungskommission, Herrn Prof. Harald Klein bedanke ich mich für die aufgebrachte Zeit und Mühe im Zusammenhang mit meinem Promotionsverfahren.

Besonderer Dank gilt meinem Bürokollegen und Freund Dr. Karl-Robert Wichmann. Mit ihm habe ich bereits das Maschinenbaustudium gemeinsam von Tag eins weg absolviert, so dass bis Ende meiner Lehrstuhlzeit über zehn Jahre gemeinsame Freuden- und Leidenszeit hinter uns liegen. Von ihm habe ich sehr viel lernen können und die fachlichen, wie auch nicht-fachlichen, Diskussionen mit ihm haben mich stets vorangebracht. Ein großer Dank gilt den Fluidleuten am Lehrstuhl, insbesondere Dr. Ursula Rasthofer, Dr. Volker Gravemeier, Dr. Magnus Winter, Dr. Benjamin Krank und Dr. Benedikt Schott, die mir regelmäßig bei meinem Verständnis und der Implementierung meiner Fluidgleichungen weitergeholfen haben. Bei Dr. Christian Roth bedanke ich mich ganz herzlich für die Unterstützung beim Lungenbeispiel. Ich freue mich meinen Partikelcode in die Hände von Dr. Jonas Eichinger und Dr. Sebastian Fuchs übergeben zu dürfen, die ihn bereits weiter verbessert und optimiert haben.

Während meiner Promotion hat mich mein “Hobbythema” Thermo-Fluid-Struktur-Interaktion begleitet, das in dieser Arbeit keinerlei Erwähnung findet. Dabei bedanke ich mich ganz herzlich bei Dr. Caroline Danowski und Dr. Alexander Seitz für die gute und angenehme Zusammenarbeit. Für die gute lehrstuhlübergreifende Arbeit in diesem Projekt bedanke ich mich bei den Aerodynamikern Dr. Muzio Grilli und Dr. Vito Pasquariello.

Ein großes Dankeschön auch an alle Korrekturleserinnen und -leser dieser Arbeit, allen voran Dr. Ursula Rasthofer, für die vielen wertvollen Hinweise.

Besonderer Dank gilt auch Frau Renata Nagl, die zu jeder Frage die Antwort hat und sich überaus zuverlässig um alles im Sekretariat kümmert.

Viele Kolleginnen und Kollegen sind zu guten Freunden geworden und ich erinnere mich gerne an gemeinsame Ausflüge, Konferenzteilnahmen, Fußball spielen, Feierabendbiere trinken, Ringkämpfe, Steckerlfischgrillen und vieles mehr.

Ein besonderer Dank gilt meinen Eltern, auf die ich mich immer verlassen kann und die mir Rückhalt geben und mich in allen meinen Entscheidungen unterstützen. Sehr viel Geduld habe ich meiner Frau Maria abverlangt. Sie hat stets zu mir gehalten, mich unterstützt und mich wieder geerdet, wenn ich es übertrieben habe. Die Zeit im Ausland, wie auch vor allem das Schreiben der Arbeit waren sehrfordernd. Für meine beiden Töchter Luzia und Julia ist nun auch wieder mehr Zeit und ich danke für euer Verständnis.

Contents

1	Introduction	1
1.1	Motivation	1
1.2	Numerical models for dispersed flows	2
1.3	Research objective and achievements	9
1.4	Outline	10
2	Mathematical model	11
2.1	Volume-averaged Navier-Stokes equations for the continuous phase	12
2.1.1	Strong form of the Navier-Stokes equations	12
2.1.2	Volume averaging procedure	13
2.2	Particle tracking in a Lagrangian frame	17
2.2.1	Rigid body kinematics	17
2.2.2	Fluid forces acting on particles	18
2.2.3	Particle-particle interaction	21
2.2.4	Particle-wall interaction	27
2.3	Discussion on the fluid-particle coupling	27
2.3.1	Fluid to particle coupling	28
2.3.2	Particle to fluid coupling	29
2.4	Particle radius variations governed by the Rayleigh-Plesset (RP) equation	31
3	Computational approach	33
3.1	Single fields	33
3.1.1	Discretized Navier-Stokes equations	33
3.1.2	Time discretization of the Lagrangian particles	40
3.2	Partitioned fluid-particle framework	43
3.2.1	Weakly coupled	44
3.2.2	Strongly coupled with Aitken relaxation	46
3.3	Quantity mapping between frames	48
3.3.1	Eulerian to Lagrangian quantity mapping	48
3.3.2	Lagrangian to Eulerian quantity mapping	49
3.4	Fluid fraction computation	49
3.4.1	Analytical integration of polynomial filtering functions	51
3.4.2	Validation	61
3.4.3	Computational cost of the dispersed phase computation approach	66
3.5	Time integration of the Rayleigh-Plesset equation	68
3.5.1	Runge-Kutta time integration with adaptive time stepping	68
3.5.2	Validation	71
3.6	Parallelization and efficiency aspects	72

4 Numerical examples	77
4.1 Particle flow through an orifice	77
4.1.1 Setup	77
4.1.2 Analysis and comparison against literature	78
4.2 Particle mixing	80
4.2.1 Setup	80
4.2.2 Scaling study	81
4.3 Taylor-Green vortex	86
4.3.1 Setup	86
4.3.2 Analysis and comparison against literature	87
4.4 Fluidized bed	91
4.4.1 Setup	91
4.4.2 Fixed bed regime	92
4.4.3 Internal spout regime	93
4.4.4 Slugging bed regime	94
4.4.5 Jet in fluidized bed regime	96
4.4.6 Drag law dependent behavior	98
4.5 NACA 0015 hydrofoil	98
4.5.1 Setup	98
4.5.2 Start-up procedure of the cavitation framework	100
4.5.3 First step towards cavitation	104
4.6 Droplets in the human lung	105
4.6.1 Setup and ventilation of a healthy lung	105
4.6.2 Pathological lung	109
5 Conclusion	111
5.1 Summary	111
5.2 Outlook	113
Bibliography	115

Nomenclature

Abbreviations

aabb	axis aligned bounding box
ALE	arbitrary Lagrangian Eulerian
BACI	Bavarian Advanced Computational Initiative
CFL	Courant-Friedrichs-Levy
CFD	Computational Fluid Dynamics
CS	cross-stress
DEM	Discrete Element Method
DNS	Direct Numerical Simulation
FEM	Finite Element Method
GD	grad-div
LBM	Lattice Boltzmann Method
lte	local truncation error
MPI	Message Passing Interface
NS	Navier-Stokes
ODE	ordinary differential equation
PFEM	Particle Finite Element Method
PSPG	Pressure Stabilized Petrov-Galerkin
rhs	right-hand side
RK	Runge-Kutta
RP	Rayleigh-Plesset
RS	Reynolds-stress
SMP	template distribution with Dirac delta filtering function
SPH	smoothed particle hydrodynamics
SUPG	Streamline/Upwind Petrov-Galerkin
TD	template distribution with constant filtering function
TD-G	template distribution with Gaussian filtering function
TD-S	template distribution with sine wave filtering function
TGV	Taylor-Green vortex
VOF	volume-of-fluid

Greek symbols

α_e	number of element nodes
α_f	generalized- α time integration parameter
α_i	angular acceleration of dispersion i

α_m	generalized- α time integration parameter
β	scalar parameter
γ	generalized- α time integration parameter
$\boldsymbol{\gamma}$	parametrization
Γ	boundary
Γ_i	boundary of dispersion i
$\delta(\cdot)$	deviation
Δt	time step size
Δt_b	particle time step size
Δt_l	fluid time step size
Δt_{RP}	bubble radius time step size
Δl_d^{bin}	bin size in direction d
ϵ_b	dispersed phase fraction
ϵ_l	fluid fraction
ϵ_R	normalized estimated local truncation error
$\boldsymbol{\epsilon}(\mathbf{u})$	rate of deformation tensor
$\boldsymbol{\epsilon}'(\mathbf{u})$	rate of deformation tensor minus divergence term
η	specific heat ratio
μ	dynamic viscosity
μ_i	Aitken factor at iteration step i
μ_s	friction coefficient
$\mu_{s,\text{dyn}}$	dynamic friction coefficient
ν	Poisson's ratio
$\boldsymbol{\xi}$	element coordinates
ξ_k	k^{th} element coordinate
ρ_b	density of disperse phase
ρ_l	density of continuous phase
ρ_∞	spectral radius
σ	surface tension
$\boldsymbol{\tau}$	stress tensor
τ_c	stabilization parameter of GD term
τ_m	stabilization parameter of SUPG and PSPG term
Φ	scalar parameter
ψ_i	filtering function of polynomial order i
$\boldsymbol{\omega}$	particle angular velocity
ω	relaxation parameter
ω_{\max}	maximal relaxation parameter
Ω	domain
Ω^e	element domain
Ω^p	particle domain
$\partial\Omega^e$	element boundary
Ω^*	union of all element interiors excluding the element boundaries

Roman symbols

a	scalar valued function
\mathbf{a}	particle acceleration
\mathbf{a}_{CS}	right-hand side vector of CS term
\mathbf{a}_{PSPG}	right-hand side vector of PSPG term
\mathbf{a}_{RS}	right-hand side vector of RS term
\mathbf{a}_{SUPG}	right-hand side vector of SUPG term
\mathbf{a}_u	right-hand side vector of stabilization terms of momentum equation
\mathbf{A}_{GD}	GD matrix
$\mathbf{A}_{p-\text{CS}}$	pressure part of CS matrix
$\mathbf{A}_{p-\text{PSPG}}$	pressure part of PSPG matrix
$\mathbf{A}_{p-\text{RS}}$	pressure part of RS matrix
$\mathbf{A}_{p-\text{SUPG}}$	pressure part of SUPG matrix
$\mathbf{A}_{u-\text{CS}}$	velocity part of CS matrix
$\mathbf{A}_{u-\text{PSPG}}$	velocity part of PSPG matrix
$\mathbf{A}_{u-\text{RS}}$	velocity part of RS matrix
$\mathbf{A}_{u-\text{SUPG}}$	velocity part of SUPG matrix
B	geometric width
c	small positive constant
\mathbf{c}_Γ	surface center
\mathbf{c}_Ω	volume center
c_{am}	added mass coefficient
c_d	drag coefficient
c_l	lift coefficient
c_p	specific heat capacity at constant pressure
c_v	specific heat capacity at constant volume
\mathbf{C}	convective matrix
C_1	constant dependent on element topology
d	damping parameter
d_0	geometric diameter
D	geometric diameter
D_0	geometric diameter
e	coefficient of restitution
E	Young's modulus
f	time step size adaption factor
\mathbf{f}	right-hand side vector of momentum equation
f_{cr}	contact dependent time step size factor
f_{dec}	maximal decrease of time step size adaption factor
f_{inc}	maximal increase of time step size adaption factor
\mathbf{F}	force
$\mathbf{F}(x, y, z)$	vector field
\mathbf{F}_{am}	added mass force
\mathbf{F}_b	buoyancy force

\mathbf{F}_c	contact force
F_{cn}	absolut value of normal contact force
\mathbf{F}_{cn}	normal contact force
\mathbf{F}_{ct}	tangential contact force
\mathbf{F}_d	drag force
\mathbf{F}_g	gravity force
\mathbf{F}_I	inertia force
\mathbf{F}_l	lift force
\mathbf{F}_p	pressure force
$\mathbf{F}_{\text{trial}}$	trial force
\mathbf{F}_{vol}	volume force
$\sum \mathbf{F}_\Gamma$	sum over all interface forces
$\sum \mathbf{F}'_\Gamma$	modified sum over all interface forces
\mathbf{F}_τ	viscous force
\mathbf{g}	gravity acceleration
\mathbf{g}	right-hand side vector of continuity equation
g_n	normal gap
g_t	tangential gap
$\mathbf{g}_{t,\text{proj}}$	projected tangential gap
$\hat{\mathbf{g}}_{t,\text{proj}}$	recovered projected tangential gap
G	shear modulus
\mathbf{G}	covariant metric tensor
\mathbf{G}	gradient matrix
\mathbf{h}	Neumann boundary momentum flux
H	geometric height
$\mathbf{H}(x, y, z)$	vector field
$H^1(\Omega)$	Sobolev space of square-integrable functions and square-integrable first derivatives
i	iterator
\mathbf{I}	identity tensor
j	iterator
k_n	normal stiffness parameter
k_t	tangential stiffness parameter
k, k_x, k_y	wave number, in x -direction, in y -direction
k_Γ	number of vertices attached to a surface
k_Ω	number of vertices attached to a volume
\mathbf{K}	summarized convective, viscous, gradient, and stabilization terms matrix
l	average distance between disperse objects
L	characteristic length of changes in mixture of two-phase flow
L_{ref}	reference length of fluid flow
$L^2(\Omega)$	Hilbert space of square-integrable functions
m	mass
\mathbf{m}	normal vector on boundary
m_{eff}	effective mass
\mathbf{M}	particle angular momentum

M	mass matrix
<i>n</i>	time step counter
n	normal vector
<i>n_e</i>	number of elements
n_i	normal pointing outward of dispersion <i>i</i>
n_l	normal pointing outward of continuous phase
<i>n_p</i>	number of particles
<i>n_{surf}</i>	number of surfaces of a single fluid element
<i>N</i>	shape function
<i>p</i>	fluid pressure
<i>p_b</i>	bubble inside pressure
<i>p_g</i>	partial gas pressure
<i>p_v</i>	vapor pressure
<i>p'</i>	dynamic fluid pressure
<i>p_∞</i>	pressure of surrounding fluid
P	vector of fluid pressure degrees of freedom
<i>q</i>	pressure weighting function
<i>r</i>	particle/bubble radius
$\langle \mathbf{r}_C \rangle$	discrete residual of continuity equation
<i>r_{inf}</i>	influence radius
<i>r_{d,rel}</i>	relative residual vector of particle position
$\langle \mathbf{r}_M \rangle$	discrete residual of momentum equation
<i>r_{p,rel}</i>	relative residual vector of fluid pressure
<i>r_{r,rel}</i>	relative residual vector of bubble radius
$\tilde{\mathbf{R}}$	radius vector in Aitken relaxation
R_C	residual vector of continuity equation
R_d	residual vector of particle position
Re	Reynolds number
Re _p	particle Reynolds number
R_M	residual vector of momentum equation
R_p	residual vector of fluid pressure
R_r	residual vector of bubble radius
<i>s</i>	parametrization parameter
<i>s_f</i>	safety factor for adaptive time stepping
<i>s</i>	interface forces
<i>s'</i>	volume averaged interface force
$\tilde{\mathbf{s}}'$	volume averaged interface force without pressure force
$\tilde{\mathbf{s}}'$	volume averaged interface force without pressure and viscous force
<i>S</i>	safety factor for critical time step size
\mathcal{S}_p	solution function space for fluid pressure
$\mathcal{S}_{\langle p \rangle}$	finite-dimensional subspace for resolved fluid pressure solution function
$\hat{\mathcal{S}}_p$	infinite-dimensional subspace for unresolved fluid pressure solution function
\mathcal{S}_u	solution function space for fluid velocity
$\mathcal{S}_{\langle u \rangle}$	finite-dimensional subspace for resolved fluid velocity solution function

$\hat{\mathcal{S}}_u$	infinite-dimensional subspace for unresolved fluid velocity solution function
t	time
t	tangent
t_{end}	time period
tol_d	tolerance for relative particle position
tol_p	tolerance for relative fluid pressure residual
tol_r	tolerance for relative bubble radius residual
tol_{RP}	tolerance for RP abort criterion
T_b	bubble inside temperature
T_∞	temperature of surrounding liquid
\mathbf{u}	velocity of continuous phase
u_{bg}	background velocity
u_{ref}	characteristic fluid velocity
u_{sp}	spout velocity
\mathbf{U}	vector of fluid velocity degrees of freedom
$\dot{\mathbf{U}}$	vector of fluid acceleration degrees of freedom
v	particle velocity magnitude
\mathbf{v}	particle velocity
v_{rel}	absolute value of relative velocity
\mathbf{v}_{rel}	relative velocity
V	averaging volume
\mathbf{V}	visous matrix
V_c	volume of continuous phase in averaging volume
V_p	volume of dispersion
\mathcal{V}_p	weighting function space for fluid pressure
$\mathcal{V}_{\langle p \rangle}$	finite-dimensional subspace for resolved fluid pressure weighting function
$\hat{\mathcal{V}}_p$	infinite-dimensional subspace for unresolved fluid pressure weighting function
\mathcal{V}_u	weighting function space for fluid velocity
$\mathcal{V}_{\langle u \rangle}$	finite-dimensional subspace for resolved fluid velocity weighting function
$\hat{\mathcal{V}}_u$	infinite-dimensional subspace for unresolved fluid velocity weighting function
w	velocity weighting function
W	mass flow rate
\mathbf{x}	position in current configuration
\mathbf{x}^{bin}	position of bound of Cartesian binning grid
\mathbf{x}	position vector in current configuration

Subscripts and Superscripts

$(\cdot)_{\text{crit}}$	critical value of quantity (\cdot)
$(\cdot)_D$	value at Dirichlet boundary

$(\cdot)_i$	of dispersion i
$(\cdot)_{ij}$	between partners i and j
$(\cdot)_{inf}$	quantity at inflow
$(\cdot)_j$	of dispersion j
$(\cdot)_{\max}$	maximal value of quantity (\cdot)
$(\cdot)_{\min}$	minimal value of quantity (\cdot)
$(\cdot)_n$	in normal direction
$(\cdot)_N$	value at Neumann boundary
$(\cdot)_{out}$	quantity at outflow
$(\cdot)_t$	in tangential direction
$(\cdot)_{weak}$	quantity (\cdot) obtained with weak coupling scheme
$(\cdot)_{str}$	quantity (\cdot) obtained with strong coupling scheme
$(\cdot)_\Gamma$	interface quantity
$(\cdot)^T$	transpose
$(\cdot)^0$	undisturbed flow quantity
$(\cdot)_0$	initial value
$\overset{\circ}{(\cdot)}$	intersection quantity
$(\cdot)_\perp$	projected quantity along a certain direction

Operators

$\nabla \cdot (\cdot)$	divergence operator
$\nabla(\cdot)$	gradient operator
$\Delta(\cdot)$	increment
\otimes	dyadic product
$\frac{\partial(\cdot)}{\partial t}$	partial time derivative
$\frac{D(\cdot)}{Dt}$	total time derivative
$\text{tr}(\cdot)$	trace of matrix
$\overline{(\cdot)}$	volume average
$\langle(\cdot)\rangle$	phase average
$ (\cdot) $	absolut value
$\ (\cdot)\ _2$	L^2 -norm
(\cdot)	derivative of a quantity
(\cdot)	second derivative of a quantity
$(\cdot, \cdot)_\Omega$	inner L_2 product in the domain Ω
$(\cdot, \cdot)_{\Gamma_N}$	inner L_2 product on the Neumann boundary Γ_N

1 Introduction

1.1 Motivation

Multiphase (or multicomponent, as preferred by Crowe et al. [33]) flows are ubiquitous in our lives. A few examples are given to show the vast variety of applications:

- Bubbly flows can be observed in daily life in any glass of sparkling water with bubbles rising in the liquid. A large scale application is the transport of oil in pipelines. Another example is cavitation in pumps and at ship propellers which can lead to power loss, noise, vibration, and material damage. At the same time, cavitation at a purposeful level is desired in high-pressure fuel injection systems to enhance mixing processes of fuel and air. There is also a medical application of cavitation in which kidney stones are broken into smaller pieces by using impulsively collapsing bubbles close to the surface of the kidney stones.
- Droplet flows are e.g. small spittle droplets released by a coughing person which follow the air flow and spread in the environment. A rain storm can be an impressive example for droplets driven by fluid flow. An important medical problem is the application of aerosols into the lung of patients in such a way that the agent reaches optimally the infected region.
- Particulate flows are common in chemical industry processes when solid particles need to be transported, dried, or coated. Also the propagation of sand dunes or abrasive water-jet cutting are applications of particulate flows.

All aforementioned examples belong to the class of dispersed flows in which a large number of rather small dispersed objects interacts with a continuous phase. This will be the focus of this thesis.

For the sake of completeness, further flow categories are distinguished, see e.g. [33], [116], or [207]. The opposite category of dispersed flows are separated flows. They consist of a small number of bulk fluids. Stratified flow in a pipe or the Rayleigh-Taylor instability induced by heavier fluid placed on top of lighter one belong to this category. A liquid jet entering a domain filled with gas or liquid is another example. This list can further be extended by a droplet hitting a free surface forming a splash or oil in water released by a damaged oil-tanker. There is also a wide transition between separated flow and dispersed flow. Dependent on the flow velocity and fill level of the phases in a pipe, stratified flow may turn into plug or slug flow. The break-up of a liquid jet into gas leads to cascades of smaller structures. Hence, regions with dispersed flow and separated flow regimes coexist.

This small summary of applications illustrates the relevance of multiphase and especially dispersed flows. In the aforementioned examples, it is desirable to predict the behavior of dispersed flows in order to improve processes with respect to certain requirements. Often, experiments

are limited due to the involved time or spatial scales. Furthermore, the effort might be large for proper experimental setups.

Computer simulations can help to gain insight into multiphase flow and to improve design processes. However, even with the help of super computers, a full resolution of real world dispersed flow applications is still not feasible. Hence, simplified models are necessary to cope with the complex phenomena included in dispersed flows.

1.2 Numerical models for dispersed flows

Many different approaches can be applied to the numerical simulation of dispersed multiphase flows. The choice is usually driven by the desired resolution of the dispersed phase, the flow around the dispersed phase and the size of the problem of interest. Inspired by the review paper of van der Hoef et al. [216], a distinction into methods with resolved, underresolved and unresolved interface between the involved phases in dispersed flow is possible.

The most simplified models are known as homogenized or mixture models. They are also denoted as one-fluid model because only one set of governing equations is solved. Hence, these models do not resolve the interface between the phases. Pioneering work goes back to Ishii [106] and different variants have been developed later on. Manninen and Taivassalo [143] reviews the mixture model with a slip-velocity between the involved phases. Dependent on the model to compute the velocity differences, drift-flux model (see Zuber and Findlay [243] or Ishii [107]), diffusion model (see Ishii [106] or Ungarish [211]) and further variants by e.g. Pericleous and Drake [165], Chao et al. [25] or Johansen et al. [110] have been developed. A common application for these models is gas-liquid mixtures in pipes. Assuming thermodynamic equilibrium between the phases, i.e. identical velocity, pressure, and temperature of the involved phases, the cavitation phenomenon has been modeled by e.g. Kubota et al. [122], Schmidt et al. [181], or Schnerr et al. [183].

The aforementioned homogenized models suffer from the difficulty of a strong link between the different phases which is not necessarily fulfilled by the problem of interest. Hence, more detailed approaches have been developed which resolve the involved phases such that an interface between the dispersions and the carrier fluid in the dispersed flow comes into play. Dependent on the detail of the resolution of the dispersed phase, several approaches can be distinguished. To the class of fictitious domain methods belongs the approach presented by Glowinski et al. [73], Glowinski et al. [74], and Patankar et al. [163]. Therein, the fluid is described in an Eulerian frame with fixed grid covering the full domain. The dispersions are driven by the fluid forces using Newton's second law. The fluid mesh resolution is finer than the size of a particle and the fluid forces are computed at the interface of the dispersions. Hence, fluid traction is integrated over the surface of each particle leading to a force resultant. In order to couple the motion of the dispersed phase with the fluid, Lagrange multipliers are applied where particles reside in such a way that the fluid velocity is identical to the particle velocity. Particle-particle and particle-wall collisions are accounted for with short-range repulsive forces which are also added in Newton's second law. Instead of using Lagrange multipliers, the particle velocity can be imposed as Dirichlet boundary condition in the fluid such that a no-slip condition between the dispersion's surface velocity and the fluid is enforced. This approach is known as fictitious boundary method and is used e.g. by Duchanoy and Jongen [51], Wan and Turek [225], or Avci

and Wriggers [9]. Also, the immersed boundary method invented by Peskin [166] belongs to the class of fictitious domain methods. A source term on the right-hand side of the fluid momentum equation is used to account for the influence of the dispersed phase. The force at points on the dispersion's surface is applied to the fluid volume using a regularized Dirac delta function. Peskin's approach belongs to the group of continuous forcing approaches, cf. Mittal and Iaccarino [151]. To overcome the possible numerical stiffness of the approach, an alternative forcing model has been applied by Goldstein et al. [76] or Saiki and Biringen [179]. Continuous forcing has been further developed by Fadlun et al. [58] to impose a consistent force term which enforces the fluid to match the interface velocity of each dispersion. This is known as discrete forcing approach. As the interior of the dispersions is still occupied with fluid, it is either possible to impose velocity coupling conditions inside the dispersion or to leave the velocity free to develop a flow without imposing anything. According to Fadlun et al. [58], the solution of the fluid around the dispersions is nearly identical for both cases. The force coupling method by Maxey and Patel [146] and Lomholt and Maxey [138] is similar to Peskin's approach as the force exerted from the dispersion onto the continuous fluid is regularized with a Gaussian curve. All aforementioned approaches of the fictitious domain method have an overlapping fluid and dispersion domain. The difference is in the coupling conditions.

Instead of using overlapping domains, the interior of the dispersed phase can be resolved separately from the outside fluid phase. Such an approach is introduced for bubbly flows by Unverdi and Tryggvason [212]. At this high level of detailedness in which both sides of the interface are fully resolved with their own set of equations, two main methods can be distinguished based on how the interface is treated. The approach of Unverdi and Tryggvason [212] belongs to the class of methods which track the interface. Also, the marker and cell method invented by Harlow and Welch [89] belongs to this category. The alternative of tracking is to capture the interface with the level set technique, see e.g. Osher and Sethian [161], Sethian and Smereka [186], or Hu et al. [99]. Another interface capturing approach is the volume-of-fluid (VOF) method introduced by Hirt and Nichols [93] and review by Fuster et al. [67]. All aforementioned approaches have in common, that the fluid equations (independently of overlapping domains or separated domains for fluid and dispersions) are solved on a fixed grid. In contrast, the arbitrary Lagrangian-Eulerian (ALE) method relies on a moving mesh in which the fluid mesh is deformed to follow the dispersions' motion. In order to resolve the problem of distorted fluid grids, continuous remeshing and data mapping is applied, cf. Hu et al. [97] or Hu et al. [98].

All approaches which rely on a resolved interface between the carrier fluid flow and the dispersed phase require the fluid mesh to be finer resolved than the smallest dispersion is in size. At least a few fluid cells in each spatial direction are necessary to enable the force computation of the fluid forces acting on the dispersions. The computation of 15,000 resolved cavitation bubbles in a fluid mesh with $13 \cdot 10^{12}$ cells on a super computer (see Rossinelli et al. [176]) was awarded with the Gordon Bell Prize in 2013. Hence, this is far beyond the scope of industrial applications.

An intermediate level of detailedness (and also of computational effort) can be achieved using so-called two-fluid models in which the equations for the carrier as well as for the dispersed phase are averaged over the whole computational domain leading to interpenetrating continua. The foundations have been laid by Anderson and Jackson [5] and Ishii [106]. Further details on the derivation can be found in Zhang and Prosperetti [238]. Source terms emerge while deriving the averaged set of equations. These source terms in the continuity and momentum equation

act as coupling terms between the phases. The two-fluid model is successfully applied in gas-fluidization problems, cf. Gidaspow [71], Sokolichin and Eigenberger [191], or van Wachem et al. [219]. The difficulty in the solid phase is to find an appropriate constitutive law which models the interaction of particles correctly, cf. Ishii and Mishima [108]. In order to circumvent the difficulties in modeling the solid constitutive law, it is valid to track each particle individually, cf. Kleinstreuer [116], van der Hoef et al. [216], or Yu and Xu [235]. It is also trivial to include poly-sized dispersions which is non-trivial in two-fluid models, see Rizk [175]. Consequently, this approach combines a continuous description of the carrier phase in Eulerian frame and a particle description of the dispersed phase in Lagrangian frame. The interface between the phases is not resolved explicitly. The dispersions are treated point-like and they are tracked individually. Hence, this approach belongs to underresolved interface models. The effort is increased compared to two-fluid models because of the potentially large number of dispersions which are tracked individually. The approach is known under many different names: particle trajectory model by Kleinstreuer [116], discrete particle model in the review paper by Deen et al. [41] or van Wachem et al. [219], combined continuum and discrete model by Yu and Xu [235] or Zeidan et al. [237], computational fluid dynamics-discrete element method (CFD-DEM) by Kloss et al. [117] or Gupta et al. [83]. The probably most commonly used notation is Euler-Lagrange model (not to be confused with the ALE method in the context of moving mesh approaches such as in fluid-structure interaction). The focus of this thesis is on the Euler-Lagrange model which will be denoted with this name in the reminder. A detailed overview over the literature of Euler-Lagrange models will be given at the end of this section.

To further clarify, in the present thesis, each particle in the Euler-Lagrange model represents a physical object (solid particle, gaseous bubble or liquid droplet) which is tracked throughout the simulation. In contrast, there are many approaches available which use a particle based discretization for the Navier-Stokes equations to model fluid flow. An overview is given in the review paper by Koumoutsakos [121]. The continuous flow field is approximated by a set of discrete particles. Each particle holds information such as position, velocity, volume, and e.g. vorticity strength in vortex methods (see Cottet and Koumoutsakos [31] or Selle et al. [185]) or densities in smoothed particle hydrodynamics (SPH) (see Gingold and Monaghan [72] or Monaghan [152]). Derived from SPH is the moving-particle semi-implicit method (see Koshizuka and Oka [119] or Koshizuka et al. [120]). These examples are just a few among many others. They have in common that a kernel function is placed at the particle position which spreads the influence in the neighborhood of the particle. Particle interaction is used to evolve the fluid field. The methods differ in the way how to compute spatial derivatives, how flow quantities are interpolated, whether explicit or implicit time integration schemes are applied, etc. Nevertheless their mesh free character unifies these methods. Meshfree particle methods have also been applied to solve structural dynamics problems, see e.g. the element-free Galerkin method by Belytschko et al. [13], the diffuse element method by Nayroles et al. [156], or the reproducing kernel particle method by Liu et al. [135]. The Lattice Boltzmann method (LBM), see Chen and Doolen [26] or He and Luo [90], is also used to model fluid flows. The underlying idea is that fictive particles residing on a discrete lattice resemble macroscopic flow behavior by repeated collision and streaming operations.

Besides pure particle discretization approaches, also combined approaches which rely on non-fixed particles and a fixed grid in the background are applied to solve partial differential equations. Parts of the computation are performed on the grid while the information is stored in the

particles. Data mapping from the particles to the grid and vice versa is necessary. To this group of methods belong e.g. the particle-in-cell method invented by Harlow [88] which has been further developed to the material point method by Sulusky et al. [200]. Instead of using a fixed grid, in the particle finite element method (PFEM) a mesh is generated in each time step via Delaunay tessellation, cf. Idelsohn et al. [104] and Oñate et al. [159]. The mesh in PFEM is used to compute the forces acting on the particles which are tracked in a Lagrangian frame. Furthermore, the governing equations are solved on this generated grid. In PFEM, the particles can represent fluid phase or solid phase and thus the Navier-Stokes equations or the solid dynamics balance of linear momentum is solved in each domain, respectively. The nontrivial task is to find the respective boundaries and keep the generated meshes well-shaped demanding for adaptive mesh refinement strategies. The distinction between fluid and solid material points enables the solution of flexible bodies submerged in fluid flow which can be used to model dispersed particulate flows, see Oñate et al. [160]. Those complex scenarios might also be tackled with fluid-structure interaction methods which are capable of handling collisions between solid sub domains, cf. e.g. Astorino et al. [7]. The latter method is currently not applied to dispersed flows due to the computational complexity. Nevertheless, it would be possible. Similar complex is the approach chosen by Leonardi et al. [133] which combines a fluid modeled with the LBM approach interacting with Lagrangian particles accounted for in a DEM framework and additionally flexible structures modeled with the classical finite element method (see e.g. the textbooks of Zienkiewicz et al. [241] or Hughes [101]) which interact with the fluid as well as with the particles.

A very interesting field, which will not be covered in this thesis, is dispersed turbulent flow. The particles are known to influence turbulence (both attenuation as well as enhancement are reported, cf. Elghobashi [55]) and proper modeling is investigated e.g. by Elghobashi [55], Sommerfeld [193], Laín et al. [128], Mazzitelli et al. [148], Kuerten [123], Uhlmann [210], Vreman et al. [222], Schwarzkopf et al. [184], Gobert and Manhart [75], Schneiderbauer and Pirker [182], or Corsini et al. [30], see also the review article by Dhotre et al. [44].

After having reviewed models for dispersed flows which will not be covered in this thesis, an overview of the literature concerning Euler-Lagrange models with underresolved interface between the phases will be given. The focus of this thesis will be on this method. The continuous phase is modeled using a fixed grid in Eulerian frame whereas the (point-) particles are tracked in a Lagrangian frame. The dispersed phase and continuous phase interpenetrate, i.e. cover the same domain, thus that the fluid covers the whole computational domain.

A distinction can be made based on the coupling between the Euler and the Lagrange phase. According to Elghobashi [55], the dilute and the dense suspension regime can be distinguished at a threshold of 0.1 % volume fraction of the dispersed phase in the mixture volume. Above this limit, it is necessary to account for collisions between dispersions in order to obtain reasonable results. The dilute regime can be further distinguished. Below 10^{-4} % volume fraction of dispersion, the effect of the dispersed phase onto the continuous phase can be neglected. Hence, only effects from the continuous phase on the dispersed phase are accounted for, which is also referred to as one-way coupling.

The first approach of combining an Eulerian description for the continuous phase and a Lagrangian description for the dispersed phase dates back to Migdal and Agosta [150]. They account for the dispersed phase with source terms in the mass, momentum and energy balance of the continuous phase. Particles are driven by the drag force exerted by the continuous phase. The reaction force of the particle drag force is included in the fluid momentum source term. The

occupied volume of the dispersions is accounted for as a source term in the continuity equation. Collisions between the dispersions are neglected. Hence, this approach belongs to the class of two-way coupled approaches including the effect of displaced volume by the dispersed phase while ignoring inter-dispersion collisions. The case of two-way coupling with including collisions between the dispersions is sometimes denoted as four-way coupling, due to the mutual interaction of continuous phase with dispersions and dispersions with each other.

One-way coupling can be found in literature especially when the focus is on turbulence modeling, e.g. Breuer et al. [21], Squires and Simonin [195], Kuerten [123], Lambert et al. [129], or Corsini et al. [30]. The assumption of a large number of small enough dispersions justifies this assumption. The same argumentation is applied in bio-medical applications when a large number of aerosol droplets enters the human lung, see e.g. Zhang et al. [240] or Feng and Kleinstreuer [60]. The latter compare results for one- and two-way coupled simulations. Further comparisons of one- and two-way coupled simulations in non-biological applications can be found in e.g. Druzhinin and Elghobashi [50], Derksen [43], or Shams et al. [187]. A one-way coupled simulation of bubbles undergoing radius changes based on the Rayleigh-Plesset equation can be found in Mattson and Mahesh [144].

In case the dispersions are very small, they can be grouped to so-called parcels. Within a parcel, one particle is analyzed in detail and the results are applied to the remaining dispersions in the parcel, cf. Subramaniam [197] or Löhner et al. [137].

A, by far not complete, overview of the two-way coupled approaches in the literature is given in Table 1.1. The approaches are distinguished whether the dispersed phase fraction is accounted for in the continuous phase, whether collisions between the dispersions are included, and whether a variable radius of the particles governed by the Rayleigh-Plesset equation is incorporated in the respective approach.

author	dispersed phase fraction?	collision model?	RP equation?	phases: continuous - dispersed
Durst et al. [54]	no	–	no	gas/liquid - solid
Laín et al. [127]	no	–	no	liquid - gas
Mazzitelli et al. [148]	no	–	no	liquid - gas
Sommerfeld et al. [194]	no	stochastic	no	liquid - gas
Decker [39]	no	stochastic	no	liquid - solid
Zohdi [242]	no	mixed	no	gas - solid
Vreman et al. [222]	no	MD	no	gas - solid
Sungkorn et al. [201]	no	stochastic	no	liquid - gas
Vallier et al. [215]	no	–	no	liquid - gas
Laín and Sommerfeld [126]	no	stochastic	no	gas - solid
Vallier [214]	no	MD	yes	liquid - gas
Löhner et al. [137]	no	DEM	no	gas - solid
Dukowicz [52]	yes	–	no	gas - liquid
Tomiyama et al. [205]	yes	–	no	liquid - gas
Sokolichin et al. [192]	yes	–	no	liquid - gas
Kitagawa et al. [115]	yes	–	no	liquid - gas/solid

author	dispersed phase fraction?	collision model?	RP equation?	phases: continuous - dispersed
Ferrante and Elghobashi [61]	yes	–	no	liquid - gas
Giannadakis et al. [69]	yes	–	yes	liquid - gas
Yakubov et al. [233]	yes	–	yes	liquid - gas
Ma et al. [141]	yes	–	yes	liquid - gas
Fuster and Colonius [66]	yes	–	yes	liquid - gas
Tsuji et al. [208]	yes	DEM	no	gas - solid
Hoomans et al. [94]	yes	MD	no	gas - solid
Delnoij et al. [42]	yes	MD	no	liquid - gas
Kawaguchi et al. [113]	yes	DEM	no	gas - solid
van Wachem et al. [220]	yes	DEM	no	gas - solid
Kafui et al. [111]	yes	MD	no	gas - solid
Shan and Mostaghimi [188]	yes	stochastic	no	gas - liquid
Yu and Xu [235]	yes	DEM	no	gas - solid
Deen et al. [40]	yes	MD	no	gas - liquid
Darmana et al. [35]	yes	MD	no	liquid - gas
Zhang and Ahmadi [239]	yes	MD	no	liquid - gas&solid
Link et al. [134]	yes	MD	no	gas - solid
Di Renzo and Di Maio [47]	yes	DEM	no	liquid/gas - solid
Shams et al. [187]	yes	DEM	yes	liquid - gas
Kloss et al. [117]	yes	DEM	no	gas - solid
Feng and Kleinstreuer [60]	yes	DEM	no	gas - solid
Gupta et al. [83]	yes	DEM	no	gas - solid

Table 1.1: Two-way coupled Euler-Lagrange approaches with underresolved interface in literature. The approaches are distinguished whether dispersed phase fraction, interdispersion collisions and variable radius governed by RP equation are included.

For the contact between the particles, two approaches are mainly used: the hard sphere and the soft sphere contact model. The former is preferred in molecular dynamics applications, see Alder and Wainwright [2] and the latter is also known as Discrete (or Distinct) Element Method (DEM) invented by Cundall and Strack [34]. In the soft sphere approach, particles are allowed to overlap and the size of the overlap is used to compute a repulsive force. In contrast, in the hard sphere approach, the particles are moved up to the point of a binary collision which is then solved for using linear and angular momentum equilibrium while neglecting all other force contributions during the collision evaluation. In the latter, an event queue is used and collision events are processed one by one. A detailed overview of both methods is given, e.g. by Sigurgeirsson et al. [189] or Luding [140]. A comparison of both contact approaches in the application of dispersed flows can be found in Di Renzo and Di Maio [46], Deen et al. [41], and Crowe et al. [33]. In Euler-Lagrange models both collision approaches can be found as obvious in Table 1.1. The advantage of the soft sphere contact model is in densely packed particle regimes with potentially persisting contact. However, a small time step size is necessary for stable time integration. The

hard sphere approach cannot handle persisting contact. However, it is superior when collisions occur less frequently because a larger time step size can be chosen. For particle applications without fluid, Luding [140], Valentini and Schwartzenruber [213], and Buist et al. [24] propose a combination of both collision methods in order to avoid the respective drawbacks. Both presented collision models belong to the class of deterministic collision models. In contrast, a stochastic collision model is developed by Sommerfeld [193] in which a fictive collision partner is created based on the particles in the neighborhood and collision probability is evaluated based on kinetic theory.

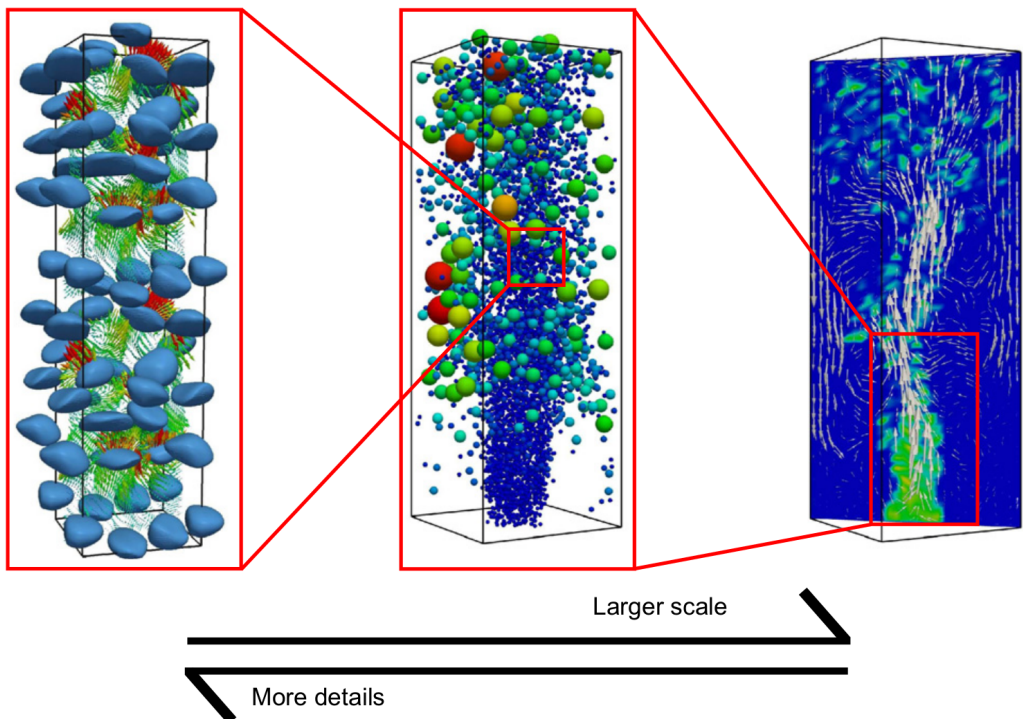


Figure 1.1: Comparison of models: Resolved (left), under resolved (center), and unresolved interface (right) (from Lau et al. [130]).

In order to summarize the vast variety of approaches for dispersed multi-phase flows, see Figure 1.1. There is a trade-off between detailedness of the results and the size of the scales which can be resolved with reasonable computational effort. The compromise is an Euler-Lagrange approach which represents each dispersion as an individual particle which is tracked over time. An advantage over mixture models is that there is no strong coupling between the phases incorporated in the model. At the same time, the interface is not resolved in detail allowing for a much coarser modeling of the continuous phase. Therefore, an Euler-Lagrange approach is suitable to solve dispersed flows with a large number of dispersions of potentially different size in a reasonable time.

1.3 Research objective and achievements

The aim of the present thesis is to develop a multipurpose simulation tool for dispersed flows based on an Euler-Lagrange approach including inner- and inter-phase interactions. The achievements of this thesis may be summarized as follows:

- To the best of the author's knowledge, a variational multiscale formulation of the volume averaged Navier-Stokes (NS) equations is derived for the first time which includes dispersed phase fraction, i.e. the effect of fluid volume displaced by the dispersions. The present formulation for dispersed flow is closely related to the variational multiscale approach of variable-density flow at low Mach number presented by Gravemeier and Wall [77]. This is extended towards the volume averaged NS equations to represent the continuous phase in the Euler-Lagrange framework.
- Furthermore, a novel second order polynomial filtering function for the dispersed phase fraction computation is proposed. The dispersed phase fraction is used to account for the displaced volume of the evolution of the dispersed phase by projecting the volume of each dispersion onto the fluid using a filtering function. Dispersed phase fraction calculation involves solving volume integrals over the fluid elements of the Eulerian grid with the filtering function in the integrand. These volume integrals are transformed to line integrals via applying divergence theorem twice and due to the polynomial filtering function, the line integrals can be integrated analytically.
- It is the first time that a strong coupling scheme using relaxation based on Aitken's Δ^2 method is applied in an Euler-Lagrange approach. In particular, dispersed bubbly flows whose radius is governed by the Rayleigh-Plesset equation are prone to convergence problems. Here, convergence is achieved with a strong coupling scheme and it is massively accelerated using Aitken's Δ^2 -method.
- The suggested framework allows for investigating a vast variety of applications. The weak and strong coupling schemes enable a convenient simulation of fluid-particle coupled problems covering the entire spectrum of dispersed flow problems from gaseous to solid particles. Due to the versatile framework, in the limit of a vanishing influence of the continuous phase, the developed framework reduces to a pure particle solver which includes freely moving and colliding particles with and without walls.
- A specifically-devised parallelization strategy accounts for the trend towards large scale simulations. Memory limitations are avoided by circumventing a fully redundant data layout. An essential feature is that coupling information between the phases is exchanged locally without the need for inter-processor communication during evaluation. This comes at cost of appropriate ghosting which needs to be provided at the processor boundaries. The number of dispersions and fluid elements covered in the examples of this thesis reaches sizes $\mathcal{O}(10^6)$.

The proposed multipurpose simulation tool for dispersed flow problems as well as pure particle problems is implemented in BACI, a parallel finite-element-based multiphysics solver which is

developed jointly at the Institute for Computational Mechanics and the Mechanics & High Performance Computing Group at the Technische Universität München. It utilizes powerful libraries provided by the open-source Trilinos project conducted by Heroux et al. [91].

The starting point for the present work is the variable-density variational multiscale formulation for the fluid flow at low Mach number developed by Gravemeier and Wall [77]. The extension of the formulation for volume averaged NS equations as well as all particle related issues including the coupling of flow and particle solver are developed in the scope of this thesis.

Parts of the numerical methods shown in this thesis have already been published in Hammerl and Wall [87] and Menner* et al. [149].

1.4 Outline

The outline of this thesis is as follows. In Chapter 2, the volume averaged Navier-Stokes equations are summarized to account for the continuous phase in an Eulerian frame. The dispersed phase is introduced as an ensemble of particles which are tracked in a Lagrangian way. Each particle is equipped with six degrees of freedom to account for translational and rotational degrees of freedom. As an extension, it is possible to account for radius changes governed by the Rayleigh-Plesset equation in case bubbly flow is investigated. Lastly, the coupling between the carrier phase and the dispersions is described. Afterwards, in Chapter 3, the proposed computational approach is presented. Herein, the residual-based variational multiscale method is derived to represent the spatial and temporal discretization of the continuous phase. Furthermore, the weakly and strongly coupled partitioned fluid-particle framework is described. The discrete coupling of continuous and dispersed phase is highlighted with special attention on the dispersed phase fraction computation which accounts for the displaced volume of the particles in the fluid domain. Next, the temporal discretization of the Rayleigh-Plesset equation is given including its adaptive time stepping scheme. Several numerical examples are provided in Chapter 4 to show the versatility of the developed framework. Two pure particle test cases are followed by dispersed flow problems which include a Taylor-Green vortex, fluidized bed from chemical industry, bubbly flow at a NACA 0015 hydrofoil, and droplet flow into the complex geometry of a human lung. The thesis is concluded in Chapter 5 with a short summary and an outlook.

2 Mathematical model

This thesis aims at developing a simulation tool for a variety of dispersed flows. As aforementioned, the dispersed phase can be solid, liquid, or gaseous and its constituents are thus denoted particle, droplet, or bubble, respectively, in a physical correct description. In order to unify this notation issue, the following convention is used throughout this thesis: The dispersions are always denoted as particles when their size is constant. Hence, particles feature translational and rotational degrees of freedom. They can contact with each other and with walls and they can also interact with surrounding fluid flow. This means, that a bubble (in physical meaning) will be denoted as a particle in case it does not change its size during the simulation. The notation of a bubble will solely be used when the particle additionally features a variable radius besides all the other aforementioned properties.

Some more assumptions are made throughout this thesis. The dispersed phase consists of particles of spherical shape which can neither break up nor coalescence. The interested reader is referred to Wachs [224] and references therein for an overview on non-spherical dispersed flow analysis. Furthermore, the content of each particle is assumed to be homogeneous. An important assumption concerns the surface of the dispersions. A no-slip condition exists between the surface of solid particles and the liquid carrier flow. In contrast, gaseous bubbles in liquid feature a slip condition between the bubble and the liquid, see Magnaudet and Eames [142]. This would lead to a different behavior especially in the drag force exerted from the carrier phase onto the dispersions. Fortunately, the slip condition of gaseous bubbles only applies to purified liquids which can exclusively be found on test rigs. Hence, any liquid found in daily life or industrial application contains so many tiny contaminants, that the dispersions' surface gets immobilized leading to a behavior identical to solid particles, see Clift et al. [28], Magnaudet and Eames [142], and Dijkhuizen et al. [48] for further explanation. Consequently, there is no difference in the coupling conditions between carrier phase and particles, drops or bubbles for all applications except those with purified liquid. The present thesis does not adapt the surface treatment of gaseous bubbles and hence, the developed formulation is capable of handling the vast majority of dispersed flows with non-purified liquids. This needs to be kept in mind when further reading this thesis. Besides the assumption of an immobilized surface, no mass and no heat transfer across the surface is considered.

In the remainder of this chapter, the volume averaged equations for the carrier phase are presented followed by the governing equations of the dispersed phase. Finally, the coupling between the phases is discussed.

2.1 Volume-averaged Navier-Stokes equations for the continuous phase

In this section, the governing equations for a single-phase continuous liquid are summarized. The volume-averaged NS equations are derived by applying volume averaging theory. The continuous fluid is described in an Eulerian frame whereas the dispersed phase is handled as discrete particles which are tracked individually in a Lagrangian frame using Newton's second law. The averaging procedure enables to evaluate the fluid also inside regions which are occupied by particles. As the interface is not resolved in this approach, it is not possible to enforce a no-slip condition between the phases. Hence, a relative velocity and relative acceleration between carrier phase and particles is allowed.

2.1.1 Strong form of the Navier-Stokes equations

The Eulerian fluid is in its phase treated as a continuous medium and conservation of mass and momentum are fundamental principles of the fluid motion which can be found in detail for example in the textbook by Batchelor [11]. The fluid is assumed incompressible. Hence, the strong form of the NS equations comprises the continuity and momentum equation, viz

$$\frac{\partial \rho_l}{\partial t} + \nabla \cdot (\rho_l \mathbf{u}) = 0 \quad \text{in } \Omega, \quad (2.1)$$

$$\frac{\partial (\rho_l \mathbf{u})}{\partial t} + \nabla \cdot ((\rho_l \mathbf{u}) \otimes \mathbf{u}) = -\nabla p + \nabla \cdot \boldsymbol{\tau} + \rho_l \mathbf{g} + \mathbf{s} \quad \text{in } \Omega \quad (2.2)$$

where ρ_l denotes the constant fluid density, \mathbf{u} the velocity, p the pressure, $\boldsymbol{\tau}$ the viscous stress tensor and \mathbf{g} the gravity force vector. In addition to the standard momentum equation, an extra source term \mathbf{s} accounts for the interface forces from the disperse phase which will be detailed later. There is no mass transfer between the continuous and the disperse phase leading to a vanishing right-hand side in the continuity equation (2.1). The stress tensor reads

$$\boldsymbol{\tau} = 2\mu \left(\boldsymbol{\epsilon}(\mathbf{u}) - \frac{1}{3} (\nabla \cdot \mathbf{u}) \mathbf{I} \right) = 2\mu \boldsymbol{\epsilon}'(\mathbf{u}) \quad (2.3)$$

using the dynamic viscosity μ . The rate of deformation tensor reads

$$\boldsymbol{\epsilon}(\mathbf{u}) = \frac{1}{2} \left((\nabla \mathbf{u}) + (\nabla \mathbf{u})^\top \right), \quad (2.4)$$

the identity tensor \mathbf{I} and the abbreviation

$$\boldsymbol{\epsilon}'(\mathbf{u}) = \boldsymbol{\epsilon}(\mathbf{u}) - \frac{1}{3} (\nabla \cdot \mathbf{u}) \mathbf{I}. \quad (2.5)$$

Equations (2.1) and (2.2) are valid in the domain Ω which is occupied by the continuous phase.

To complete the set of equations, initial and boundary conditions need to be given. The initial velocity reads

$$\mathbf{u}(\mathbf{x}, t=0) = \mathbf{u}_0(\mathbf{x}). \quad (2.6)$$

The boundary of the domain $\partial\Omega$ can be divided into non-overlapping parts $\Gamma_D \cup \Gamma_N = \partial\Omega$ with Dirichlet boundary conditions and Neumann boundary conditions prescribed at Γ_D and at Γ_N , respectively, reading

$$\mathbf{u} = \mathbf{u}_D \quad \text{on } \Gamma_D, \quad (2.7)$$

$$\boldsymbol{\tau} \cdot \mathbf{n}_l = \mathbf{h} \quad \text{on } \Gamma_N \quad (2.8)$$

where \mathbf{n}_l denotes the outward pointing unit normal on the boundary and \mathbf{h} the prescribed Neumann boundary momentum flux.

2.1.2 Volume averaging procedure

2.1.2.1 Basics

Following the argumentation of Crowe et al. [33], it is essential not to use single phase fluid equations which are enhanced solely by source terms to account for a second phase. The shortcoming is that the quantities of the fluid are not defined in regions occupied by the dispersion and therefore an evaluation using single phase equations is invalid at points inside the disperse phase. To overcome this problem, volume averaging based on the ideas of Anderson and Jackson [5] is applied to the fluid equations. Hence, the fluid properties of an averaged fluid can be evaluated at each point. It is important to note that the averaged NS equations do not describe the mixture of continuous and disperse phase, only the continuous phase is treated as an averaged continuum. The following derivations are taken from Crowe et al. [33], which the reader is referred to for more details. An essential requirement for proper volume averaging is the choice of the size of the averaging volume. Assuming a distribution of dispersion as shown in Figure 2.1 with l being

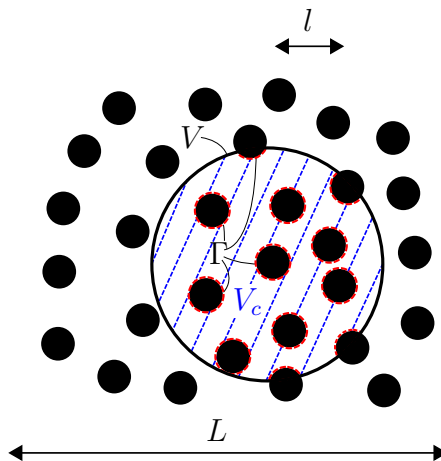


Figure 2.1: Length scales and averaging volume.

the average distance between disperse objects and L being the characteristic length of changes in the mixture properties, a proper averaging volume V is constrained by

$$l^3 \ll V \ll L^3. \quad (2.9)$$

The averaging volume comprises continuous phase and disperse phase. As only the continuous phase is volume averaged in the present thesis, the volume average of a quantity such as the velocity then reads

$$\bar{\mathbf{u}} = \frac{1}{V} \int_{V_c} \mathbf{u} dV \quad (2.10)$$

in which V_c is the volume of the continuous phase in the averaging volume V . An overbar denotes volume averaged quantities. The requirement in (2.9) leads to an average that does not vary significantly when the size of the averaging volume is modified. More relevant than the volume average is the phase average

$$\langle \mathbf{u} \rangle = \frac{1}{V_c} \int_{V_c} \mathbf{u} dV \quad (2.11)$$

which relates to V_c instead of the averaging volume V . It is denoted with angle brackets. Phase averaged quantities are of physical relevance as they are an average of the fluctuating flow around the submerged disperse phase. The interpretation of the volume averaged values is similar, but the crucial difference is in the division by a volume that is larger (or equal in case of pure liquid) than the volume occupied by the continuous phase. This means that the normalization volume is too large. So, the physically relevant average is the phase average for describing the flow. Also, the coupling forces to the disperse phase are based on phase averaged quantities. The naming should not be confused with Whitaker [228] who denotes the phase average as “intrinsic phase average” and the volume average as “phase average”. Due to the relation

$$V_c = \epsilon_l V \quad (2.12)$$

the volume and phase average of exemplarily the velocity is linked by the fluid fraction ϵ_l via

$$\bar{\mathbf{u}} = \epsilon_l \langle \mathbf{u} \rangle . \quad (2.13)$$

The fluid fraction represents the fill level of the averaging volume with continuous phase and it is restricted to $\epsilon_l \in]0, 1]$. Due to (2.9), it cannot vanish completely leading to $\epsilon_l > 0$.

2.1.2.2 Application to the continuity equation

The theory of volume averaging with its treatment of spatial and temporal derivatives can be found in Anderson and Jackson [5] and Whitaker [229]. The following derivations of the volume averaged NS equations are taken from Crowe et al. [33] and modified at certain places which are marked explicitly.

The volume average of the continuity equation (2.1) reads

$$\overline{\frac{\partial \rho_l}{\partial t}} + \overline{\nabla \cdot (\rho_l \mathbf{u})} = 0 . \quad (2.14)$$

Applying the theory of volume averaging, see Whitaker [229] for further details, the averages of the temporal and spatial derivative in (2.14) are shifted to the quantities themselves reading

$$\overline{\frac{\partial \rho_l}{\partial t}} + \frac{1}{V} \int_V \rho_t \mathbf{v}_i \cdot \mathbf{n}_i dV + \nabla \cdot (\overline{\rho_l \mathbf{u}}) - \frac{1}{V} \int_V \rho_t \mathbf{v}_i \cdot \mathbf{n}_i dV = 0 \quad (2.15)$$

which introduces integrals over all boundaries

$$\Gamma = \sum_i (\Gamma_i \in V) \quad (2.16)$$

of the included dispersions i in the averaging volume V , compare Figure 2.1. The velocity of the included dispersion i is denoted with \mathbf{v}_i , and its outward pointing normal is \mathbf{n}_i . The integrals have been simplified using the assumption of a homogeneous and rigid content in the dispersions and that there is no mass transfer between the phases. Finally, due to the different signs, the integrals cancel out each other. In the theory of volume averaging, it is possible to decompose any quantity into a phase averaged portion and a deviation thereof, see Whitaker [229], reading exemplarily for the velocity

$$\mathbf{u} = \langle \mathbf{u} \rangle + \delta \mathbf{u} \quad (2.17)$$

in which the deviation is denoted with $\delta(\cdot)$. The averaged mass flux in (2.15) reads with (2.13) and (2.17)

$$\overline{\rho_l \mathbf{u}} = \overline{\rho_l (\langle \mathbf{u} \rangle + \delta \mathbf{u})} = \epsilon_l \langle \rho_l \langle \mathbf{u} \rangle + \rho_l \delta \mathbf{u} \rangle = \epsilon_l \langle \rho_l \langle \mathbf{u} \rangle \rangle + \epsilon_l \langle \rho_l \delta \mathbf{u} \rangle . \quad (2.18)$$

The approximation $\langle \langle \mathbf{u} \rangle \rangle = \langle \mathbf{u} \rangle$ holds when the averaging volume is sufficiently smaller than the characteristic length scale of the fluid flow which is already contained in (2.9), for the derivation, see Whitaker [229] or Wood et al. [231]. However, the important point is the last term in (2.18) which is zero because the average over the deviation of a quantity vanishes by hypothesis, see Whitaker [229]. Hence, this term is no longer tracked in Crowe et al. [33] and elsewhere. As this thesis aims on casting the volume averaged NS equations into a variational multiscale framework, this term is kept and further explanations follow in Section 3.1.1.1. To continue with the derivation of the volume averaged continuity equation, the volume averaged fluid density in the time derivative in (2.15) is replaced with a phase averaged quantity using (2.13). Hence, the continuity equation expressed in phase averaged quantities and deviations thereof follows as

$$\frac{\partial (\epsilon_l \langle \rho_l \rangle)}{\partial t} + \nabla \cdot (\epsilon_l \langle \rho_l \mathbf{u} \rangle) + \nabla \cdot (\epsilon_l \langle \rho_l \delta \mathbf{u} \rangle) = 0 . \quad (2.19)$$

At this point, it has to be noted that the volume averaged density $\overline{\rho_l}$ is not constant as it is dependent on the time- and space-varying fluid fraction. In contrast, the temporal and spatial phase averaged fluid density $\langle \rho_l \rangle$ is constant as it is solely the property of the fluid as already assumed in Section 2.1.1. This leads to

$$\rho_l = \langle \rho_l \rangle , \quad (2.20)$$

$$\frac{\partial \rho_l}{\partial t} = 0 , \quad (2.21)$$

$$\nabla \rho_l = \mathbf{0} \quad (2.22)$$

which can be inserted into (2.19) leading to

$$\epsilon_l \frac{\partial \rho_l}{\partial t} + \rho_l \frac{\partial \epsilon_l}{\partial t} + \nabla \rho_l \cdot (\epsilon_l \langle \mathbf{u} \rangle) + \rho_l \nabla \cdot (\epsilon_l \langle \mathbf{u} \rangle) + \nabla \rho_l \cdot (\epsilon_l \langle \delta \mathbf{u} \rangle) + \rho_l \nabla \cdot (\epsilon_l \langle \delta \mathbf{u} \rangle) = 0 . \quad (2.23)$$

Finally, after division by the non-zero fluid density and the non-zero fluid fraction, (2.23) can be reordered as

$$\nabla \cdot \langle \mathbf{u} \rangle + \nabla \cdot \langle \delta \mathbf{u} \rangle = -\frac{1}{\epsilon_l} \left(\frac{\partial \epsilon_l}{\partial t} + \langle \mathbf{u} \rangle \cdot \nabla \epsilon_l + \langle \delta \mathbf{u} \rangle \cdot \nabla \epsilon_l \right). \quad (2.24)$$

This can be interpreted as a continuity equation of a non-divergency free fluid field with a source term that is driven by the temporal and spatial derivatives of the fluid fraction. In the limit case of a vanishing disperse phase such that $\epsilon_l = 1$ everywhere in the domain for all times and a sufficiently small averaging volume, the continuity equation of the incompressible NS equations $\nabla \cdot \langle \mathbf{u} \rangle = 0$ is recovered.

2.1.2.3 Application to the momentum equation

After having derived the continuity equation, the volume averaged momentum equation is deduced in the following. Again, the basic concepts are taken from Crowe et al. [33].

First, the left-hand side of the momentum equation (2.2) is volume averaged, viz

$$\overline{\frac{\partial(\rho_l \mathbf{u})}{\partial t}} + \overline{\nabla \cdot ((\rho_l \mathbf{u}) \otimes \mathbf{u})}. \quad (2.25)$$

Analogue to the procedure for the continuity equation from (2.14) to (2.15), the momentum equation reads

$$\overline{\frac{\partial(\rho_l \mathbf{u})}{\partial t}} + \frac{1}{V} \int_{\Gamma} \rho_l \mathbf{u} (\mathbf{v}_i \cdot \mathbf{n}_i) dV + \nabla \cdot \overline{((\rho_l \mathbf{u}) \otimes \mathbf{u})} - \frac{1}{V} \int_{\Gamma} \rho_l \mathbf{u} (\mathbf{v}_i \cdot \mathbf{n}_i) dV. \quad (2.26)$$

Again, the integrals have been simplified using the assumption of a homogeneous and rigid content in the dispersions and that there is no mass transfer between the phases. The integrals cancel out each other due to the different signs. Next, (2.13) and (2.20) are applied to (2.26), reading

$$\overline{\frac{\partial(\epsilon_l \rho_l \langle \mathbf{u} \rangle)}{\partial t}} + \nabla \cdot (\epsilon_l \langle \rho_l \mathbf{u} \otimes \mathbf{u} \rangle). \quad (2.27)$$

The decomposition of the velocities (2.17) and assuming constant fluid density leads to

$$\overline{\frac{\partial(\epsilon_l \rho_l \langle \mathbf{u} \rangle)}{\partial t}} + \nabla \cdot (\epsilon_l \rho_l \langle \mathbf{u} \rangle \otimes \langle \mathbf{u} \rangle + \epsilon_l \rho_l \langle \delta \mathbf{u} \rangle \otimes \langle \mathbf{u} \rangle + \epsilon_l \rho_l \langle \mathbf{u} \rangle \otimes \langle \delta \mathbf{u} \rangle + \epsilon_l \rho_l \langle \delta \mathbf{u} \otimes \delta \mathbf{u} \rangle) \quad (2.28)$$

in which the variations of volume averaged quantities are neglected, compare Whitaker [229]. The second and third summand in the divergence operator in (2.28) are neglected in Crowe et al. [33] and elsewhere because the average of deviations vanish by hypothesis, see also Whitaker [229]. Here, they are kept for further derivations to obtain the variational multiscale method, see Section 3.1.1.1. The last term in the divergence operator in (2.28) is designated by Crowe et al. [33] as ‘‘volume-averaged Reynolds stress’’ and it is comparable to the Reynolds stress as known from single-phase flow after having applied temporal averaging, cf. Launder et al. [131]. Again, it is neglected by Crowe et al. [33] and will be kept here for further derivations.

The next step is to apply volume averaging to the standard NS terms on the right-hand side of the momentum equation (2.2), reading

$$-\overline{\nabla p} + \overline{\nabla \cdot \boldsymbol{\tau}} + \overline{\rho_l g}. \quad (2.29)$$

The averages of the spatial derivatives are shifted to the quantities themselves in a next step

$$-\nabla (\epsilon_l \langle p \rangle) + \frac{1}{V} \int_{\Gamma} p \mathbf{n}_i dS + \nabla \cdot (\epsilon_l \langle \boldsymbol{\tau} \rangle) - \frac{1}{V} \int_{\Gamma} \boldsymbol{\tau} \cdot \mathbf{n}_i dS + \epsilon_l \rho_l \mathbf{g} \quad (2.30)$$

while using (2.20). A decomposition of pressure and stress tensor into the phase average and its deviation

$$p = \langle p \rangle + \delta p, \quad (2.31)$$

$$\boldsymbol{\tau} = \langle \boldsymbol{\tau} \rangle + \delta \boldsymbol{\tau} \quad (2.32)$$

is used to replace the pressure and the stress tensor in the integrals over the entire interface Γ between the phases in the averaging volume. The following transformations are given in full detail in Crowe et al. [33] in Appendix C thus that only the result is given here for the volume averaged right-hand side of the momentum equation:

$$-\nabla \langle p \rangle + \frac{1}{V} \int_{\Gamma} \delta p \mathbf{n}_i dS + \nabla \cdot \langle \boldsymbol{\tau} \rangle - \frac{1}{V} \int_{\Gamma} \delta \boldsymbol{\tau} \cdot \mathbf{n}_i dS + \epsilon_l \rho_l \mathbf{g} = -\nabla \langle p \rangle + \nabla \cdot \langle \boldsymbol{\tau} \rangle + \epsilon_l \rho_l \mathbf{g} + \mathbf{s}'. \quad (2.33)$$

The surface integrals are summed into \mathbf{s}' . They represent the volume averaged equivalent to the interface forces \mathbf{s} from the disperse phase in (2.2) in the strong form of the NS equations. As neither the exact interface Γ nor the fluctuations of the pressure δp or the viscous stress tensor $\delta \boldsymbol{\tau}$ is available, closure models are required. Details on the closure and the coupling procedure to the disperse phase will be given in Section 2.3.2.

2.2 Particle tracking in a Lagrangian frame

In this thesis, each particle represents a single physical object. It can be described by its position, velocity, acceleration, radius and homogenized density. Each particle is tracked on its individual path in a Lagrangian frame. The particles are assumed to be of spherical shape. This section contains the considered forces acting on each individual particle.

2.2.1 Rigid body kinematics

Assuming a rigid and homogeneous spherical particle, Newton's second law

$$m_i \frac{D\mathbf{v}_i}{Dt} = \left(\sum \mathbf{F} \right)_i \quad (2.34)$$

allows for computing the acceleration $D\mathbf{v}_i/Dt$ of particle i with mass m_i . The total time derivative is denoted with D/Dt . Moreover, $(\sum \mathbf{F})_i$ denotes the sum over all forces acting on the particle. In general, one can distinguish body and surface forces. The forces will be specified in the following

sections. The balance of angular momentum with respect to the particle center, which coincides with the center of gravity for a homogeneous particle, reads

$$I_i \boldsymbol{\alpha}_i = \mathbf{M}_i . \quad (2.35)$$

The angular acceleration $\boldsymbol{\alpha}_i$ can be computed based on the acting moments \mathbf{M}_i and the moment of inertia

$$I_i = \frac{2}{5} m_i r_i^2 \quad (2.36)$$

for a homogeneous sphere with radius r_i around an arbitrary axis through its center.

2.2.2 Fluid forces acting on particles

The forces acting on a single particle i submerged in a fluid can be written as

$$\mathbf{F}_i = \mathbf{F}_{vol,i} + \int_{\Gamma_i} -p \mathbf{n}_i + \boldsymbol{\tau} \cdot \mathbf{n}_i dS . \quad (2.37)$$

They can be divided into volume forces $\mathbf{F}_{vol,i}$, such as the gravity force, and surface forces acting on the particle surface Γ_i . The integral over the pressure and the viscous stress contributions of the fluid considering the unit outward normal \mathbf{n}_i enables an exact computation of the fluid forces. This integral can only be solved in case the interface is fully resolved which is not the case for the approach proposed in this work. The available fluid velocities and pressure are volume averaged and do not resolve the detailed flow around each single particle. Due to (2.9), the volume (and phase) averaged fluid properties are assumed to be constant over the volume occupied by the particle. Therewith, the interface forces in (2.37) can be modeled using (2.31) and (2.32) as

$$\int_{\Gamma_i} -p \mathbf{n}_i + \boldsymbol{\tau} \cdot \mathbf{n}_i dS = \int_{\Gamma_i} -\langle p \rangle \mathbf{n}_i + \langle \boldsymbol{\tau} \rangle \cdot \mathbf{n}_i dS + \int_{\Gamma_i} -\delta p \mathbf{n}_i + \delta \boldsymbol{\tau} \cdot \mathbf{n}_i dS . \quad (2.38)$$

Early works on the forces exerted from fluid to a rigid sphere go back to Stokes [196]. A summary of relevant forces acting on a sphere submerged to nonuniform flow is given by Maxey and Riley [147] and by Magnaudet and Eames [142]. Reviewing the literature of several decades leads to the conclusion that only for creeping flows valid models can be found and for all other cases a good modeling approach is still an open issue. An exhaustive discussion on each of the forces to be considered can be found in Crowe et al. [33], on which the following summary is based. A necessary assumption is that the resulting sum over all forces consists of a linear combination of distinct forces which do not interact, see Kleinstreuer [116]. This assumption applied to (2.34) reads

$$m_i \frac{D\mathbf{v}_i}{Dt} = \mathbf{F}_{g,i} + \mathbf{F}_{p,i} + \mathbf{F}_{\tau,i} + \mathbf{F}_{d,i} + \mathbf{F}_{l,i} + \mathbf{F}_{am,i} = \mathbf{F}_{g,i} + \sum \mathbf{F}_{\Gamma,i} , \quad (2.39)$$

$$\frac{D\mathbf{x}_i}{Dt} = \mathbf{v}_i . \quad (2.40)$$

The gravity force acting on a particle is

$$\mathbf{F}_{g,i} \stackrel{!}{=} \rho_{b,i} V_{p,i} \mathbf{g} \quad (2.41)$$

with the mass of a particle being simply its density $\rho_{b,i}$ times its volume $V_{p,i} = 4/3\pi r_i^3$ due to the assumption of a homogeneous and spherical particle with radius r_i . The coupling forces across the surface in (2.38)

$$\sum \mathbf{F}_{\Gamma,i} = \underbrace{\int_{\Gamma_i} -\langle p \rangle \mathbf{n}_i + \langle \boldsymbol{\tau} \rangle \cdot \mathbf{n}_i dS}_{\text{always present}} + \underbrace{\int_{\Gamma_i} -\delta p \mathbf{n}_i + \delta \boldsymbol{\tau} \cdot \mathbf{n}_i dS}_{\text{accounts for relative velocity/acceleration}} \quad (2.42)$$

can be distinguished into contributions which already occur when the particle follows the fluid flow and those that account for relative velocity and relative acceleration between particle and the conveying fluid. According to the derivations by Crowe et al. [33], the surface integral with the averaged pressure in (2.38) can be transformed to a volume integral by applying divergence theorem

$$\int_{\Gamma_i} -\langle p \rangle \mathbf{n}_i dS = - \int_{V_{p,i}} \nabla \langle p \rangle dV. \quad (2.43)$$

Assuming that the pressure gradient is constant over the volume of the particle due to (2.9) gives the so-called pressure force

$$\mathbf{F}_{p,i} \stackrel{!}{=} -V_{p,i} \nabla \langle p \rangle. \quad (2.44)$$

The same argumentation is used for reformulating the viscous forces:

$$\mathbf{F}_{\tau,i} \stackrel{!}{=} \int_{\Gamma_i} \langle \boldsymbol{\tau} \rangle \cdot \mathbf{n}_i dS = \int_{V_{p,i}} \nabla \cdot \langle \boldsymbol{\tau} \rangle dV = V_{p,i} \nabla \cdot \langle \boldsymbol{\tau} \rangle. \quad (2.45)$$

The divergence of the stress tensor can be computed using (2.3). An estimation for the relation of the norms of the latter two forces is given by Crowe et al. [33]:

$$\frac{|\nabla \cdot \langle \boldsymbol{\tau} \rangle|}{|\nabla \langle p \rangle|} \sim \frac{1}{\text{Re}} \quad (2.46)$$

with $\text{Re} = u_{\text{ref}} L_{\text{ref}} \rho_l / \mu$ being the Reynolds number of the fluid flow with some characteristic velocity u_{ref} and reference length L_{ref} . In the majority of applications in industry and daily life, $\text{Re} \gg 1$ leading to a negligible contribution of the viscous force term. However, in this thesis, the viscous force is included as it aims on a vast number of applications which might include low-Reynolds number flows.

Having reviewed the pressure and viscous force that already act when a particle perfectly follows the carrier fluid flow, the following forces contribute to the coupling due to a relative velocity or acceleration between the particle and the volume averaged fluid flow. The relative motion between the phases is a key aspect in the developed Euler-Lagrange framework. This allows for more flexibility regarding the applications because of a potentially looser coupling of the phases, compare Section 1.2.

The drag force due to the relative velocity reads

$$\mathbf{F}_{d,i} \stackrel{!}{=} \frac{1}{2} c_d \rho_l \pi r_i^2 \| \langle \mathbf{u} \rangle_i - \mathbf{v}_i \|_2 (\langle \mathbf{u} \rangle_i - \mathbf{v}_i) \quad (2.47)$$

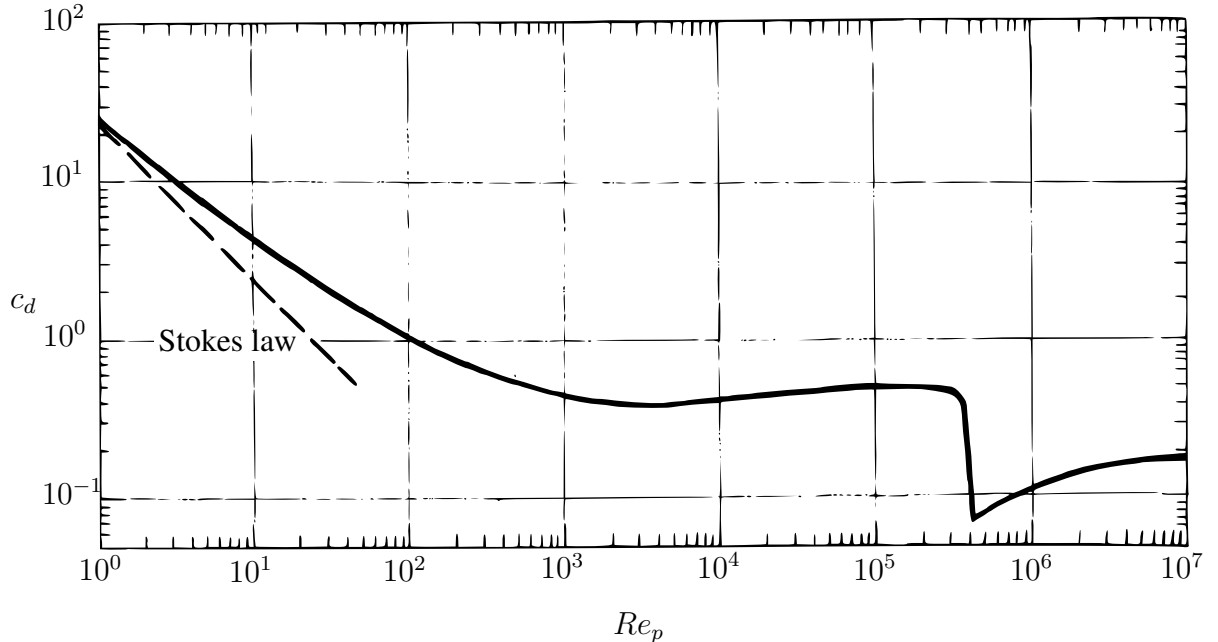


Figure 2.2: Standard drag curve for a spherical particle in steady motion (from Clift et al. [28]).

with $\|\cdot\|_2$ being the L^2 -norm and the drag coefficient

$$c_d = \begin{cases} \frac{24}{Re_p}, & \text{if } Re_p \leq 0.1 \\ \frac{24}{Re_p} (1.0 + 0.15 Re_p^{0.687}), & \text{if } 0.1 < Re_p \leq 1000 \\ 0.44, & \text{if } 1000 < Re_p \end{cases} \quad (2.48)$$

according to Schiller and Naumann [180] or Rowe [178]. Therein, the particle Reynolds number

$$Re_{p,i} = 2r_i \|\langle \mathbf{u} \rangle_i - \mathbf{v}_i\|_2 \frac{\rho_l}{\mu} \quad (2.49)$$

can be identified. This composed drag correlation is an approximation of the standard drag curve for a rigid sphere (see Figure 2.2) up to a particle Reynolds number of approximately $3 \cdot 10^5$. It has to be noted that the surface of a gaseous bubble is non-rigid leading to a different drag correlation. However, gaseous bubbles in clean water behave different compared to gaseous bubbles in contaminated water. Clean water can usually only be found in laboratories on test rigs, whereas applications of relevance always include contaminations which immobilize the bubble surface leading to a behavior similar to a solid surface, see e.g. Magnaudet and Eames [142]. Hence, a drag coefficient valid for solid spheroids is applied for all applications.

The shear induced lift force (or Saffman lift force) reads

$$\mathbf{F}_{l,i} \stackrel{!}{=} c_l \rho_l V_{p,i} (\langle \mathbf{u} \rangle_i - \mathbf{v}_i) \times (\nabla \times \langle \mathbf{u} \rangle_i) \quad (2.50)$$

with a constant lift coefficient $c_l = 0.5$, cf. Auton [8].

In the wake of an instationary moving particle, fluid flow is accelerated leading to the added mass force

$$\mathbf{F}_{am,i} \stackrel{!}{=} c_{am} \rho_l V_{p,i} \left(\frac{D \langle \mathbf{u} \rangle_i}{Dt} - \frac{D \mathbf{v}_i}{Dt} \right) \quad (2.51)$$

using a constant added mass coefficient $c_{am} = 0.5$ and the substantial derivative

$$\frac{D}{Dt}(\cdot) = \frac{\partial}{\partial t}(\cdot) + \langle \mathbf{u} \rangle_i \cdot \nabla(\cdot) \quad (2.52)$$

of a quantity (\cdot) for the fluid flow, for details see Magnaudet and Eames [142] or Brennen [20].

The drag, lift and added mass force are driven by relative velocity and relative acceleration of the particle with respect to the underlying fluid. They are summed up to

$$\sum \mathbf{F}'_{\Gamma,i} = \mathbf{F}_{d,i} + \mathbf{F}_{l,i} + \mathbf{F}_{am,i} \quad (2.53)$$

in order to later be used for deriving the coupling term to the continuous phase in Section 2.3.

Further forces could be accounted for, which are all neglected in this thesis. The Magnus force is a lift force developed due to the rotation of a particle, for details see Crowe et al. [33]. Furthermore, also Basset history force is neglected. It accounts for the temporal delay of the boundary layer in order to adapt to a change in relative velocity, cf. Magnaudet and Eames [142]. This additional resistance force is dependent on the accumulated acceleration from the initial to the current time which makes its computation very involved. For further details and an attempt to improve efficiency in computing Basset history, see Nijssen et al. [158]. Also, a force due to volume change of the bubble is neglected here. For an interesting discussion on this force see Vallier [214]. In case, gradients in the surface tension are considered on a single gaseous bubble, the Marangoni effect leads to a force in the direction of decreasing surface tension, cf. Brennen [20].

Important to note is that all forces given so far build on the assumption of undisturbed flow around a single rigid spheroid. However, the scenario of interest includes many particles that might form a dense suspension. In order to account for multiple particle systems, correction terms can be added. E.g. Tryggvason et al. [207] or Lau et al. [130] performed simulations of dispersed flow with a fully resolved interface in order to derive dispersed phase fraction-dependent correlations for the drag force. Hence, instead of using the drag coefficient as given in (2.48), a correlation of the form $c_d(\epsilon_l)$ is derived to account for dense dispersed flows. Alternatively, e.g. Tomiyama et al. [206], van Nierop Ernst et al. [217], Dijkhuizen et al. [48], or Rastello et al. [172] used experiments to derive correction terms based on dimensionless characteristic numbers such as the Morton number or the Eötvös number. Usually, these approaches have in common that they are only valid in a limited range of particle diameters and flow conditions. Hence, these corrections are neglected in this work as no general model is available.

2.2.3 Particle-particle interaction

In Section 2.2.2, the forces acting on a particle are summarized, namely gravity force and fluid forces. The sum over the distinct contributions is given in (2.40) which allows for solving for the equation of motion. In pure particle problems or in an Euler-Lagrange problem with a void fraction larger than 10^{-3} , particle-particle collisions must be taken into account for proper modeling of the system behavior, cf. Elghobashi [55]. As this work targets towards possibly dense particle systems as it might locally occur at the stagnation point of an obstacle in a flow field, DEM particle contact is employed here. Coalescence and break up of particles are neglected as well as the effect of surrounding fluid which might influence the collision event. There is made

no distinction between collisions of gaseous, liquid and solid particles because of the assumption of an immobilized surface of gaseous and liquid dispersions, cf. remarks at the beginning of Chapter 2.

2.2.3.1 Normal contact

Normal contact conditions can be stated as

$$g_{n,ij} \geq 0, \quad (2.54)$$

$$F_{cn,i} \leq 0, \quad (2.55)$$

$$g_{n,ij} F_{cn,i} = 0 \quad (2.56)$$

which are known as Kuhn-Tucker conditions, cf. Laursen [132]. The first inequality represents the non-penetration of contact partners using the gap function $g_{n,ij}$ in normal direction between collision partner i and j . The second inequality excludes cohesive forces and limits the normal contact force $F_{cn,i}$ to be negative. The third equation is a complementary condition which enforces the gap to be zero when contact forces act and the forces to be zero when the gap is open. For further information on contact mechanics, the reader is exemplarily referred to Simo and Hughes [190] or Popp [170] from which the following derivations are taken. As usual for DEM, the Kuhn-Tucker conditions are weakened and a (small) overlap between the collision partners is allowed. Hence, the Kuhn-Tucker conditions are no longer fulfilled exactly and it is possible to compute the contact forces dependent on the overlap, i.e. the gap, using an artificial stiffness k_n . Usually, in solid mechanics, this artificial stiffness parameter is denoted as penalty parameter which penalizes the overlap of collision partners. An infinitely large penalty parameter leads to an exact fulfillment of the contact condition without overlap. However, in particle contact scenarios, this non-physical parameter can be used to adjust the properties of the contact event to model a physical behavior. This advantage comes at the drawback of the necessity of small time steps because a contact event needs to be discretized with several time steps which will be introduced in Section 3.1.2.1. Usually, the resulting differential equation has a stiff character demanding for careful stability considerations.

There are many different contact laws available of which a linear spring-damper model is chosen due to its simplicity. The normal force component for particle i reads

$$\mathbf{F}_{cn,i} = \underbrace{k_n g_{n,ij} \mathbf{n}_{ij}}_{\text{elastic}} - \underbrace{d v_{rel,n,ij} \mathbf{n}_{ij}}_{\text{viscous}} = F_{cn,i} \mathbf{n}_{ij} \quad (2.57)$$

with the unit normal vector \mathbf{n}_{ij} from particle i to particle j , the damping parameter d and the relative velocity in normal direction

$$v_{rel,n,ij} = (\mathbf{v}_i - \mathbf{v}_j) \cdot \mathbf{n}_{ij}. \quad (2.58)$$

See also Figure 2.3 for an overview of relevant quantities and directions. An elastic part and a viscous part of the normal contact force can be distinguished in (2.57). The stiffness parameter k_n will be determined in Section 3.1.2. It is important to keep k_n constant during one collision because otherwise the energy contained in the system changes artificially. The gap

$$g_{n,ij} = \|\mathbf{x}_j - \mathbf{x}_i\|_2 - (r_j + r_i) \quad (2.59)$$

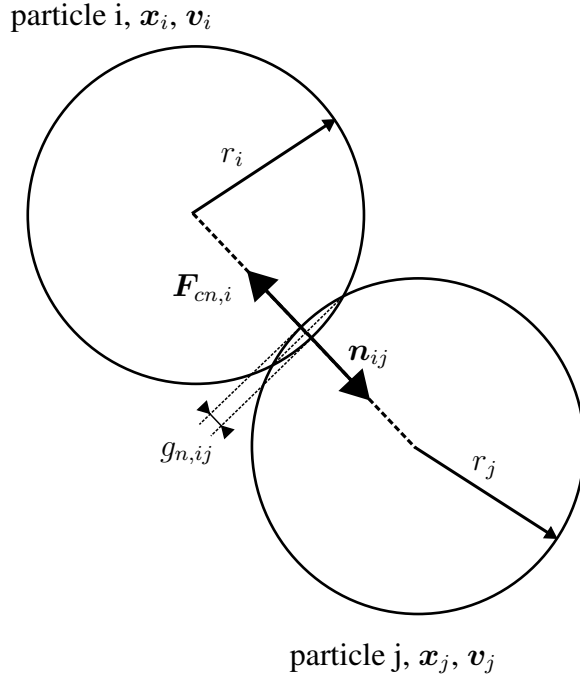


Figure 2.3: Normal contact of two particles.

and the unit normal

$$\mathbf{n}_{ij} = \frac{\mathbf{x}_j - \mathbf{x}_i}{\|\mathbf{x}_j - \mathbf{x}_i\|_2} \quad (2.60)$$

are purely geometrical quantities. The damping parameter of the viscous part of the force is computed as

$$d = 2 |\ln(e)| \sqrt{\frac{k_n m_{\text{eff},ij}}{\ln^2(e) + \pi^2}} \quad (2.61)$$

with the limit case

$$d(e=0) = \lim_{e \rightarrow 0} 2 |\ln(e)| \sqrt{\frac{k_n m_{\text{eff},ij}}{\ln^2(e) + \pi^2}} = 2 \sqrt{k_n m_{\text{eff},ij}}, \quad (2.62)$$

cf. Deen et al. [41] and the appendix of Tsuji et al. [208] for the derivation. The damping parameter is based on the effective mass

$$m_{\text{eff},ij} = \frac{m_i m_j}{m_i + m_j} \quad (2.63)$$

and the coefficient of restitution which is defined as

$$e = -\frac{v_{\text{rel},n,ij}(t^f)}{v_{\text{rel},n,ij}(t^i)}. \quad (2.64)$$

Therein, the normal part of the relative velocity $v_{\text{rel},n}(t^i)$ before and after the collision $v_{\text{rel},n}(t^f)$ is contained. The damping parameter d is chosen such that (2.64) is fulfilled. Applying Newton's third law, the normal contact force on particle j is given by

$$\mathbf{F}_{cn,j} = -\mathbf{F}_{cn,i}. \quad (2.65)$$

2.2.3.2 Tangential contact

When friction is considered, additional tangential forces emerge. Frictional contact leads to a rotation of the particles in case of an eccentric collision of two particles. Therefore, the angular velocity ω of the particles is tracked in addition to the translational degrees of freedom. The assumption of a rigid particle allows to determine the velocity of the contact point via

$$\mathbf{v}_{c,i} = \mathbf{v}_i + \boldsymbol{\omega}_i \times (r'_i \mathbf{n}_{ij}) , \quad (2.66)$$

$$\mathbf{v}_{c,j} = \mathbf{v}_j + \boldsymbol{\omega}_j \times (-r'_j \mathbf{n}_{ij}) \quad (2.67)$$

with

$$r'_i = r_i + \frac{g_{n,ij}}{2} , \quad (2.68)$$

$$r'_j = r_j + \frac{g_{n,ij}}{2} . \quad (2.69)$$

The relative velocity in the contact point then reads

$$\mathbf{v}_{rel,ij} = \mathbf{v}_{c,i} - \mathbf{v}_{c,j} \quad (2.70)$$

and the relative tangential velocity follows as

$$\mathbf{v}_{rel,t,ij} = \mathbf{v}_{rel,ij} - \mathbf{v}_{rel,n,ij} =: \dot{\mathbf{g}}_{t,ij} \quad (2.71)$$

which is the relative gap velocity in tangential direction $\dot{\mathbf{g}}_{t,ij}$ between the two particles in the contact point. Two contact states can be distinguished based on $\dot{\mathbf{g}}_{t,ij}$. *Stick* is defined as

$$\dot{\mathbf{g}}_{t,ij} = \mathbf{0} \quad (2.72)$$

whereas *slip* occurs when

$$\dot{\mathbf{g}}_{t,ij} \neq \mathbf{0} . \quad (2.73)$$

In this work, Coulomb friction is considered which limits the contact force in tangential direction to $\mu_s |F_{cn}|$ using the friction coefficient μ_s and the norm of the normal contact force in (2.57). This relation can also be written using Kuhn-Tucker conditions

$$\phi := \|\mathbf{F}_{ct,i}\|_2 - \mu_s |F_{cn,i}| \leq 0 , \quad (2.74)$$

$$\dot{\mathbf{g}}_{t,ij} - \beta \frac{\mathbf{F}_{ct,i}}{\|\mathbf{F}_{ct,i}\|_2} = \mathbf{0} , \quad (2.75)$$

$$\beta \geq 0 , \quad (2.76)$$

$$\phi \beta = 0 \quad (2.77)$$

which includes Coulomb's friction law in the first inequality, cf. Laursen [132]. The scalar parameter β is zero in the *stick* case leading to a zero tangential relative velocity in the contact point. In the *slip* case, a relative movement parallel to the tangential contact force $\mathbf{F}_{ct,i}$ occurs as obvious from the second equation of the Kuhn-Tucker conditions. In order to satisfy the last equation, ϕ must be zero, leading to a tangential contact force at maximal amplitude.

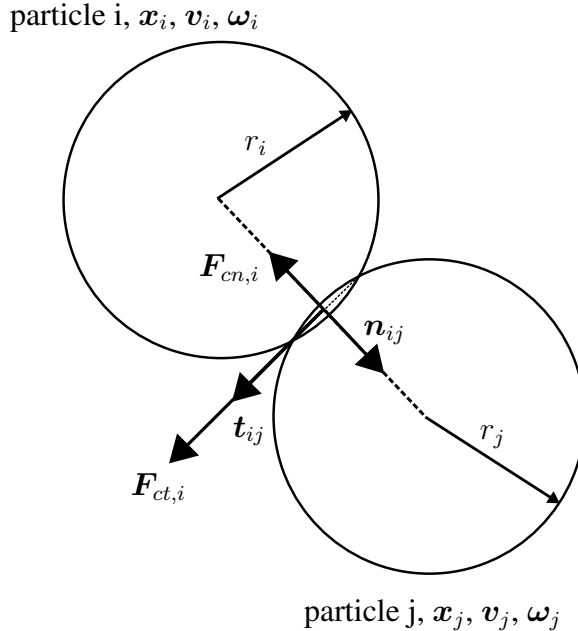


Figure 2.4: Tangential contact of two particles.

In accordance with the normal force model, also a linear spring-damper model is used for the tangential force, reading

$$\mathbf{F}_{ct,i} = -k_t \mathbf{g}_{t,ij} - d \mathbf{v}_{rel,t,ij} \quad (2.78)$$

for the *stick* case which is shown in Figure 2.4. Analogue to Di Renzo and Di Maio [46], the relation of the tangential stiffness κ_t to the normal stiffness κ_n

$$\frac{k_t}{k_n} = \frac{\frac{1-\nu_i}{G_i} + \frac{1-\nu_j}{G_j}}{\frac{1-0.5\nu_i}{G_i} + \frac{1-0.5\nu_j}{G_j}} \quad (2.79)$$

depends on the Poisson's ratio ν and the shear modulus G of the involved materials from particles i and j . The damping coefficient d is assumed to be identical for normal and tangential contact as done in Di Maio and Di Renzo [45] such that (2.61) can be reused. The tangential gap

$$\mathbf{g}_{t,ij} = \int_{t'}^t \mathbf{v}_{rel,t,ij} dt. \quad (2.80)$$

needs to be integrated over the duration of the contact process of two collision partners starting at time t' with $\mathbf{g}_{t,ij} = \mathbf{0}$ in the *stick* state. In order to cope with the problem of a varying tangential plane as it occurs e.g. when one particle rolls over another one, a projection into the current tangential plane as proposed in Luding [140] is applied in each time step. In the following, the procedure is presented for the progress from time step n to $n+1$. The expression

$$\mathbf{g}_{t,proj}^n = \mathbf{g}_{t,ij}^n - (\mathbf{g}_{t,ij}^n \cdot \mathbf{n}_{ij}^{n+1}) \mathbf{n}_{ij}^{n+1} \quad (2.81)$$

delivers a tangential gap $\mathbf{g}_{t,ij,proj}^n$ which lies in the tangential plane at t^{n+1} . Care must be taken in order to not change the size of the gap due to the projection and therefore, the size is recovered

via

$$\hat{\mathbf{g}}_{t,ij,\text{proj}}^n = \frac{\|\mathbf{g}_{t,ij}^n\|_2}{\|\mathbf{g}_{t,ij,\text{proj}}^n\|_2} \mathbf{g}_{t,ij,\text{proj}}^n. \quad (2.82)$$

Depending on the current state, either the tangential gap

$$\mathbf{g}_{t,ij}^{n+1} = \hat{\mathbf{g}}_{t,ij,\text{proj}}^n + \mathbf{v}_{rel,t,ij}^{n+\frac{1}{2}} \Delta t_b \quad (2.83)$$

is incremented in the *stick* case similar to (3.57) according to the employed time integration scheme for the particles, which will be described in Section 3.1.2, or the tangential gap is kept constant in size in case of *slip* such that

$$\mathbf{g}_{t,ij}^{n+1} = \hat{\mathbf{g}}_{t,ij,\text{proj}}^n. \quad (2.84)$$

After having determined the gap, a tangential trial force

$$\mathbf{F}_{\text{trial},i}^{n+1} = -k_t \mathbf{g}_{t,ij}^{n+1} - d \mathbf{v}_{rel,t,ij}^{n+\frac{1}{2}} \quad (2.85)$$

is computed and compared to its upper limit given by Coulomb's friction law, reading

$$\|\mathbf{F}_{\text{trial},i}^{n+1}\|_2 \leq \mu_s |F_{cn,i}|. \quad (2.86)$$

If the inequality is fulfilled, the tangential contact force reads

$$\mathbf{F}_{ct,i}^{n+1} = \mathbf{F}_{\text{trial},i}^{n+1} \quad (2.87)$$

and the contact state is declared as *stick*. If the inequality is not fulfilled, the tangential contact force is computed according to

$$\mathbf{F}_{ct,i}^{n+1} = \mu_s |F_{cn,i}| \mathbf{t}_{ij}^{n+1} \quad (2.88)$$

for the *slip* case. The direction \mathbf{t}_{ij} is prescribed by the tangential trial force

$$\mathbf{t}_{ij}^{n+1} = \frac{\mathbf{F}_{\text{trial},i}^{n+1}}{\|\mathbf{F}_{\text{trial},i}^{n+1}\|_2} \quad (2.89)$$

while the magnitude of the force is given by the product of friction coefficient and the normal contact force. Therefore, the tangential gap needs to be corrected via

$$\mathbf{g}_{t,ij}^{n+1} = -\frac{1}{k_t} \left(\mu_s |F_{cn,i}| \mathbf{t}_{ij}^{n+1} + d \mathbf{v}_{rel,t,ij}^{n+\frac{1}{2}} \right). \quad (2.90)$$

In order to compute the tangential contact force on particle j , again Newton's third law is used

$$\mathbf{F}_{ct,j} = -\mathbf{F}_{ct,i}. \quad (2.91)$$

Finally, the angular momentum around the center of particle i reads

$$\mathbf{M}_i = (r'_i \mathbf{n}_{ij}) \times \mathbf{F}_{ct,i} \quad (2.92)$$

and accordingly for particle j , the angular momentum reads

$$\mathbf{M}_j = (-r'_j \mathbf{n}_{ij}) \times \mathbf{F}_{ct,j} = \frac{r'_j}{r'_i} \mathbf{M}_i \quad (2.93)$$

2.2.3.3 Contact force and application to the equation of motion

After having derived the normal and tangential contact force, they can be summed to obtain the total contact force

$$\mathbf{F}_{c,i} = \mathbf{F}_{cn,i} + \mathbf{F}_{ct,i} \quad (2.94)$$

for particle i which then can be added to the right-hand side of the equation of motion (2.39):

$$m_i \frac{D\mathbf{v}_i}{Dt} = \mathbf{F}_{g,i} + \sum \mathbf{F}_{\Gamma,i} + \mathbf{F}_{c,i}. \quad (2.95)$$

2.2.4 Particle-wall interaction

In order to account for walls with which the particles can collide, the same normal force model (2.57) and tangential contact force model (2.78) as for particle-particle interaction can be used after applying minor modifications. The mass of wall elements is assumed to be infinitely large such that (2.63) simplifies to

$$m_{\text{eff},ij} = \lim_{m_j \rightarrow \infty} \frac{m_i m_j}{m_i + m_j} = m_i. \quad (2.96)$$

Furthermore, the radius r_j is set to zero in all relevant equations. The position \mathbf{x}_j of the collision partner is the closest point projection of particle i onto the wall. The velocity of this projection point is inserted for \mathbf{v}_j . Care has to be taken while searching for the closest point projection of a particle on a wall as this might also be an edge or a corner point. A hierarchical procedure is applied which first checks whether the closest point projection along the surface normal lies on the surface element. If so, the projection point is accepted and otherwise, the edges are checked using a closest point projection of the particle position onto the edges. Again, a distinction between a projection point lying on one of the edges and projection points outside the edge are made. In the latter case, the distances between particle and the corner points of the wall element are computed. After this search on the surface, the edges and the corners, the closest point on the wall element is found. As the contact normal is the difference between the closest point on the wall and particle i , it does not necessarily coincide with the wall normal. The computational effort in finding the closest point on wall elements is large compared to particle-particle interaction evaluation due to the hierarchical procedure which includes the solution of several small nonlinear systems of equations in case of general curvilinear grid.

2.3 Discussion on the fluid-particle coupling

The literature on multiphase flows using an Euler-Lagrange framework has been dealing with two crucial questions for several decades now. The first intense discussion is on the appropriate model for computing the forces exerted by fluid on submerged particles, see Section 2.3.1. The second uncertainty is on the details of the volume averaged NS equations which will be discussed in Section 2.3.2.

2.3.1 Fluid to particle coupling

A widely used interpretation of the pressure force (2.44) and viscous force (2.45) can be found in literature. They are replaced by the so-called inertia force and the buoyancy force. The respective assumptions/simplifications are given in the following. The particle is assumed so small that its influence vanishes far away from its body and thus undisturbed fluid flow equations are used far away of the body, see e.g. Maxey and Riley [147], Druzhinin and Elghobashi [50], or Magnaudet and Eames [142]. Subsequently, this assumption is used to simplify the computation of the pressure force (2.44) and viscous force (2.45). The difficulty to circumvent is the computation of the viscous force which contains second spatial derivatives of the fluid velocity. The momentum equation of the NS equations (2.2) is reordered as follows

$$-\nabla p^0 + \nabla \cdot \boldsymbol{\tau}^0 = \rho_l \frac{D\mathbf{u}^0}{Dt} - \rho_l \mathbf{g}. \quad (2.97)$$

with the material derivative in the first term on the right-hand side. The superscript $(\cdot)^0$ denotes undisturbed flow quantities (\cdot) , as denoted by Maxey and Riley [147], Druzhinin and Elghobashi [50] and Magnaudet and Eames [142], far way from the particle under consideration. During force computation of particle i with its volume $V_{p,i}$, the reordered momentum equation (2.97) is multiplied with $V_{p,i}$ reading

$$-V_{p,i} \nabla p^0 + V_{p,i} \nabla \cdot \boldsymbol{\tau}^0 = \rho_l V_{p,i} \frac{D\mathbf{u}^0}{Dt} - \rho_l V_{p,i} \mathbf{g}. \quad (2.98)$$

Therein, the pressure force (2.44) and viscous force (2.45) can be identified on the left hand side. So, the terms on the left hand side are approximated with the terms on the right hand side. The arising forces are denoted as particle inertia force

$$\mathbf{F}_{I,i} = \rho_l V_{p,i} \frac{D\mathbf{u}_i^0}{Dt} \quad (2.99)$$

and buoyancy force

$$\mathbf{F}_{b,i} = -\rho_l V_{p,i} \mathbf{g}. \quad (2.100)$$

The evaluation of the particle forces is usually performed with fluid quantities (velocity, acceleration and pressure) at the particle center or in the close neighborhood of the particle. However, the validity of the basic assumption (2.97) lies in a far distance from the particle. Hence, the evaluation conflicts with the assumptions made. Nevertheless, the use of inertia force and buoyancy force can be found very often in literature.

Besides the afore presented questionable replacement of pressure and viscous forces, many different combinations of accounting one force and neglecting another one can be found in literature. Most of the arguments are physically motivated, e.g. on the density ratio between the phases. The gravity force can be neglected if $\rho_b/\rho_l \ll 1$ or the buoyancy force if $\rho_b/\rho_l \gg 1$. The added mass force (2.51) is of minor importance when $\rho_b/\rho_l \gg 1$ and the drag force likely dominates all other forces. In case of $\rho_b/\rho_l \ll 1$, the equation of motion (2.34) is simplified to $(\sum \mathbf{F})_i = 0$ by, e.g. Giannadakis et al. [70] and Druzhinin and Elghobashi [50]. Applying the latter, the particle acceleration is dropped at a first glance but it is still included in the added mass force such that the equation of motion can be evaluated. An alternative of computing the

pressure force can be found in Shams et al. [187], which includes the buoyancy force \mathbf{F}_b to account for the static fluid pressure and a pressure force $V_p \nabla p'$ which only includes the dynamic fluid pressure p' . This list can be extended arbitrarily which points out that the task of finding an appropriate model for the forces exerted from a carrier flow on a submerged particle needs to be considered carefully.

2.3.2 Particle to fluid coupling

After having commented on the forces which are used to model the influence of the carrier phase onto the disperse phase, the reaction forces from the dispersions onto the carrier phase will be discussed in the following. Parts of this section have already been published by Hammerl and Wall [87].

From mechanical principles, it is obvious that all interface forces in (2.37) which act on a submerged body need to be applied to the fluid with an inverse sign. This corresponds to Newton's third law. Thus the closure that has been left open at the end of Section 2.1.2 in (2.33) reads

$$\mathbf{s}' = -\frac{1}{V} \int_{\Gamma} -\delta p \mathbf{n}_i + \delta \boldsymbol{\tau} \cdot \mathbf{n}_i dS \stackrel{!}{=} -\frac{1}{V} \sum_i \mathbf{F}_{\Gamma,i} \quad (2.101)$$

and it includes all interface forces acting on the particle with an inverse sign, see also Crowe et al. [33] or Di Renzo and Di Maio [47].

In literature, different approaches can be found. For example, Darmana et al. [36] incorporate in addition to the interface forces the gravity force of the particles into the coupling force. In the respective application, only a minor difference is introduced because $\rho_b/\rho_l \ll 1$ and it can be interpreted as an approximation not to subtract the gravity force from the coupling forces. A probably larger error is introduced by Shams et al. [187] who incorporate the collision forces into the coupling force from the disperse phase to the continuous phase. Apart from a few exceptions, the literature is consistent with respect to the reaction forces from the disperse phase onto the continuous phase.

The discussion in literature becomes controversial when the question arises which is the correct formulation of the carrier phase equations in an Euler-Lagrange framework. Kafui et al. [111], van Wachem et al. [219] and Di Renzo and Di Maio [47] have addressed this point while showing inconsistencies of the equations used by many research groups. The crux is in the pressure gradient and the divergence of the viscous stress term in the momentum equation (2.2) of the NS equations. The right-hand side of the NS equations after volume averaging (2.33) is repeated

$$-\nabla \langle p \rangle + \nabla \cdot \langle \boldsymbol{\tau} \rangle + \epsilon_l \rho_l \mathbf{g} + \mathbf{s}'$$

to have the starting point at hand.

The pressure term can be reformulated as done by e.g. Di Renzo and Di Maio [47], van der Hoef et al. [216], or Shams et al. [187] which is shown in the following. The sum over all forces acting on the particle in the equation of motion (2.39) contains the pressure force (2.44). The reaction force thereof enters the momentum coupling \mathbf{s}' in (2.33). The contribution of the pressure force to \mathbf{s}' reads

$$-\frac{1}{V} \sum_i -V_{p,i} \nabla \langle p \rangle = \nabla \langle p \rangle \frac{\sum_i V_{p,i}}{V} \quad (2.102)$$

with the sum over all particles in the averaging volume and the division by the respective averaging volume V . The averaged pressure gradient $\nabla \langle p \rangle$ is assumed to be constant in the averaging volume due to (2.9) and thus it can be put in front of the sum over all particles. The definition of the fluid fraction (2.12) allows to rewrite (2.102) as

$$(1 - \epsilon_l) \nabla \langle p \rangle = \epsilon_b \nabla \langle p \rangle \quad (2.103)$$

with the dispersed phase fraction ϵ_b defined as $\epsilon_b = 1 - \epsilon_l$. Therefore, two valid options emerge how to include consistently the pressure term. One option is to compute it explicitly and include it in \tilde{s}' in (2.33) as shown in the preceding equations. The second valid option is to write (2.33) as

$$-\nabla \langle p \rangle + \nabla \cdot \langle \tau \rangle + \epsilon_l \rho_l \mathbf{g} + \tilde{s}' + (1 - \epsilon_l) \nabla \langle p \rangle \quad (2.104)$$

with a source term \tilde{s}' that excludes the reaction of the pressure force (2.103). Then, it is possible to combine terms in (2.104) reading

$$-\epsilon_l \nabla \langle p \rangle + \nabla \cdot \langle \tau \rangle + \epsilon_l \rho_l \mathbf{g} + \tilde{s}' \quad (2.105)$$

as the correct right-hand side of the momentum equation of the volume averaged NS equations.

The treatment of reaction to the particle viscous force follows. The ambiguity in literature is in the starting point which is used for the derivation. For example Ishii [106] and Gidaspow [71] start from (2.30) which is repeated here

$$-\nabla (\epsilon_l \langle p \rangle) + \frac{1}{V} \int_{\Gamma} p \mathbf{n}_i dS + \nabla \cdot (\epsilon_l \langle \tau \rangle) - \frac{1}{V} \int_{\Gamma} \tau \cdot \mathbf{n}_i dS + \epsilon_l \rho_l \mathbf{g}$$

which is one step ahead of (2.33) during volume averaging procedure. Therein, they drop the integral over the stress over the interface Γ between the phases and motivate it with the inclusion of this term in the drag force (2.47) leading to a modified drag law. This argumentation is valid, however the problem arises when one uses this formulation although a drag law such as Stokes drag law or the standard drag law is applied which does not account for the modification, see for example Deen et al. [40], Ferrante and Elghobashi [61], Zhang and Ahmadi [239], or Finn et al. [63].

The second possible starting point is identical to the derivations for the pressure term at the beginning of this section in using (2.33). A similar transformation for the viscous force is possible as for the pressure force, viz

$$-\frac{1}{V} \sum_i V_{p,i} \nabla \cdot \langle \tau \rangle = -\nabla \cdot \langle \tau \rangle \frac{\sum_i V_{p,i}}{V} \quad (2.106)$$

which is a contribution to the momentum coupling s' in (2.33). The averaged divergence of the stress tensor $\nabla \cdot \langle \tau \rangle$ is again assumed to be constant in the averaging volume due to (2.9) and thus it can be put in front of the sum over all particles. Again, using (2.12), (2.106) is reformulated as

$$(1 - \epsilon_l) \nabla \cdot \langle \tau \rangle = \epsilon_b \nabla \cdot \langle \tau \rangle \quad (2.107)$$

which can be inserted into (2.105) leading to

$$-\epsilon_l \nabla \langle p \rangle + \epsilon_l \nabla \cdot \langle \tau \rangle + \epsilon_l \rho_l \mathbf{g} + \tilde{s}' . \quad (2.108)$$

Therein, the source term $\tilde{\mathbf{s}}'$ does neither include the reaction to the pressure force nor the reaction to the viscous force. Hence, both reaction forces, which emerge already when a dispersion perfectly follows the carrier flow, are eliminated by directly including them into the carrier flow equation, compare Section 2.2.2. The remaining terms which rely on a relative velocity or relative acceleration between the phases have already been summed in (2.53) and it can be concluded

$$\tilde{\mathbf{s}}' = -\frac{1}{V} \sum_i \mathbf{F}_{\Gamma,i}' . \quad (2.109)$$

To summarize, the two valid options which do not require a modified drag law are shown:

$$-\nabla \langle p \rangle + \nabla \cdot \langle \boldsymbol{\tau} \rangle + \epsilon_l \rho_l \mathbf{g} + \mathbf{s}' = -\epsilon_l \nabla \langle p \rangle + \epsilon_l \nabla \cdot \langle \boldsymbol{\tau} \rangle + \epsilon_l \rho_l \mathbf{g} + \tilde{\mathbf{s}}' . \quad (2.110)$$

This equality is valid when the Lagrangian quantities can be transformed into Eulerian quantities such that no error is introduced in the mapping. As this is difficult to achieve, the carrier phase flow equations in the developed framework rely on the latter coupling approach in (2.110) because the fluid incorporates already the particle pressure force and viscous force. The coupling terms in $\tilde{\mathbf{s}}'$ solely rely on relative velocities and accelerations between the phases.

After having derived the missing closure terms in (2.33), the final volume averaged NS equations are given which are used for further derivations in the remainder of this thesis:

$$\begin{aligned} \rho_l \frac{\partial \langle \mathbf{u} \rangle}{\partial t} + \rho_l \langle \mathbf{u} \rangle \cdot \nabla \langle \mathbf{u} \rangle + \rho_l \langle \delta \mathbf{u} \rangle \cdot \nabla \langle \mathbf{u} \rangle + \rho_l \langle \mathbf{u} \rangle \cdot \nabla \langle \delta \mathbf{u} \rangle \\ + \rho_l \langle \delta \mathbf{u} \rangle \cdot \nabla \langle \delta \mathbf{u} \rangle = -\nabla \langle p \rangle + \nabla \cdot \langle \boldsymbol{\tau} \rangle + \rho_l \mathbf{g} + \frac{1}{\epsilon_l} \tilde{\mathbf{s}}' , \end{aligned} \quad (2.111)$$

$$\nabla \cdot \langle \mathbf{u} \rangle + \nabla \cdot \langle \delta \mathbf{u} \rangle = -\frac{1}{\epsilon_l} \left(\frac{\partial \epsilon_l}{\partial t} + \langle \mathbf{u} \rangle \cdot \nabla \epsilon_l \right) \quad (2.112)$$

which comprises the left-hand side (2.28) and right-hand side (2.110) of the momentum equation in convective form and the continuity equation (2.24) in which the last term is ignored. The momentum equation has been divided by the non-zero fluid fraction ϵ_l .

2.4 Particle radius variations governed by the Rayleigh-Plesset (RP) equation

So far, only particles with a constant radius have been considered. For the modeling of gas/vapor bubbles in liquid, the RP equation governs the bubble radius based on the ambient fluid pressure. The RP equation was derived by Lord Rayleigh [139] and applied to cavitating bubbles by Plesset [167]. A summary of modeling aspects regarding the RP equation and a detailed derivation can be found in Brennen [19] on which the following summary is based on and to which the reader is referred to for more details. The following assumptions are used:

- The bubble is spherical with time-dependent radius $r = r(t)$.
- The bubble interior pressure $p_b(t)$ and temperature $T_b(t)$ are uniformly distributed.

- No mass and no heat transfer between bubble and surrounding fluid.
- The density ρ_l , dynamic viscosity μ , and temperature T_∞ of the surrounding fluid is homogeneous and constant over time.
- Surface tension σ and vapor pressure p_v are constant over time.
- The domain of the surrounding fluid is infinitely large with time-dependent pressure $p_\infty(t)$ at a large distance from the bubble.

Inserting the aforementioned assumptions in the momentum equation of the NS equations in radial coordinates leads to the RP equation

$$\rho_l \left[r(t) \ddot{r}(t) + \frac{3}{2} (\dot{r}(t))^2 \right] = p_b(t) - p_\infty(t) - \frac{2\sigma}{r(t)} - \frac{4\mu}{r(t)} \dot{r}(t) \quad (2.113)$$

with pressure inside the bubble being defined as

$$p_b(t) = p_v + p_g(t) = p_v + p_{g0} \left(\frac{r_0}{r(t)} \right)^{3\eta}. \quad (2.114)$$

The pressure inside the bubble consists of the vapor pressure p_v and the partial pressure $p_g(t)$ of contaminant gas. The partial gas pressure is based on the partial pressure p_{g0} at initial state, the initial bubble radius r_0 and the exponent η . According to Moss et al. [154], either an isothermal process is assumed leading to $\eta = 1$ when the dynamics are slow ($r(t) \geq r_0$) or an adiabatic process is assumed, with $\eta = \frac{c_p}{c_v} = 1.4$ being the specific heat ratio of the gas, when the dynamics are high ($r(t) < r_0$).

Furthermore, it is assumed that the bubble is initially at equilibrium

$$r_0 = r(t = 0) \quad (2.115)$$

$$\dot{r}(t = 0) = \ddot{r}(t = 0) = 0 \quad (2.116)$$

which can be inserted in (2.113) in order to solve for the initial gas partial pressure

$$p_{g0} = p_\infty(t) - p_v + \frac{2\sigma}{r_0}. \quad (2.117)$$

3 Computational approach

3.1 Single fields

3.1.1 Discretized Navier-Stokes equations

The method of lines is used to discretize the governing equations as given in (2.111) and (2.112), meaning that first the spatial discretization is applied in Section 3.1.1.1 followed by the time discretization in Section 3.1.1.2.

The Eulerian domain Ω is discretized with n_e non-overlapping elements of the domain Ω^e . Hence,

$$\Omega = \cup_{e=1}^{n_e} \Omega^e \quad \text{and} \quad \Omega^e \cap \Omega^f = \emptyset \quad \forall e \neq f. \quad (3.1)$$

This discretization in space introduces a spatial filtering into resolved scales and those which are below the size of the elements considered. The volume averaged NS equations also filter the governing equations and lead to a lower limit of the element size. Hence, a possible choice is to link the spatial discretization with the filtering size introduced in the volume averaging procedure. This is inspired by the approach of implicit turbulence modeling, see e.g. Hickel et al. [92], where the element size is linked to the introduced dissipation in the turbulent flow. In order to show the close link between the size of the volume average and the size of elements, the volume averaged velocity $\langle \mathbf{u} \rangle$ and its deviations $\langle \delta \mathbf{u} \rangle$ are replaced by \mathbf{u}^h and $\hat{\mathbf{u}}$, respectively, exclusively in the following section. The same replacement is applied for the fluid pressure p . This also eases reading for someone who is used to the notation common in the derivations of variational multiscale methods.

3.1.1.1 Residual-based variational multiscale finite element method

A finite element method (FEM) is applied for spatial discretization throughout this thesis. Here, a brief summary of the basic ideas is given and the interested reader is referred to the corresponding literature, e.g. to Hughes [101] and Zienkiewicz et al. [241] for the general FEM and to textbooks exclusively dealing with FEM for flow problems, e.g. Gresho and Sani [80, 81] and Donea and Huerta [49]. For details on the variational multiscale method, the reader is referred to Hughes et al. [103], Bazilevs et al. [12], and Gravemeier et al. [78].

In the work of Guerra et al. [82], the governing equations for particle-laden flow are derived using the residual-based variational multiscale method. However, they neglect the influence of the dispersed phase in the continuity equation due to the assumption of negligible volume fraction of the dispersions. Hence, an incompressible fluid is modeled and the influence of the dispersed phase is only included in the momentum equation as an additional source term. In contrast, the formulation used in this thesis includes effects of the dispersed phase in the continuity equation.

The weak formulation of the governing equations is obtained via multiplying (2.111) and (2.112) with appropriate weighting functions. The admissible solution and test function space for the velocity \mathbf{u} is

$$\mathcal{S}_u = \left\{ \mathbf{u} \in [H^1(\Omega)]^3 \mid \mathbf{u} = \mathbf{u}_D \text{ on } \Gamma_D \right\}, \quad \mathcal{V}_u = \left\{ \mathbf{w} \in [H^1(\Omega)]^3 \mid \mathbf{w} = \mathbf{0} \text{ on } \Gamma_D \right\}. \quad (3.2)$$

The corresponding solution and test function space for the pressure is identical

$$\mathcal{S}_p = \{p \in L^2(\Omega)\}, \quad \mathcal{V}_p = \{q \in L^2(\Omega)\}. \quad (3.3)$$

Therein, the Hilbert space of square-integrable functions on the domain Ω is denoted as $L^2(\Omega)$ and the Sobolev space is denoted as $H^1(\Omega)$ which additionally includes the functions with square-integrable first derivatives, see Donea and Huerta [49] for more details. As already explained in Section 3.1.1, a separation into resolved and unresolved scales is applied which can either be seen as introduced by the volume averaging or by the discretization. The resolved scales span a finite-dimensional subspace whereas the unresolved scales cover an infinite-dimensional subspace and a sum decomposition is applied which reads as follows

$$\mathcal{S}_u = \mathcal{S}_u^h + \hat{\mathcal{S}}_u, \quad \mathcal{V}_u = \mathcal{V}_u^h + \hat{\mathcal{V}}_u, \quad (3.4)$$

$$\mathcal{S}_p = \mathcal{S}_p^h + \hat{\mathcal{S}}_p, \quad \mathcal{V}_p = \mathcal{V}_p^h + \hat{\mathcal{V}}_p. \quad (3.5)$$

Analogue to splitting the solution functions (compare (2.17) and (2.31))

$$\mathbf{u} = \mathbf{u}^h + \hat{\mathbf{u}}, \quad (3.6)$$

$$p = p^h + \hat{p}, \quad (3.7)$$

the weighting functions q and \mathbf{w} can be separated into a resolved and an unresolved part reading

$$\mathbf{w} = \mathbf{w}^h + \hat{\mathbf{w}}, \quad (3.8)$$

$$q = q^h + \hat{q}. \quad (3.9)$$

The momentum equation (2.111) and the continuity equation (2.112) are multiplied with the resolved-scale part $\mathbf{w}^h \in \mathcal{V}_u^h$ and $q^h \in \mathcal{V}_p^h$ of the test functions in order to achieve the aforementioned scale separation property. Integration over the domain Ω is performed. Integration by parts is applied to the viscous and pressure term while accounting for the boundary conditions (2.7) and (2.8) in the emerging boundary integrals. For details on the derivation, see Hughes et al. [103] and Bazilevs et al. [12]. Finally, the weak formulation tested with the resolved part of the testing function follows: find $p^h \in \mathcal{S}_p^h$ and $\mathbf{u}^h \in \mathcal{S}_u^h$ such that

$$(q^h, \nabla \cdot \mathbf{u}^h)_\Omega + (q^h, \nabla \cdot \hat{\mathbf{u}})_\Omega = \left(q^h, -\frac{1}{\epsilon_l} \left(\frac{\partial \epsilon_l}{\partial t} + \mathbf{u}^h \cdot \nabla \epsilon_l \right) \right)_\Omega \quad \forall q^h \in \mathcal{V}_p^h \quad (3.10)$$

$$\begin{aligned} & \left(\mathbf{w}^h, \rho_l \frac{\partial \mathbf{u}^h}{\partial t} \right)_\Omega + (\mathbf{w}^h, \rho_l \mathbf{u}^h \cdot \nabla \mathbf{u}^h)_\Omega + (\mathbf{w}^h, \rho_l \hat{\mathbf{u}} \cdot \nabla \mathbf{u}^h)_\Omega + (\mathbf{w}^h, \rho_l \mathbf{u}^h \cdot \nabla \hat{\mathbf{u}})_\Omega \\ & \quad + (\mathbf{w}^h, \rho_l \hat{\mathbf{u}} \cdot \nabla \hat{\mathbf{u}})_\Omega - (\nabla \cdot \mathbf{w}^h, p^h)_\Omega + (\boldsymbol{\epsilon}(\mathbf{w}^h), 2\mu \boldsymbol{\epsilon}'(\mathbf{u}^h))_\Omega \\ & = \left(\mathbf{w}^h, \frac{1}{\epsilon_l} \tilde{\mathbf{s}}' + \rho_l \mathbf{g} \right)_\Omega + (\mathbf{w}^h, \mathbf{h})_{\Gamma_N} \quad \forall \mathbf{w}^h \in \mathcal{V}_u^h. \end{aligned} \quad (3.11)$$

with $(\cdot, \cdot)_\Omega$ and $(\cdot, \cdot)_{\Gamma_N}$ being the inner L_2 product in the domain Ω and on the Neumann boundary Γ_N , respectively.

Instead of using the resolved part of the test functions in (3.10) and (3.11), a multiplication with the unresolved counterparts can be used to obtain a model for the unresolved scales, see, e.g. Hughes et al. [103], Bazilevs et al. [12], and the review paper by Rasthofer and Gravemeier [173]. Therewith, the element-wise unresolved scales read as

$$\hat{\mathbf{u}} = -\tau_M \mathbf{r}_M^h \quad (3.12)$$

with the stabilization parameter τ_M and the discrete residual of the momentum equation

$$\mathbf{r}_M^h = \rho_l \frac{\partial \mathbf{u}^h}{\partial t} + \rho_l \mathbf{u}^h \cdot \nabla \mathbf{u}^h + \nabla p^h - \nabla \cdot 2\mu \epsilon(\mathbf{u}^h) - \rho_l \mathbf{g} - \frac{1}{\epsilon_l} \tilde{\mathbf{s}}' \quad (3.13)$$

which only contains resolved quantities. The stabilization parameter proposed in Taylor et al. [203] and Whiting and Jansen [230], and adapted to variable-density flow by Gravemeier and Wall [77], read as follows

$$\tau_M = \frac{1}{\sqrt{\left(\frac{2\rho_l}{\Delta t_l}\right)^2 + (\rho_l \mathbf{u}^h) \cdot \mathbf{G}(\rho_l \mathbf{u}^h) + C_1 \mu^2 \mathbf{G} : \mathbf{G}}} \quad (3.14)$$

where

$$G_{ij} = \sum_{k=1}^3 \frac{\partial \xi_k}{\partial x_i} \frac{\partial \xi_k}{\partial x_j} \quad (3.15)$$

is the covariant metric tensor describing the mapping between global coordinates \mathbf{x} and the local element coordinates $\boldsymbol{\xi}$. The time step size is denoted as Δt_l and C_1 is a constant independent of the characteristic element length which is 36.0 for tri-linearly-interpolated hexahedral elements and linear tetrahedral elements. Introducing (3.12) in (3.10) and (3.11) leads to finding $p^h \in \mathcal{S}_p^h$ and $\mathbf{u}^h \in \mathcal{S}_u^h$ such that

$$(q^h, \nabla \cdot \mathbf{u}^h)_\Omega + (\nabla q^h, \tau_M \mathbf{r}_M^h)_{\Omega^*} = \left(q^h, -\frac{1}{\epsilon_l} \left(\frac{\partial \epsilon_l}{\partial t} + \mathbf{u}^h \cdot \nabla \epsilon_l \right) \right)_\Omega \quad \forall q^h \in \mathcal{V}_p^h \quad (3.16)$$

$$\begin{aligned} & \left(\mathbf{w}^h, \rho_l \frac{\partial \mathbf{u}^h}{\partial t} \right)_\Omega + (\mathbf{w}^h, \rho_l \mathbf{u}^h \cdot \nabla \mathbf{u}^h)_\Omega + (\mathbf{w}^h, -\rho_l \tau_M \mathbf{r}_M^h \cdot \nabla \mathbf{u}^h)_{\Omega^*} \\ & + (\rho_l \mathbf{u}^h \cdot \nabla \mathbf{w}^h, \tau_M \mathbf{r}_M^h)_{\Omega^*} + (-\rho_l \tau_M \mathbf{r}_M^h \cdot \nabla \mathbf{w}^h, \tau_M \mathbf{r}_M^h)_{\Omega^*} - (\nabla \cdot \mathbf{w}^h, p^h)_\Omega \\ & + (\epsilon(\mathbf{w}^h), 2\mu \epsilon'(\mathbf{u}^h))_\Omega + (\nabla \cdot \mathbf{w}^h, \tau_C \mathbf{r}_C^h)_{\Omega^*} \\ & = \left(\mathbf{w}^h, -\frac{1}{\epsilon_l} \tilde{\mathbf{s}}' + \rho_l \mathbf{g} \right)_\Omega + (\mathbf{w}^h, \mathbf{h})_{\Gamma_N} \quad \forall \mathbf{w}^h \in \mathcal{V}_u^h \end{aligned} \quad (3.17)$$

in which integration by parts of some terms is performed. To simplify the derivation, the unresolved quantities are assumed to vanish on the boundary of each element as discussed in Hughes [100]. Moreover, Ω^* is the union of all element interiors excluding the element boundaries, i.e.

$$\Omega^* = \Omega \setminus \cup_{e=1}^{n_e} \partial \Omega^e. \quad (3.18)$$

3 Computational approach

Finally, this formulation of the residual-based variational multiscale approach represents the volume averaged NS equations and it only includes resolved scales. The following comments on the terms in the final formulation are taken from Gresho and Sani [80, 81] and Donea and Huerta [49] which the reader is referred to for more details:

- $(\nabla q^h, \tau_M r_M^h)_{\Omega^*}$ constitutes a Pressure Stabilizing Petrov-Galerkin (PSPG) term which suppresses spurious pressure oscillations in case equal order discretization for the velocity and the pressure is chosen; for details see Brezzi and Fortin [22].
- $(\rho_l \mathbf{u}^h \cdot \nabla \mathbf{w}^h, \tau_M r_M^h)_{\Omega^*}$ constitutes a Streamline/Upwind Petrov-Galerkin (SUPG) term which is necessary to overcome numerical instabilities in convection-dominated flows when using the FEM, see Brooks and Hughes [23].
- $(\mathbf{w}^h, -\rho_l \tau_M r_M^h \cdot \nabla \mathbf{u}^h)_{\Omega^*}$ constitutes a cross-stress (CS) term enhancing global momentum conservation for the convective formulation, for details see Hughes and Wells [102].
- $(-\rho_l \tau_M r_M^h \cdot \nabla \mathbf{w}^h, \tau_M r_M^h)_{\Omega^*}$ constitutes a subgrid-scale Reynolds-stress (RS) term which can be seen as a stabilization term for the aforementioned cross-stress term, see also Hughes and Wells [102].
- The only term that is missing compared to the variational multiscale framework by Gresho and Sani [80, 81] and Donea and Huerta [49] is a grad-div (GD) term. It penalizes deviations of the discrete mass conservation which is assumed to be important as a non-divergency free continuity equation (2.112) is used. Therefore, a GD term

$$(\nabla \cdot \mathbf{w}^h, \tau_C r_C^h)_{\Omega^*} \quad (3.19)$$

is added to (3.17) which includes the discrete residual of the continuity equation

$$\mathbf{r}_C^h = \nabla \cdot \mathbf{u}^h + \frac{1}{\epsilon_l} \left(\frac{\partial \epsilon_l}{\partial t} + \mathbf{u}^h \cdot \nabla \epsilon_l \right) \quad (3.20)$$

and the stabilization parameter

$$\tau_C = \frac{1}{\tau_M \text{tr}(\mathbf{G})}, \quad (3.21)$$

with being $\text{tr}(\cdot)$ the trace of a matrix, for details see De Mulder [38] and Bazilevs et al. [12]. As this term vanishes when the mass conservation is fulfilled exactly, consistency is ensured.

During the derivation of the volume averaged NS equations in Section 2.1.2, four terms were not removed as usual, one on the left-hand side of (2.24) and three in (2.28). Each of this terms included the variation of the velocity $\delta \mathbf{u} \equiv \hat{\mathbf{u}}$. After deriving the variational multiscale method, these four terms can be identified as the PSPG, SUPG, CS and RS term. It is the first time that these terms which are usually neglected in the derivation of the volume averaged NS equations are matched with terms in a variational multiscale method.

The derivations in this section have been performed in a very similar way by Gravemeier and Wall [77] for variable-density low-Mach number flows. Their starting point are the compressible NS equations consisting of conservation of mass, momentum, and energy. In contrast, the volume

averaged incompressible NS equations are used in the present framework to start the derivation of the residual-based the variational multiscale method. Strong similarities can be found in the continuity equation which reads

$$\nabla \cdot \mathbf{u} = \frac{1}{T} \left(\frac{\partial T}{\partial t} + \mathbf{u} \cdot \nabla T \right) - \frac{1}{p_{\text{the}}} \frac{dp_{\text{the}}}{dt} \quad (3.22)$$

in their case. Ignoring the latter part with the thermodynamic pressure p_{the} and replacing the temperature T with the fluid fraction ϵ_l leads to the formulation used in this thesis. However, there is no need to solve the energy equation in the present thesis due to the Lagrangian particles which are used to compute the fluid fraction based on their position and volume.

As a FEM is applied in this thesis, the discrete solution is approximated using shape functions $N_\alpha(\mathbf{x})$ and solution vectors $\mathbf{u}_\alpha(t)$ and $p_\alpha(t)$ each corresponding to a node α which are multiplied and summed over all nodes of the discretization as follows

$$\mathbf{u}^h(\mathbf{x}, t) = \sum_{\alpha} N_\alpha(\mathbf{x}) \mathbf{u}_\alpha(t) \quad (3.23)$$

$$p^h(\mathbf{x}, t) = \sum_{\alpha} N_\alpha(\mathbf{x}) p_\alpha(t). \quad (3.24)$$

Lagrangian polynomials are chosen for the shape functions which are also used for the test functions \mathbf{w}^h and q^h . Inserting this approximation of the discrete solution and test functions in (3.16) and (3.17) leads to a time-continuous Galerkin formulation which reads without stabilization parameters in the following matrix system

$$\begin{bmatrix} \mathbf{M} & \mathbf{0} \\ \mathbf{0} & \mathbf{0} \end{bmatrix} \begin{bmatrix} \dot{\mathbf{U}}^h \\ \mathbf{0} \end{bmatrix} + \begin{bmatrix} \mathbf{C}(\mathbf{U}^h) + \mathbf{V} & -\mathbf{G} \\ \mathbf{G}^\top & \mathbf{0} \end{bmatrix} \begin{bmatrix} \mathbf{U}^h \\ \mathbf{P}^h \end{bmatrix} = \begin{bmatrix} \mathbf{f} \\ \mathbf{g} \end{bmatrix} \quad (3.25)$$

where \mathbf{M} , $\mathbf{C}(\mathbf{U}^h)$, \mathbf{V} , and \mathbf{G} are the matrices containing the transient, nonlinear convective, viscous, and pressure term of the left-hand side of (3.17). The first term of (3.16) is contained in the transpose of \mathbf{G} . The right hand side terms of (3.17) and (3.16) are contained in \mathbf{f} and \mathbf{g} , respectively. The vectors \mathbf{U}^h , $\dot{\mathbf{U}}^h$, and \mathbf{P}^h hold the nodal degrees of freedom for the velocity, the acceleration, and the pressure.

3.1.1.2 Time discretization

The generalized- α time integration scheme, as originally proposed by Chung and Hulbert [27] for structural dynamics, is used for the fluid. The application to first-order systems such as the NS equations can be found in Jansen et al. [109] which the following brief summary is based on. The time of interest $[0, t_{\text{end}}]$ is divided into discrete time steps of size Δt_l and time stepping from step n to step $n+1$ is performed such that $t^{n+1} = t^n + \Delta t_l$ holds. The generalized- α time integration relies on two additional intermediate time levels defined as

$$t^{n+\alpha_f} = (1 - \alpha_f)t^n + \alpha_f t^{n+1} \quad (3.26)$$

$$t^{n+\alpha_m} = (1 - \alpha_m)t^n + \alpha_m t^{n+1} \quad (3.27)$$

3 Computational approach

in which α_f and α_m are two parameters to control the properties of the method. A stable method can only be obtained if

$$\alpha_m \geq \alpha_f \geq \frac{1}{2} \quad (3.28)$$

holds, cf. Jansen et al. [109]. Applied to a generic model problem

$$\frac{da(t)}{dt} = f(a(t), t) \quad (3.29)$$

with the scalar valued function $a(t)$, the time stepping procedure from t^n to t^{n+1} using the generalized- α method reads

$$a^{n+\alpha_f} = (1 - \alpha_f)a^n + \alpha_f a^{n+1} \quad (3.30)$$

$$\dot{a}^{n+\alpha_m} = f(a^{n+\alpha_f}, t^{n+\alpha_f}) \quad (3.31)$$

$$\dot{a}^{n+\alpha_m} = (1 - \alpha_m)\dot{a}^n + \alpha_m \dot{a}^{n+1} \quad (3.32)$$

$$a^{n+1} = a^n + \Delta t_l \dot{a}^n + \Delta t_l \gamma (\dot{a}^{n+1} - \dot{a}^n) \quad (3.33)$$

which iteratively leads to the solution of the problem as this is an implicit time integration scheme. According to Jansen et al. [109], the third free parameter γ can be chosen as

$$\gamma = \frac{1}{2} + \alpha_m - \alpha_f \quad (3.34)$$

in order to reach second-order accuracy in time. The generalized- α time integration scheme allows to control the high-frequency dissipation by the spectral radius ρ_∞ . It is used to define the remaining parameters as

$$\alpha_m = \frac{1}{2} \left(\frac{3 - \rho_\infty}{1 + \rho_\infty} \right), \quad (3.35)$$

$$\alpha_f = \frac{1}{1 + \rho_\infty}. \quad (3.36)$$

Analogue to Jansen et al. [109] and Gravemeier and Wall [77], the spectral radius is chosen as $\rho_\infty = 1/2$ resulting in the coefficients as displayed in Table 3.1 leading to a second-order accurate time integration scheme.

α_m	α_f	γ
$\frac{5}{6}$	$\frac{2}{3}$	$\frac{2}{3}$

Table 3.1: Coefficients for generalized- α time integration scheme.

Analogue to Gravemeier et al. [79], the afore presented generalized- α time integration scheme is applied to the variational multiscale method presented in Section 3.1.1.1. This results for the Galerkin formulation without stabilization parameters in the following matrix system

$$\begin{bmatrix} \mathbf{M} & \mathbf{0} \\ \mathbf{0} & \mathbf{0} \end{bmatrix} \begin{bmatrix} \langle \dot{\mathbf{U}} \rangle^{n+\alpha_m} \\ \mathbf{0} \end{bmatrix} + \begin{bmatrix} \mathbf{C} (\langle \mathbf{U} \rangle^{n+\alpha_f}) + \mathbf{V} & -\mathbf{G} \\ \mathbf{G}^\top & \mathbf{0} \end{bmatrix} \begin{bmatrix} \langle \mathbf{U} \rangle^{n+\alpha_f} \\ \langle \mathbf{P} \rangle^{n+\alpha_f} \end{bmatrix} = \begin{bmatrix} \mathbf{f}^{n+\alpha_f} \\ \mathbf{g}^{n+\alpha_f} \end{bmatrix} \quad (3.37)$$

where the nodal degrees of freedom of the state vectors and of the right-hand sides are held at the respective points in time, in contrast to (3.25). The state vectors are subject to

$$\langle \mathbf{U} \rangle^{n+1} = \langle \mathbf{U} \rangle^n + \gamma \Delta t_l \langle \dot{\mathbf{U}} \rangle^{n+1} + (1 - \gamma) \Delta t_l \langle \dot{\mathbf{U}} \rangle^n, \quad (3.38)$$

$$\langle \dot{\mathbf{U}} \rangle^{n+\alpha_m} = \alpha_m \langle \dot{\mathbf{U}} \rangle^{n+1} + (1 - \alpha_m) \langle \dot{\mathbf{U}} \rangle^n, \quad (3.39)$$

$$\langle \mathbf{U} \rangle^{n+\alpha_f} = \alpha_f \langle \mathbf{U} \rangle^{n+1} + (1 - \alpha_f) \langle \mathbf{U} \rangle^n, \quad (3.40)$$

$$\langle \mathbf{P} \rangle^{n+\alpha_f} = \alpha_f \langle \mathbf{P} \rangle^{n+1} + (1 - \alpha_f) \langle \mathbf{P} \rangle^n. \quad (3.41)$$

As proposed by Gravemeier et al. [79], a Picard (or fixed-point-like) iteration scheme is applied to account for the non-linearity in the matrix system (3.37). An incremental formulation of the matrix system is used to solve for the velocity increment

$$\Delta \langle \mathbf{U} \rangle^{n+1,i+1} = \langle \mathbf{U} \rangle^{n+1,i+1} - \langle \mathbf{U} \rangle^{n+1,i} \quad (3.42)$$

and the pressure increment

$$\Delta \langle \mathbf{P} \rangle^{n+1,i+1} = \langle \mathbf{P} \rangle^{n+1,i+1} - \langle \mathbf{P} \rangle^{n+1,i} \quad (3.43)$$

in each iteration step. A steady-state predictor

$$\langle \mathbf{U} \rangle^{n+1,0} = \langle \mathbf{U} \rangle^n \quad \text{and} \quad \langle \mathbf{P} \rangle^{n+1,0} = \langle \mathbf{P} \rangle^n \quad (3.44)$$

starts the iteration procedure. The iteration procedure requires the residual of the momentum equation in (3.37), reading

$$\mathbf{R}_M^i = \mathbf{M} \langle \dot{\mathbf{U}} \rangle^{n+\alpha_m,i} + \mathbf{K}_{wu}^{n+\alpha_f,i} \langle \mathbf{U} \rangle^{n+\alpha_f,i} + \mathbf{K}_{wp}^{n+\alpha_f,i} \langle \mathbf{P} \rangle^{n+\alpha_f,i} - \mathbf{f}^{n+\alpha_f} - \mathbf{a}_u^{n+\alpha_f,i} \quad (3.45)$$

and the residual of the continuity equation in (3.37), reading

$$\mathbf{R}_C^i = \mathbf{K}_{pu}^{n+\alpha_f,i} \langle \mathbf{U} \rangle^{n+\alpha_f,i} + \mathbf{A}_{p-\text{PSPG}}^{n+\alpha_f,i} \langle \mathbf{P} \rangle^{n+\alpha_f,i} - \mathbf{g}^{n+\alpha_f} - \mathbf{a}_{\text{PSPG}}^{n+\alpha_f,i}. \quad (3.46)$$

in which the matrices from modeling the unresolved scales are introduced. The matrices are defined as

$$\mathbf{K}_{wu}^{n+\alpha_f,i} = \mathbf{C} \left(\langle \mathbf{U} \rangle^{n+\alpha_f,i} \right) + \mathbf{V} + \mathbf{A}_{u-\text{SUPG}}^{n+\alpha_f,i} + \mathbf{A}_{u-\text{CS}}^{n+\alpha_f,i} + \mathbf{A}_{u-\text{RS}}^{n+\alpha_f,i} + \mathbf{A}_{\text{GD}}^{n+\alpha_f,i}, \quad (3.47)$$

$$\mathbf{K}_{wp}^{n+\alpha_f,i} = -\mathbf{G} + \mathbf{A}_{p-\text{SUPG}}^{n+\alpha_f,i} + \mathbf{A}_{p-\text{CS}}^{n+\alpha_f,i} + \mathbf{A}_{p-\text{RS}}^{n+\alpha_f,i}, \quad (3.48)$$

$$\mathbf{K}_{pu}^{n+\alpha_f,i} = \mathbf{G}^T + \mathbf{A}_{u-\text{PSPG}}^{n+\alpha_f,i} \quad (3.49)$$

and they contain the matrices $\mathbf{A}_{u-\text{SUPG}}^{n+\alpha_f,i}$, $\mathbf{A}_{p-\text{SUPG}}^{n+\alpha_f,i}$, $\mathbf{A}_{u-\text{PSPG}}^{n+\alpha_f,i}$, $\mathbf{A}_{p-\text{PSPG}}^{n+\alpha_f,i}$, $\mathbf{A}_{\text{GD}}^{n+\alpha_f,i}$, $\mathbf{A}_{u-\text{CS}}^{n+\alpha_f,i}$, $\mathbf{A}_{p-\text{CS}}^{n+\alpha_f,i}$, $\mathbf{A}_{u-\text{RS}}^{n+\alpha_f,i}$, and $\mathbf{A}_{p-\text{RS}}^{n+\alpha_f,i}$ which contain the stabilization terms from SUPG, PSPG, GD, CS, and RS of which all except the GD term are split with respect to their velocity and pressure degrees of freedom. The vectors

$$\mathbf{a}_u^{n+\alpha_f,i} = \mathbf{a}_{\text{SUPG}}^{n+\alpha_f,i} + \mathbf{a}_{\text{CS}}^{n+\alpha_f,i} + \mathbf{a}_{\text{RS}}^{n+\alpha_f,i} \quad (3.50)$$

and $\mathbf{a}_{\text{PSPG}}^{n+\alpha_f,i}$ contain the right-hand side contributions of the SUPG, CS, RS, and PSPG stabilization term. The superscript $(\cdot)^{n+\alpha_f,i}$ denotes a dependency on the velocity $\langle \mathbf{U} \rangle^{n+\alpha_f,i}$.

The linearization of the residuals with respect to the variables to obtain the increments reads

$$\begin{bmatrix} \frac{\partial \mathbf{R}_M^i}{\partial \langle \mathbf{U} \rangle^{n+1}} & \frac{\partial \mathbf{R}_M^i}{\partial \langle \mathbf{P} \rangle^{n+1}} \\ \frac{\partial \mathbf{R}_C^i}{\partial \langle \mathbf{U} \rangle^{n+1}} & \frac{\partial \mathbf{R}_C^i}{\partial \langle \mathbf{P} \rangle^{n+1}} \end{bmatrix} \begin{bmatrix} \Delta \langle \mathbf{U} \rangle^{n+1,i+1} \\ \Delta \langle \mathbf{P} \rangle^{n+1,i+1} \end{bmatrix} = - \begin{bmatrix} \mathbf{R}_M^i \\ \mathbf{R}_C^i \end{bmatrix} \quad (3.51)$$

which contains approximations to the consistent tangent matrix using

$$\frac{\partial \langle \dot{\mathbf{U}} \rangle^{n+\alpha_m}}{\partial \langle \mathbf{U} \rangle^{n+1}} = \frac{\partial \langle \dot{\mathbf{U}} \rangle^{n+\alpha_m}}{\partial \langle \dot{\mathbf{U}} \rangle^{n+1}} \frac{\partial \langle \dot{\mathbf{U}} \rangle^{n+1}}{\partial \langle \mathbf{U} \rangle^{n+1}} = \frac{\alpha_m}{\gamma \Delta t_l}, \quad (3.52)$$

$$\frac{\partial \langle \mathbf{U} \rangle^{n+\alpha_f}}{\partial \langle \mathbf{U} \rangle^{n+1}} = \frac{\partial \langle \mathbf{P} \rangle^{n+\alpha_f}}{\partial \langle \mathbf{P} \rangle^{n+1}} = \alpha_f. \quad (3.53)$$

Inserting (3.52) and (3.53) into (3.51) leads to the final linear system of equations

$$\begin{bmatrix} \mathbf{M} + \frac{\alpha_f}{\alpha_m} \gamma \Delta t_l \mathbf{K}_{wu}^{n+\alpha_f, i} & \frac{\alpha_f}{\alpha_m} \gamma \Delta t_l \mathbf{K}_{wp}^{n+\alpha_f, i} \\ \frac{\alpha_f}{\alpha_m} \gamma \Delta t_l \mathbf{K}_{pu}^{n+\alpha_f, i} & \frac{\alpha_f}{\alpha_m} \gamma \Delta t_l \mathbf{A}_{p-\text{PSPG}}^{n+\alpha_f, i} \end{bmatrix} \begin{bmatrix} \Delta \langle \mathbf{U} \rangle^{n+1,i+1} \\ \Delta \langle \mathbf{P} \rangle^{n+1,i+1} \end{bmatrix} = - \frac{\gamma \Delta t_l}{\alpha_m} \begin{bmatrix} \mathbf{R}_M^i \\ \mathbf{R}_C^i \end{bmatrix} \quad (3.54)$$

within the iterative procedure to obtain the increments for the velocity and the pressure.

3.1.2 Time discretization of the Lagrangian particles

3.1.2.1 Central difference time integration

The particles are tracked in a Lagrangian frame and for each particle the equations of motion (2.40) and (2.95) are solved individually. The particles are discretized in time with an explicit time integration scheme opposed to the fluid with its implicit time integrator as presented in Section 3.1.1.2. The literature dealing with the discrete element method (DEM), as invented in Cundall and Strack [34], favors explicit time integration schemes due to their simplicity and the need to solve for a possibly very large number of particles in the system, cf. Tuley et al. [209]. Moreover, contact between small particles may pose the necessity for a small time step size in order to resolve the discontinuity properly, such that a small time step size is already imposed by the physics. In Tuley et al. [209], a comparison of different time integrators is performed which reveals that higher order methods such as 4th-order Runge-Kutta methods loose their expected order of accuracy when it comes to contact at a point in time which does not coincide with one of the stage times. It is concluded that lower order time integration schemes are superior in DEM applications. Therefore, the central difference time integration scheme, also known as velocity Verlet algorithm, is applied exclusively in this thesis. It has already been applied in Cundall and Strack [34]. Its advantage is second order accuracy in time in case undamped contact is considered, and, in addition, it demands for only one evaluation of the forces within one time step. In contrast to the fluid, the time of interest $[0, t_{\text{end}}]$ is divided into discrete time steps of size Δt_b which does not necessarily coincide with Δt_l . Then, time stepping from t^m to t^{m+1} with $t^{m+1} = t^m + \Delta t_b$ comprises four steps for each particle i :

1. Advance velocity and angular velocity to $t^{m+1/2}$:

$$\mathbf{v}_i^{m+1/2} = \mathbf{v}_i^m + \frac{\Delta t_b}{2} \mathbf{a}_i^m \quad (3.55)$$

$$\boldsymbol{\omega}_i^{m+1/2} = \boldsymbol{\omega}_i^m + \frac{\Delta t_b}{2} \boldsymbol{\alpha}_i^m \quad (3.56)$$

2. Advance position to t^{m+1} :

$$\mathbf{x}_i^{m+1} = \mathbf{x}_i^m + \Delta t_b \mathbf{v}_i^{m+1/2} \quad (3.57)$$

3. Compute forces

$$\mathbf{F}_i^{m+1} = \mathbf{F}_{g,i} + \sum \mathbf{F}_{\Gamma,i}(\mathbf{x}_i^m, \mathbf{v}_i^m, \mathbf{a}_i^m, r^{m+1}) + \mathbf{F}_{c,i}(\mathbf{x}^{m+1}, \mathbf{v}^{m+1/2}, \boldsymbol{\omega}^{m+1/2}, r^{m+1}) \quad (3.58)$$

and moments

$$\mathbf{M}_i^{m+1} = \mathbf{M}_i(\mathbf{x}^{m+1}, \mathbf{v}^{m+1/2}, \boldsymbol{\omega}^{m+1/2}, r^{m+1}), \quad (3.59)$$

to obtain acceleration

$$\mathbf{a}_i^{m+1} = \frac{1}{m_i} \mathbf{F}_i^{m+1}, \quad (3.60)$$

and angular acceleration

$$\boldsymbol{\alpha}_i^{m+1} = \frac{1}{I_i} \mathbf{M}_i^{m+1} \quad (3.61)$$

at t^{m+1} using (2.95) and (2.35).

4. Advance velocity and angular velocity to t^{m+1} :

$$\mathbf{v}_i^{m+1} = \mathbf{v}_i^{m+1/2} + \frac{\Delta t_b}{2} \mathbf{a}_i^{m+1} \quad (3.62)$$

$$\boldsymbol{\omega}_i^{m+1} = \boldsymbol{\omega}_i^{m+1/2} + \frac{\Delta t_b}{2} \boldsymbol{\alpha}_i^{m+1} \quad (3.63)$$

It should be noted that the orientation in space is irrelevant for the computation of the moments and the angular acceleration. Hence, regarding the rotational degrees of freedom, only the angular velocity and angular acceleration are tracked throughout the simulation whereas the orientation is omitted.

3.1.2.2 Critical time step size

The central difference algorithm is only conditionally stable leading to a restriction on the admissible time step size in order to preserve stability. Before coming to assess the critical time step size, the penalty parameter introduced in (2.57) needs to be defined. Theoretically, an arbitrary positive value could be chosen for this artificial stiffness parameter, i.e. $k_n \in \mathbb{R}^+$. However, a reasonable choice limits the stiffness such that neither a too large penetration occurs nor that the time step size restriction gets too severe which leads to unaffordable computational cost. The approach chosen to determine k_n is based on energy conservation during the contact process while neglecting viscous and numerical damping. The larger the kinetic energy of the system the larger the penetration during contact while keeping k_n constant. It is assumed that the overall kinetic energy of the particles right before collision is transformed into potential energy in the point of maximal penetration in which $\mathbf{v}_i = \mathbf{0}$ for both collision partners. This reads for two particles approaching centrically with velocity magnitude v_{\max}

$$2 \frac{1}{2} m_{\max} v_{\max}^2 \stackrel{!}{=} \frac{1}{2} k_n |g_n|_{\max}^2. \quad (3.64)$$

This represents the contact scenario with maximal penetration of two particles, because a central collision of two particles with maximal mass m_{\max} and maximal velocity, of all particles involved, is considered. In order to obtain a realistic collision behavior, the maximal allowed penetration is restricted to

$$|g_n|_{\max} \stackrel{!}{\leq} c 2 r_{\max} \quad (3.65)$$

with a positive constant $c \ll 1$ and the maximal involved radius r_{\max} . Inserting

$$m_{\max} = \frac{4}{3} r_{\max}^3 \pi \rho_b \quad (3.66)$$

and (3.65) into (3.64) allows for computing a lower bound for the stiffness, viz

$$k_n \geq \frac{2}{3} \pi \rho_b \frac{r_{\max} v_{\max}^2}{c^2}. \quad (3.67)$$

In summary, having a good estimate for the maximal radius and the maximal velocity in advance allows for choosing k_n such that the prescribed maximal penetration is not exceeded. Tuley et al. [209] propose c in the range of 0.1 – 1.0 % of the particle diameter which is denoted as “realistic” or “ideal”. Nevertheless, there is no numerical reason for such a small value of c . Consequently, several contributions can be found in the literature that allow for much larger relative penetrations. In the examples of this thesis, $0.02 r_{\max} \leq c \leq 0.08 r_{\max}$ is chosen to weaken the time step size restriction while still having “physical” collision results.

After having determined the required stiffness to account for contact, the critical time step size can be assessed. For simple linear and undamped systems, such as a single particle, the critical time step size for the central difference time integrator reads

$$\Delta t_{\text{crit}} = 2 \sqrt{\frac{m_i}{k_n}}. \quad (3.68)$$

The corresponding derivation can be found in O’Sullivan and Bray [162] and references therein. Essential in (3.68) is the proportionality $\Delta t_{\text{crit}} \sim \sqrt{1/k_n}$ revealing that a higher stiffness leads to a more severe restriction on the time step size. Therefore, always the lower bound in (3.67) is chosen for k_n . Usually, particle problems are 3D, and random packings occur. This is accounted for by O’Sullivan and Bray [162] who investigate in detail the central difference time integration scheme combined with a linear spring model. They found a critical time step size

$$\Delta t_{\text{crit}} = S f_{cr} \sqrt{\frac{m_{\min}}{k_n}} \quad (3.69)$$

for 3D analysis of colliding particles with a safety factor $S = 0.75$ and m_{\min} the minimal particle mass. A distinction is made by O’Sullivan and Bray [162] whether only normal contact forces are considered, leading to $f_{cr} = 0.348$, or also accounting for tangential contact forces leading to a more severe restriction of the time step size with $f_{cr} = 0.221$. The time step size in (3.69) is a worst case scenario which may not necessarily arise during a simulation but keeping this limit for Δt_b leads to a stable time integration scheme.

3.1.2.3 Implicit treatment of added mass force

As summarized in Section 2.2, different forces contribute to the sum of forces acting on each particle which is necessary for computing the acceleration during time integration, cf. (3.58). Special attention has to be given to the added mass force \mathbf{F}_{am} introduced in (2.51). A small example with an initially resting air bubble which is released in an initially quiescent fluid that starts ascending due to buoyancy is used to reveal the instability. Contact forces are neglected for a moment. Right after releasing the particle, only $F_b = \rho_l V_p g$ is relevant because particle and fluid are still at rest and due to $\rho_l/\rho_b \approx 1000 \gg 1$ gravity force can be neglected in the explicit treatment. During time integration, the particle acceleration is computed according to (3.60) leading to an acceleration of $\mathcal{O}(g \rho_l/\rho_b) \approx \mathcal{O}(10^4 \text{ m/s}^2)$ at the end of the first time step. This acceleration is far too high leading to an added mass force

$$\mathbf{F}_{am,i} = c_{am}\rho_l V_{p,i} \left(\frac{D\langle \mathbf{u} \rangle_i}{Dt} - \frac{D\mathbf{v}_i}{Dt} \right) = c_{am}\rho_l V_{p,i} \left(\mathcal{O}(0) - \mathcal{O}\left(g \frac{\rho_l}{\rho_b}\right) \right) \quad (3.70)$$

via (2.51) in the second step. This added mass force dominates all forces acting on the particle in the second step such that it counteracts the particle motion and it even reverses the motion direction. Hence, an instability is introduced and the orders involved clearly show that after a few steps the system goes out of bounds. A remedy is an implicit treatment of the added mass force while all other forces are still treated explicitly. As the particle acceleration is only included linearly in the added mass force, (2.39) can be reordered as

$$(m_i + c_{am}\rho_l V_{p,i}) \frac{D\mathbf{v}_i^{m+1}}{Dt} = \mathbf{F}_{g,i} + \mathbf{F}_{p,i} + \mathbf{F}_{\tau,i} + \mathbf{F}_{d,i} + \mathbf{F}_{l,i} + c_{am}\rho_l V_{p,i} \frac{D\langle \mathbf{u} \rangle_i}{Dt} \quad (3.71)$$

with all terms on the right-hand side evaluated at time step m . Hence, the new acceleration for particle i in (3.60) can be updated independently of all other particles without the need of iteration steps. This procedure enables to resolve the stability issue in the aforementioned example while the computational cost is almost unchanged. Due to conceptual constraints, the contact force is not included in (3.71). Either an error is accepted here or an implicit treatment of all particles is necessary which can be obtained using the strong coupling scheme including an outer loop which will be presented in Section 3.2.2.

3.2 Partitioned fluid-particle framework

The relevant time scales included in a particulate flow simulation may be different for the physics involved. Considering dispersed flow with particles of constant radius, two different relevant time scales can be identified as depicted in the first two scales of Figure 3.1.

1. In the carrier fluid, the speed of sound in air and water is in the range of 1500 m/s and 330 m/s, respectively. The velocities considered are smaller than 100 m/s such that the flow can be assumed incompressible. Usually, a time step size Δt_l is of $\mathcal{O}(10^{-4}\text{s} \dots 10^{-2}\text{s})$ to appropriately resolve the larger flow characteristics.
2. When taking into account the contact of submerged very small particles, a finer temporal resolution Δt_b is necessary which might be of $\mathcal{O}(10^{-8}\text{s} \dots 10^{-5}\text{s})$.

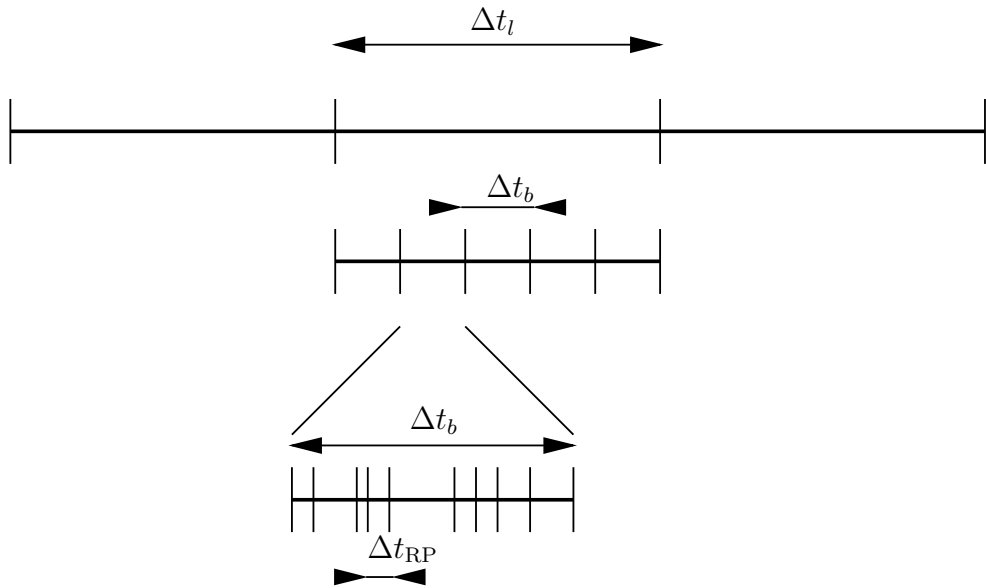


Figure 3.1: Different time scales in a fluid-particle problem.

In case, a variable radius is considered which is governed by the RP equation, a third time scale becomes relevant, see Figure 3.1. An appropriate time step size Δt_{RP} of $\mathcal{O}(10^{-12} \text{ s} \cdots 10^{-7} \text{ s})$ resolves the collapse of cavitation bubbles, compare Alehossein and Qin [3].

To account efficiently for these broad range of relevant time scales, a natural choice is to apply subcycling between fluid and particles in order to reduce the computational effort. Fields are only solved when noticeable changes are expected, and coupling states are interpolated to the intermediate levels for the finer resolved field, i.e. for the particles.

3.2.1 Weakly coupled

A summary of the sequence of steps for the loosely coupled Euler-Lagrange approach including subcycling is given in Algorithm 1. After initializing all fields and setting up the connectivity, the time loop starts. In each time step, first, the fluid is solved at $t + \Delta t_l$ using the generalized- α time integration scheme as presented in Section 3.1.1.2. The coupling variables, namely the fluid fraction and the momentum source term, are evaluated from the latest available particle position and radius which nevertheless lag behind Δt_l . Next, the particles are advanced in time applying a subcycling procedure. The position, velocity, and acceleration of the particles are updated as described in Section 3.1.2. The relevant coupling data from the fluid, i.e., velocity, acceleration, and pressure, are linearly interpolated in time to the current evaluation time. Then, the fluid and the particles have reached the same time t . To conclude the fluid time step, the velocity and pressure are updated. In case inflow of particles into the domain is considered, this is linked to the update at the end of each fluid time step. This whole procedure is repeated until the final time t_{end} is reached.

For the special case of a variable radius governed by the RP equation, the afore presented procedure is supplemented by the evolution of the particle radius. Before the translational and rotational motion of the particles is integrated in the fluid-particle subcycling procedure (see line

Algorithm 1 Loosely coupled fluid-particle coupling algorithm.

```

1: initialize fluid and particle solver and setup connectivity:  $t = n = m = k = 0$ 
2: while time loop not finished:  $t \leq t_{\text{end}}$  do
3:   calculate fluid fraction  $\epsilon_l^n$  with  $\mathbf{x}^m, r^k$ 
4:   // integrate fluid
5:   solve fluid for time  $t^{n+1}$  with particle forces from time  $t^n$  and  $\epsilon_l^n$ 
6:   // start subcycling for bubbles
7:    $t' = 0$ 
8:   while  $t' < \Delta t_l$  do
9:     // advance bubble radius with adaptive time stepping
10:     $t'' = 0$ 
11:    while  $t'' < \Delta t_b$  do
12:      normalized local truncation error  $\epsilon_R^{k+1} = +\infty$ 
13:      // repeat steps while not converged
14:      while  $\epsilon_R^{k+1} > tol_{\text{RP}}$  do
15:        Runge-Kutta time stepping:  $r^k \rightarrow r^{k+1}$  with linearly interpolated pressure  $p$  in
         time at each stage to position  $\mathbf{x}^m$ 
16:        compute  $\epsilon_R^{k+1}$ 
17:        adapt time step size  $\Delta t_{\text{RP}}^{k+1}$ 
18:      end while
19:      update  $\{r^k \leftarrow r^{k+1}\}, t'' += \Delta t_{\text{RP}}^{k+1}$  and  $\{k \leftarrow k + 1\}$ 
20:    end while
21:
22:    // advance particle position
23:    compute forces on particle with  $\mathbf{x}^m, \mathbf{v}^m, \mathbf{a}^m, r^{k+1}$  and fluid states  $\mathbf{u}$  and  $\mathbf{p}$  linearly
       interpolated in time to  $t + t' + \Delta t_b$ 
24:    central difference time stepping:  $\mathbf{x}^m, \mathbf{v}^m, \mathbf{a}^m \rightarrow \mathbf{x}^{m+1}, \mathbf{v}^{m+1}, \mathbf{a}^{m+1}$ 
25:    update  $\{\mathbf{x}^m, \mathbf{v}^m, \mathbf{a}^m \leftarrow \mathbf{x}^{m+1}, \mathbf{v}^{m+1}, \mathbf{a}^{m+1}\}, t' += \Delta t_b$  and  $\{m \leftarrow m + 1\}$ 
26:    update connectivity for neighborhood search of particles
27:  end while
28:  insert inflowing particles into the domain
29:  update  $\{\mathbf{u}^n, p^n \leftarrow \mathbf{u}^{n+1}, p^{n+1}\}, t += \Delta t_l$  and  $\{n \leftarrow n + 1\}$ 
30: end while

```

22 to 26 in Algorithm 1), another subcycling procedure is included, see line 9 to 20 in Algorithm 1, using the adaptive time stepping scheme as will be presented in Section 3.5.1. While the particle radius is evolved up to the time period Δt_b , using the variable time step size Δt_{RP} , the particle position is kept constant and a linear interpolation in time is performed for the ambient pressure of the surrounding fluid. Afterwards, the latest available particle radius is kept constant while the translational motion of the particle is integrated in time. The alternating evolution of radius and position/velocity/acceleration is repeated until subcycling is finished for this fluid time step. A special treatment of the radius evolution is included. Due to the adaptive time stepping procedure, particle radius evolution time steps are only accepted if the normalized estimated local truncation error ϵ_R^{k+1} does not exceed some given tolerance tol_{RP} , otherwise they are repeated with a smaller time step size Δt_{RP}^k .

The rotational degrees of freedom are linked to the integration of the translational degrees of freedom and they are skipped in the previously described algorithm in order not to increase complexity further. As there is neither a coupling between the rotation of the particles and the fluid, nor the rotation and the radius evolution, this step of integrating the rotational degrees of freedom can easily be added.

3.2.2 Strongly coupled with Aitken relaxation

The loosely coupled algorithm as presented in the previous section may lack of stability and lead to a diverging solution. Preliminary tests revealed this issue especially when a variable radius based on the RP equation is considered. A possible remedy is a strong coupling scheme which iterates between the fluid and particle field within one time step until convergence is achieved. The most sensitive quantities are the pressure of the fluid field and the radii of the bubbles. Hence, the increment from iteration i to $i + 1$ of these two quantities define the residual vectors

$$\mathbf{R}_p = \langle \mathbf{P} \rangle_{i+1}^{n+1} - \langle \mathbf{P} \rangle_i^{n+1} \quad \text{and} \quad \mathbf{R}_r = \mathbf{R}_{i+1}^{n+1} - \mathbf{R}_i^{n+1}. \quad (3.72)$$

For simplicity, the index n is also used for the radius in order to show that radius and pressure are evaluated at t^n and t^{n+1} , although many subcycling steps are necessary for advancing the radius while one fluid time step is performed. To simplify the definition of a good tolerance for the residual, a relative error is defined using the pressure and the radius from the last converged solution, viz

$$r_{p,\text{rel}} = \frac{\|\mathbf{R}_p\|_2}{\|\langle \mathbf{P} \rangle^n\|_2}, \quad r_{r,\text{rel}} = \frac{\|\mathbf{R}_r\|_2}{\|\mathbf{R}^n\|_2}. \quad (3.73)$$

The abort criterion for the outer iteration then reads

$$r_{p,\text{rel}} < tol_p \quad \text{and} \quad r_{r,\text{rel}} < tol_r \quad (3.74)$$

with $tol_p = tol_r = 10^{-5}$ if not stated otherwise.

It turned out that applying strong coupling leads to a very slow convergence and iteration numbers of 100 and more occurred regularly. Zohdi [242] proposes a strong coupling scheme in which the time step size is adapted in order to meet a target number of iterations. For steady state simulations, Laín and Sommerfeld [126] propose under-relaxation with a fixed relaxation parameter between 0.5 and 0.1 leading to typically 25 to 35 iterations between the fluid and the

particle field. In Ansys CFX (see [1]), under-relaxation with a default value of 0.75 is recommended for steady state fluid-particle problems. In the latter two cases, the relaxed quantities are the source terms in the (volume averaged) Navier-Stokes equations. In order to accelerate convergence, a dynamic relaxation strategy, namely Aitken's Δ^2 method as originally proposed by Irons and Tuck [105] and later applied to fluid-structure-interaction by Küttler and Wall [125] is applied in this thesis. Here, the bubble radius is the preferred variable to be relaxed because it is advanced with the RP equation and it enters the fluid fraction in the right-hand side of (2.24), directly influencing the fluid pressure. Instead of using the latest radius to compute the fluid fraction, the following relaxation

$$\mathbf{R}_{i+1}^{n+1} = \omega_i \tilde{\mathbf{R}}_{i+1}^{n+1} + (1 - \omega_i) \mathbf{R}_i^{n+1} \quad (3.75)$$

is used, in which ω_i is the relaxation parameter. Starting with \mathbf{R}_i^{n+1} , the solution for the radius after iterating the fluid and the bubbles once is denoted with $\tilde{\mathbf{R}}_{i+1}^{n+1}$. The relaxed solution \mathbf{R}_{i+1}^{n+1} is then inserted in the fluid fraction computation in order to start the next outer iteration step $i + 1$. The relaxation parameter is specified according to Aitken's Δ^2 method. Therein, two differences of the radius: $\mathbf{R}_{r,i+1} = \tilde{\mathbf{R}}_{i+1}^{n+1} - \mathbf{R}_i^{n+1}$ and $\mathbf{R}_{r,i+2} = \tilde{\mathbf{R}}_{i+2}^{n+1} - \mathbf{R}_{i+1}^{n+1}$ are used to compute the Aitken factor

$$\mu_{i+1} = \mu_i + (\mu_i - 1) \frac{-(\mathbf{R}_{r,i+1})^\top (\mathbf{R}_{r,i+2} - \mathbf{R}_{r,i+1})}{\|\mathbf{R}_{r,i+2} - \mathbf{R}_{r,i+1}\|_2^2} \quad (3.76)$$

which is then used to evaluate the relaxation parameter

$$\omega_{i+1} = 1 - \mu_{i+1}. \quad (3.77)$$

For starting the relaxation, an initial guess $\mu_0 = 0.67$ is chosen and a startup procedure is applied in order to obtain two residuals. In the first relaxation step in which only one residual is available, ω is taken from the last converged time step, viz $\omega_{i_{\max}}^n$, and it is limited via

$$\omega_0 = \min(\omega_{i_{\max}}^n, \omega_{\max}) \quad (3.78)$$

with a maximal allowed relaxation parameter ω_{\max} . According to Küttler and Wall [125], this limitation improves stability for the application of fluid-structure interaction as $\omega_{i_{\max}}^n$ might be too large.

In case the strong coupling scheme should be applied to fluid-particle coupled problems featuring constant-size particles, it is not possible to use the radius vector for relaxation. Instead, a residual vector

$$\mathbf{R}_d = \mathbf{x}_{i+1}^{n+1} - \mathbf{x}_i^{n+1} \quad (3.79)$$

based on the position \mathbf{x} of the particles at iteration i and $i + 1$ can be used. The corresponding relative residual reads

$$r_{d,\text{rel}} = \frac{\|\mathbf{R}_d\|_2}{\|\mathbf{x}^n\|_2} \quad (3.80)$$

with the positions from the last converged step \mathbf{x}^n in the denominator. The abort criterion for the outer iteration is

$$r_{d,\text{rel}} < tol_d \quad (3.81)$$

with the tolerance tol_d . The relaxation with its start-up procedure to compute the first residual does not have to be altered, see (3.78). Also, the computation of the relaxation parameter ω according to (3.76) can be reused. Eventually, the relaxed particle positions are applied in the particle force calculation.

3.3 Quantity mapping between frames

3.3.1 Eulerian to Lagrangian quantity mapping

The coupling from the fluid to the particles consists of evaluating the force contributions as given in (2.39). Therein, it is necessary to evaluate the fluid quantities, i.e. velocities, pressure and material fluid acceleration, at the particle (center) position. The pressure and velocities are primary variables of the fluid which can easily be accessed whereas the material fluid acceleration is computed via

$$\frac{D\mathbf{u}}{Dt} = \frac{\partial \mathbf{u}}{\partial t} + \mathbf{u} \cdot \nabla \mathbf{u} \quad (3.82)$$

in the continuous setting. This is discretized using the latest available fluid acceleration state for the first summand and fluid velocity state for the second summand. For the mapping of the quantities from the Eulerian to the Lagrangian frame, several approaches can be found in literature. Volume weighted interpolation is used e.g. in Delnoij et al. [42] for a finite difference scheme of the underlying fluid field. For a finite volume discretization, often distribution kernels or template functions are used to weight the influence of nearby cells to obtain the fluid quantities at the particle position, see e.g. Shams et al. [187] or Darmana et al. [36] which use a Gaussian filtering function or a fourth order polynomial. In this work, the FEM is used for the fluid and thus a natural choice is to use an interpolation using the shape functions of the underlying fluid element evaluated at the particle position. Hence, the fluid velocity and acceleration can be evaluated using (3.23) and for evaluating the pressure, (3.24) can be used. Instead of using the pressure value at the particle center for evaluating the RP equation, Hsiao et al. [95] propose the so-called surface averaged pressure scheme which takes the average of the fluid pressure at the six polar points of the particle surface. This increases accuracy which might be interesting for larger particles. As the particles are expected to be small, the additional effort is avoided for the moment although the implementation is straight forward. Hence, the interpolation of e.g. the fluid velocity at the center position of particle i reads

$$\langle \mathbf{u} \rangle_i(t) = \langle \mathbf{u} \rangle(\mathbf{x}_i, t) = \sum_{\alpha_e} N_{\alpha_e}(\boldsymbol{\xi}(\mathbf{x}_i)) \langle \mathbf{u} \rangle_{\alpha_e}(t) \quad (3.83)$$

in which the task is to find the natural coordinates $\boldsymbol{\xi}(\mathbf{x}_i)$ of the particle center in the host (or underlying) element e . Then, the summation over the α_e nodes of the element can be performed. The same interpolation is used for the pressure and the material fluid acceleration. In case of distorted elements in an unstructured grid, the computation of the natural coordinates evolves to the solution of a small nonlinear system of equations with the help of a Newton scheme. The respective equation to be solved is

$$\left(\sum_{\alpha_e} N_{\alpha_e}(\boldsymbol{\xi}(\mathbf{x}_i)) \right) - \mathbf{x}_i = \mathbf{0}. \quad (3.84)$$

In order to find the underlying fluid element for a particle, the natural coordinates corresponding to the particle position must be computed. Then, it is possible to decide whether the underlying fluid element is found based on the natural coordinates. For example, the inside of a tri-linearly interpolated hexahedral element cover $[-1, 1]$ in each direction in natural coordinates. In order to reduce the computational effort, a two step procedure is applied. First, a cheap bounding box approach is applied to sort out the vast majority of elements. Second, those elements which are found to be close during the first step are checked in detail using (3.84).

3.3.2 Lagrangian to Eulerian quantity mapping

The fluid forces acting on the particles have been presented in Section 2.2.2. These forces are computed in the Lagrangian frame of the particles. However, the reaction forces (2.53) onto the fluid need to be applied in the Eulerian frame in the fluid momentum equation (2.111) as described by Crowe et al. [32]. This coupling from the dispersed to the continuous phase can again be performed using the shape functions of the underlying fluid element evaluated at the particle position as presented by Löhner et al. [137]. The shape functions fulfill partition of unity which leads to a conservative coupling scheme. This technique has already been used in the context of fluid-structure interaction by Farhat et al. [59]. This approach is also consistent with (3.17) which states that the coupling forces need to be weighted with weighting functions which finally ends up in a multiplication with the ansatz function.

A different approach is common when using a finite volume discretization for the underlying fluid. It is possible to distribute the volume of a particle among the cells in its neighborhood using a filtering (or interpolation kernel) function as already described in the previous section. Consequently, the particle reaction forces are divided onto the cells according to the respective volume fractions. This procedure is described in Darmana et al. [36], which the reader is referred to for more details. It might be also applicable to a finite element based discretization. However, the question arises how to distribute the forces onto the nodes of the elements. Thus, for rather small particles, the more natural choice is to use the shape functions of the underlying fluid element to distribute the reaction forces.

3.4 Fluid fraction computation

The content of this Section 3.4 has already been published by the author of this thesis in Menner* et al. [149] and it is repeated here with minor changes.

The fluid fraction as introduced in (2.13) gives the ratio between the volume of continuous phase within the averaging volume and the averaging volume itself. The particles are treated point-like in the Euler-Lagrange framework and therefore a filtering function is applied at each particle position to smear the volume of the corresponding dispersion onto the fluid domain. Hence, the particles make up the dispersed phase volume which is subtracted from the fluid domain, leaving the volume purely occupied with fluid. Finally, the fluid fraction is computed as

$$\epsilon_l^e = 1 - \frac{\sum_{k=1}^{k_p} V_{p,k} \int_{\Omega^e} \psi_i(x, y, z) d\Omega}{\int_{\Omega^e} 1 d\Omega}, \quad (3.85)$$

where k_p is the number of particles whose filtering cubes lie partially or fully in the fluid element Ω^e and $V_{p,k}$ is the volume of particle k . Therein, $\psi_i(x, y, z)$ and i denote the filtering function and its order, respectively.

Several options for filtering functions can be found in literature depending on the desired accuracy and the computational effort to be invested. The most trivial approach, known as *center of volume* or *point approximate method*, assumes that the particle's volume is not distributed across several fluid elements. The corresponding filtering function is a Dirac delta at the particle center. Thus, the volume is assigned to the element in which the center of the particle resides. This leads to jumps in the dispersed phase fraction when a particle passes element boundaries which leads to artificial pressure waves and detrimental pulsatile fluid flow profiles. A common assumption in Euler-Lagrange approaches are spherical shapes of the particles under consideration. Also, the support of the filtering function is assumed spherical and hence, the volume integral during dispersed phase volume computation includes spherical domains. Dependent on the discretization of the continuous phase, Freireich et al. [65] and Peng et al. [164] present an exact method to compute the dispersed phase volume when a Cartesian grid for the fluid is used and Wu et al. [232] give the equations to compute the dispersed phase volume on an unstructured fluid grid. In the latter, tetrahedral, hexahedral and wedge elements are considered. Although both methods lead to an exact analytical solution, the former is restricted to Cartesian grids which might not be appropriate in case of flow in complex domains and the latter contains expensive trigonometric calculations. Boyce et al. [18] state that the proposed look-up table introduced by Wu et al. [232] only circumvents the expensive calculations, nevertheless finding the position of the particle relative to the element boundaries remains very costly.

In case the assumption of spherical particles might not hold, Tomiyama et al. [205] propose to use an approximation with cubic shape for the possibly complex particle contour in order to ease computation. Hence, the filtering function has a cubic support. This approximation can also be plugged in when sphericity is prevailing which then leads to a filtering function with cubic support that circumscribes the sphere. According to Khawaja et al. [114], this can lead to errors up to 20 % compared to a spherical support of the filtering function and therefore a correction is proposed to reduce the error significantly. Kitagawa et al. [115] apply a cubic support for the filtering function and they span different filtering functions, namely a (clipped and enhanced) Gaussian function and a sine wave function, in the cube. The different filtering functions are compared with respect to velocity fluctuations when the dispersed phase passes across elements of the underlying fluid. A clear relationship between the choice of the filtering function and velocity fluctuations is reported with an improvement when the filtering function is smoother, i.e. the value and its first derivative of the filtering function are zero at the boundary of the filtering function. Unfortunately, there is no hint given by Kitagawa et al. [115] how the arising volume integrals are solved.

The procedure developed in this thesis is based on the ideas of Rathod and Govinda Rao [174] and Dasgupta [37] in which the volume integral in the dispersed phase volume computation (3.85) is transformed into a surface integral and in a second step into a parametric line integral via applying divergence theorem twice. Rathod and Govinda Rao [174] perform symbolic integration of the integrand and Dasgupta [37] applies Gaussian quadrature to solve the resulting line integrals. As the developed approach aims on solving a priori known filtering functions it is possible to perform the integration and implement the resulting equation in order to circumvent the need of repeated symbolic integration during the simulation. Three different filtering func-

tions, namely a constant, a quadratic and a quartic polynomial will be compared. The constant polynomial filtering function is included for validation purpose. The quartic polynomial was proposed in the context of Euler-Lagrange simulations in Deen et al. [40] and it is now investigated in detail for the first time. The quadratic polynomial has never been applied as filtering function before.

3.4.1 Analytical integration of polynomial filtering functions

The complexity in (3.85) is in

$$\int_{\Omega^e} \psi_i(x, y, z) d\Omega, \quad (3.86)$$

which will be integrated analytically using polynomial filtering functions and an appropriate description of the underlying geometry. The conceptual idea is to formulate the three-dimensional volume integral as a collection of one-dimensional line integrals over the volume's boundaries. A three step procedure proposed by Sudhakar and Wall [198] and Sudhakar et al. [199] is applied:

- (i) first, the volume integral (3.86) is described as surface integrals over the volume's bounding surfaces with the divergence theorem according to Morse and Feshbach [153] and Arens et al. [6],
- (ii) then, the surfaces are projected alongside the divergence directions in (i), and
- (iii) solve the surface integrals with line integrals along the edges of the surfaces by applying the divergence theorem again.

Remark to (i): The divergence theorem states that the divergence of a flux, the vector field $\mathbf{F}(x, y, z)$, integrated within a volume Ω is equal to the flux through the closed surfaces Γ of the same volume:

$$\int_{\Omega} \nabla \cdot \mathbf{F}(x, y, z) d\Omega = \int_{\Gamma} \mathbf{F}(x, y, z) \cdot \mathbf{n}(x, y, z) d\Gamma, \quad (3.87)$$

where

$$\mathbf{n}(x, y, z) = [n_x(x, y, z) \ n_y(x, y, z) \ n_z(x, y, z)]^T \quad (3.88)$$

is the outward pointing unit normal field to the surface Γ .

Remark to (ii): In order to solve a surface integral, the surface is projected along the vector field $\mathbf{F}(x, y, z)$. The projected surface and projected normal field are denoted by Γ_{\perp} and by $\mathbf{n}_{\perp}(x, y, z)$, respectively.

Remark to (iii): The surface integral with surface Γ_{\perp} is solved with line integration over its boundary $\partial\Gamma_{\perp}$ by applying the divergence theorem for the second time:

$$\int_{\Gamma_{\perp}} \nabla \cdot \mathbf{H}(x, y, z) d\Gamma = \int_{\partial\Gamma_{\perp}} \mathbf{H}(x, y, z) \cdot \mathbf{m}(x, y, z) ds \quad (3.89)$$

with a vector field $\mathbf{H}(x, y, z)$ and the outward pointing unit normal field to $\partial\Gamma_{\perp}$:

$$\mathbf{m}(x, y, z) = [m_x(x, y, z) \ m_y(x, y, z) \ m_z(x, y, z)]^T. \quad (3.90)$$

The line integral on the right-hand side of (3.89) has to be solved anti-clockwise considering the orientation of the normal field $\mathbf{n}_\perp(x, y, z)$.

Figure 3.2 shows the geometric interpretation of the procedure with the projection of a surface alongside a vector field $\mathbf{F}(x, y, z) = [1 \ 0 \ 0]^\top$. The projection of the surface Γ is done such that $x(\Gamma_\perp) = 0$.

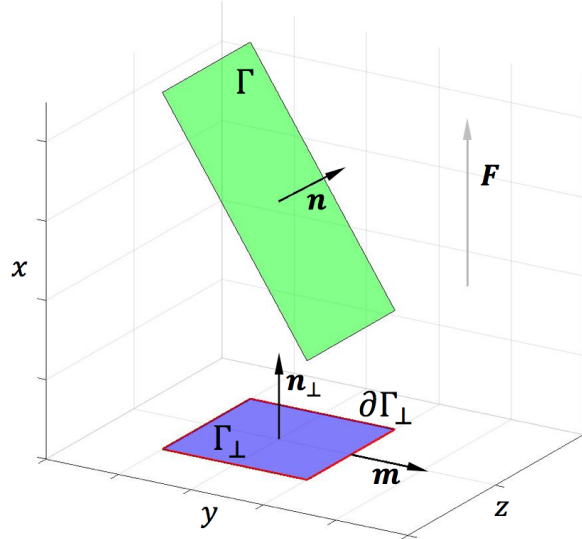


Figure 3.2: Projection of a surface Γ with outward pointing unit normal field $\mathbf{n}(x, y, z)$ along a vector field $\mathbf{F}(x, y, z) = [1 \ 0 \ 0]^\top$. The projected surface in the y - z plane is Γ_\perp with normal field $\mathbf{n}_\perp(x, y, z) = [1 \ 0 \ 0]^\top$. The outward pointing unit normal field to the red colored edge $\partial\Gamma_\perp$ is $\mathbf{m}(x, y, z)$.

Remark 1: As the interest lies only in flat surfaces, the projection cannot cause singularities. The mapping is bijective.

3.4.1.1 Polynomial filtering functions

Filtering functions are used to project the influence of particles on the fluid (cf. Darmana et al. [36]). The interest is on the distribution of the disperse volume onto the fluid which depends on the particle center (x_m, y_m, z_m) and the influence radius r_{inf} . The latter does not necessarily coincide with the particle's physical radius. The influence of a particle is modeled via the filtering function $\psi_i(x, y, z) = \psi_i^1(x)\psi_i^1(y)\psi_i^1(z)$, with the one-dimensional filtering function $\psi_i^1(\cdot)$, in a cubic domain. In this thesis, the influence of three different filtering functions is investigated: A constant influence $i = 0$, a second order influence $i = 2$, and a fourth order influence $i = 4$. The basic requirements for any filtering function $\psi_i(x, y, z)$ are axis-symmetry at the center of the particle (x_m, y_m, z_m) and that the volume integral over the entire particle Ω^p is equal to one:

$$\psi_i(x, y, z) = \psi_i(-x, -y, -z) \quad (3.91)$$

$$\int_{\Omega^p} \psi_i(x, y, z) d\Omega = 1. \quad (3.92)$$

A constant influence model $\psi_0(x, y, z) = \psi_0^1(x)\psi_0^1(y)\psi_0^1(z)$ with

$$\psi_0^1(x) = \begin{cases} \frac{1}{2r_{\inf}}, & -r_{\inf} \leq x - x_m \leq r_{\inf} \\ 0, & \text{else} \end{cases} \quad (3.93)$$

and $\psi_0^1(y), \psi_0^1(z)$ analogously fulfills (3.91) and (3.92). The additional degree of freedom, which arises with a second order filtering function $\psi_2(x, y, z)$ with

$$\psi_2^1(x) = \begin{cases} \frac{3}{4} \left[-\frac{(x-x_m)^2}{r_{\inf}^3} + \frac{1}{r_{\inf}} \right], & -r_{\inf} \leq x - x_m \leq r_{\inf} \\ 0, & \text{else} \end{cases} \quad (3.94)$$

is used to let the function decay at the particle influence radius r_{\inf} to zero in order to make $\psi_2(x, y, z)$ continuous:

$$\psi_2^1(x_m \pm r_{\inf}) = 0. \quad (3.95)$$

A fourth order filtering function $\psi_4(x, y, z)$ with

$$\psi_4^1(x) = \begin{cases} \frac{15}{16} \left[\frac{(x-x_m)^4}{r_{\inf}^5} - \frac{2(x-x_m)^2}{r_{\inf}^3} + \frac{1}{r_{\inf}} \right], & -r_{\inf} \leq x - x_m \leq r_{\inf} \\ 0, & \text{else} \end{cases} \quad (3.96)$$

provides additionally the opportunity to model the influence continuously differentiable:

$$\left. \frac{\partial \psi_4^1(x)}{\partial x} \right|_{x=x_m \pm r_{\inf}} = 0. \quad (3.97)$$

Figure 3.3 displays the one-dimensional filtering functions $\psi_0^1(x)$, $\psi_2^1(x)$, and $\psi_4^1(x)$ with the parameters $x_m = 0$ and $r_{\inf} = 1$. The constant, second order, and fourth order filtering functions are drawn in solid blue, dashed-dotted red, and dashed green curves, respectively.

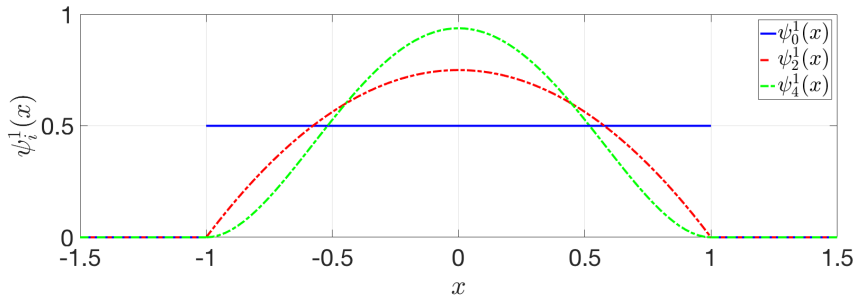


Figure 3.3: Constant (blue), quadratic (red), and quartic (green) one-dimensional filtering functions $\psi_i^1(x)$ with particle center $x_m = 0$ and influence radius $r_{\inf} = 1$.

3.4.1.2 Analytical calculation of the dispersed phase fraction using the divergence theorem

The filtering functions in section 3.4.1.1 are used to derive the solution of the line integral (3.89). The vector field is chosen as $\mathbf{F}(x, y, z) = [F_x(x, y, z) \ 0 \ 0]^T$. With

$$F_x(x, y, z) = \int_x \psi_i(x, y, z) dx, \quad (3.98)$$

the surface integral in (3.87) becomes

$$\int_{\Gamma} \mathbf{F}(x, y, z) \cdot \mathbf{n}(x, y, z) d\Gamma = \int_{\Gamma} F_x(x, y, z) n_x(x, y, z) d\Gamma. \quad (3.99)$$

The projection of the surface along the flux $\mathbf{F}(x, y, z)$ is achieved by dividing the argument of the integral in (3.99) by $|n_x(x, y, z)|$ as proposed by Sudhakar and Wall [198] and Sudhakar et al. [199].

Considering a projected surface Γ_{\perp} , the surface integration is solved by replacing the x -coordinate of the surface Γ explicitly with $x(y, z)$:

$$\int_{\Gamma_{\perp}} F_x(x(y, z), y, z) \frac{n_x(x(y, z), y, z)}{|n_x(x(y, z), y, z)|} dy dz. \quad (3.100)$$

Next, the divergence theorem is applied for the second time

$$F_x(x(y, z), y, z) = \nabla \cdot \mathbf{H}(x(y, z), y, z) \quad (3.101)$$

with $\mathbf{H}(x(y, z), y, z) = [0 \ H_y(x(y, z), y, z) \ 0]^T$ and

$$H_y(x(y, z), y, z) = \int_y F_x(x(y, z), y, z) dy. \quad (3.102)$$

Hence, (3.100) becomes the desired line integral:

$$\int_{\partial\Gamma_{\perp}} H_y(x(y, z), y, z) m_y(x(y, z), y, z) \frac{n_x(x(y, z), y, z)}{|n_x(x(y, z), y, z)|} dl. \quad (3.103)$$

Finally, following Arens et al. [6], the line integral (3.103) is solved with a parametrization $\gamma(s) = [y(s) \ z(s)]^T$ for every vertex of Γ_{\perp} :

$$\int_0^1 H_y(\gamma(s)) m_y(\gamma(s)) \|\dot{\gamma}(s)\|_2 \frac{n_x(\gamma(s))}{|n_x(\gamma(s))|} ds. \quad (3.104)$$

Hence, a volume integral (3.86) can be solved with line integrals (3.104), both divergence fields (3.98) and (3.102), and the appropriate description of the geometry of the surface Γ .

3.4.1.2.1 Geometry of a surface Γ and its normal field n

A general planar surface Γ can be described geometrically as

$$[x \ y \ z]^\top - \mathbf{c}_\Gamma \cdot \mathbf{n} = 0 \quad (3.105)$$

with an arbitrary point $\mathbf{c}_\Gamma = [c_x \ c_y \ c_z]^\top \in \Gamma$ and the normal field \mathbf{n} . Considering a surface Γ with $k_\Gamma \geq 3$ vertices \mathbf{v}_i with $i = 1, \dots, k_\Gamma$, the geometric center \mathbf{c}_Γ of the vertices is calculated via

$$\mathbf{c}_\Gamma = \sum_{i=1}^{k_\Gamma} \frac{\mathbf{v}_i}{k_\Gamma}. \quad (3.106)$$

Furthermore, the normal vector of the surface Γ is calculated with

$$\mathbf{n} = \pm \frac{(\mathbf{v}_3 - \mathbf{v}_1) \times (\mathbf{v}_j - \mathbf{v}_2)}{\|(\mathbf{v}_3 - \mathbf{v}_1) \times (\mathbf{v}_j - \mathbf{v}_2)\|_2}, \quad (3.107)$$

where $j = 4$ if $k_\Gamma \geq 4$ and $j = 1$ if $k_\Gamma = 3$. Considering a volume Ω with k_Ω vertices \mathbf{w}_i with $i = 1, \dots, k_\Omega$, the geometric center of the volume \mathbf{c}_Ω is computed as

$$\mathbf{c}_\Omega = \sum_{i=1}^{k_\Omega} \frac{\mathbf{w}_i}{k_\Omega}. \quad (3.108)$$

The sign of \mathbf{n} is determined such that

$$\mathbf{n} \cdot (\mathbf{c}_\Gamma - \mathbf{c}_\Omega) > 0. \quad (3.109)$$

In case of planar surfaces, the geometry can be represented exactly. However, for non-planar surfaces, this is only an approximation. Figure 3.4 illustrates the volume Ω_j in green with center \mathbf{c}_Ω and one normal vector \mathbf{n} . The normal vector \mathbf{n} of surface Γ is calculated with vertices $\mathbf{v}_{\{1,2,3,4\}}$. The red highlighted vectors are used for the cross product as in (3.107).

An explicit expression for $x(y, z)$ as per (3.105) is:

$$x(y, z) = -\frac{(y - c_y)n_y + (z - c_z)n_z}{n_x} + c_x. \quad (3.110)$$

Note, that potential singularities due to the denominator n_x are irrelevant because surfaces with $n_x = 0$ do not have a projection surface when projecting in x -direction.

3.4.1.2.2 Geometry of an edge $\partial\Gamma_\perp$ and its normal vector m

In the following, a projected surface Γ_\perp with k_Γ vertices $\mathbf{v}_{\{1, \dots, k_\Gamma\}}$ is considered. The normal vectors of each edge i are calculated as

$$\mathbf{m}_i = \frac{\mathbf{v}_{i+1} - \mathbf{v}_i}{\|\mathbf{v}_{i+1} - \mathbf{v}_i\|_2} \times \mathbf{n}_\perp \quad (3.111)$$

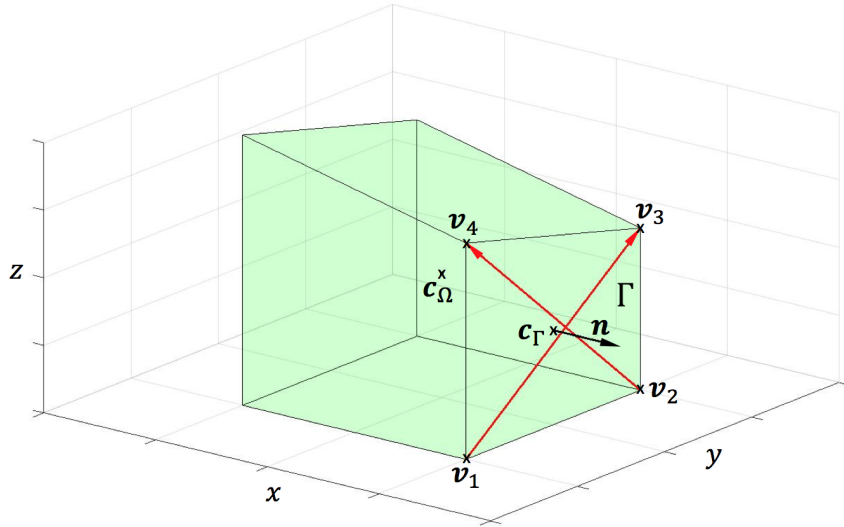


Figure 3.4: Calculation of a normal vector \mathbf{n} of surface Γ with red highlighted diagonal vectors of surface Γ , calculated with vertices $\mathbf{v}_{\{1,2,3,4\}}$ as in (3.107).

with $\mathbf{v}_{k_\Gamma+1} = \mathbf{v}_1$ and

$$\mathbf{n}_\perp = \frac{n_x(x(y, z), y, z)}{|n_x(x(y, z), y, z)|} [1 \ 0 \ 0]^\top. \quad (3.112)$$

The calculation of \mathbf{m}_i with (3.111) automatically leads to a correct integration order due to the following considerations: The normal vector is calculated such that it points to the outside of Γ_\perp if the vertices are ordered anti-clockwise considering the orientation of \mathbf{n}_\perp , which is the correct orientation according to (3.89). However, it points to the inside if the vertices are ordered clockwise. The negative integration direction equalizes the negative orientation of the normal vector \mathbf{m}_i leading to

$$m_{y,i} = \frac{z_{i+1} - z_i}{\sqrt{(y_{i+1} - y_i)^2 + (z_{i+1} - z_i)^2}} \frac{n_x(x(y, z), y, z)}{|n_x(x(y, z), y, z)|} \quad (3.113)$$

using (3.111). Figure 3.5 illustrates the calculation of the normal vector \mathbf{m} from the projected surface boundary $\partial\Gamma_\perp$. The normal vector \mathbf{n}_\perp points outward the sheet and the line integration is done anti-clockwise with outward pointing normal vector \mathbf{m} .

3.4.1.2.3 General solution of the line integral for piecewise straight edges

Each line integral is solved with the parametrization

$$\gamma_i(s) = \begin{pmatrix} y_i + (y_{i+1} - y_i)s \\ z_i + (z_{i+1} - z_i)s \end{pmatrix}, \quad (3.114)$$

$$\|\dot{\gamma}_i(s)\|_2 = \sqrt{(y_{i+1} - y_i)^2 + (z_{i+1} - z_i)^2}.$$

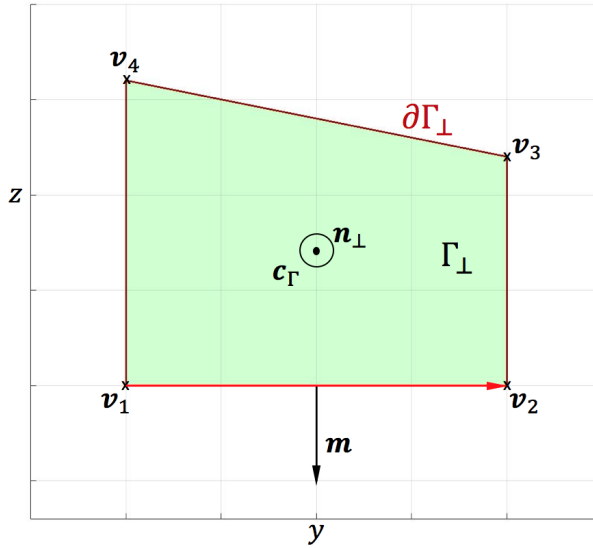


Figure 3.5: Calculation of a normal vector \mathbf{m} of surface boundary $\partial\Gamma_\perp$ with red highlighted edge vectors. The normal vector \mathbf{m} is calculated with vertices $\mathbf{v}_{\{1,2,3,4\}}$ as in (3.111).

The solution of (3.104) for every edge i with the derived geometry (3.113) and (3.114) reads

$$\int_0^1 H_y(\gamma_i(s)) (z_{i+1} - z_i) \frac{(n_x(\gamma_i(s)))^2}{|n_x(\gamma_i(s))|^2} ds = \int_0^1 H_y(\gamma_i(s)) (z_{i+1} - z_i) ds. \quad (3.115)$$

3.4.1.2.4 Solution of a line integral with the constant filtering function

Exemplarily, (3.99) is solved with the filtering function $\psi_0(x, y, z)$ defined in (3.93) from which the normalization $2r_{\text{inf}}$ is neglected to shorten the notation in this section. The vector field (3.98) becomes

$$\mathbf{F}(x, y, z) = x \quad (3.116)$$

and the surface integral (3.100) evaluates to

$$\int_{\Gamma} x(y, z) n_x dy dz = \int_{\Gamma_\perp} x(y, z) \frac{n_x}{|n_x|} dy dz. \quad (3.117)$$

With the geometry of the surface (3.110), (3.117) becomes

$$\int_{\Gamma_x} \left(-\frac{(y - c_y)n_y + (z - c_z)n_z}{n_x} + c_x \right) \frac{n_x}{|n_x|} dy dz \quad (3.118)$$

and (3.102) evaluates to

$$H_y(y, z) = -\frac{n_y}{2n_x} y^2 + \left(c_x - \frac{-c_y n_y + (z - c_z) n_z}{n_x} \right) y. \quad (3.119)$$

With the parametrization in (3.114), (3.118) becomes

$$\int_0^1 \left(-\frac{n_y}{2n_x} y(s)^2 + \left(c_x - \frac{-c_y n_y + (z - c_z) n_z}{n_x} \right) y(s) \right) (z_{i+1} - z_i) ds \quad (3.120)$$

with $y(s) = y_i + (y_{i+1} - y_i)s$ and $z(s) = z_i + (z_{i+1} - z_i)s$. Solving (3.120) leads to

$$\Delta z \left[-\frac{n_y(y_i^2 + y_i \Delta y + \Delta y^2/3)}{2n_x} - \frac{n_z(z_i(y_i + \Delta y/2) + \Delta z(y_i/2 + \Delta y/3))}{n_x} + \left(y_i + \frac{\Delta y}{2} \right) \left(c_x + c_y \frac{n_y}{n_x} + c_z \frac{n_z}{n_x} \right) \right] \quad (3.121)$$

with

$$\Delta y = y_{i+1} - y_i, \Delta z = z_{i+1} - z_i. \quad (3.122)$$

The solution of one line integral in (3.121) takes around 30 operations. Note that the normal vector \mathbf{m} is never calculated explicitly.

The solution of a line integral with higher order filtering function is computationally more expensive. The same procedure as presented in this section can be applied for the filtering function of second and fourth order. For the second and fourth order, it takes around 5,000 and 64,000 operations, respectively.

3.4.1.3 Geometrical operations to obtain integration lines

In this section, the procedure is outlined to obtain the lines on which the integration (3.115) is performed. This involves geometrical operations such as intersections of the fluid volume with the cubic support of the filtering function and necessary simplifications. As there is no closed analytical expression for the filtering functions $\psi_i(x, y, z)$ in (3.93), (3.94), and (3.96), an integral over the intersection volume $\dot{\Omega} = \Omega^p \cap \Omega^e$ of a particle volume Ω^p and a fluid element volume Ω^e is calculated. This allows to evaluate the dispersed phase fraction with only the nonzero part of the filtering functions at the expense of explicitly calculating the boundaries of the intersection area $\dot{\Omega}$.

Theorem 1: Consider two convex geometries Ω^p, Ω^e . Then the intersection $\Omega^p \cap \Omega^e$ is convex.

Proof: Let $\mathbf{x}_1, \mathbf{x}_2 \in \Omega^p \cap \Omega^e$. Then $\mathbf{x}_1, \mathbf{x}_2 \in \Omega^p$ and $\mathbf{x}_1, \mathbf{x}_2 \in \Omega^e$. Since Ω^p and Ω^e are convex sets, it follows that $\mathbf{x} \in \Omega^p$ and $\mathbf{x} \in \Omega^e$, where

$$\mathbf{x} = \lambda \mathbf{x}_1 + (1 - \lambda) \mathbf{x}_2 \quad \text{and} \quad \lambda \in [0, 1]. \quad (3.123)$$

Hence $\mathbf{x} \in \Omega^p \cap \Omega^e$. Since this is true for any $\mathbf{x}_1, \mathbf{x}_2 \in \Omega^p \cap \Omega^e$ and any $\lambda \in [0, 1]$, $\Omega^p \cap \Omega^e$ is convex (cf. Zadeh [236]). \square

Consider an intersection volume $\dot{\Omega} = \Omega^p \cap \Omega^e$ of one particle Ω^p with one fluid element Ω^e . The volume $\dot{\Omega}$ is bounded by parts of the particle surfaces $\Gamma^p = \partial\Omega^p$ and fluid surfaces $\Gamma^e = \partial\Omega^e$. With (3.87), the volume integral of the domain $\dot{\Omega}$ can be computed with surface integrals $\dot{\Gamma} = \partial\dot{\Omega}$. In the following, the developed approach to determine the geometry of these surfaces $\dot{\Gamma}$ is presented. Note that only surfaces, whose normal vector satisfies $|n_x| > 0$, contribute to the calculation of the dispersed phase fraction, since surfaces with $|n_x| = 0$ vanish

through projection. This fact is particularly interesting for the particle surfaces because only two of the six surfaces have to be evaluated.

If a fluid element is detected to be in proximity of the particle, an iteration over the surfaces of the element is started. The center of surface \mathbf{c}_Γ and the normal vector \mathbf{n} as in (3.106) and (3.107) are calculated for each surface Γ_j^e with $j = 1, \dots, n_{\text{surf}}$ and n_{surf} being the number of surfaces of this fluid element. For unstructured grids, the constant \mathbf{c}_Γ and \mathbf{n} approximate the geometry. For a Cartesian domain, \mathbf{c}_Γ and \mathbf{n} mirror the exact geometry. As first step, the vertices $\mathbf{w}_{\{1, \dots, k_\Omega\}}$ of the fluid element described by \mathbf{c}_Γ and \mathbf{n} are calculated. In a Cartesian domain, these vertices $\mathbf{w}_{\{1, \dots, k_\Omega\}}$ are exact, too.

Four categories of points are of interest for the geometric description, where $\mathbf{c}_m = (x_m, y_m, z_m)$ and r_{inf} mark the center of the particle and influence radius, respectively:

- (i) penetration points \mathbf{v}_p , which are located at the edges of the fluid surface Γ_j^e and penetrate the particle surface Γ^p , $\mathbf{v}_p \in \Gamma_j^e \cap \Gamma^p$, where $\Gamma^p = \{(x, y, z) : \|\mathbf{v}_p - \mathbf{c}_m\|_1 = r_{\text{inf}}\}$ (cf. $\mathbf{v}_{\{1,3,4,5\}}$ in Figure 3.6),
- (ii) edge points \mathbf{v}_e , which are situated alongside the particle edges $\partial\Gamma^p$ and penetrate the fluid surface Γ_j^e , $\mathbf{v}_e \in \Gamma_j^e \cap \partial\Gamma^p$ (cf. \mathbf{v}_2 in Figure 3.6),
- (iii) fluid vertices \mathbf{v}_f , which are located inside the particle Ω^p , $\mathbf{v}_f \in \mathcal{V}_k \cap \Omega^p = \{\mathbf{v}_k : \|\mathbf{v}_k - \mathbf{c}_m\|_1 < r_{\text{inf}}\}$, where $\mathcal{V}_k = \{\mathbf{v}_k\}$ denotes the set of all fluid vertices \mathbf{v}_k , and
- (iv) particle corner points \mathbf{v}_c , which mark a corner of the particle $\partial\Gamma_c^p$ and are located inside the fluid element Ω^e , $\mathbf{v}_c \in \Omega^e \cap \partial\Gamma_c^p$, where $\partial\Gamma_c^p = \{(x, y, z) : (x \pm x_m, y \pm y_m, z \pm z_m) = (0, 0, 0)\}$.

It has to be noted that these distinct points are calculated with the potentially approximated geometry of the fluid described by the n_{surf} flat surfaces \mathbf{c}_Γ and \mathbf{n} .

While iterating over the n_{surf} surfaces of one fluid element, these distinct points are gathered. If penetration points \mathbf{v}_p in (i) penetrate the $+x$ or $-x$ surface of the particle, they are stored for evaluation of the particle surface integrals $(x(\mathbf{v}_p) + x_m = \pm r_{\text{inf}})$. If the particle edge points \mathbf{v}_e in (ii) are situated alongside the particle edges, which bound the $+x$ or $-x$ surface of the particle, they are stored, too ($x(\mathbf{v}_e) + x_m = \pm r_{\text{inf}}$).

Once all relevant vertices \mathbf{v}_p , \mathbf{v}_e , \mathbf{v}_f , and \mathbf{v}_c are determined, they are ordered using a *convex hull* algorithm to ensure an integration along the correct edges. *Theorem 1* ensures that the *convex hull* exists. Figure 3.6 displays an intersection of a fluid surface with a particle. The *convex hull* is highlighted in red and ensures that the vertices $\mathbf{v}_{\{1,2,3,4,5\}}$ are in order. This approach is done for every fluid surface of $\dot{\Gamma}$, which bounds the intersection volume $\dot{\Omega}$.

Algorithm 2 summarizes the integration routine for the calculation of the dispersed phase fraction for one fluid element Ω^e and Algorithm 3 outlines the evaluation of the contribution $\epsilon_{l,j}^e$ of one fluid surface to the dispersed phase fraction. In the same fashion as for fluid surfaces, the particle $+x$ or $-x$ surface integrals are evaluated with the stored penetration and edge points, in addition to particle corner points \mathbf{v}_c .

The evaluation of $+x$ and $-x$ particle surfaces proceeds in a similar manner. Instead of line 1 in Algorithm 3, particle corner points \mathbf{v}_c are determined and stored together with the predetermined relevant penetration points \mathbf{v}_p and edge points \mathbf{v}_e of the $+x$ and $-x$ particle surface. The normal vector is $\mathbf{n} = [\pm 1 \ 0 \ 0]^\top$. Finally, lines 3 – 8 are applied for both $+x$ and $-x$ surfaces.

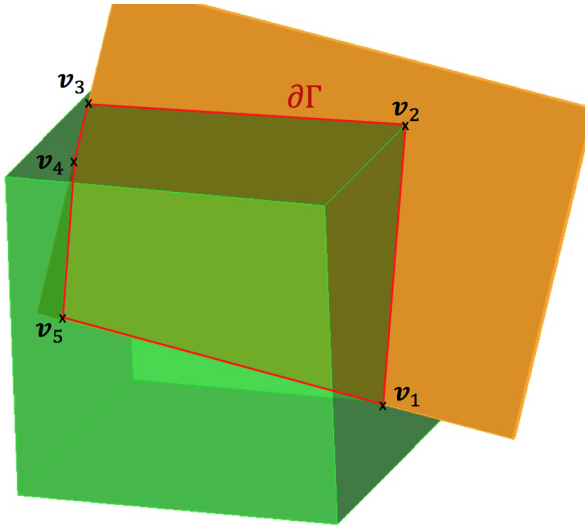


Figure 3.6: Intersection of a fluid surface with a particle. The resulting *convex hull* is colored in red as connection of the vertices $v_{\{1,2,3,4,5\}}$ and is equivalent to one surface of $\partial\Gamma$.

Algorithm 2 Calculate dispersed phase fraction for one fluid element Ω^e

Input: Vertices of the potentially unstructured fluid element Ω^e , particle center c_m , particle influence radius r_{inf}

Output: ϵ_l^e

- 1: Determine c_Γ , $\mathbf{n} \forall \Gamma_j^e \in \partial\Omega^e$ and calculate $\mathbf{w}_{\{1,\dots,k_\Omega\}}$
 - 2: **for** each fluid surface Γ_j^e **do**
 - 3: Evaluate surface Γ_j^e using Algorithm 3 to obtain contribution ϵ_j^e
 - 4: Store $\mathbf{v}_p, \mathbf{v}_e$ of particle $+x, -x$ surfaces
 - 5: **end for**
 - 6: Evaluate $+x$ and $-x$ particle surfaces to obtain contributions ϵ_{+x}^p and ϵ_{-x}^p , respectively
 - 7: $\epsilon_l^e = \epsilon_{+x}^p + \epsilon_{-x}^p + \sum_{n_{\text{surf}}} \epsilon_j^e$
-

Algorithm 3 Evaluate surface Γ_j^e

Input: Vertices $v_{\{1,\dots,k_\Gamma\}}$ of the fluid surface, element center c_Ω (3.108), and particle center c_m , particle influence r_{inf}

Output: $\epsilon_j^e, \{\mathbf{v}_p : \|x(\mathbf{v}_p) + x_m = \pm r_{\text{inf}}\}, \{\mathbf{v}_e : \|x(\mathbf{v}_e) + x_m = \pm r_{\text{inf}}\}$

- 1: Determine penetration points \mathbf{v}_p (i), edge points \mathbf{v}_e (ii), and fluid vertices \mathbf{v}_f (iii)
 - 2: **if** $n_x > 10^{-08}$ **then**
 - 3: Build *convex hull* to obtain one surface of Γ
 - 4: Calculate c_Γ (3.106)
 - 5: **for** each edge $\partial\Gamma_k$ of $\partial\Gamma$ **do**
 - 6: Calculate line integral analytically with e.g. (3.121) to obtain $\epsilon_{j,k}^e$
 - 7: **end for**
 - 8: $\epsilon_j^e = \sum_k \epsilon_{j,k}^e$
 - 9: **else**
 - 10: $\epsilon_j^e = 0$
 - 11: **end if**
-

3.4.2 Validation

3.4.2.1 Dispersed phase fraction computation on structured fluid grids

The validation of the developed method is started for the case of a Cartesian fluid grid. Kitagawa et al. [115] proposed a test case in which a single particle is moved through a Cartesian domain, see Figure 3.7. In the following, important details are briefly summarized and the reader

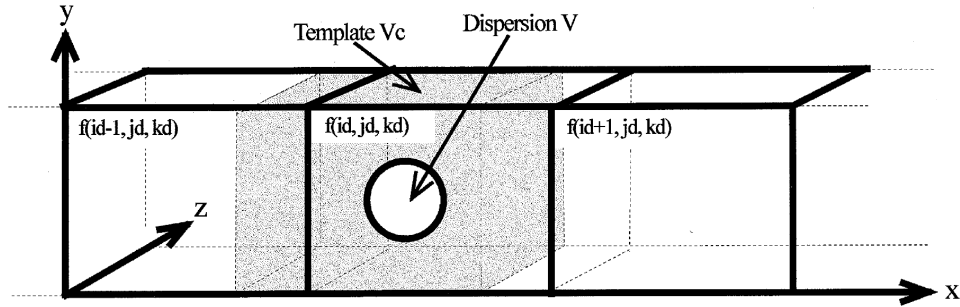


Figure 3.7: Setup of Cartesian grid test case (taken from Kitagawa et al. [115]).

is referred to Kitagawa et al. [115] for more details on the setup. The cubic template domain has always the same size as a fluid element. The polynomial filtering functions (3.93) (const polyn.), (3.94) (quad polyn.) and (3.96) (quartic polyn.) are compared against the filtering functions proposed by Kitagawa et al. [115]. They propose a clipped Gaussian function (TD-G) and a sine wave function (TD-S) and compare them to a template-distribution method (TD) with a constant filtering function. The latter is identical to the constant polynomial of zeroth order introduced in (3.93) which allows for direct comparison. The quantities of interest are the dispersed phase fraction, i.e. the volume fraction of the dispersion divided by the element volume, and a measure which is related to the discretized form of the mass conservation equation reading

$$u = \frac{-\epsilon_l^{n+1} + \epsilon_l^n}{\Delta t} \cdot \frac{1}{\left(2\epsilon_l^n \left(\frac{1}{\Delta x} + \frac{1}{\Delta y} + \frac{1}{\Delta z}\right)\right)} \quad (3.124)$$

where $\Delta t = t^{n+1} - t^n$ is the time step size and $\Delta x = \Delta y = \Delta z$ is the grid spacing of the fluid in the respective direction. The velocity u in (3.124) is denoted as “outward liquid velocity component” by Kitagawa et al. [115] and here, it is evaluated for each element in a post processing step in order to enable a comparison.

Figure 3.8 displays the dispersed phase fraction over time for a single element when a dispersion with radius $0.3 \cdot \Delta x$ passes with a constant velocity. The time axis is normalized by the time the particle needs to pass one element. The graph using the simplest method (SMP), cf. Kitagawa et al. [115], which assigns the dispersion volume to the element in which the dispersion center is located, is included in the figure because it allows to easily identify the time when the particle reaches the element. Furthermore, the maximal dispersed phase fraction can be directly seen because no distribution across neighboring elements is performed.

A validation of the analytical integration scheme is possible. The constant polynomial filtering function is identical to the TD method of Kitagawa et al. [115] regarding the shape of the filtering function. A linear increase in the dispersed phase fraction up to the center of the fluid

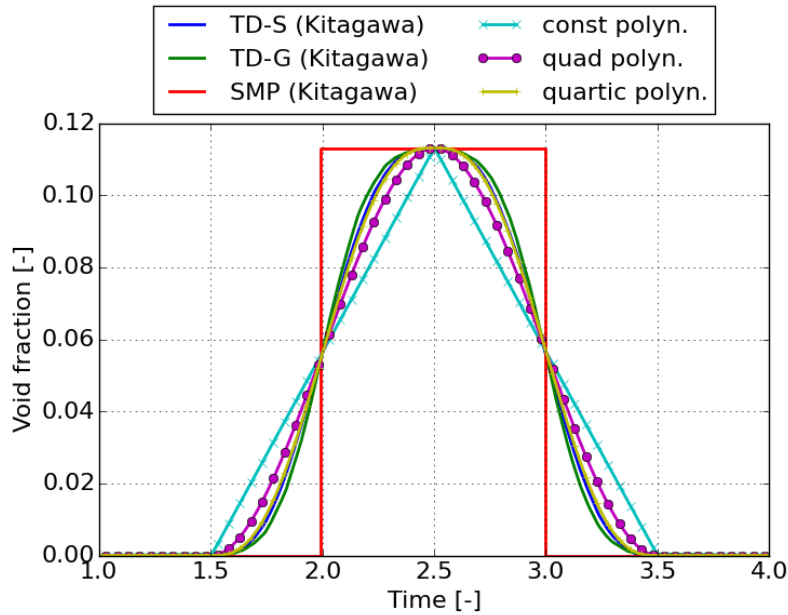


Figure 3.8: Dispersed phase fraction over time of an element for structured grids.

element with a subsequent linear decrease can be seen in Figure 3.8. This result coincides with results given for TD by Kitagawa et al. [115] and hence, it can be concluded that the developed analytical integration of the constant polynomial is correct for Cartesian grids. This does of course not allow for assessing the validity of the integration of the proposed higher order polynomial filtering functions but the general framework with the derivation of the line integrals and the geometrical operations can be assumed to work correctly. The TD-S method is chosen as optimal filtering function by Kitagawa et al. [115] due to its compact support without the need for truncation as necessary for TD-G and a better approximation of a potential flow velocity solution which will be discussed later in this section. The dispersed phase fraction distribution of the present analytical integration with the quartic polynomial filtering function lies almost on top of the graph from the TD-S solution. Hence, a very similar distribution property can be achieved while the present approach does not require the expensive evaluation of a trigonometric function such that the developed approach using the quartic polynomial might serve as a cheap surrogate. The quadratic polynomial filtering function is between the constant and quartic one and it spreads the dispersed phase fraction slightly wider than the fourth order polynomial. It is important that the maximal value in dispersed phase fraction is identical for all methods when the particle center coincides with the fluid element center. At this position, the support of the filtering function is fully lying within one fluid element and the dispersion volume is fully assigned to this single element. Hence, there is no distribution of volume across neighboring elements and the conservation of volume demands to recover an identical maximal value for all methods.

Figure 3.9 displays the velocity as defined in (3.124) normalized by the velocity of the particle over time. Therein, an additional reference curve (P-Flow) is given that is obtained when three dimensional potential flow around a rigid sphere is solved for; see Kitagawa et al. [115] for details. The aim is to approximate the solution of the potential flow by choosing an appropriate filtering function. This can be seen as a trick to obtain a realistic flow field solution although an

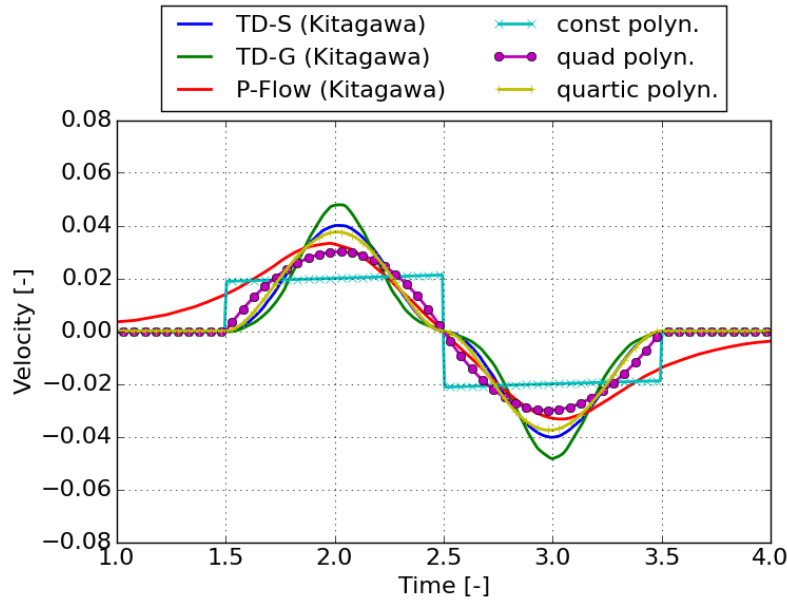


Figure 3.9: Normalized velocity over time.

unresolved framework is used in which the interface between the phases is not computed explicitly. Both, TD-G and TD-S, overestimate the maximal velocity while ramping smoothly from zero in the beginning. The curve when using the fourth order polynomial is as smooth as TD-G and TD-S and it approximates the target solution with a maximal velocity that is closer to the P-Flow solution. In comparison, the present quadratic polynomial recovers the maximal velocity very well. Furthermore, the run of the velocity curve between $1.7 < t < 3.2$ is approximated better than with all other filtering functions. Only the ramp up is not as smooth as with TD-S, TD-G and the fourth order polynomial. All velocity graphs discussed have in common, that a continuous profile is obtained. Solely, the constant polynomial filtering function reveals the undesired jump behavior at $t = 1.5$, $t = 2.5$, and $t = 3.5$ as already presented in Kitagawa et al. [115]. Hence, the use of the constant polynomial filtering function leads to undesired pulsatile flow profiles although an analytical integration is performed.

Analogue to Kitagawa et al. [115], a grid dependency study is performed. Therefore, the ratio of particle size and grid length is varied, and the corresponding maximal normalized velocity is shown in Figure 3.10. It is desirable that the maximal velocity can be reproduced over a wide range of particle size to fluid element size ratios. TD-S is closer to the target curve P-Flow than TD-G. Hence, TD-S is selected as more suitable by Kitagawa et al. [115]. Comparing these filtering functions with the present filtering functions reveals that the maximal velocities with the fourth order polynomial influence function is closer to the potential theory solution over the whole range of considered dispersed phase fractions. However, the curves of maximal velocities lay almost on top of the P-Flow curve when using the quadratic polynomial filtering function. The results obtained with the constant polynomial are identical to the results with TD by Kitagawa et al. [115] and they underestimate the maximal velocity. In summary, the quartic polynomial filtering function in the developed analytically integrated dispersed phase fraction framework delivers similar results as the TD-S solution by Kitagawa et al. [115] regarding smoothness and slightly closer results to the reference solution of a potential flow field than

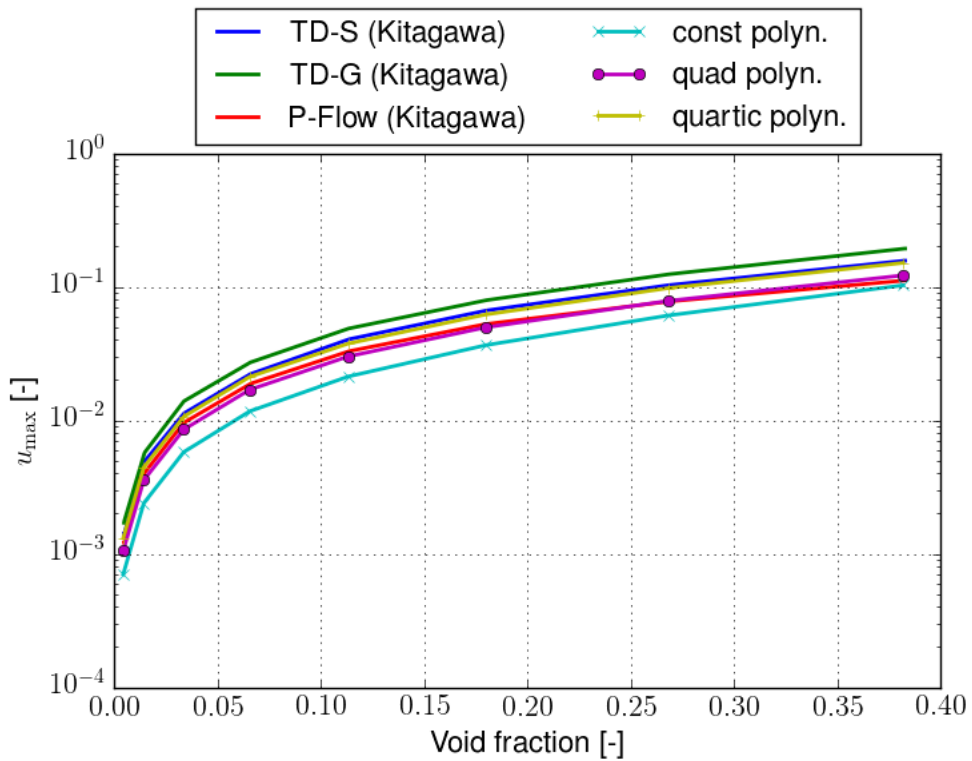


Figure 3.10: Maximal normalized velocity over dispersed phase fraction.

the TD-S approach. Furthermore, the evaluation of the polynomial filtering function does not require the expensive evaluation of trigonometric functions. The quadratic filtering function delivers better results in approximating the maximal velocity of a potential flow solution than all other approaches. However, the run of the curve is not as smooth as with higher order filtering functions which might lead to undesired pulsatile flow behavior.

3.4.2.2 Dispersed phase fraction computation on distorted fluid grids

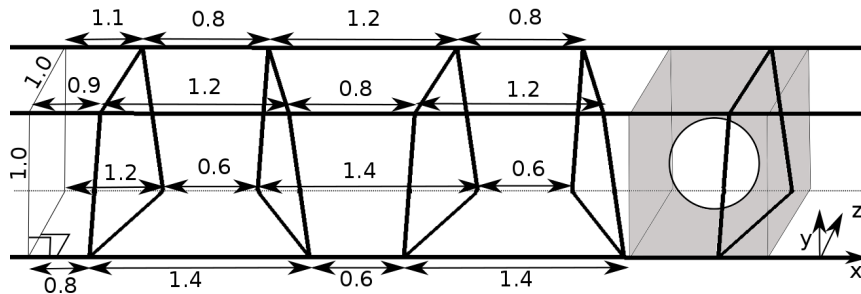


Figure 3.11: Distorted grid.

The test cases considered by Kitagawa et al. [115] only include Cartesian fluid grids. As the developed method also works for unstructured grids, the test case from the previous section is

modified such that each element has the same volume but non-planar surfaces in $\pm x$ -direction, see Figure 3.11.

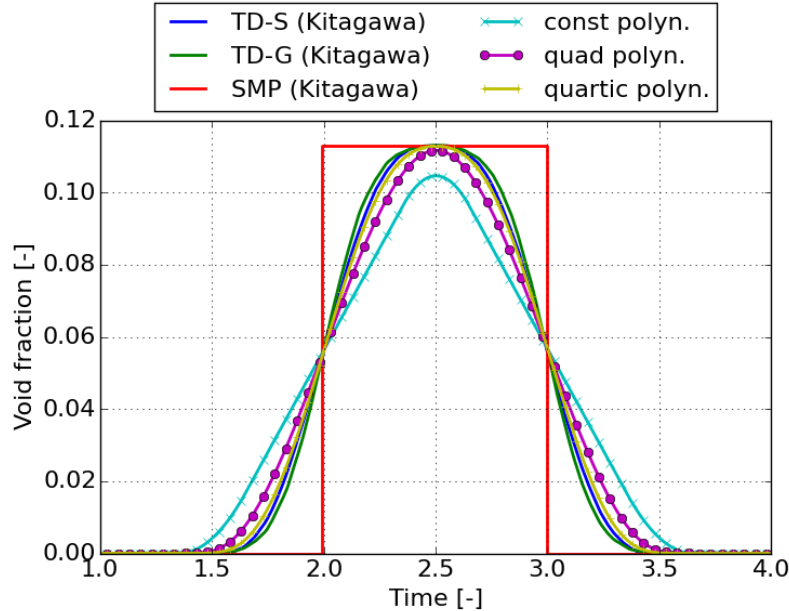


Figure 3.12: Dispersed phase fraction over time of an element for distorted grids.

Again, a single bubble with a cubic influence volume of edge length 1.0 is moved with constant velocity through the domain. The resulting dispersed phase fraction using the polynomial filtering functions is presented in Figure 3.12. Care has to be taken because the reference solution by Kitagawa et al. [115] is computed using a Cartesian grid whereas the present solutions are computed with the unstructured grid. Essentially, the curves are as smooth as for a Cartesian grid which shows that the developed method is able to deal with unstructured grids. Due to the warped surfaces of the fluid elements, the bubble touches an element earlier as can be seen nicely for the constant polynomial influence. Also due to the chosen size of the influence volume and the warped surfaces, the maximal value of dispersed phase fraction is reduced compared to the Cartesian grid test case because the dispersion volume is always spread over more than one fluid element. The maximal values for the dispersed phase fraction occur when the bubble center coincides with the element center and they are 0.1046, 0.1117 and 0.1128 for the constant, quadratic and quartic polynomial template function, respectively.

In Figure 3.13, the velocity as defined in (3.124) normalized by the velocity of the particle is displayed over time. Although, the unstructured grid is used, the curves for the quadratic and quartic polynomial template function are smooth, and they are very similar to the results with Cartesian fluid grid. This shows the capability of the developed method to cope with unstructured grids.

A final remark when using unstructured grids shall be given. The proposed approach relies on many geometrical operations which are necessary to find the integration points for the line integrals as described in Section 3.4.1.3. Usually, geometrical operations demand for tolerances, e.g. to decide when a projection is parallel, see line 2 of Algorithm 3, or when a penetration is accounted for. Otherwise, it might be possible that results are not reproducible due to round-off

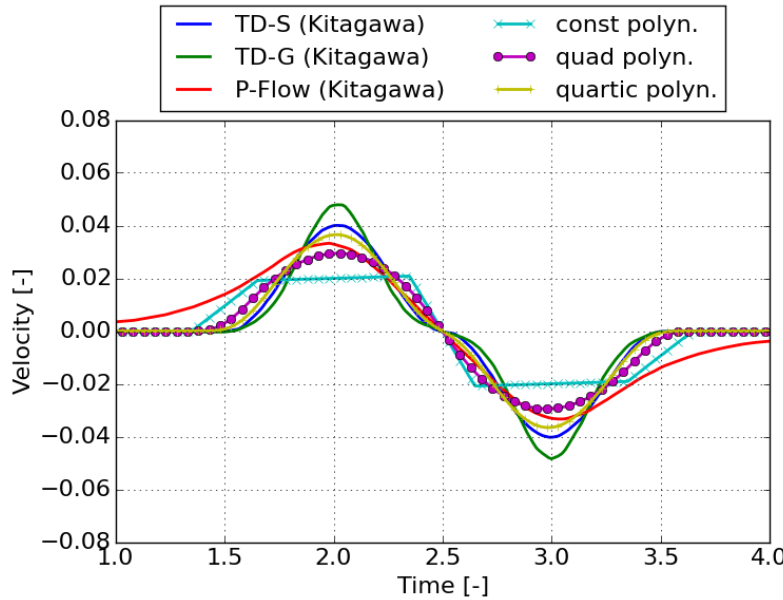


Figure 3.13: Normalized velocity over time for distorted grids.

errors as we are limited in numeric precision. These situations can lead to a single remaining integration point for which a line integral cannot be evaluated. To circumvent such problematic geometrical configurations, the computation for the respective particle is repeated with a slightly reduced size (99.9 %) of the filtering function support. This remedy can be tolerated in an Euler-Lagrange approach as the size of the support only determines how far the influence of a single particle is spread within the continuous phase. There is no rule available how to choose the influence radius and the proposed remedy showed to be a reliable solution for geometrical round-off problems.

3.4.3 Computational cost of the dispersed phase computation approach

In this section, several issues are discussed related to the computational cost of the proposed analytical dispersed phase computation approach. The test cases from section 3.4.2.1 with the structured fluid grids and from section 3.4.2.2 with the distorted fluid grids are evaluated regarding the wall time spent in the dispersed phase fraction computation. To enable a comparison against existing approaches, the sine wave filtering function TD-S from [115] with cubic support is applied together with Gauss integration. 2 ... 10 Gauss points in each direction of the fluid element are considered, leading to 8 ... 1000 integration points within a single fluid element. Due to the choice of the size of the filtering function, at most two fluid elements are touched by the dispersion at one time instance.

The wall time for the structured fluid grids is displayed in Figure 3.14. All timings are normalized with the time spent for the analytical integration of the constant polynomial filtering function (3.93). The timings for the constant and quadratic polynomial filtering function, (3.93) and (3.94) respectively, are slightly above the cost of 64 Gauss points in each fluid element.

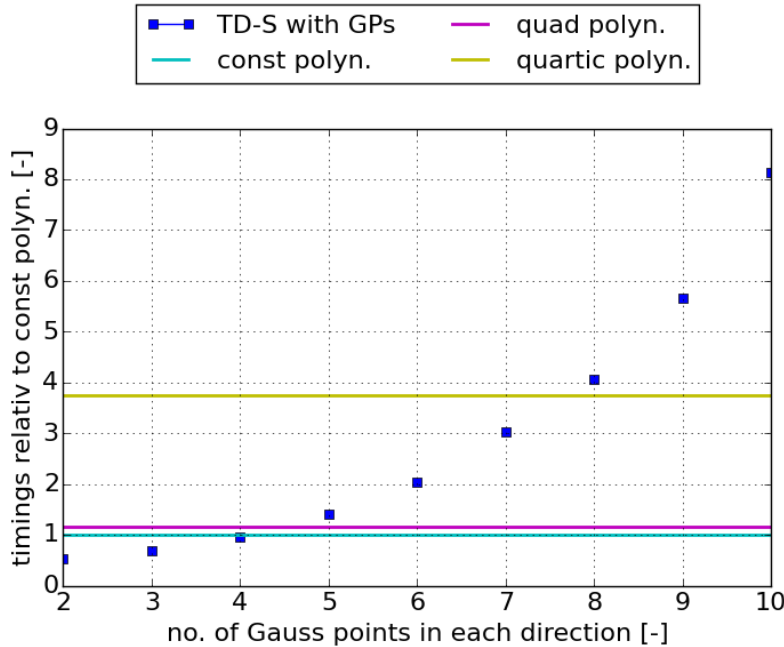


Figure 3.14: Timings comparison for structured fluid grids.

The evaluation of the quartic polynomial filtering function is almost as expensive as 256 Gauss points. Interesting to observe is that the evaluation of the quadratic polynomial filtering function is only 15 % more expensive than the evaluation of the constant polynomial filtering function. In fact, the evaluation of (3.121) for the constant polynomial filtering function is almost negligible. Hence, the cost of finding the integration points using the geometrical operations dominates the computational expenses of the proposed dispersed phase fraction computation approach. However, the cost of the mathematical operations for the quartic polynomial (3.96) becomes noticeable and is higher than for the constant polynomial filtering function by a factor of 3.7. This leads to the conclusion that deriving the integration points for the line integrals with the proposed geometrical evaluations is comparable to roughly 15,000 mathematical operations.

The same analysis as for structured fluid grids is displayed in Figure 3.15 for distorted fluid grids. The absolute computational cost for the Gauss integration of the TD-S sine wave filtering function is increased by a factor of 20 % because more evaluations are necessary due to the distorted fluid element faces which lead to a larger spread in x -direction. However, this applies to all runs with TD-S and Gaussian integration such there are no differences in relative cost compared to the case with structured fluid grids. In contrast, the evaluation of the proposed polynomial filtering functions is more expensive. The constant filtering function is close to 125 Gauss points in evaluation cost and the quartic polynomial filtering function is between 256 and 512 Gauss points. The search for the integration points of the line integrals is more complex for distorted fluid grids leading to an increased effort.

In a brute force approach, all particles are considered to participate to the dispersed phase volume of a fluid element. In order to reduce the computational effort, only particles in a close neighborhood to a fluid element are considered in this work. Therefore, the bin framework and the use of axis aligned bounding boxes (aabb) as will be presented in Section 3.6 are employed.

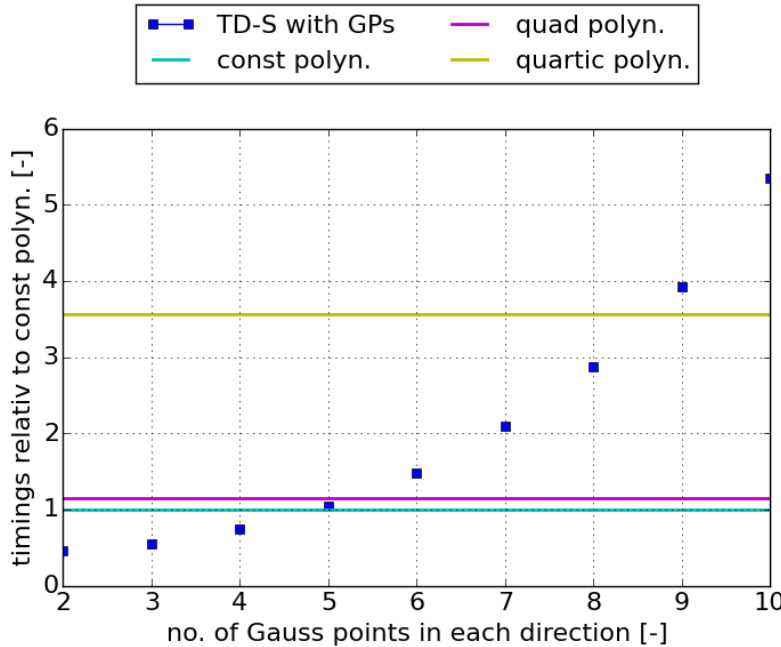


Figure 3.15: Timings comparison for distorted fluid grids.

Using these aabb, non-overlap with the support of the filtering function can be evaluated at little computational cost and in case, the respective fluid element can be skipped for detailed intersection analysis.

Applying these tricks reduces computational effort massively. The cost of finding close fluid elements for each particle in the examples is less than 5 % of the cost for evaluating the remaining close fluid elements with the proposed dispersed phase computation approach. There are further tricks, such as tree-like structures to perform a fast search for close neighbors or any combinations of the aforementioned possibilities.

To summarize, a novel approach for efficient dispersed phase fraction calculations also capable of handling unstructured grids in an Euler-Lagrange model has been developed in the scope of this thesis. The presented theoretical part and numerical validation examples for fluid fraction computation have already been published by the author of this thesis in Menner* et al. [149].

The quadratic polynomial filtering function is used exclusively in the test cases considered in the remainder of this thesis.

3.5 Time integration of the Rayleigh-Plesset equation

3.5.1 Runge-Kutta time integration with adaptive time stepping

The RP equation in (2.113) is considered a stiff 2nd-order ordinary differential equation (ODE) which demands for a time step size $< 10^{-12}$ s during the collapse process of a bubble, cf. Alehossein and Qin [3]. In case this small time step size is kept constant during computation, the overall cost lead to undesired long computation times. Hence, an adaptive time stepping

approach is applied to increase the time step size whenever possible while still having a stable time integration scheme.

In general, all approaches known for time step adaptivity are applicable to the RP equation. In Shams et al. [187], the 2nd-order ODE is cast to two 1st-order ODEs which are advanced in time with the 1st-order explicit Euler time integration scheme. An amplification matrix based on the Jacobi matrix is computed and the eigenvalues are used to adapt the time step size. Another approach is proposed by Alehossein and Qin [3], in which the change of the radius from consecutive time steps is used for triggering the adaption. The time step size is kept constant up to two percent change in radius and adaptation is applied when this limit is exceeded. Richardson extrapolation is applied to the RP equation by Babu Salapakkam [10], which estimates the truncation error by comparing the solution of one step with size Δt and two steps each with $\Delta t/2$. The most appealing approach is to use Runge-Kutta (RK) time integration with an embedded solution of lower order which can be computed efficiently. This is also the finding in Babu Salapakkam [10], in which a 5th-order RK scheme is used and the embedded 4th-order solution is used to estimate the local truncation error. In order to reduce the computational cost, a three stage 3rd-order RK scheme with an embedded solution of 2nd-order as proposed by Bogacki and Shampine [17] is used in this work. The corresponding Butcher-Tableau is given in Table 3.2. In

0				
1/2	1/2			
3/4	0	3/4		
1	2/9	1/3	4/9	
	2/9	1/3	4/9	0
	7/24	1/4	1/3	1/8

Table 3.2: Butcher-Tableau of RK3(2) scheme.

order to apply the RK3(2) scheme, the RP equation is reformulated as two 1st-order ODEs, viz

$$\dot{r}(t) = \frac{dr(t)}{dt}, \quad (3.125)$$

$$\ddot{r}(t) = \frac{1.0}{\rho_l r(t)} \left[-\frac{3}{2} (\dot{r}(t))^2 + p_b(t) - p_\infty(t) - \frac{2\sigma}{r(t)} - \frac{4\mu}{r(t)} \dot{r}(t) \right] \quad (3.126)$$

which then can be integrated via the following three step procedure:

$$\ddot{r}^{j+1} = \frac{1.0}{\rho_l r(t^j)} \left[-\frac{3}{2} (\dot{r}(t^j))^2 + p_b(t^j) - p_\infty(t^{j+1}) - \frac{2\sigma}{r(t^j)} - \frac{4\mu}{r(t^j)} \dot{r}(t^j) \right], \quad (3.127)$$

$$\dot{r}^{j+1} = \dot{r}(t^j) + \Delta t^j \ddot{r}^{j+1}, \quad (3.128)$$

$$r^{j+1} = r(t^j) + \Delta t^j \dot{r}^{j+1}. \quad (3.129)$$

The index j specifies the current RK step with its time step size Δt^j . For details on RK methods and the Butcher tableau, the interested reader is referred to Hairer et al. [85]. For more details on this specific application of RK methods, the reader is referred to Mattson [145], in which a

3 Computational approach

RK4(3) scheme is used for integrating the RP equation and time adaptivity based on the estimated local truncation error (lte) is applied. The same procedure is performed for the RK3(2) method here such that the adaption reads

$$\Delta t_{\text{RP}}^{k+2} = \min \left(\max \left(f^{k+1} \cdot \Delta t_{\text{RP}}^{k+1}, \Delta t_{\text{min}} \right), \Delta t_{\text{max}} \right), \quad (3.130)$$

in which the factor f^{k+1} contains the estimated lte. An upper and lower bound Δt_{max} and Δt_{min} , respectively, for the time step size is introduced to keep the step size in a reasonable range. Motivated by the physics of interest, namely the collapse of cavitation bubbles, the minimal time step size is chosen as $\Delta t_{\text{min}} = 10^{-12}$ s and the maximal step size $\Delta t_{\text{max}} = 0.3 \cdot \Delta t_b$ with Δt_b as introduced in Section 3.2. The normalized estimated lte reads

$$\epsilon_r^{k+1} = \frac{\|r_{\text{emb}}^{k+1} - r^{k+1}\|_2}{\|r^{k+1}\|_2}, \quad (3.131)$$

in which the solution at time t^{k+1} is denoted as r^{k+1} and the respective solution of lower order is denoted as r_{emb}^{k+1} . The idea is to specify a target value tol_{RP} for the lte allowed in each time step and the step size is adapted such that tol_{RP} is met. Based on Hairer et al. [85], the factor to adapt the step size reads

$$f^{k+1} = \min \left(\max \left(sf \cdot \frac{tol_{\text{RP}}}{\epsilon_r^{k+1}}, f_{\text{dec}} \right)^{\frac{1}{p+1}}, f_{\text{inc}} \right) \quad (3.132)$$

with a safety factor sf , a limit for the maximal increase f_{inc} and a limit for the maximal decrease f_{dec} of the adaption factor. The exponent contains the order of the embedded solution which yields for the chosen RK3(2): $p = 2$. This gives a hint that actually the lte of the lower order solution is estimated and not the other way round. Nevertheless, the higher order solution is chosen to advance the solution in time. The safety factor is included to reduce the number of time steps to be repeated because the tolerance tol_{RP} is exceeded. The constants are summarized in Table 3.3 which have been found in Hammerl [86] to yield reasonable results.

parameter	value
sf	0.9
f_{inc}	1.3
f_{dec}	1/1.3

Table 3.3: Constants for time adaption scheme.

Several technical details need to be taken into account in order to synchronize the adaptive time stepping with the larger time step size Δt_b . Firstly, the step size of the adaptive scheme Δt_{RP} must not exceed the bubble time step size Δt_b . Secondly, adaption is suspended when the remaining time during subcycling is less than twice the current time step size Δt_{RP} . Instead, the remaining time is divided in two equally sized pieces such that the end of the bubble time step is met exactly. This means that in line 17 of Algorithm 1, the step size is not computed based on the lte but instead by dividing the remaining time in two equally sized pieces. As the lte should not exceed the limit tol_{RP} , the remaining time is divided by three in case the step size was decreasing

during the previous steps. In the rare case of exceeding tol_{RP} during this last step size adaption, an endless loop would be generated in line 14 of Algorithm 1. To circumvent this issue, time steps are further halved at the end of the subcycling to reduce the lte and reach exactly the end of the bubble time step.

3.5.2 Validation

A test case proposed by Popinet and Zaleski [169] is used to validate the present implementation of the Rayleigh-Plesset equation with variable time stepping based on local truncation error estimation. Therein, a spherical bubble in quiescent fluid is investigated using the RP equation and a fully resolved direct numerical simulation (DNS) approach. The bubble undergoes size changes due to the choice of non-equilibrium starting conditions. The fluid properties are given by a dynamic viscosity $\mu = 0.001 \text{ Pas}$, a density $\rho_l = 1000 \text{ kg/m}^3$, a surface tension $\sigma = 0.07 \text{ N/m}$, and a vapor pressure $p_v = 0$. These quantities resemble roughly water at 20°C. The fluid pressure is kept constant at 10^5 Pa which is close to standard conditions. The initial bubble radius is $r(t = 0) = 10 \mu\text{m}$. In summary, realistic conditions for the collapse of a cavitation bubble in water are chosen. In order to initiate the highly transient radius evolution, the equilibrium radius is artificially set to $r_0(t = 0) = 5 \mu\text{m}$ which is subsequently used to compute the initial bubble pressure p_{g0} using (2.117). Hence, the bubble starts collapsing because the initial radius is larger than the equilibrium radius. The initial velocity $\dot{r}(t = 0)$ and acceleration $\ddot{r}(t = 0)$ in radial direction are set to zero as usual. Furthermore, it is necessary to choose the exponent $\eta = 1.4$ in (2.114) in order to comply with the setup in Popinet and Zaleski [169]. The latter corresponds to an adiabatic compression and expansion of the bubble content. The tolerance for the local truncation error is $tol_{RP} = 1.0 \cdot 10^{-3}$ and the fluid time step is assumed to be $\Delta t_l = 2.0 \mu\text{s}$. Hence, the simulation time $t \in [0, t_{\text{end}}]$ with $t_{\text{end}} = 10.0 \mu\text{s}$ is passed with five fluid time steps and the time step size for solving the RP equation is adapted based on (3.130). For this test case, the fluid subproblem is of minor importance. Hence, the fluid pressure is prescribed via a Dirichlet boundary condition and the fluid velocity is fixed at rest. The bubble resides centrically in the single element used for the fluid domain.

Figure 3.16 contains the radius evolution over time obtained by Popinet and Zaleski [169] and from the present implementation. A very good agreement can be observed with an error < 0.5 % at t_{end} . The first collapse takes $0.93 \mu\text{s}$ and further rebounds follow. The maximal radius of the bubble decreases from rebound to rebound due to the dissipative nature of the last term in (2.113). The figure also includes the time step size Δt_{RP} which is used for the time integration of the RP equation. It is beneficial that a small time step size is chosen when the rebounds take place and a large time step size is chosen at times of smooth radius evolution. Hence, the estimated temporal truncation error is bounded using the given tolerance while the simulation advances as fast as possible. The smallest time step size during the first rebound is $\Delta t_{b,\min} = 0.0059 \mu\text{s}$, whereas the largest time step is $\Delta t_{b,\max} = 0.3 \mu\text{s}$ in portions of smooth radius evolution. Hence, the time step size increases up to a factor of 51 compared to the smallest time step size. In total, 152 successful time steps of the RK time integration scheme are necessary to perform time integration. In addition, 73 steps are repeated because the prescribed tolerance is violated. In sum, 225 time steps are computed compared to 1695 time steps which would be necessary in case the smallest time step size $\Delta t_{b,\min}$ is used throughout the simulation. Hence, the correctness of the present implementation of the RP equation is shown while the computation time could

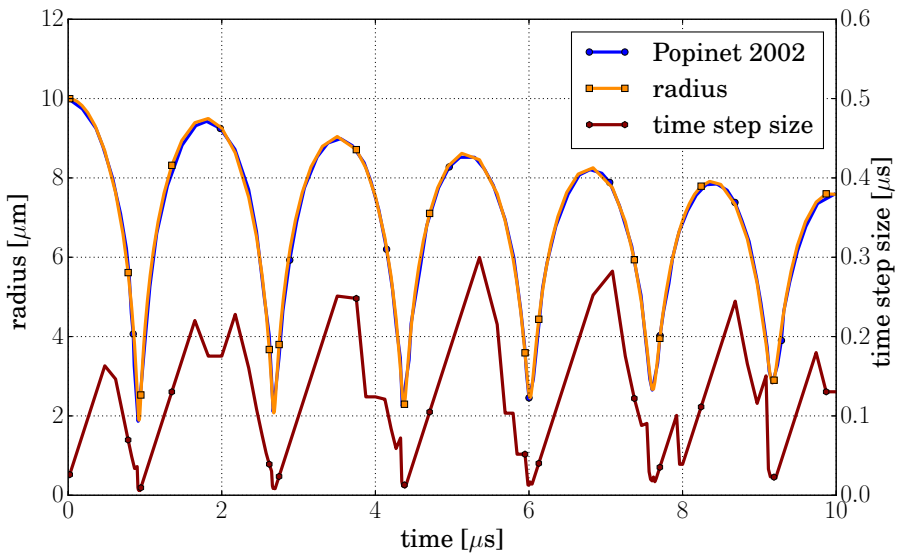


Figure 3.16: Validation of the adaptive time stepping for RP equation.

be reduced by a factor of 7.7 in this test case due to the adaptive time stepping scheme without loosing relevant accuracy.

3.6 Parallelization and efficiency aspects

The aim of this work is to simulate large systems including vast numbers of particles. In order to reduce the time to solution, a parallel framework is crucial. Several aspects need to be considered in order to end up with an efficient parallel Euler-Lagrange framework. The developed framework is based on Message Passing Interface (MPI). One essential feature is a distributed memory layout, meaning that a processor cannot access all data from the fluid or the particle field. The fields are distributed among the processors and each processor can only access a certain part of it. This needs to be considered for example when inter-particle interaction is encountered. The particles need information about their neighborhood for proper contact evaluation. Also neighboring wall elements must be known to each particle in order to correctly detect collisions with those. Furthermore, the particles interact with fluid elements in their close neighborhood. In the developed framework, the fluid domain is assumed to be fixed in space whereas the particles are free to move through the fluid field.

Several approaches to track neighbor information for each particle can be found in literature. For pure particle problems, mainly a Verlet-list method or a linked cell approach are used. In the former, a list of neighboring particles is stored and updated frequently in order to always provide the current neighborhood for proper contact evaluation. The latter is based on a geometrical decomposition of the domain in box-like shaped cells. Alternatively, the cells can also be arranged in tree-like structures, cf. Warren and Salmon [226] or Fleissner and Eberhard [64]. Each particle is assigned to exactly one of those cells whose size is chosen in a way that all possible interaction partners are found within one layer of cells. The cells are denoted as bins in the following. Hence, contact evaluation for a single particle involves gathering the particles residing in its own

bin and in the 26 neighboring bins. Details on these approaches can be found e.g. in Allen and Tildesley [4], Plimpton [168], Pöschel and Schwager [171], Muth et al. [155], or Kamath et al. [112]. Combinations of the Verlet-list method and the linked cell approach are frequently used, too and details can also be found in the aforementioned literature. A further improvement to reduce the list of possible collision partners is to remove those particles from the neighbor list which are blocked by closer neighbors as proposed by Löhner and Perazzo [136].

As the developed framework includes a fluid domain which is geometrically overlapping with the particles, the most appealing approach is a spatial decomposition strategy for the particle as well as the fluid field. Therefore, a binning approach with Cartesian boxes is chosen in the present work. Particles as well as fluid elements are assigned to the bin they are residing in. Each bin is addressed using three indices i , j and k each ranging from zero to the maximal number of bins in the respective spatial direction. Each particle is assigned to the bin in which its center is located, see Figure 3.17. As the bins are equally sized in one spatial direction, it is trivial to

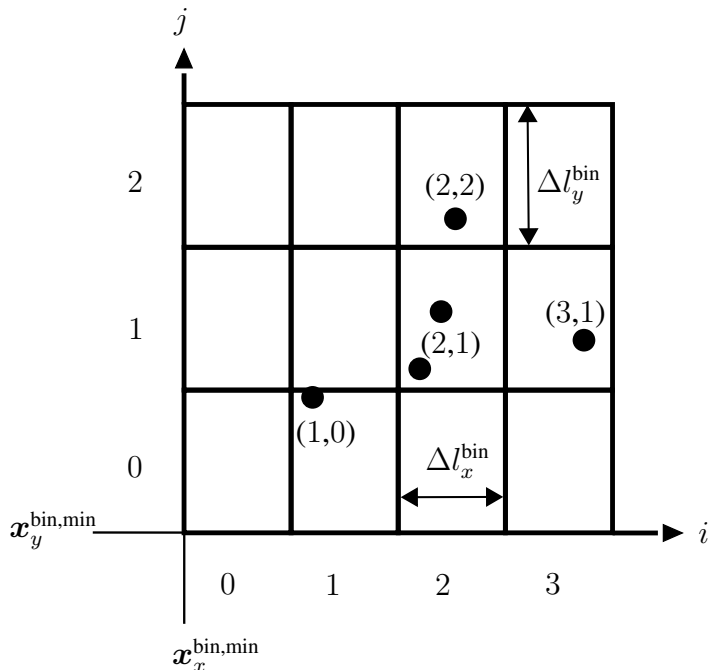


Figure 3.17: Particles and the bins they are assigned to in brackets (2D example).

determine the host bin for a particle at current position \boldsymbol{x} according to

$$ijk_d = (\text{int}) \left(\frac{\left(\boldsymbol{x}_d - \boldsymbol{x}_d^{\text{bin},\text{min}} \right)}{\Delta l_d^{\text{bin}}} \right) \quad (3.133)$$

in which the minimal extent of the Cartesian grid is denoted with $\boldsymbol{x}^{\text{bin},\text{min}}$ and the bin size in direction $d \in \{x, y, z\}$ is denoted with Δl^{bin} . The result of the division needs to be truncated to an integer in order to obtain the indices of the bin. As a division is costly for the processing unit, it is possible to replace it with a multiplication by $1.0/\Delta l_d^{\text{bin}}$ which can be precomputed once in the beginning. This improves performance at little effort.

3 Computational approach

The assigning procedure of particle to bin needs to be updated frequently to always provide the correct neighborhood when contact is evaluated or when fluid-particle coupling takes place. Depending on the chosen time step size and bin size, it might be possible to reuse the neighborhood information for several particle time steps until the next update is performed. This is again a question of efficiency.

The task of assigning fluid elements to bins is more difficult as the fluid elements might be of arbitrary shape, i.e. hexahedral or tetrahedral, and additionally distorted. In contrast to the particles which can be assigned uniquely to a bin, a fluid element resides only rarely in a single bin. A partly overlapping scenario covering multiple bins is the standard case for a fluid element. The option chosen in the developed framework realizes a cheap assigning procedure while accepting that a fluid element might possibly be assigned to too many bins. This does not pose further problems because a detailed analysis of the particle-fluid element interaction is performed anyway when the close neighborhood of the particles is evaluated. The procedure of assigning a fluid element to a bin reads as follows:

1. An aabb is computed for each fluid element.
2. The fluid element is assigned to each bin which is touched by the aabb.

Both steps are straightforward and can be efficiently performed. In the second step, (3.133) is used to compute the i , j , and k values for the left lower and right top corner of the aabb which are subsequently used to determine the range of the corresponding bins. The procedure is illustrated

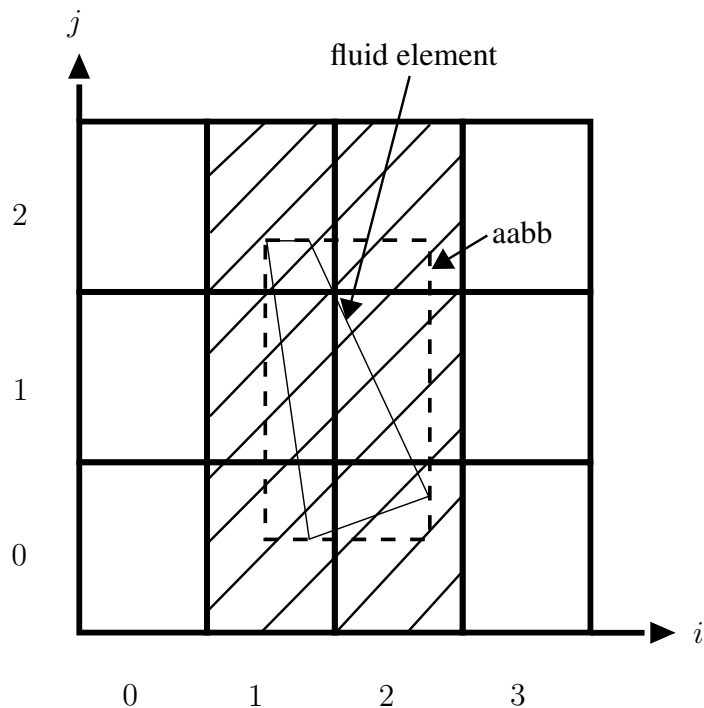


Figure 3.18: A distorted quadrilateral fluid element with its aabb represented with dashed lines. The fluid element is assigned to the hatched bins (2D example).

in Figure 3.18. An advantage of this approach is that there is no restriction on the size ratio

between fluid element and bin. A fluid element can be smaller than a bin and possibly residing within a single bin or it may cover a large number of bins. For large fluid elements, there is a clear trade-off whether to assign it only to those bins they are residing in at higher cost or to a possibly too large number of bins at little effort. So far, the fluid domain remains fixed during the simulation and the initial assigning persists throughout the whole computation.

After properly assigning particles and fluid elements to their corresponding bins, two aspects remain to be clarified. The first aspect is about the parallel distribution including the ghosting (or halo) information which needs to be provided to a neighboring processor in order to enable proper particle, fluid and coupling evaluation. This is necessary because a distributed memory layout is applied in the developed framework which is based on MPI, as already mentioned earlier. In contrast, the approach presented by Wachs [223] relies on particle information which is available on each processor, meaning that a fully overlapping layout for the particles is chosen. Evaluation of particles is distributed among the processors but the bottleneck may become the necessary memory consumption as all particle information can be addressed on all processors. The so-called mirror domain approach described by Darmana et al. [36] reduces the fully overlapping layout to the main particle variables such as radius and velocity whereas a distributed memory layout regarding the nearest neighbor lists is employed to save memory resources. Both mentioned approaches have in common that at least some particle data is stored in a fully overlapping manner which can be detrimental for large computations as the available memory limits the problem size.

The present approach does not rely on fully redundant particle information because only the particles and fluid elements in one additional layer of bins are ghosted around the owned particles. The data within the ghost or halo layer is updated in each time step with data from the processor that owns the data, leading to communication effort. A crucial assumption in this approach is the restriction of the interaction range to one layer of bins. This constraint ensures that no event is missed when one layer of ghost bins (with ghost particles and ghost fluid elements inside) is provided at processor boundaries in parallel computations. Therefore, it is necessary to estimate the bin size a priori or to recompute it based on the current particle information. The estimation might be difficult because the maximal travel distance per time step and the maximal radius of the particles need to be known in advance. In contrast, the recomputation of the bin size during run time enables a dynamic adaption of the bin size which removes the necessity for a priori estimations. However, this comes at higher computational cost as both fields need to be reassigned to the modified bin configuration. Therefore, the developed framework relies on a sophisticated a priori guess and the dynamic reassigning is not performed.

In summary, no information is stored in a fully redundant manner that would limit the problem size in the developed framework. However, this comes with an increased communication effort due to the repeated update of the information in the ghost layer.

The remaining aspect concerns again a parallel distribution issue. It is a very difficult task to ensure load balancing throughout the simulation for a parallel Euler-Lagrange framework. The continuous part, i.e. the underlying fluid, does not pose a problem since connectivity does not change, and an initial distribution based on graph partitioning gives a reasonable load balanced setup. In contrast, the particles can freely move within the domain such that clustering on a single processor might occur. Hence, particles also require a geometrical distribution which possibly does not fit to the fluid partitioning. It is crucial to store a particle and its underlying fluid element on the same processor such that the coupling can be evaluated locally without the need for inter-

processor communication. Furthermore, the chosen coupling approach is of sequential nature, see Section 3.2, and both fields should be ideally balanced while enforcing that each particle and its underlying fluid element reside on the same processor. Herein, the difficulty is hidden and the solution is a non-trivial (re-)partitioning with respect to two different objective functions, i.e. the cost of the fluid evaluation and the cost of the particle evaluation, whilst demanding for coupling partners (fluid element and particle) to reside on the same processor. A remedy is proposed by Yakubov et al. [233] with a hybrid parallelization strategy that uses OpenMP threads whose number is related to the number of particles, i.e. the work load. This might be seen as a first step towards load balancing for both fields simultaneously but it does not achieve an optimal distribution for both fields over all processors.

To avoid the difficulties of the aforementioned approach, the procedure followed in this work reads as follows: The fluid is optimally distributed to the processors using graph partitioning based on Zoltan provided by the Trilinos package by Heroux et al. [91]. Next, the bins, i.e. the Cartesian grid, is created and the fluid elements are assigned to the bins. As mentioned above, a fluid element can be assigned to several bins. The processor which has most owned fluid elements in a bin becomes owner of this bin. Doing so, a Cartesian grid of bins is distributed over the processors while roughly approximating the distribution of the fluid mesh. Particles are also assigned to the bin in which their center is located. The owner of the bin and particle is always identical, and thus a unique distribution of particles is generated. While floating around, the particles are reassigned to bins and transferred between processors when necessary. The additional ghost layer always needs to be added before the evaluation of the involved fields takes place.

In summary, the developed framework includes a load balanced fluid problem, an on-processor coupling between the continuous and the disperse phase and additionally, it is memory distributed with a single layer of bins (particles and fluid elements therein) at processor boundaries. The latter means that no data need to be provided fully redundant on all processors which would limit the overall problem size. This comes at the drawback of additional communication effort. As no rebalancing is performed so far, an unbalanced load while evaluating the particles is likely to occur.

4 Numerical examples

After having introduced the governing equations and the computational approach to solve dispersed flow problems, some examples will be presented in this chapter to show the versatility of the proposed method. Initially, pure particle problems will be presented with a focus on particle-particle and particle-wall interaction as well as the scaling of the proposed approach. Next, fluid-particle interaction is considered with two well-known test cases, namely a Taylor–Green vortex and a fluidized bed example. In the former test case, contact forces are neglected such that only fluid-particle forces drive the problem while the latter shows the ability of the framework to cope with a very large particle-fluid density ratio and fluid fractions down to 35 %.

4.1 Particle flow through an orifice

Due to its modularity, the proposed framework is able to run pure particle problems as well. A benchmark test available in literature is the outflow of grains from a cylindrical container through an orifice in its bottom under gravity load. Its advantages are on the one hand the existence of experimental results which can be used for validation and on the other hand the simple setup. An empirical correlation was derived by Beverloo et al. [15] after performing experiments using many different grains. Among others, the review paper by Nedderman et al. [157] confirms the validity of the findings. Numerical results for this setup are reported by Bertrand et al. [14], which are used as comparison for the developed framework.

4.1.1 Setup

As illustrated in Figure 4.1, a cylindrical container of height $H = 0.5$ m and diameter $D = 0.3$ m with a circular orifice of diameter D_0 in the bottom is filled with spherical particles of diameter $d_0 = 16$ mm. Due to gravity load with gravitational acceleration $\mathbf{g} = (0.0, 0.0, -9.81)^\top \text{ m/s}^2$ in negative z -direction, the grains leave the container through the orifice. The particle density is $\rho_b = 2500 \text{ kg/m}^3$, the Young's modulus is $E = 2.16 \text{ MPa}$ and the Poisson ratio is $\nu = 0.3$. As a glass bead is modeled by Bertrand et al. [14], the coefficient of restitution e is experimentally found to be around 0.8 depending on the impact velocity and impact angle, cf. Gütler et al. [84]. The latter value is only relevant for damping effects and thus assumed to be constant. A distinction between static and dynamic friction coefficient for the Coulomb friction law is made by Bertrand et al. [14]. Unfortunately, the threshold velocity is not specified below which the static friction coefficient is used. Although, the static friction coefficient is varied over a wide range, the resulting mass flow only deviates up to 5 %. In Beverloo et al. [15], the experimentally derived correlation is applied and deviations of 5 % in average and 12.5 % at maximum are reported. Therefore, the distinction between static and dynamic friction coefficient is omitted in the remainder of this section. In the developed framework, there is no analytical

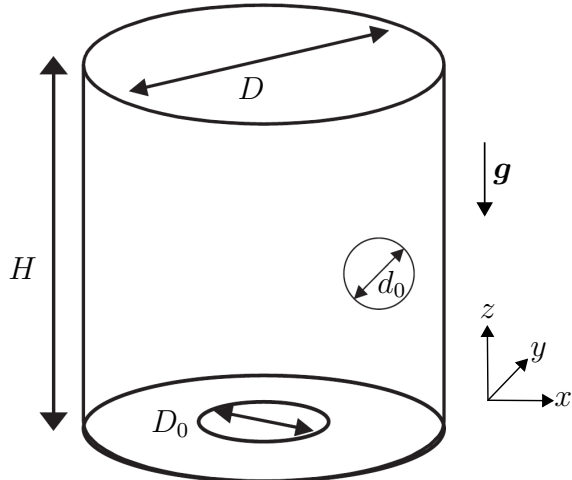


Figure 4.1: Setup of particle through an orifice test case (from Bertrand et al. [14]).

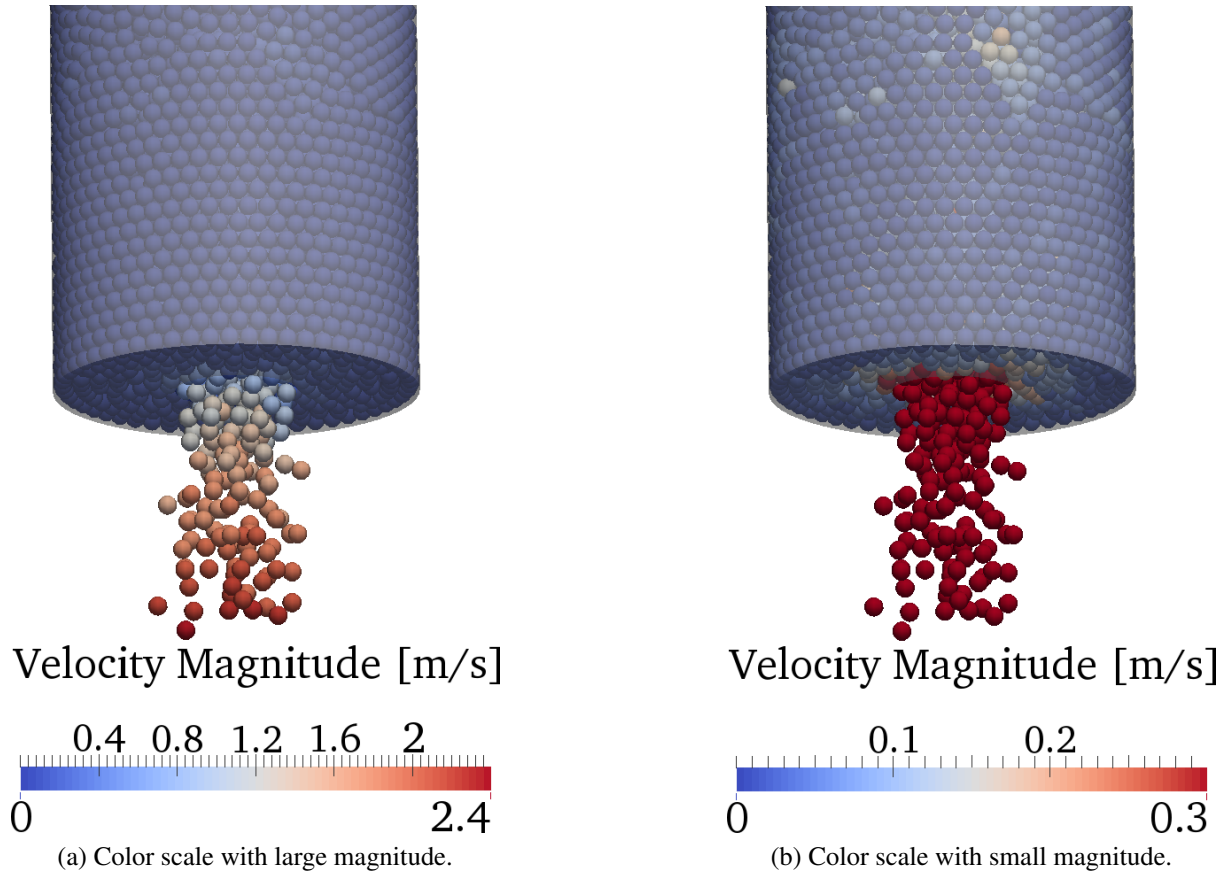
description of the circular orifice available and therefore, a polygon with 64 elements along the circumference of the orifice is chosen for discretization. Another discretization with 256 elements along the circumference revealed almost identical results. The time step size is chosen to be $\Delta t_b = 2.5 \cdot 10^{-5}$ s. For each simulation, a preliminary run is performed in which the orifice in the bottom is occluded in order to obtain a random initial packing of the 9360 particles in the container. After the particles came to rest, the occlusion is removed and the particles start leaving the container through the orifice. The first 0.2 s of the dropping process are omitted until a steady state develops. During the following 0.8 s, particles leaving the container are counted in order to compute the mass flow rate through the orifice as the quantity of interest.

4.1.2 Analysis and comparison against literature

In Bertrand et al. [14], numerous simulations are performed with different sized grains, different friction coefficients and different orifice sizes. Therein, good agreement was achieved with the empirical correlation by Beverloo et al. [15]. Finally, the following correlation was obtained to estimate the mass flow rate

$$W = 0.6\rho_b \sqrt{\|\mathbf{g}\|_2} (D_0 - 1.4 d_0)^{\frac{5}{2}} \quad (4.1)$$

through a circular orifice which is almost identical to the empirical correlation. In Figure 4.2, the outflow through an orifice with $D_0 = 100$ mm is illustrated. The particles are colored according to their velocity magnitude. In Figure 4.2(a), a scale spanning the full range of velocities is displayed and in Figure 4.2(b), the distribution of small velocities is highlighted. As expected, close to the rim of the orifice, the particles start moving while the bulk of particles has a very small velocity. A remark on the small oscillations visible in the top part of the container is necessary. As the interaction of the particles is realized with a penalty approach as described in Section 2.2.3, artificial springs connect the particles and oscillations propagate through the domain. In case these oscillations are small enough, the overall system behavior is not disturbed and a physically realistic simulation result is obtained. This stability related issue is directly linked to the time step size which must be chosen carefully obeying (3.69).


 Figure 4.2: Particle outflow through $D_0 = 100$ mm orifice.

The discharge rates for different orifice sizes and friction coefficients are summarized in Table 4.1. The mass flow rates obtained with the developed approach (denoted as “DEM”) range between 70 – 80 % of the mass flow rates obtained by Bertrand et al. [14]. As the reference does not provide results for an equal static and dynamic friction coefficient, the result in which the static and dynamic friction coefficient are closest is always chosen in order to be as comparable as possible with the assumption that the static and the dynamic friction coefficient are equal. Using the empirical correlation given in (4.1), the discharge rates even range slightly above the values from Bertrand et al. [14]. Although the absolute mass flow rates are smaller than the reference solution, the trend of a decreasing mass flow rate for an increasing friction coefficient can be observed. This can be explained with an increased resistance in the particle flow due to the additional friction.

There are several possible explanations for the deviations. In Bertrand et al. [14], there is no information available on the allowed penetration of the soft particle approach which might influence the results. In order to test whether this parameter has an effect, the case with $D_0 = 100$ mm and a friction coefficient $\mu_{s,dyn} = 0.05$ is chosen and the maximal allowed relative penetration c as defined in (3.65) is varied. This directly enters the computation of the stiffness used in the particle contact according to (3.67). The discharge rates displayed in Table 4.2 reveal that there is almost no influence by the stiffness parameter. This result shows that the artificial spring stiff-

D_0 [mm]	$\mu_{s,\text{dyn}}$	DEM [kg/s]	Bertrand et al.	Bertrand et al. [14] [kg/s]	Eq. (4.1) [kg/s]	
100	0.05	5.73	7.545		7.88	
	0.10	5.57	6.906			
	0.15	4.54	6.357			
120	0.05	9.77	13.41		13.98	
	0.10	8.89	12.32			
	0.15	8.09	11.49			
140	0.05	15.38	21.35		22.28	
	0.10	14.32	19.88			
	0.15	13.06	18.49			

Table 4.1: Discharge rates for different orifice and friction coefficient combinations.

c	0.02	0.04	0.06	0.08
DEM [kg/s]	5.70	5.73	5.64	5.65

Table 4.2: Discharge rates for different relative penetration values.

ness, which is necessary to model the soft particles with their overlap, does not influence the outcome within the chosen range of $c \in [0.02, 0.08]$. This is very beneficial as it does not pose restrictions on the choice of the relative allowed penetration.

Another unclear aspect is the way the container, i.e. the walls which bound the particles, is introduced in the computational framework of Bertrand et al. [14]. As the walls are a critical element in particle simulations, this might be a source for the deviations. It can be concluded that the results obtained with the developed framework are 20 – 30 % lower than the reference values while the reason for this deviation could not be identified.

4.2 Particle mixing

4.2.1 Setup

In order to investigate the parallel performance of the developed framework, the mixing of 571,787 particles driven by two paddles is used. Initially, the particles with a diameter of 2 mm are settled due to gravity acceleration $\mathbf{g} = (0.0, 0.0, -9.81)^T$ m/s² in a cubic box of size 200 × 200 × 200 mm up to time $t = 0.25$ s. Next, at $0.25 \text{ s} < t < 0.45 \text{ s}$, two planar paddles of thickness 2 mm dive into the bulk of particles until a gap of 20 mm remains to the bottom of the box. The paddles are placed symmetrically in the box and their geometry is given in Figure 4.3. The rigid paddles rotate with prescribed angular velocity

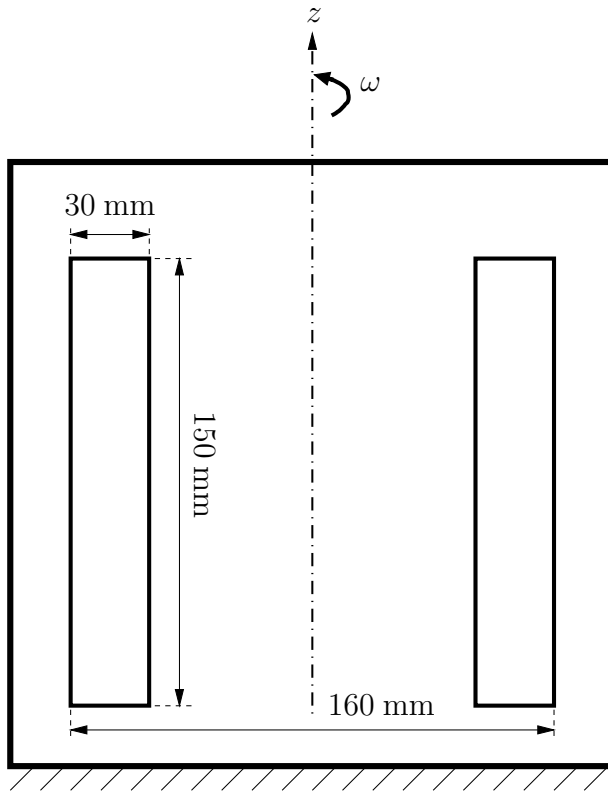


Figure 4.3: Setup of particle mixer with paddles.

$$\omega = \begin{cases} 0, & \text{if } 0 < t < 0.45 \text{ s} \\ 60 \frac{1}{\text{s}^2} \cdot (t - 0.45 \text{ s}), & \text{if } 0.45 \text{ s} < t < 0.60 \text{ s} \\ 9.0 \frac{1}{\text{s}}, & \text{if } 0.60 \text{ s} < t < 1.40 \text{ s} \\ 9.0 \frac{1}{\text{s}} - 60 \frac{1}{\text{s}^2} \cdot (t - 1.4 \text{ s}), & \text{if } 1.40 \text{ s} < t < 1.55 \text{ s} \end{cases} \quad (4.2)$$

around the z -axis. Additionally, the angular velocity over time is illustrated in Figure 4.4. The time step size is $\Delta t_b = 4.0 \cdot 10^{-6}$ s leading to 387,500 time steps for the full simulation.

The temporal evolution of the mixing process is displayed in Figure 4.5. The paddles intruding the particles are shown in Figure 4.5(a), Figure 4.5(b), and Figure 4.5(c). The particles are colored with four different colors for better visualization of the mixing process driven by the paddles. The paddles are at their maximal angular velocity in Figure 4.5(d) to Figure 4.5(h). The top layers of the particles are already well stirred at $t = 1.5$ s which is displayed in Figure 4.5(i). These results show the ability of the developed framework to cope with a large number of particles in a pure particle setup including moving walls.

4.2.2 Scaling study

The Discrete Element Method is known to be computational expensive due to two reasons. Firstly, a vast amount of time steps is necessary in order to obtain a stable simulation because each contact event must be resolved with several time steps. Secondly, relevant systems usually include a large number of particles which can easily reach $10^5 - 10^7$. Therefore, it is important

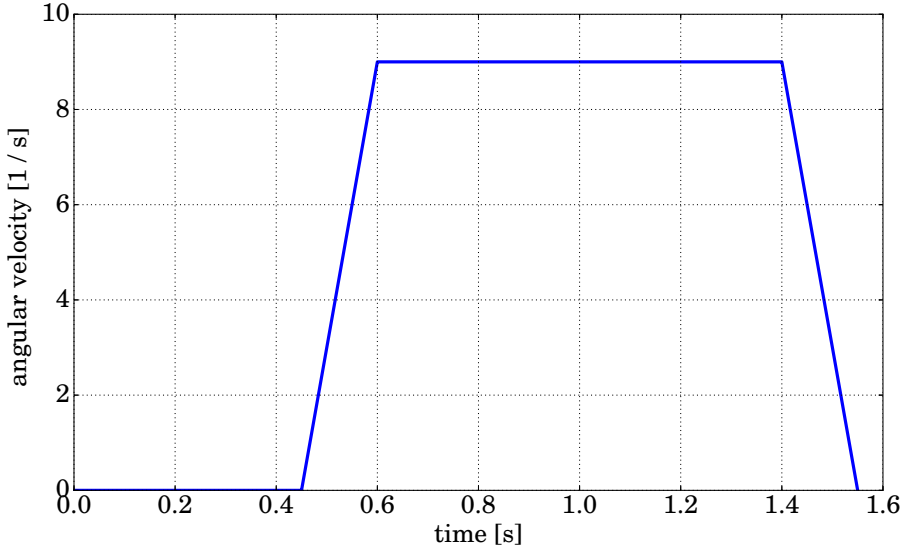


Figure 4.4: Paddles' angular velocity.

to test whether the developed framework scales in parallel in order to shorten the time to solution and not to waste computational resources. As described in Section 3.6, a binning strategy is used for the neighborhood search. The bin size must be chosen large enough to include all close particles in order to evaluate the contact events correctly. Thus, it is enough to provide one layer of ghost bins around the domain each processor owns. This coincides with Sigurgeirsson et al. [189] who state that the bin size must be greater than the diameter of the largest particle involved, i.e.

$$\Delta l^{\text{bin}} > 2 \cdot r_{\max}. \quad (4.3)$$

According to Kloss et al. [117], there is no closed solution available on how to choose the bin size such that the run time is minimal due to the complex influence of particle size distribution, particle shape and interaction force implementation. Hence, three different bin sizes are chosen to evaluate the parallel performance. Furthermore, each run is repeated three times in order to obtain its minimal run time. By doing so, the disturbance of the time monitorings of other simulations are minimized which run at the same time on the cluster.

The wall times of the simulation for five different number of processors ranging from 24 to 120 and three different bin sizes are displayed in Figure 4.6. The timings are gathered over 4000 time steps in $t \in [0.448 \text{ s}, 0.464 \text{ s}]$ in which the paddles have already been fully intruded into the bulk of particles. The rotation starts at $t = 0.45 \text{ s}$. Hence, contact between the paddles and the particles as well as massive inter-particle penetration occurs. Two main contributions of the overall run time and their sum are included in the figure. The first dominant part is the contact evaluation and the second part is the transfer of particles in order to update the information in the bins on the respective processors. The latter comprises the transfer of particles across processors, setting up the new ghosting and updating all the state vectors to the latest parallel layout. The timings can only be seen as a rough estimation of the parallel performance as other simulations were run on the cluster while this performance study was performed. The smallest bin size is $\Delta l_x^{\text{bin}} = \Delta l_y^{\text{bin}} = \Delta l_z^{\text{bin}} = 2.08 \text{ mm}$ which is slightly larger than two times the particle radius

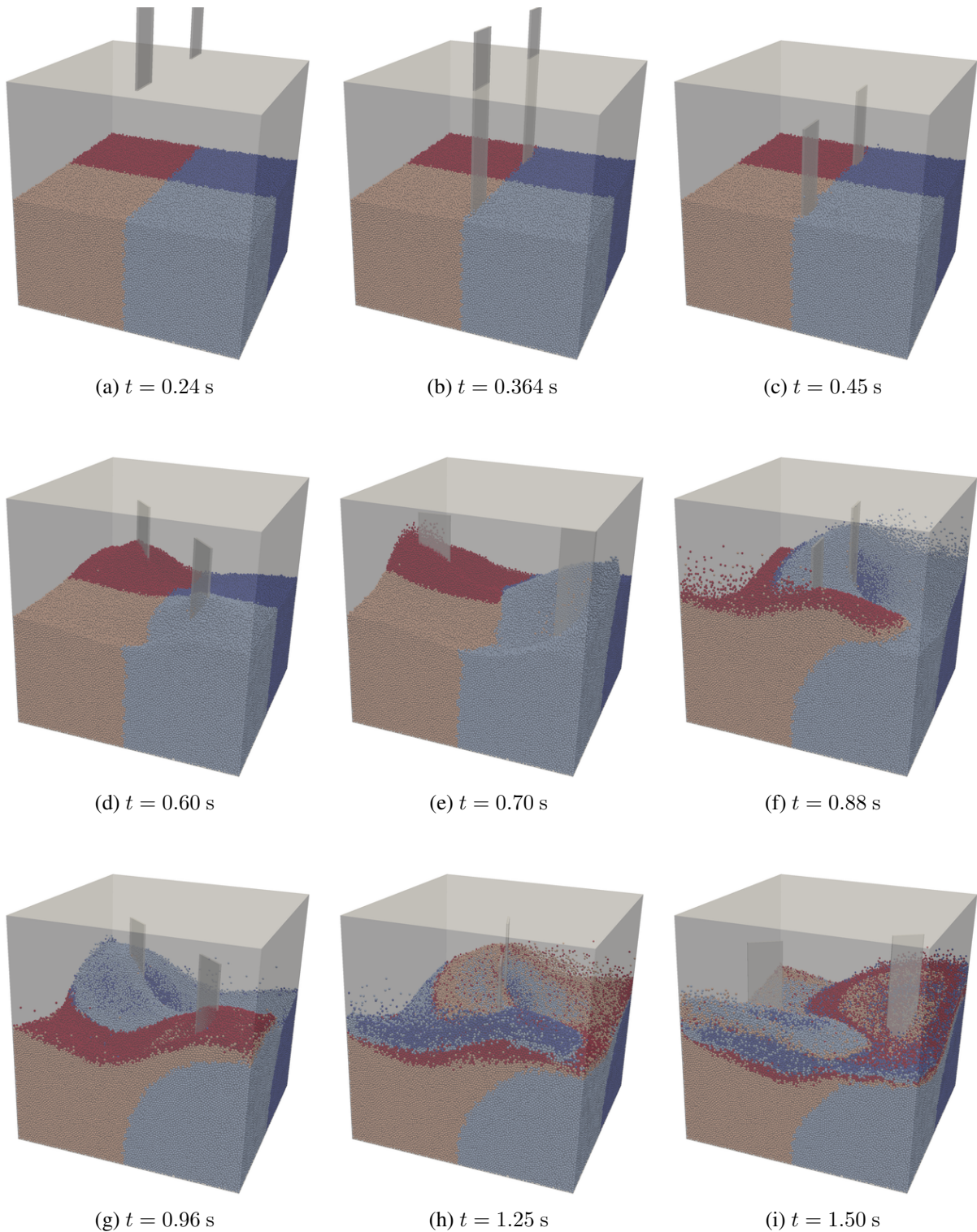


Figure 4.5: Particle mixing.

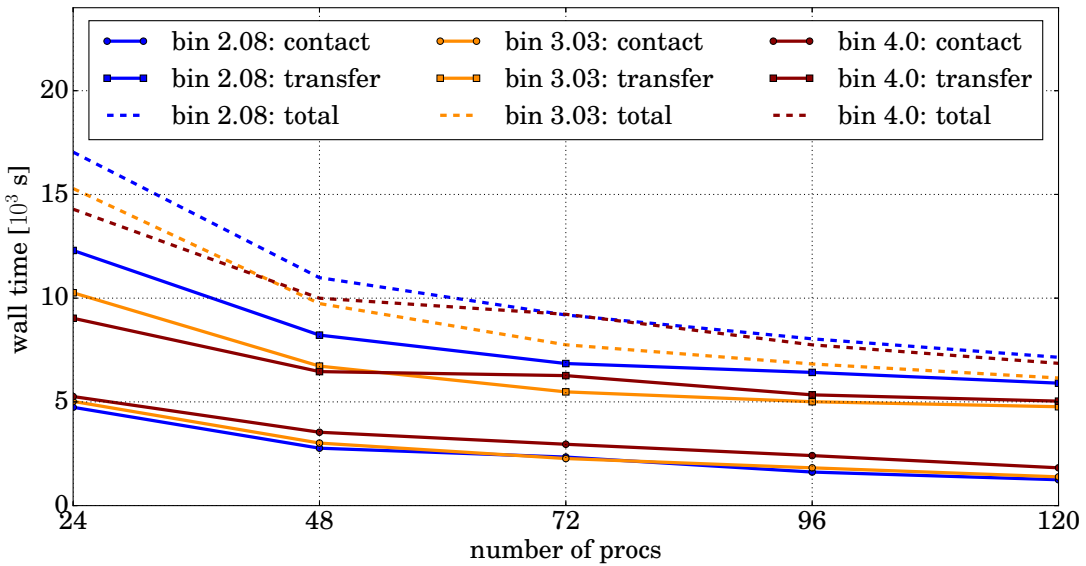


Figure 4.6: Timings for different bin sizes.

which yields the shortest timings for evaluating the contact as obvious in Figure 4.6. The least effort is necessary to check contact between particles and their neighborhood due to its small size. At the same time, an enormous overhead is generated by the large number of bins because more transfer operations and more information for the ghosting is needed. Hence, the overall run time is larger than for a simulation with a bin size of 3.03 mm and 4.0 mm. The larger the bin size, the more expensive becomes the contact evaluation but at the same time, the overhead can be reduced. This is a clear trade-off and the shortest overall wall time can be obtained using a bin size of 3.03 mm which is approximately 1.5 times the size of the minimal possible bin size. Hence, it can be concluded that the bin size should be chosen rather small to shorten time to solution.

For the case with a bin size of 3.03 mm, a detailed overview of the scaling of the contributions to the simulation is given in Figure 4.7. A strong scaling study is performed in which the number of particles in the system is kept constant. The reference timings are obtained from a simulation using 24 processors and the parallel efficiency is displayed which can be achieved using 48, 72, 96 and 120 processors. As one node of the cluster is equipped with 24 processors, only simulations with full nodes are performed. The parallel efficiency for the contact evaluation gradually decreases and goes down to 69 % and 72 % for the run using 96 and 120 processors, respectively. As in average only approximately 5000 owned particles reside on a single processor for the case using 120 processors, the overhead is growing rapidly because more and more contact events between owned and ghost particles occur. This indeed explains the decrease in efficiency. The transfer across processors scales with a similar trend as the contact evaluation. The portion of wall time caused by the inter-processor transfer is in a range of 10 – 15 % and thus it cannot counterbalance the badly scaling part of setting up the ghosting. Setting up the ghosting information in the discretization is quite expensive and it takes more than 50 % of the run time. Unfortunately, it includes parts that scale very badly which need further investigation. Hence,

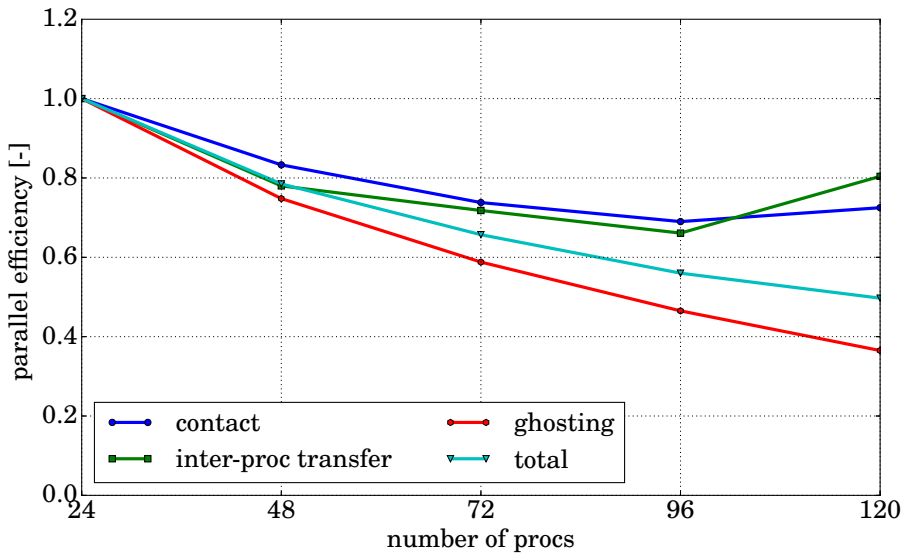


Figure 4.7: Parallel efficiency of respective contributions of the simulation for a bin size of 3.03 mm.

due to the dominant work load necessary for setting up the ghosting, the overall performance goes down to 56 % when using 120 processors.

An advantage that has not been exploited in the previous considerations is that particles reside longer within one bin in case of an increased bin size. This allows to reduce the number of calls to the expensive transfer procedure. The previous investigations included a transfer in each time step leading to the overall bad scaling as shown in Figure 4.7. The smallest bin size of 2.08 mm is determined from the sum of the largest particle diameter (2.0 mm) and twice the maximal travel distance of a particle ($2 \cdot 0.04 \text{ mm} = 0.08 \text{ mm}$) within one time step. This covers the worst case scenario of two particles approaching each other at maximal velocity. A test is included in the developed framework to ensure that the bin size is chosen large enough according to these considerations. Hence, for the test case with a bin size of 3.03 mm, it is possible to skip the transfer at least for

$$\frac{3.03 \text{ mm} - 2.08 \text{ mm}}{0.08 \text{ mm}} = 11.875 \approx 11$$

time steps without missing a single contact event. This rough calculation includes the worst case assumption of two particles approaching each other with the maximal velocity over several time steps in one of the axis' directions. The timings which can be achieved when the expensive transfer operation is only performed every 11th time step is displayed in Figure 4.8. Compared to the results in Figure 4.6, the effort for the contact evaluation dominates. An overall parallel efficiency of 66 % is achieved for this test case with 96 and 120 processors.

These results can be compared with the work of Kloss et al. [117] using their open-source DEM code LIGGGHTS. They placed 100,000 particles in a rotating drum such that the drum volume is partly filled with particles ($\approx 30\%$). They ran the simulation on 32 processors and a parallel efficiency of 32 % and 85 % compared to a run with a single processor was achieved without and with load balancing, respectively.

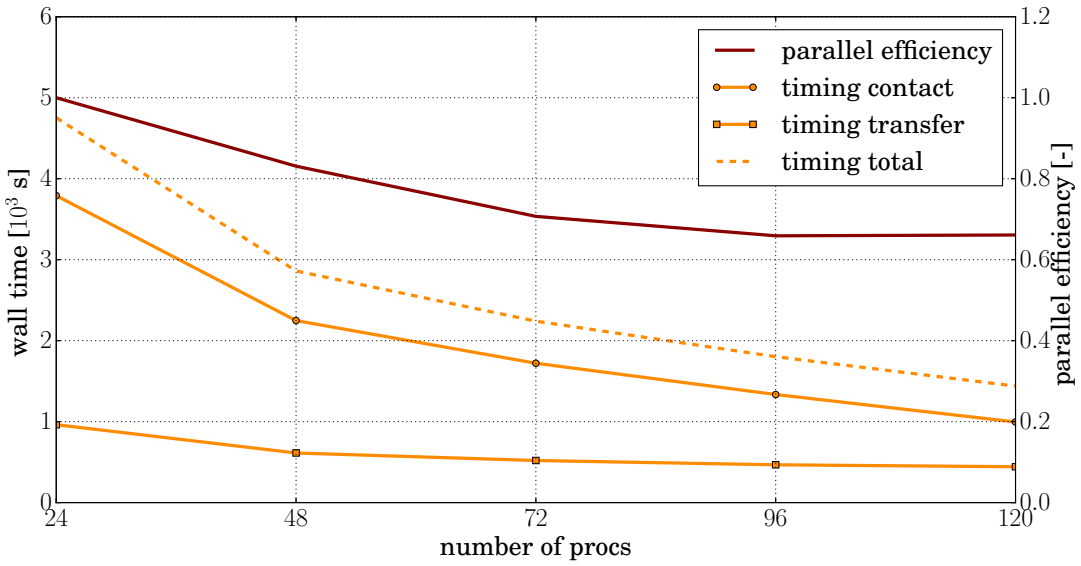


Figure 4.8: Timings and parallel efficiency for a bin size of 3.03 mm with a transfer every 11th time step.

4.3 Taylor-Green vortex

The Taylor-Green vortex (TGV) flow is a fluid flow of counter rotating vortices which can be used to investigate vorticity dynamics. It was proposed by Taylor [204] for single-phase flow and used by Ferrante and Elghobashi [62] to investigate the influence of particles on the decay rate of the vortices. In the latter, a two-fluid model is used for the main investigations but in the appendix, also results obtained with a Lagrangian particle tracking approach are given. Details on the numerical approach can be found in an earlier work by Ferrante and Elghobashi [61]. This test case is used to validate the developed Euler-Lagrange approach for setups with $\mathcal{O}(10^5)$ particles.

4.3.1 Setup

The setup can be found in Ferrante and Elghobashi [62] from which case A is chosen. The initial conditions for the fluid field are

$$\langle \mathbf{u} \rangle (x, t = 0) = -\omega_0 \cdot \frac{k_y}{k^2} \cos(k_x x) \cdot \sin(k_z z) \quad (4.4)$$

$$\langle \mathbf{u} \rangle (y, t = 0) = \omega_0 \cdot \frac{k_x}{k^2} \sin(k_x x) \cdot \cos(k_z z) \quad (4.5)$$

$$\langle \mathbf{u} \rangle (z, t = 0) = 0 \quad (4.6)$$

$$\langle p \rangle (t = 0) = -\omega_0 5\pi (\cos(k_x \cdot 2x) + \cos(k_y \cdot 2y)) \quad (4.7)$$

with the wave number $k_x = k_y = 2\pi/B$ in x - and y -direction and $k^2 = k_x^2 + k_y^2$. The fully periodic domain covers $[-B/2, B/2] \times [-B/2, B/2] \times [-\Delta x, \Delta x]$ with length $B = 0.1$ m. The initial vorticity is $\omega_0 = 1000$ /s. The material properties are taken from water, i.e. density $\rho_l = 1000$ kg/m³

and dynamic viscosity $\mu = 10^{-3}$ Pa·s. Identical to Ferrante and Elghobashi [62], a uniform mesh with $96 \times 96 \times 2$ elements is chosen for the fluid leading to $\Delta x = B/96$. A time step size $\Delta t_l = 10^{-5}$ s is applied for the fluid leading to a Courant-Friedrichs-Levy (CFL) number of approximately 0.1. A short remark has to be given owing to the purely Dirichlet bounded fluid problem leading to an undefined pressure level. To solve the resulting singular system, a discrete projection as presented by Bochev and Lehoucq [16] is used to keep the right-hand side orthogonal to the constant mode introduced in the pressure degrees of freedom. The pressure level is kept constant in an integral sense throughout the simulation. The stopping tolerance for the nonlinear iterations is set to 10^{-7} in the L^2 -norm of the residual of the velocity/pressure as well as for the increment of the velocity/pressure. The cross-stress term and the Reynolds-stress term as given in (3.17) needed to be switched off in order to achieve a converging fluid solution. The particles have a diameter of $95\ \mu\text{m}$ and a density of $\rho_l = 1\ \text{kg/m}^3$ leading to a density ratio of $\rho_b/\rho_l = 1/1000$. The initial placement of the $480 \times 480 \times 2$ particles is uniform on a Cartesian grid in $[-B/2+B/K, B/2-B/K] \times [-B/2+B/K, B/2-B/K] \times [-\Delta x/2, \Delta x/2]$ with $K = 480 \cdot 2$. Periodicity for the particles is triggered by the outer surfaces of the fluid domain. The initial size and distribution of the particles leads to an initial uniform dispersed phase fraction of 1 % throughout the fluid domain. The initial particle velocity is determined from the underlying fluid at their respective position. The time step size for the particles is $\Delta t_b = 10^{-7}$ s which coincides with a subcycling of 1 : 100 between fluid and particles. Contact between particles is not considered in this test case in accordance to Ferrante and Elghobashi [62], as such an overlap of particles is possible. The final simulation time is $t_{\text{end}} = 0.02$ s which correlates to $20/(8 \cdot \pi^2) \approx 0.25$ turnovers of the vortex assuming the initial rotational speed is constant.

4.3.2 Analysis and comparison against literature

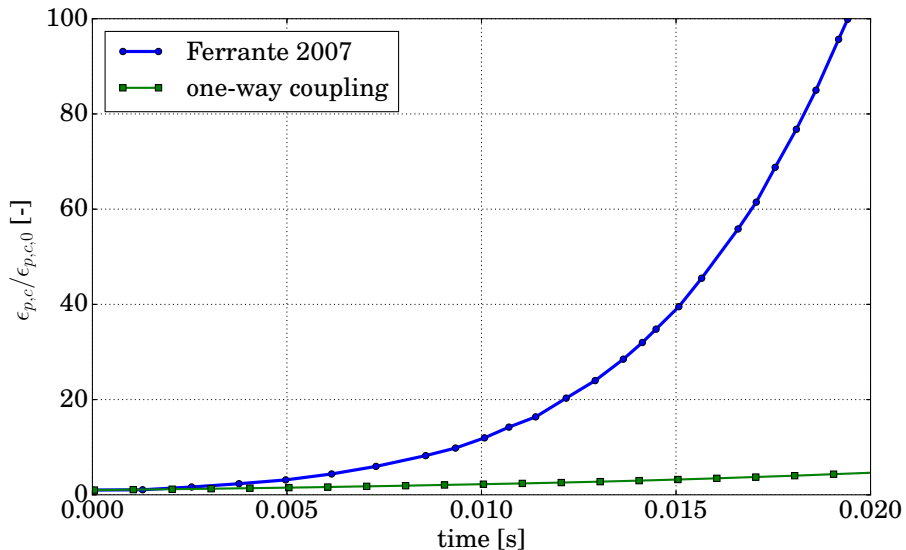


Figure 4.9: TGV: One-way coupling comparison literature.

In Figure 4.9, the dispersed phase fraction over time normalized by its initial value at the vortex center is given for a one-way coupled solution. Thus, the fluid is unaffected by the particles

which are solely driven by the fluid forces. The dispersed phase fraction is only computed in a postprocessing step for analyzing purpose. As contact between particles is not included, the reference solution by Ferrante and Elghobashi [62] reveals an unbounded increase in the dispersed phase fraction because particle overlap occurs. The one-way coupled solution of the developed framework also shows an increasing dispersed phase fraction in the center but the maximal value increases only by a factor of 4.6 instead of a factor greater than 100. Several reasons might be responsible for the deviations. The reference simulation by Ferrante and Elghobashi [62] is performed dimensionless and thus it is possible that during transformation of the units an error is introduced. In the reference, it is stated that it takes a non-dimensional time of 0.2 to perform 20 turnovers of the vortex at the initial vorticity. This is impossible with the stated initial conditions, and thus, it is assumed here that the initial conditions are specified correctly and only $20/(8 \cdot \pi^2) \approx 0.25$ turnovers are performed during the mentioned time interval. The denominator $8 \cdot \pi^2$ can also be found in the equations specifying the initial velocity field. Trying to reproduce initial conditions for the velocity that corresponds to 20 turnovers in the respective time leads to a dispersed phase fraction in the vortex center that increases way faster than the reference solution does. Further reasons for the deviations could be the assumption of mass-less particles in the reference solution whereas here, a density ratio of $\rho_b/\rho_l = 1/1000$ is chosen. Furthermore, as already described in Section 2.2.2, there is no consensus in the community on which model to use for the fluid forces acting on the particles. As described in Ferrante and Elghobashi [61], a drag force according to Stokes law (valid for low particle Reynolds numbers), a Saffman lift force, and most important an inertial force due to fluid acceleration (2.99) are applied in the reference simulation. The latter incorporates the pressure gradient force which is the main fluid force contribution in this example when using the set of fluid forces as presented in Section 2.2.2. In summary, it remains unclear where the difference comes from and in the following, the emphasis is on analyzing trends instead of comparing numbers.

In the following, the full coupling between fluid and particles is investigated, which also accounts for the particle forces and the dispersed phase fraction in the fluid. In the figures, it is denoted as two-way coupling to emphasize the difference to the previous investigations in which only the forces on the particles were considered during one-way coupling. The rotational speed of the vortex is reduced due to the presence of the particles and a slower accumulation of the particles in the vortex core can be expected. Analogue to the one-way coupled setup, the dispersed phase fraction normalized by its initial value at the vortex center is displayed in Figure 4.10(a). The results with two-way coupling give a 3 % at $t = 0.01$ s and 6.5 % at $t = 0.015$ s reduced dispersed phase fraction compared to the one-way coupled solutions. The same trend can also be observed in the reference solutions. The drop of the dispersed phase fraction for the two-way coupling is reduced by 19 % at $t = 0.01$ s and by 45 % at $t = 0.015$ s compared to the one-way coupled reference solution. Although, the absolute numbers of the dispersed phase fraction increase do not match, the increasing factor from time $t = 0.01$ s to $t = 0.015$ s of the present result $6.5\% / 3\% = 2.2$ is similar to the increasing factor of the reference solution $45\% / 19\% = 2.4$. Hence, this trend is reproduced.

In Ferrante and Elghobashi [62], a nearly linear relationship is reported between the decreasing vorticity in the vortex center and the increasing particle concentration. The vorticity normalized by its initial value at the vortex center is shown in Figure 4.10(b). The present results reveal a slower vorticity decay, viz 85 % at $t = 0.01$ s and 89 % at $t = 0.015$ s, than the reference. Having a brief look at the deviations in the dispersed phase fraction between the present two-way

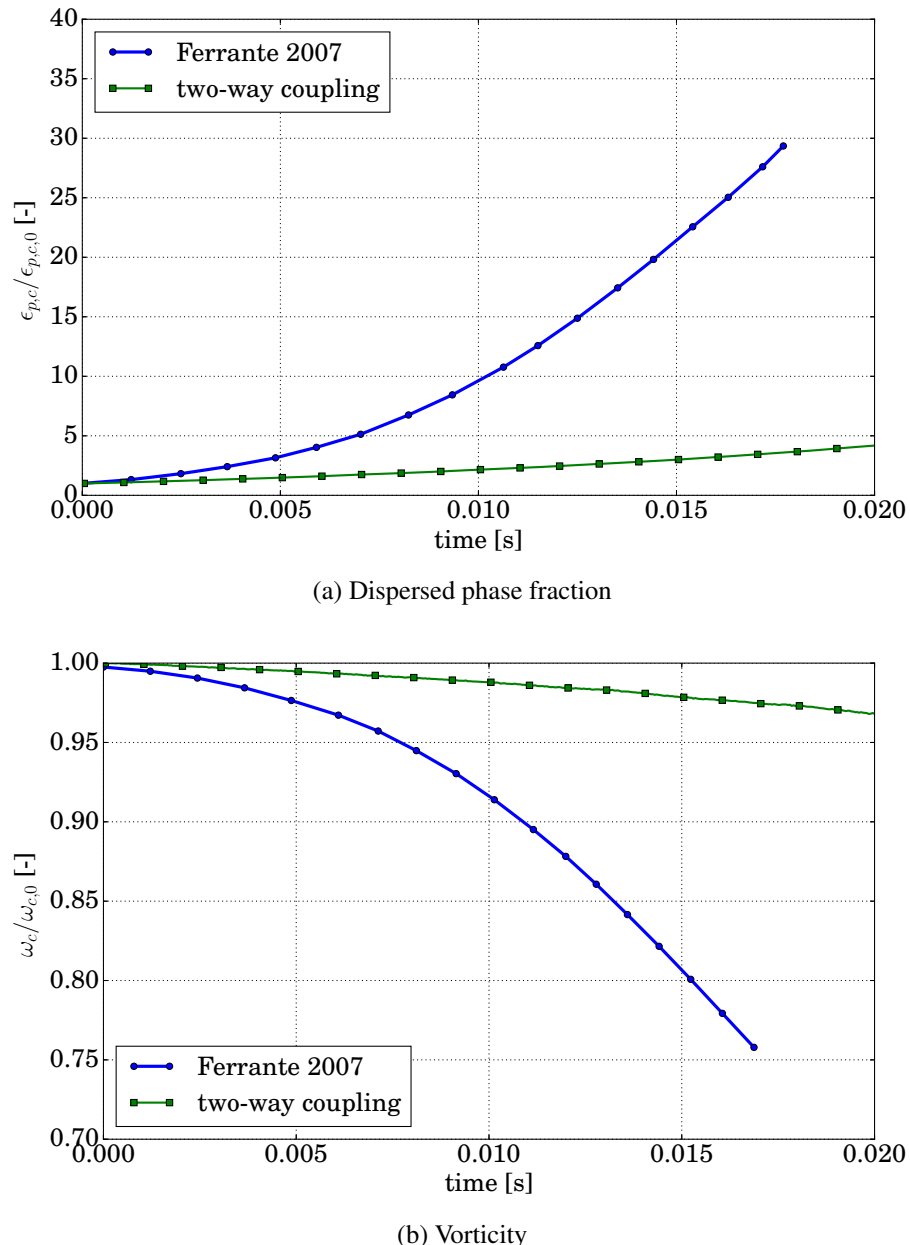


Figure 4.10: TGV: two-way coupling comparison literature.

coupled solution and the reference solution gives a reduced dispersed phase fraction by 78 % at $t = 0.01$ s and by 86 % at $t = 0.015$ s. These numbers coincide very well with the proposed linear relationship between dispersed phase fraction and vorticity in the vortex center as found by Ferrante and Elghobashi [62]. The latter observation might lead to the conclusion that only a mismatch in the initial conditions is responsible for the deviating results. This can likely be caused by an erroneous unit transformation from dimensionless to dimensional simulation. The

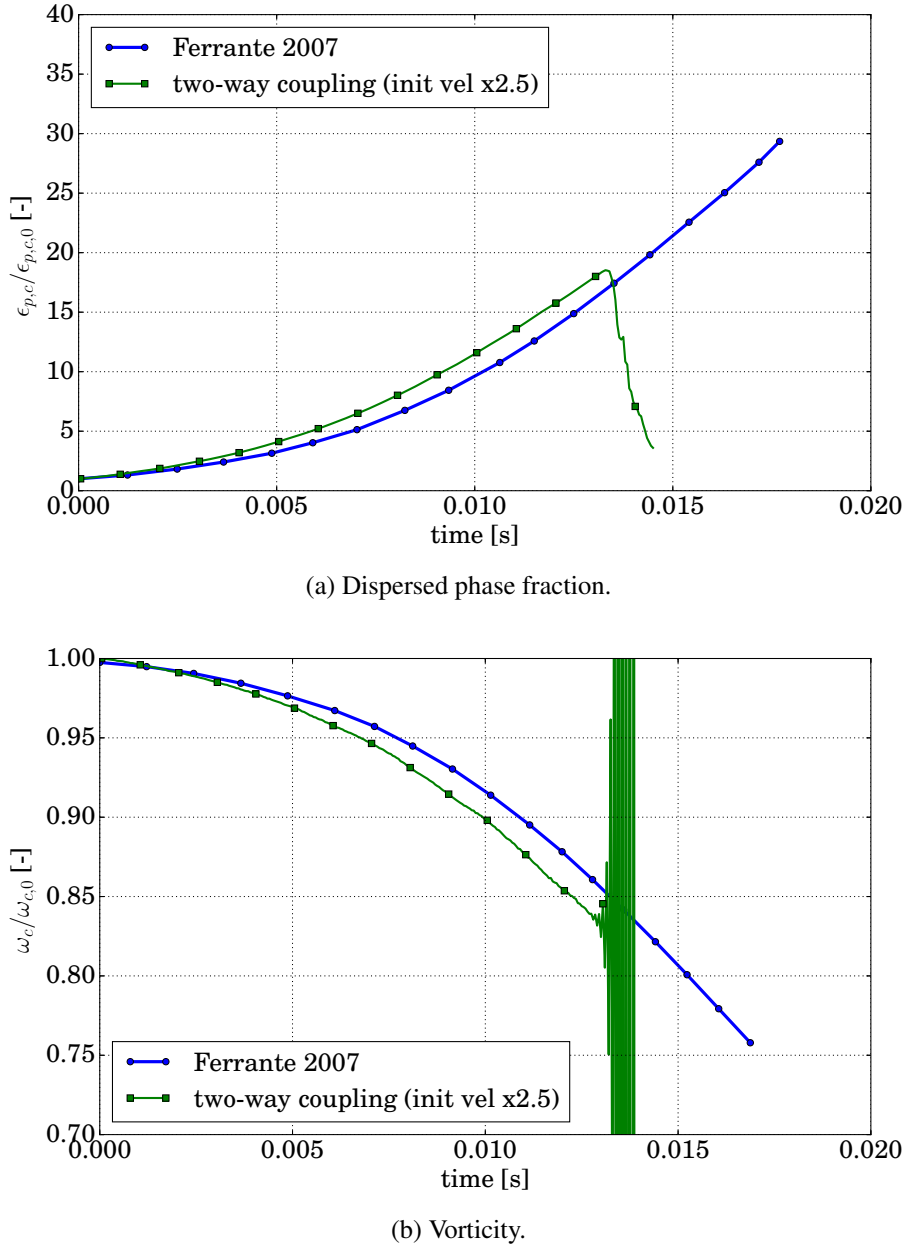


Figure 4.11: TGV: two-way coupling with adapted initial velocity compared to literature.

results using the developed framework with an initial velocity for the TGV which is increased by a factor of 2.5, is displayed in Figure 4.11. Again, the reference solution is by Ferrante and Elghobashi [62]. In Figure 4.11(a), the resulting graphs for the dispersed phase fraction normalized

by its initial value at the vortex center over time lie quite close. A slight reduction of the scaling factor for the initial velocity will further reduce the difference between the results. An identical behavior can be seen for the vorticity normalized by its initial value at the vortex over time in Figure 4.11(b). Again, a slight reduction of the scaling factor would reduce the differences.

These results may lead to the conclusion that the developed framework is able to reproduce the results presented by Ferrante and Elghobashi [62] for the TGV and just an error in the initial velocity profile is responsible for the deviating results presented in the first part of this section. Unfortunately, the results in Figure 4.11 start oscillating at $t = 0.013$ s which is caused by a loss of symmetry. The vortex core is no longer located at the center of the domain and a diverging result can be observed. Trying to reduce the time step size did not cure the loss of symmetry, and thus, it remains an open issue to be investigated.

4.4 Fluidized bed

Fluidized bed applications are common in process and chemical industry and contain systems of particles which are streamed with gas from the bottom of the enclosing container. Dependent on the fluid inflow velocity and the involved particles, different regimes develop which can be used to improve the desired process such as e.g. drying, coating, gasification, or combustion. The reader is referred to e.g. Kunii and Levenspiel [124], Gidaspow [71], or Epstein and Grace [56] for an overview of industrial applications and details thereon. Also, the physics of fluidized beds with different regimes can be found in the given references.

4.4.1 Setup

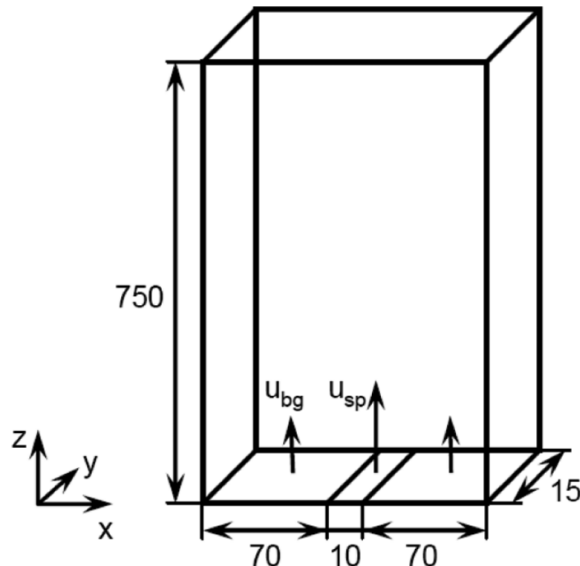


Figure 4.12: Setup of fluidized bed (geometry in [mm], from Kloss et al. [117]).

A 2D fluidized bed is considered as shown in Figure 4.12 which is investigated with the developed framework using 96 processors. A thorough investigation of this test case is performed

in Link et al. [134] and it was used by e.g. Kloss et al. [117] for validation of their numerical approach. The fluid dynamic viscosity $\mu = 1.8 \cdot 10^{-5}$ Pa·s and density $\rho_l = 1.0 \text{ kg/m}^3$ are taken from air. The prescribed inflow velocity at the bottom is $u_{sp} = 30 \text{ m/s}$ and $u_{bg} = 1.5 \text{ m/s}$ in the spout region and in both regions next to the spout, respectively. The inflow is directed in positive z -direction. The nodes located at the border between both regions are assigned to the spout region regarding the boundary condition. Slip conditions are applied at the walls whereas a zero-traction Neumann boundary is assumed at the lid in order to allow outflow of air. The fluid domain is discretized with $30 \times 1 \times 250$ tri-linearly interpolated hexahedral fluid elements in space and a time step size of $\Delta t_l = 1.0 \cdot 10^{-4}$ s is chosen such that the resulting CFL-number is around one. The particles have a density of $\rho_b = 2505 \text{ kg/m}^3$ and radius of $r = 1.5 \text{ mm}$. The coefficient of restitution is $e = 0.97$, the friction coefficient is $\mu_s = 0.1$ and the relative penetration is set to $c = 0.04$. Subcycling of 1 : 500 between fluid and particles is used such that the particle time step size is $\Delta t_b = 2.0 \cdot 10^{-7}$ s. Due to the density ratio $\rho_b/\rho_l \gg 1$, the added mass force in (2.51) is neglected. The dominating force is the gravity force due to gravitational acceleration $\mathbf{g} = (0.0, 0.0, -9.81)^T \text{ m/s}^2$ which is counteracted mainly by the drag and pressure force. The cross-stress term and the Reynolds-stress term as given in (3.17) are switched off in the fluidized bed example.

Several steps are necessary to start-up the actual simulation. Initially, the 24,500 particles are placed on a $35 \times 4 \times 175$ lattice located within the fluid domain from where they sediment due to gravity while the fluid inflow is turned off. To break symmetry, a small offset is added to each initial particle position. In a second step, the fluid inflow profile at the bottom is accelerated from zero to its final magnitude.

4.4.2 Fixed bed regime

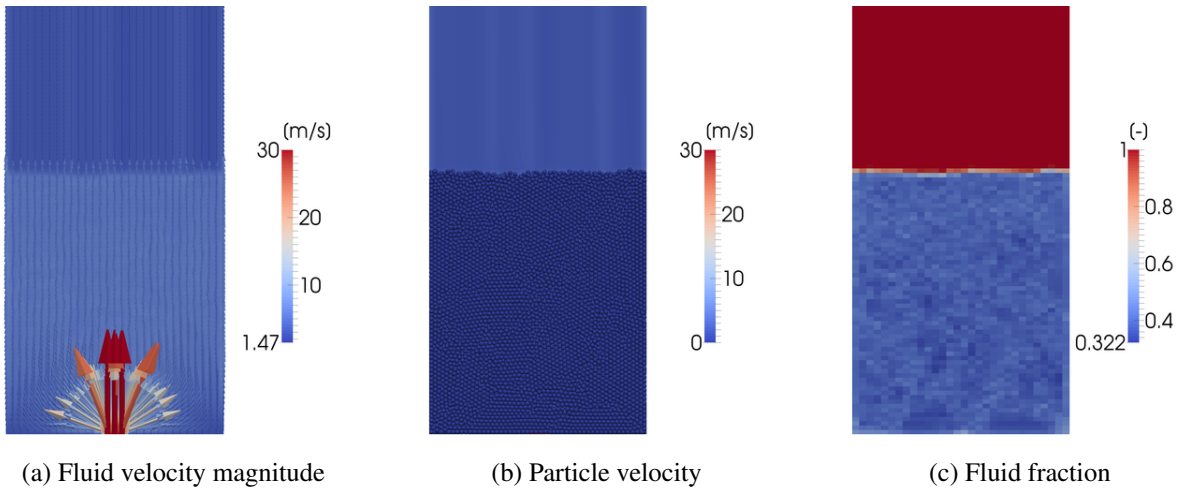


Figure 4.13: Fixed bed regime.

As the particles keep resting after the setup procedure as described in the previous section, a fixed bed regime is obtained. In Figure 4.13(b), the fluid domain is clipped half in y -direction to open the fluid domain. This half-clipping of the fluid domain is applied in all figures displaying

fluidized bed results in the remainder of this section without further remark. In Figure 4.13(a), the fluid velocity is illustrated showing that the fluid flows through the particles. The fluid jet rapidly expands and the velocity profile along the x -direction flattens with increasing z -direction. The jump in the fluid velocity can be seen at the upper border of the particle bed at $z = 0.18$ m. The fluid velocity is approximately 2.47 times faster in the particle bed than above the bed because the particles displace volume such that the fluid needs to flow around the obstacles. The distribution of the fluid fraction is displayed in Figure 4.13(c) and the average fluid fraction in the particle bed is $\epsilon_l = 0.384$. The inverse of the average fluid fraction is 2.6 which agrees well with the factor in the velocity jump. Hence, the developed framework using the volume averaged Navier-Stokes equations can represent very accurately the effect of volume displaced by the particles using the concept of a fluid fraction.

4.4.3 Internal spout regime

An essential aspect to obtain good results is the choice of the fluid-particle coupling. Therein, the focus is on the choice of the drag law which is still an open research topic, see Link et al. [134]. Often, the drag correlation proposed by Wen and Yu [227] for a fluid fraction $\epsilon_l > 0.8$ and the correlation of Ergun [57] for $\epsilon_l < 0.8$ are combined to obtain reasonable results, compare Gidaspow [71]. Another approach is to use the minimum of both drag laws as presented by Link et al. [134]. More recently, a drag correlation was proposed by Koch and Hill [118] to overcome shortcomings in certain regimes as reported by Link et al. [134]. As it is neither the aim of this work to assess the existing drag correlations nor to provide a new drag law, the particle forces as introduced in Section 2.2 are applied. The used drag correlation in (2.47) is not well suited for fluidized bed applications because the assumption of an isolated sphere surrounded by fluid is violated. Hence, the drag force on the particles is underestimated and the particles keep resting although fluidization is expected. In order to overcome this problem and to develop a transient fluidized bed, the density of the particles is reduced. Hence, it is possible to show the versatility of the proposed framework dealing with such a complex phenomenon while suppressing the need for a sophisticated drag correlation. Initially, the packed bed needs to be disturbed in order to enable the jet to develop. Therefore, the gravity is reduced to 1 % of the initial value following a sine curve for a time period of 0.05 s. Afterwards, the particle density is reduced to $\rho_b = 1503 \text{ kg/m}^3$, which is 60 % of the original particle density, leading to an internal spout regime as depicted in Figure 4.14. Only one screenshot is depicted for this regime as the shape of the cavity does not change significantly over time. A small internal cavity forms above the spout within the bulk of particles because the air jet is not strong enough to break through the compacted zone of particles above the cavity, cf. Epstein and Grace [56]. The cavity is almost empty such that the fluid fraction therein is close to one, see Figure 4.14(c). In Figure 4.14(b), the fluid domain is clipped half in y -direction to open the fluid such the particles become visible. The particles are colored according to their velocity magnitude. Only the particles at the bound of the cavity are in motion while the bulk of particles is still at rest. The shape of the cavity does only change marginally over time. The velocity magnitude of the particles is less than 5 % of the fluid inflow velocity. In contrast, the maximal fluid velocity above the spout is about 10 % larger than the inflow velocity because the incoming jet is narrowed by the bulk of particles before the velocity is dissipated in the region of resting particles. There, the velocity profile is rapidly homogenized and a behavior similar to a fixed bed prevails, compare Figure 4.13(a).

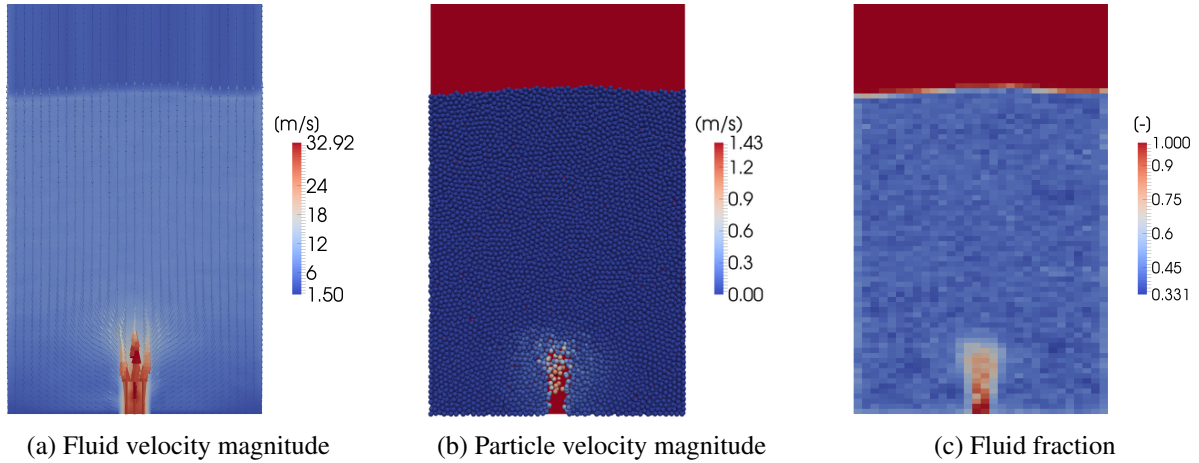
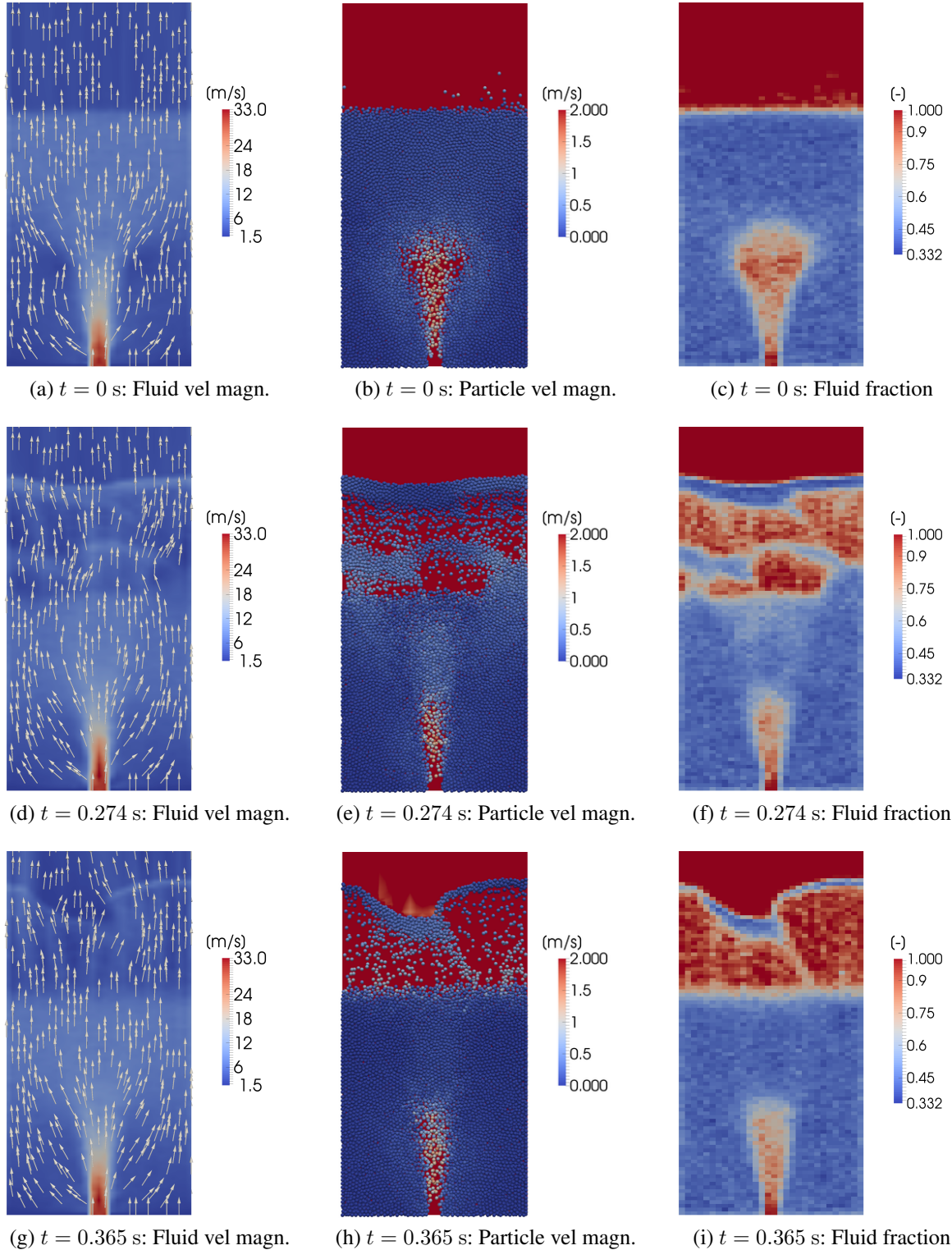


Figure 4.14: Internal spout regime.

4.4.4 Slugging bed regime

Another formation which can occur in fluidization is the slugging bed regime. Whole layers of particles move upward which are then called slugs, cf. Link et al. [134]. The process of slug formation and propagation repeats periodically in time. Similar to the internal spout simulation from the previous section, the particle bed needs to be disturbed once in the beginning to initiate the slugging process. Therefore, gravity is reduced to 1 % of the initial value for a time period of 0.05 s following a sine curve. Afterwards, the particle density is reduced to $\rho_b = 1252.5 \text{ kg/m}^3$, which is 50 % of the original particle density. The reduced density is necessary to counteract the non-appropriate drag law which underestimates the particle force due to drag.

The temporal evolution of the slugging bed is illustrated in Figure 4.15. Initially, an internal spout is present which can be seen in the particle distribution and the fluid fraction in Figure 4.15(b) and Figure 4.15(c), respectively. A small region directly above the bottom section with high inflow velocity is cleared from particles. The cavity reaches half the height of the particle bed in its center. In the present setup, the fluid is strong enough to break-up the internal cavity. One cycle takes approximately 0.55 s and almost half of the time is necessary to form the slug as obvious as in Figure 4.15(e) which displays the particle distribution at $t = 0.274 \text{ s}$. The upper part of the particles propagates upward in form of a five particles thick layer which is followed by a layer which contains mostly fluid with a fluid fraction around 87 % as can be seen in the fluid fraction in Figure 4.15(f). At time $t = 0.365 \text{ s}$, the particles have just passed their maximal position in z -direction and they have started falling back to top of the bed, see Figure 4.15(g) to Figure 4.15(i). At time $t = 0.365 \text{ s}$, remnants of the former slug are still in the falling process while most of the particles have already reached the bed again, cf. Figure 4.15(k). The fluid flow is still disturbed by the presence of the few particles, as can be seen in Figure 4.15(j) where the fluid velocity is increased in the narrow band of particles in the remaining part of the slug. The plot is colored with the fluid velocity magnitude and arrows indicate the flow direction. After 0.55 s, the slug has fully unified with the particle bed again which delivers a frequency of 1.82 Hz. The fluid velocity in the bottom half of the particle bed is nearly constant over time



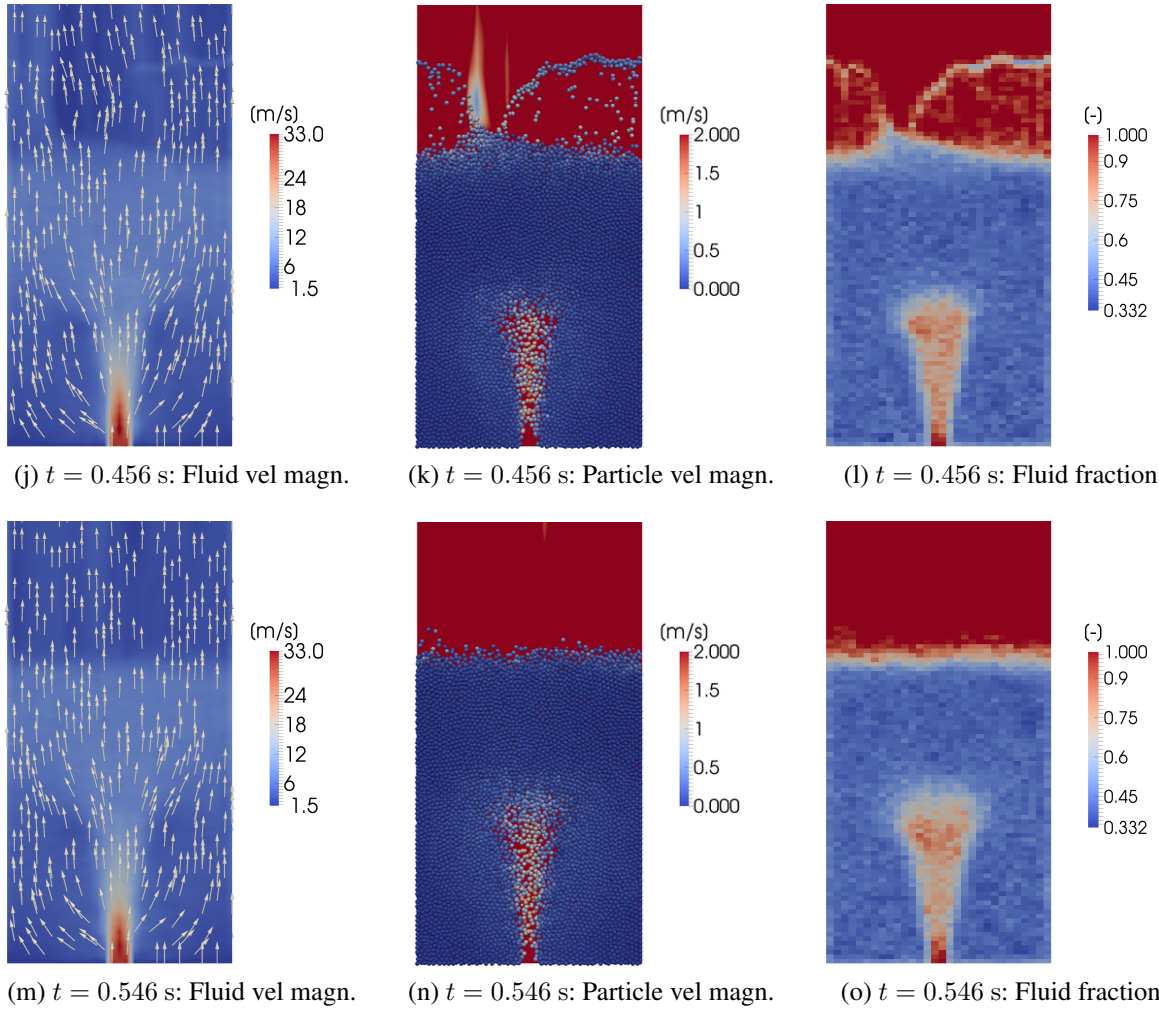


Figure 4.15: Slugging bed regime.

and fluctuations are restricted to the top region where the slugs form, compare Figure 4.15(a), Figure 4.15(d), Figure 4.15(g), Figure 4.15(j) and Figure 4.15(m).

4.4.5 Jet in fluidized bed regime

Another regime can be identified in this fluidization setup when the particle density is reduced down to $\rho_b = 751 \text{ kg/m}^3$, which is 30 % of the original particle density. The same start-up procedure is applied as in the previous sections. The gravity is reduced down to 1 % of the initial value for a time period of 0.05 s following a sine curve to disturb the initial packing. The resulting velocity and fluid fraction distribution are displayed in Figure 4.16. The inflowing jet is strong enough to transport particles upwards to the top of the particle bed similar to a fountain. From there, the particles move to the left and right and drop down along the walls, see Figure 4.16(b), Figure 4.16(e) and Figure 4.16(h) which display the z -component of the particle velocity. Almost all particles are in motion except those residing in the left and right bottom corners. The

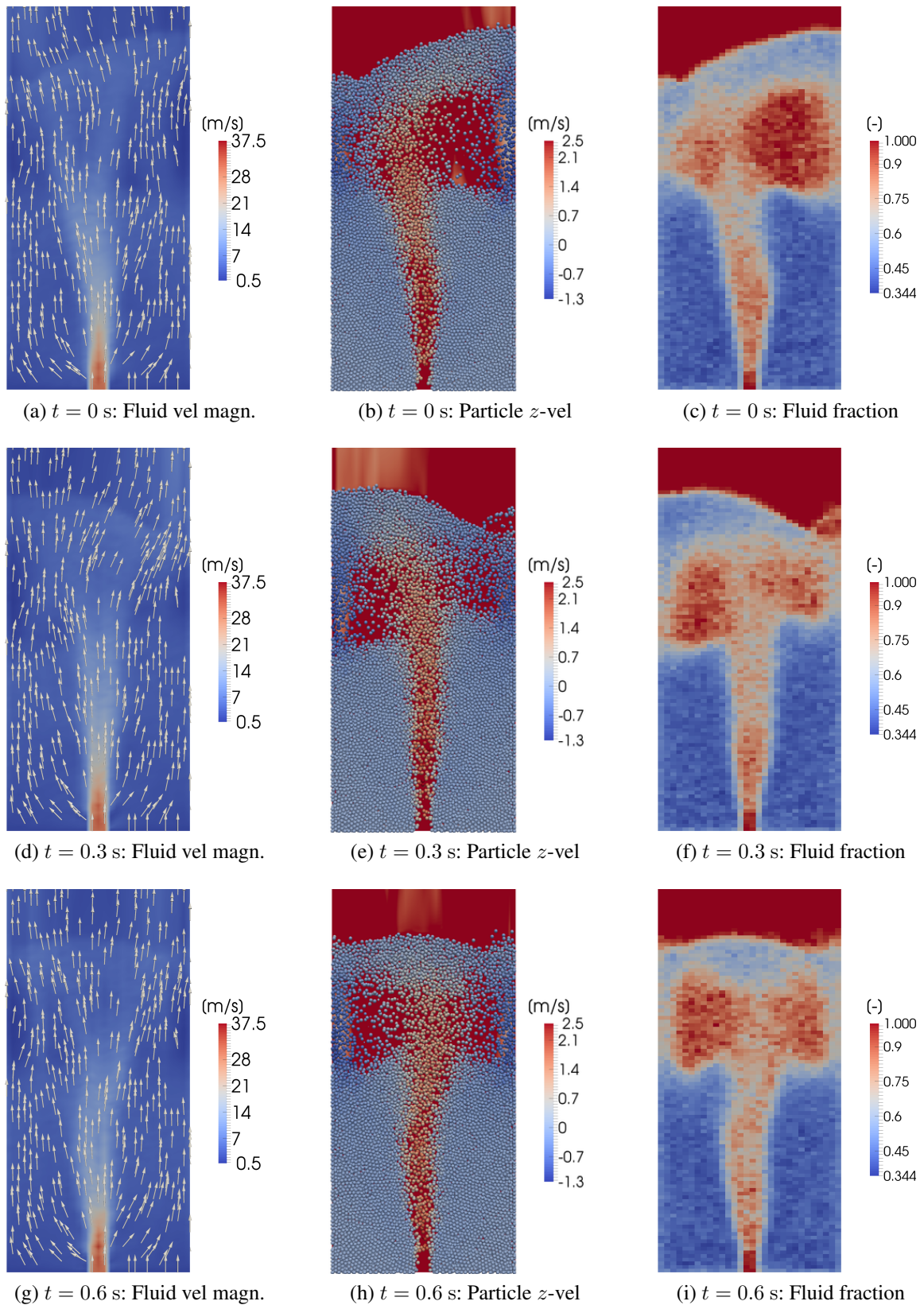


Figure 4.16: Jet in fluidized bed regime.

upward flowing fluid jet oscillates gently from right to left which can be observed in the fluid fraction in Figure 4.16(c), Figure 4.16(f) and Figure 4.16(i) leading to a change in shape of the upper cavity. As reported by Link et al. [134], the jet in fluidized bed regime can have different cavity shapes of which the mushroom shaped one is similar to the present results. Also, slightly off center jet positions may occur which can be seen in the current results.

4.4.6 Drag law dependent behavior

The results obtained with the developed framework show its ability to reproduce different flow regimes occurring in a fluidized bed problem. However, this could only be achieved by modifying the particle density because the drag force is underestimated with the current drag law. A proper drag law is essential for this test case which does account for dense particle packings. As it is not the aim of this thesis to investigate the numerously proposed drag laws, a simple drag law is used. In case further effort is conducted on the used drag law, a quantitative analysis of a fluidized bed problem is possible with the developed framework.

4.5 NACA 0015 hydrofoil

One aspect of the developed framework has not been investigated so far. Each particle can be assigned an ODE which is used to compute the radius evolution of the particle. The size of such a bubble is influenced by its initial conditions and the ambient pressure of the fluid field. The Rayleigh-Plesset (RP) equation, as introduced in Section 2.4, with its numerical treatment including adaptive time stepping, is presented in Section 3.5.1. This submodel is incorporated in the strong fluid-particle coupling scheme, as introduced in Section 3.2.2, in which it represents the time scale with the most strict limitations on the allowed time step size due to its highly nonlinear behavior. A relevant application for this framework is the formation of cavitation bubbles starting from small nuclei. Usually, nuclei contain non-condensable gas and can be found in abundance in any liquid. In case the ambient pressure falls below the vapor pressure of the liquid, due to an acceleration of the fluid, each nucleus can be the starting point for a vapor bubble. Therefore, the nuclei are tracked in the Lagrangian frame and the RP equation is solved to model the radius variation according to the ambient conditions. Similar approaches have already been reported by Hsiao et al. [95], Giannadakis et al. [70], Mattson [145], Shams et al. [187], Yakubov et al. [233], and Vallier [214].

4.5.1 Setup

Flow with properties summarized in Table 4.3 around a NACA 0015 hydrofoil with a chord length of 12 cm and an angle of attack of 8° is considered as shown in Figure 4.17. The test case is mainly based on Hsiao et al. [96]. The fluid properties resemble water with a viscosity that is a factor of 100 larger than original to reduce the Reynolds number of the problem. The leading edge of the hydrofoil is located at the origin. The fluid domain of the pseudo-2D problem covers $[-18, 78] \times [-12, 12] \times [0, 0.0785]$ cm. The prescribed inflow velocity upstream of the foil is $\mathbf{u}_{inf} = (10.0, 0, 0)^T$ m/s and the pressure downstream at the outflow is set to $p_{out} = 178,233.5$ Pa. A slip boundary condition is applied at the y -oriented top and bottom

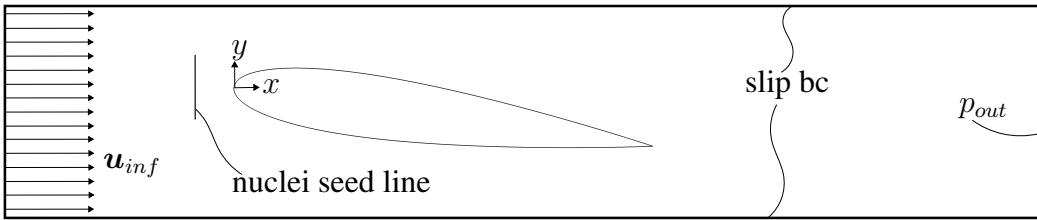


Figure 4.17: NACA 0015 hydrofoil at 8° angle of attack (not to scale).

Property	Value	Unit
Dynamic viscosity μ	0.091084	Pas
Density ρ	997.0	kg/m³
Surface tension coefficient σ	0.0728	N/m
Vapor pressure p_v	2981.0	Pa

Table 4.3: Fluid properties for NACA 0015 test case.

surface as well as the z -oriented front and back wall. The fluid is not boundary resolved at the surface of the hydrofoil in order to reduce computational effort. The Reynolds number of this problem is

$$\text{Re} = \frac{10.0 \frac{\text{m}}{\text{s}} \cdot 0.12 \text{ m} \cdot 997.0 \frac{\text{kg}}{\text{m}^3}}{0.091084 \text{ Pas}} = 13,135.$$

First tests with a no-slip boundary condition at the hydrofoil revealed oscillations as the velocity gradient at the surface could not be resolved with the coarse fluid mesh. To circumvent this problem, the boundary layer is ignored and a weakly imposed Dirichlet boundary condition in normal direction of the hydrofoil is applied, for details see Gamnitzer [68]. This boundary condition is used to surrogate a slip boundary condition along the curved hydrofoil surface. The fluid domain is discretized with a C-shaped mesh with one layer in z -direction and an overall number of 4888 tri-linearly interpolated hexahedral fluid elements. The minimal fluid element extension in normal direction to the hydrofoil is 0.144 cm. A time step size of $\Delta t_l = 5.0 \cdot 10^{-5}$ s is chosen such that the resulting CFL-number is approximately 0.5. The abort tolerance for the nonlinear iterations of the fluid is set to 10^{-6} in the L^2 -norm of the residual of the velocity/pressure as well as for the increment of the velocity/pressure.

Each bubble starts from a nucleus which contains non-condensable gas. This implies that nucleus and bubble can be interchanged in notation in this problem. Inflowing nuclei have a density of 1.12 kg/m³ which resembles air. The initial radius of the nuclei is normally distributed with a mean radius of 30 μm and a standard deviation of 5 μm. The initial radii are limited to 5 – 75 μm in order to stay in a realistic range. The number of inflowing nuclei is determined as follows. According to Brennen [19], the nuclei number density distribution function is up to $10^{13}/\text{m}^4$ in sea water. As the radius of these nuclei is approximately 10 – 40 μm, they cover a range of 30 μm and their number can be computed to

$$10^{13} \frac{1}{\text{m}^4} \cdot 30 \mu\text{m} = 3 \cdot 10^8 \frac{1}{\text{m}^3} = 300 \frac{1}{\text{cm}^3}.$$

In order to arrange the inflowing nuclei homogeneously, the inflow procedure is performed in every 4th fluid time step on a line holding 20 seed points for nuclei. The seed line is located upstream of the leading edge at $x = -2.5$ cm ranging $y \in [-2, 2]$ cm, see Figure 4.17. The resulting spacing in x - and y -direction of the nuclei is similar right after the inflow. To disturb this grid-like arrangement, a random offset of up to 50 % of the initial bubble radius is added to the initial position. The nuclei are only allowed to be placed and to move in the middle plane of the fluid domain in order to obtain a 2D problem. The fluid velocity and pressure at the seeding points are used to initialize the bubbles' initial velocity and the initial pressure according to (2.117). Bubbles far from the hydrofoil do not undergo significant radius changes and therefore bubbles are restricted to the domain $[-3, 24] \times [-4, 4]$ cm in x - and y -direction. Bubbles leaving this region are removed from the simulation. As the existence of bubbles is linked to the existence of a bin at the bubble position, it is possible to shrink the domain filled with bins to the aforementioned size which only covers a part of the fluid domain. Hence, the overall number of bins is reduced and efficiency is improved. However, this demands for a careful treatment in parallel computations due to the choice of the parallelization strategy, cf. Section 3.6. After the initial filling time, a constant number of roughly 2500 bubbles resides in the computational domain as the number of inflowing and outflowing bubbles is similar.

4.5.2 Start-up procedure of the cavitation framework

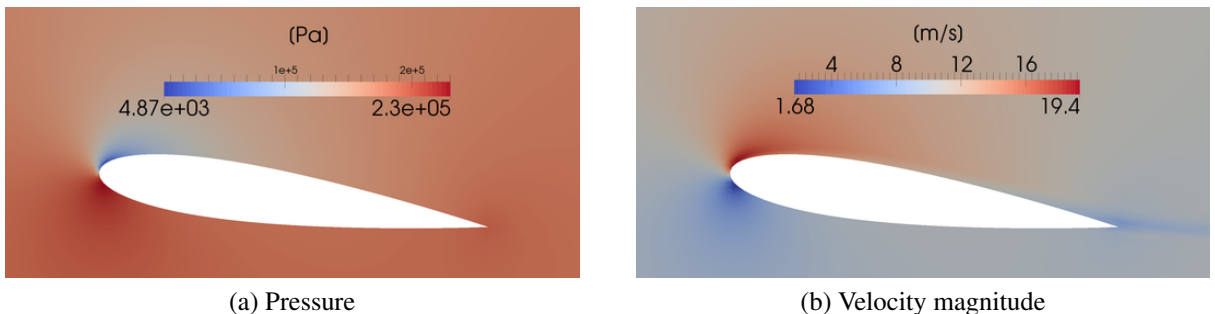


Figure 4.18: Steady state for the NACA 0015 test case without bubbles.

Before adding bubbles into the simulation, a steady state solution without bubbles is created. This is necessary because the initial ambient pressure p_{g0} for the nuclei is computed at their seeding position which does not yet provide useful values during the start-up phase of the fluid field. The steady state pressure and velocity magnitude distribution are displayed in Figure 4.18. The minimal pressure on the suction side of the hydrofoil is 4870 Pa which is larger than the vapor pressure. The fluid velocity is accelerated from the inflow velocity up to 19.4 m/s in the low pressure region. Due to the weak Dirichlet boundary condition in normal direction at the hydrofoil, no boundary layer develops and the flow does not separate.

After the steady state of the fluid flow is reached, bubbles are inserted using the seeding points described in the previous section. It turned out that the inflow of bubbles disturbs the pressure field of the fluid such that the solution diverged. The problem can be traced back to the time derivative $\partial \epsilon_l / \partial t$ in (2.112) which is a source term in the continuity equation. During

the initial filling time in which only bubbles enter the domain, the sum over all changes in fluid fraction over time is proportional to the number of bubbles entering the domain. Furthermore, the incompressible character of the governing equations is still present such that a source of bubbles in a small region is able to modify the pressure field in the whole domain. Hence, the initial filling of the domain with bubbles modifies artificially the pressure level via the continuity equation. In order to suppress this start-up phenomenon, a quasi-static assumption is made. The problematic time derivative term on the right-hand side of the continuity equation is disabled until a steady state is generated. Finally, a similar number of bubbles enters and leaves the domain such that the overall number of bubbles stays almost constant over time. Hence, the sum over all source contributions is mainly reduced to the volume change of the bubbles which depends on their radii. It is important to note that this influence is minor compared to the impact of many bubbles being inserted simultaneously at the seeding spots.

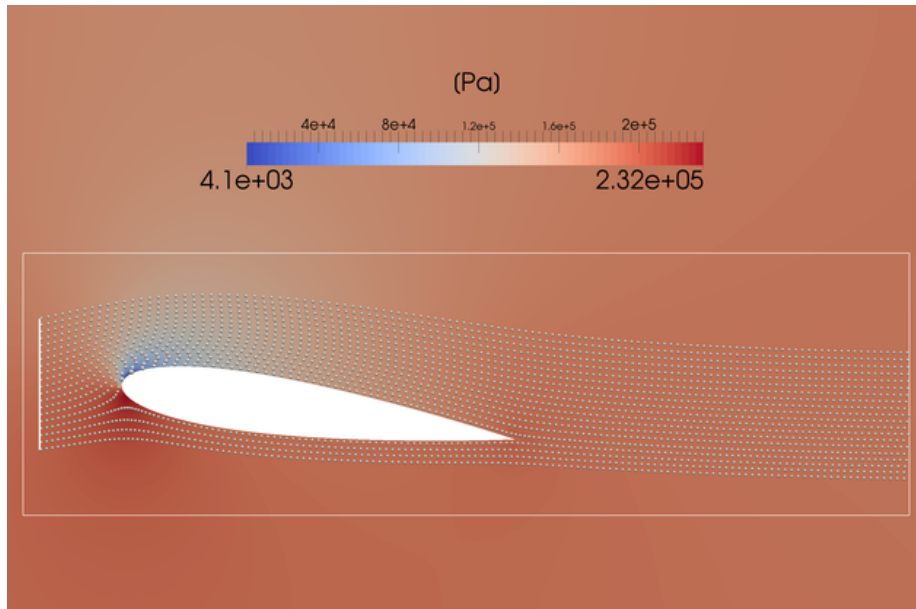


Figure 4.19: Steady state for NACA 0015 after start-up procedure (bubbles magnified 30 times).

A first analysis can already be done after the setup procedure led to the steady state solution as depicted in Figure 4.19. The line holding the seeding points is displayed upstream of the hydrofoil and the box to which the existence of bubbles is limited is added in the figure. Every bubble that crosses the boundary of the box downstream the hydrofoil is removed from the simulation. The minimal pressure in the flow field is slightly reduced to 4130 Pa due to the presence and interaction with the bubbles. When this steady state is reached, the strong coupling scheme needs two outer iterations to converge below $tol_p = tol_r = 10^{-5}$. The small number of iterations is owed to the neglected time derivative term in the right-hand side of the continuity equation. The behavior of a single bubble which passes closest to the suction side of the hydrofoil is depicted in Figure 4.20. The x -position of the bubble is used for the abscissa such that it is trivial to assess its relative position to the hydrofoil which spans $x \in [0, 12]$ cm. It takes the bubble 29 ms to travel from its seeding spot to the point where it is removed. The fluid pressure evaluated at the bubble position is included in the figure which is relevant for the evaluation of the radius governed by the Rayleigh-Plesset equation (2.113). Therein, the ambient pressure is

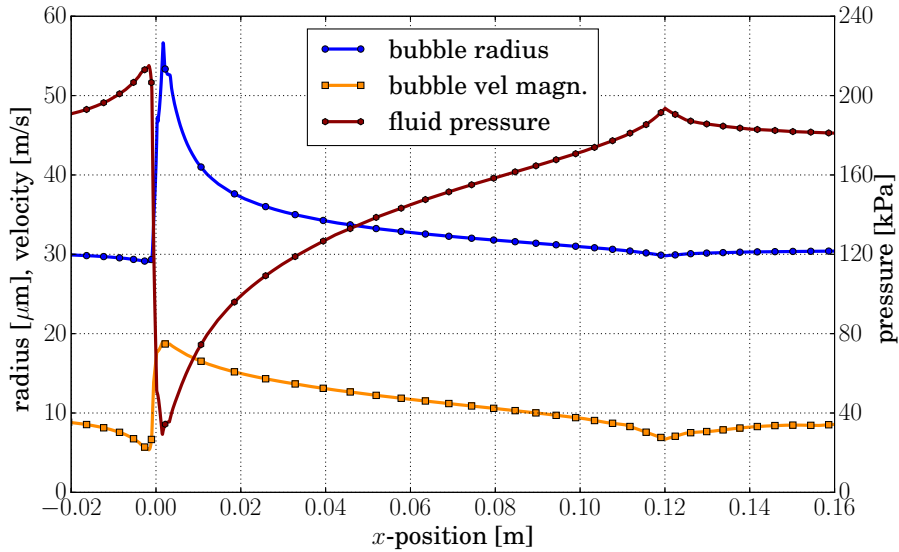


Figure 4.20: Single bubble after start-up procedure.

replaced with the fluid pressure at the bubble center. The minimal pressure that is felt by the bubble is 29.2 kPa which is approximately 10 times the vapor pressure. At the point of minimal fluid pressure, the radius of the bubble is largest. It almost doubles its size to a radius of 5.7 μm compared to its initial value. The bubble follows the fluid flow accurately and the maximal bubble velocity is 19.0 m/s which is close to the maximal fluid velocity.

Although the minimal pressure in the whole fluid domain is close to the vapor pressure, the minimal pressure felt by the bubble is larger as the bubble does not pass the hydrofoil directly at its surface where the minimal fluid pressure occurs. In order to make the test case more challenging for the developed framework, the fluid pressure is reduced leading to a larger variation of the bubble radius. There are two options to obtain a lower pressure level. Either an increase of the inflow velocity or a reduction of the pressure at the outflow leads to the desired pressure drop. The easier approach is to reduce the pressure level of the whole fluid field via reducing the outflow pressure p_{out} by 25 kPa. The solution is investigated after a steady state has emerged. Again, one of the bubbles which passes closest to the suction side of the hydrofoil is displayed in Figure 4.21. The fluid pressure along the trajectory is shifted down by approximately 25 kPa leading to a minimal fluid pressure of 3678 Pa felt by the bubble. This value is only 23 % above the vapor pressure. In the low pressure region, the bubble radius increases up to 102 μm which is more than three times its initial value. Due to the increased non-linearity of the problem, four outer iterations of the strong coupling scheme are necessary to converge to the same tolerances as before.

These preliminary investigations of single bubbles were performed while the time derivative term on the right-hand side of the continuity equation is disabled. Hence, the effect of bubble size changes on the fluid is reduced and thus the coupling of particle to fluid is weakened. In Figure 4.22, the minimal fluid pressure in the domain over time is displayed. Only the pressure value of the converged outer iteration is shown. The time scale covers three passes of bubbles from the seeding to their removal. The mean value is constant at 4120 Pa with a deviation of ± 105 Pa.

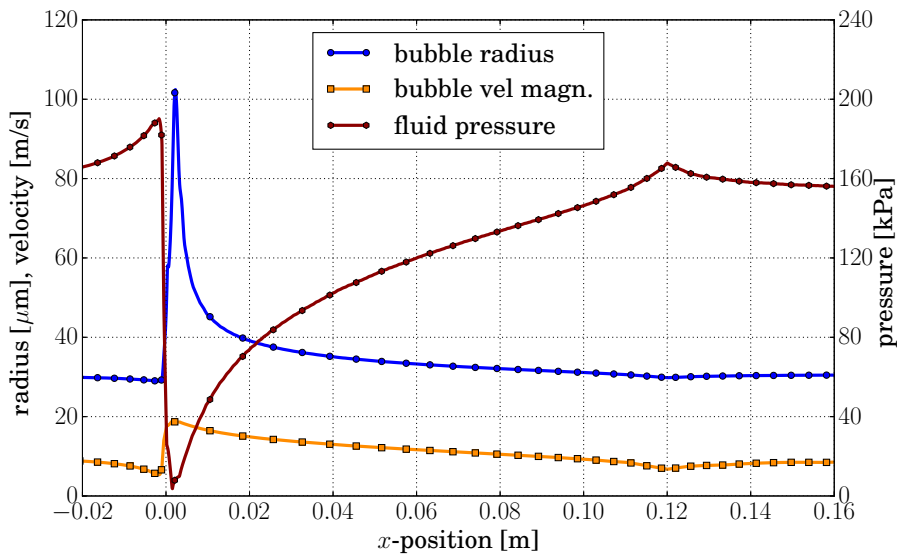


Figure 4.21: Single bubble after start-up procedure with reduced fluid pressure.

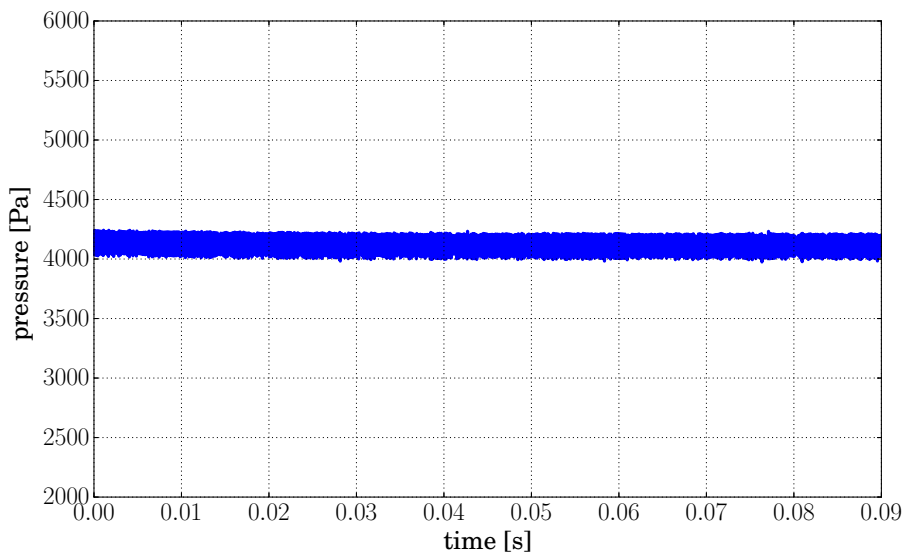


Figure 4.22: Minimal fluid pressure after start-up procedure.

4.5.3 First step towards cavitation

The steady state with the original pressure level as described in the previous section with a similar number of inflowing and outgoing bubbles is used as starting point for the investigation in this section. The quasi-static assumption is dropped and the disabled source term in the continuity equation is enabled now.

In Figure 4.23, the result for a single bubble is depicted which is on the trajectory closest to the hydrofoil. Small wiggles can be seen in the fluid pressure and bubble radius graphs. When

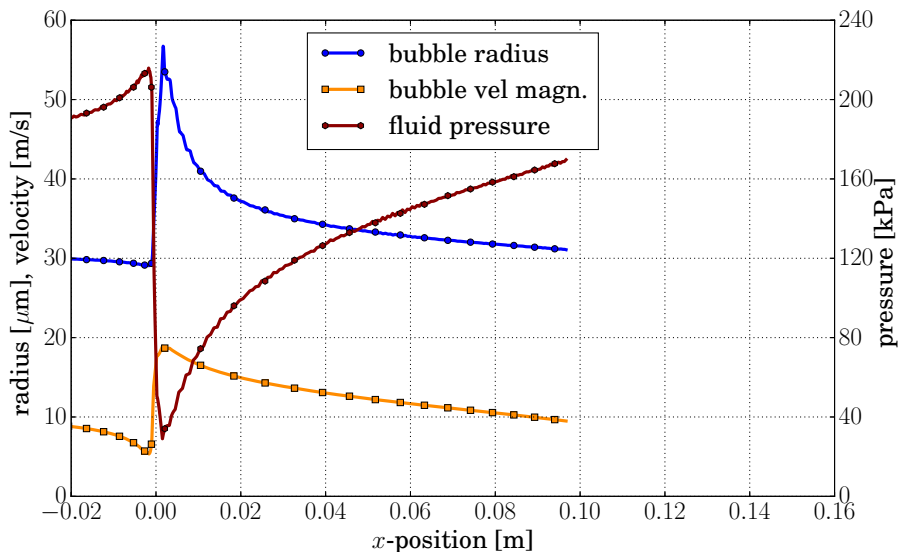


Figure 4.23: Single bubble in full cavitation framework.

ignoring the small wiggles, the evolution is almost identical to the case when the source term is neglected, see Figure 4.21. This implies that the full coupling of the bubbles to the fluid only disturbs the fluid while the overall behavior is similar. This may be attributed to the fact that only few small bubbles interact with the fluid.

The simulation does not go beyond 12 ms after which divergence of the outer iteration occurs. The relaxation parameter for the outer iterations as introduced in Section 3.2.2 tends to zero after a few iterations leading to a stagnated solution. A remedy with a minimal relaxation parameter $\omega_{\min} = 0.1$ did not improve the convergence behavior. No clear cause is available, which could explain the convergence problems.

A further indicator for the problematic behavior of the full cavitation framework is the minimal fluid pressure over time as illustrated in Figure 4.24. The mean value is slightly increased to 4350 Pa compared to Figure 4.22. However, deviations within a few time steps of ± 750 Pa are observed, which is more than seven times the amplitude compared to the case without the problematic source term in the continuity equation. The number of outer iterations ranges between 6 and 13 which is an enormous increase compared to the two iterations necessary when the source term is neglected. This again shows the impact of the time derivative of the fluid fraction on the right-hand side of the continuity equation which needs further investigation.

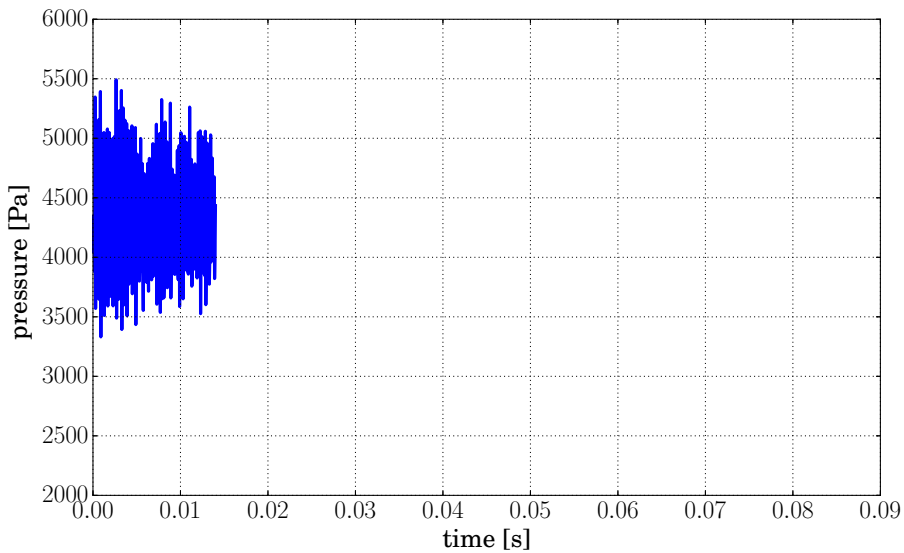


Figure 4.24: Minimal fluid pressure in full cavitation framework.

4.6 Droplets in the human lung

4.6.1 Setup and ventilation of a healthy lung

In an earlier work at the Institute for Computational Mechanics of the Technische Universität München, the time-dependent transport of nanoparticles ranging from 1.5 to 11 nm in a human lung was investigated using an Euler-Euler approach, see Comerford et al. [29]. For a large amount of small particles, the assumption of a continuum is valid. However, when considering larger particles, such as droplets in aerosols which are used for medication, it is favorable to monitor each single particle including its interaction with the airway walls. A possible question might be, in which area of the lung the aerosol is absorbed and how a certain aerosol dose has to be applied in order to achieve a certain distribution in the lung. The developed framework with its Euler-Lagrange approach is able to investigate the flow of particles with a diameter ranging from 8.0 to 19.0 μm in the time-dependent fluid flow. This particle size corresponds to the size of therapeutic aerosols. The geometry of the lung is extracted from CT images of a patient in order to obtain a realistic fluid domain with its full complexity. The modeling approach has been derived by Yoshihara et al. [234] and details on the model are given by Verdugo et al. [221]. The branches up to the eighth generation of the bronchial tree are considered in the following setup. A parabolic inflow profile is applied and the inflow rate is prescribed as given in Figure 4.25. The inhalation phase takes 1300 ms until the exhalation phase starts. This procedure is very close to ventilation of patients in hospitals in the intensive care. The upper part, the glottis, is included in the fluid domain in order to generate a realistic inflow profile in the lower region when the two main branches start. As usual in literature, a zero-traction Neumann boundary condition is applied at the 61 outlets of the fluid domain. This neglects the resistance further downstream. However, in the next section it will be shown that this assumption needs to be investigated carefully. In order to introduce particles in the lung, an inflow region in the upper part of the glottis close to the fluid inflow is defined in which $72 = 12 \cdot 6$ particles are placed on

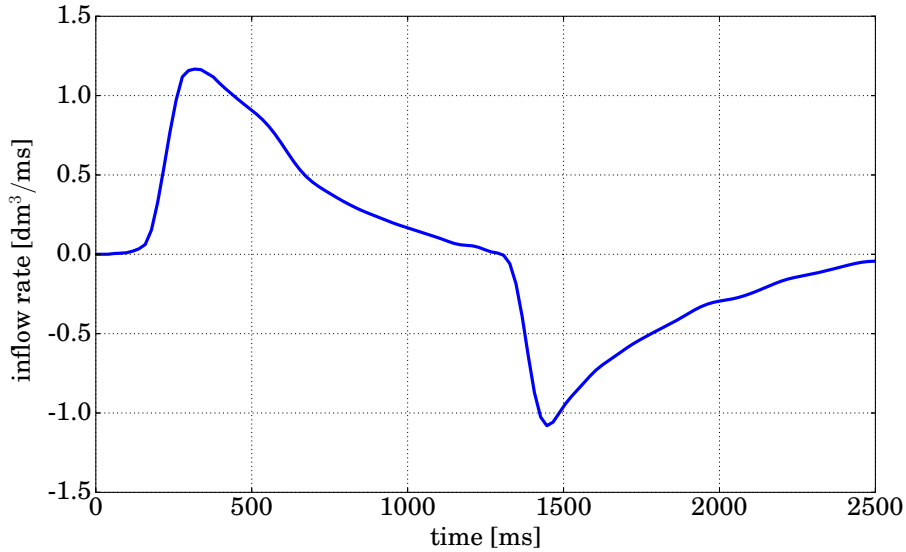
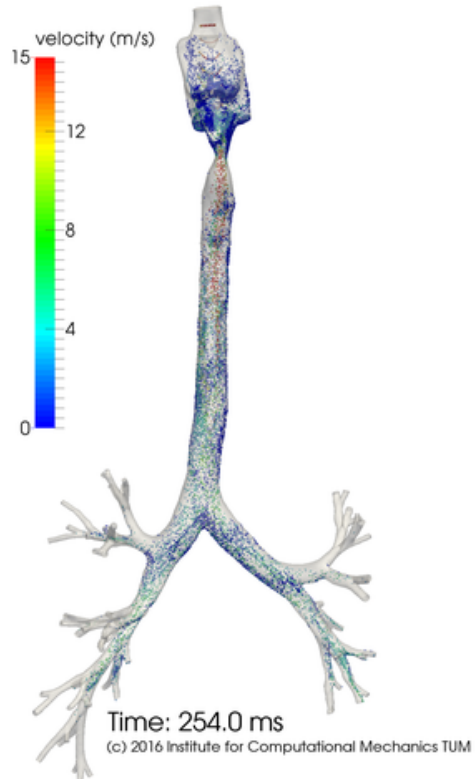
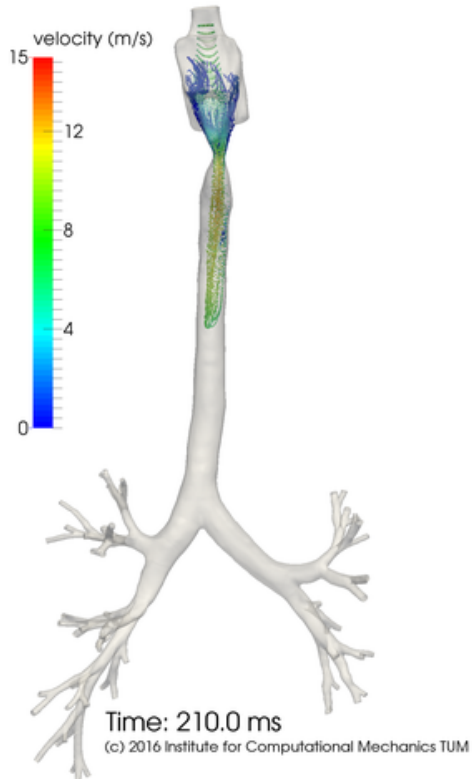
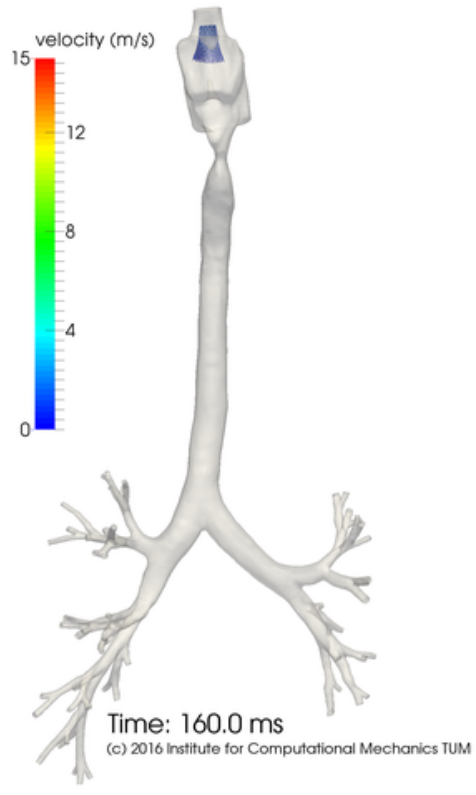
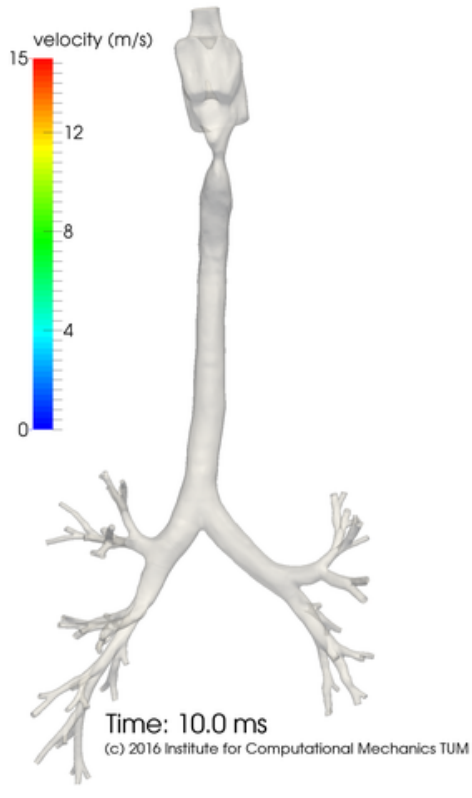


Figure 4.25: Inflow rate into lung

a rectangular grid every 0.5 ms and initialized with the underlying fluid velocity. Particle inflow starts at $t = 100$ ms when noticeable fluid velocity prevails in order to avoid initial placing of particles in contact and it stops at $t = 1280$ ms right before the exhalation phase starts. Finally, approximately 170,000 particles have entered the human lung. As inter-particle and particle-wall contact is considered, a coefficient of restitution $e = 0.8$ is used and the relative penetration is set to $c = 0.05$. The patient-specific lung geometry is discretized with 2,307,139 linear tetrahedral elements and a time step size of $\Delta t_l = 0.5$ ms is applied. Subcycling of 1 : 50 between fluid and particles is used such that the particle time step size is $\Delta t_b = 0.01$ ms. The simulation is carried out on 48 processors. A special treatment for the binning strategy is necessary due to the large number of bins which is not covered with fluid elements. All those bins are removed to decrease their number as they cannot be filled with particles anyway due to the airway walls which bound the particle motion. As the size of the particles is small, the right-hand side contributions to the continuity equation (2.112) are neglected such that the computation of the dispersed phase fraction can be omitted.

The temporal evolution of the particle distribution is illustrated in Figure 4.26. The particles are colored according to their velocity magnitude. During the steep inflow velocity ramp in $150 \text{ ms} \leq t \leq 300 \text{ ms}$, the flow is accelerated up to approximately 37 m/s in the narrowest cross section such that a fluid jet emerges. Initially, the particles are entrained in the jet and pass the constriction quickly. Later, due to the continuous inflow, a recirculation zone forms in the glottis where the particles are mixed before they enter the constriction. After 250 ms, the first particles reach the outflow boundaries of the fluid domain where they leave the domain using the assumption that they are fully absorbed in the outlets. During the exhalation phase, particles leave the lung through the glottis. Few particles are trapped in the boundary layer of the fluid flow in regions of low velocity such that they do not leave the lung within this exhalation phase. In reality, these particles are absorbed by the airway walls. It can be concluded that the developed framework is able to cope with extraordinary complex fluid domains while still keeping track of the particles and their interactions.



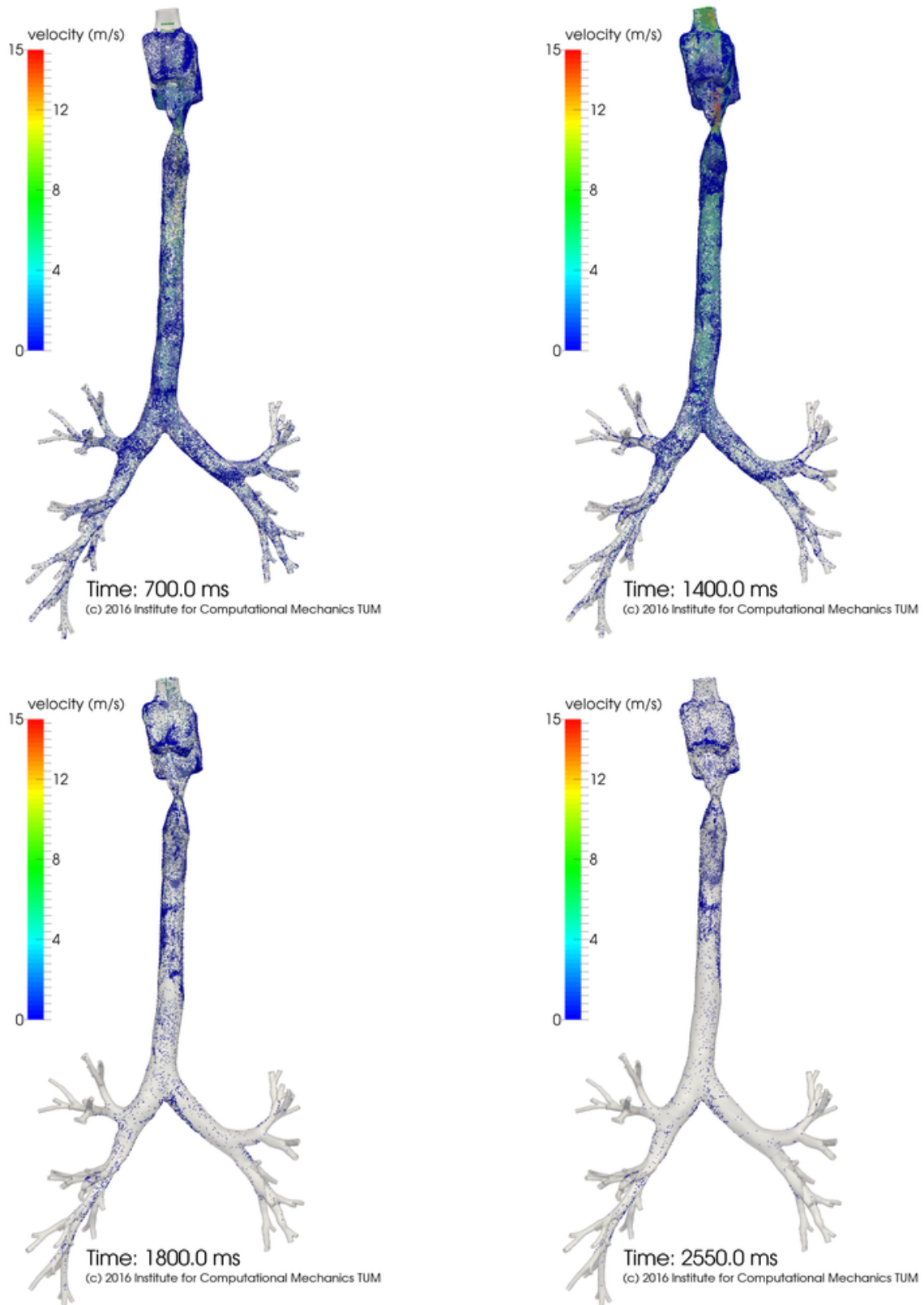


Figure 4.26: Particle distribution during a full breathing cycle.

4.6.2 Pathological lung

The lung considered so far has zero-traction Neumann boundary conditions at its outflows. Hence, all outlets exhibit a similar resistance and the area of the outlet is decisive for the number of particles which enter the subsequent branches of the lung. In contrast, a pathological lung behaves stiffer in injured parts. In Roth [177], a methodology is presented which allows to account for stiffer regions in parts of the lung. Using this approach, a correlation is deduced for each outlet which is used to compute the pressure value at the outlet based on the flow rate and the fluid volume in the subsequent branches of the lung. Eventually, it is possible to model a partly injured lung and to obtain the resulting distribution of particles in the respective parts of the lung. In Figure 4.27, a zoom on the left main branch of the lung is displayed with the healthy lung on

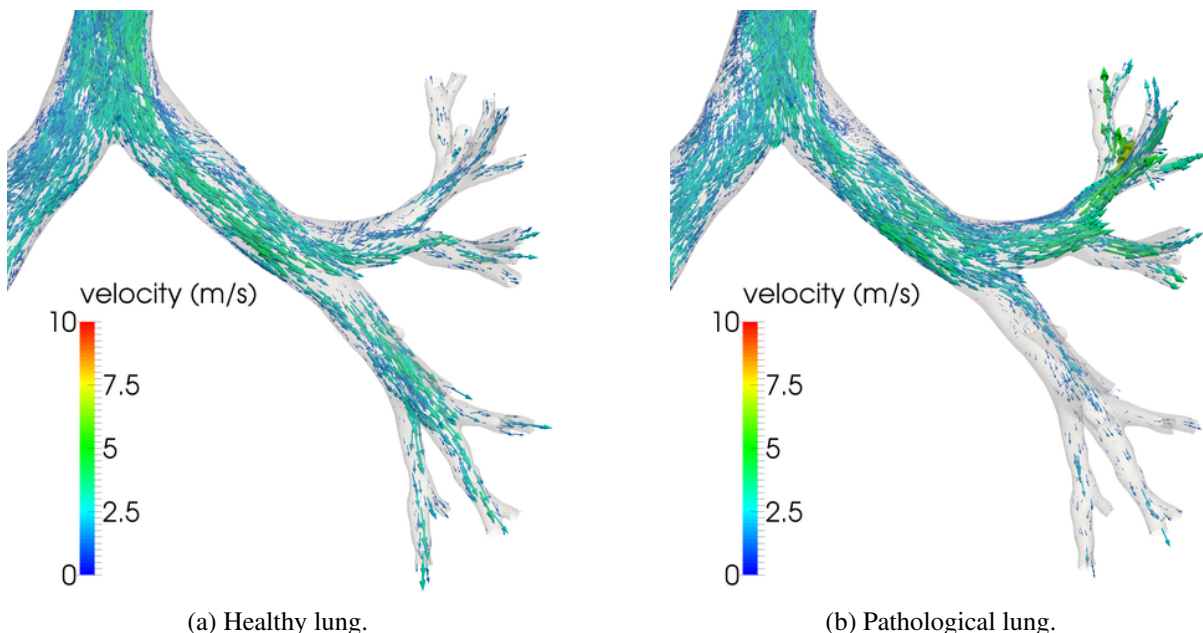


Figure 4.27: Particle flow comparison.

the left-hand side and the injured lung on the right-hand side. The particles are illustrated as arrows with size and color related to their velocity magnitude. The bottom branches of the injured lung are loaded with a higher pressure value because a model with a five times higher stiffness of the tissue is attached to these outlets, see Roth [177]. The number of particles entering the bottom branches is reduced in the pathological lung whereas the number of particles entering the upper branch is largely increased. The remaining particles which still enter the injured branches propagate at a reduced velocity. These results are expected as the fluid flow rate into the injured branches is reduced due to the increased resistance for the fluid flow.

5 Conclusion

5.1 Summary

A multipurpose Euler-Lagrange framework has been developed which aims at simulating a vast number of different dispersed flow problems. Due to the versatile framework, also the limit case of vanishing influence of the fluid on the dispersed phase can be investigated leading to a pure particle solver. The fluid field is always assumed to be continuous and described in an Eulerian frame. In contrast, the dispersed phase is an ensemble of interacting particles which are tracked in a Lagrangian frame. The dispersions interpenetrate the continuous phase.

The theory of volume averaging is applied to the fluid flow around the dispersions leading to the volume-averaged Navier-Stokes equations. They have been solved numerically by a residual-based variational multiscale finite element method. The coupling from the fluid to the particles includes the drag, lift, added mass, pressure and viscous force. Besides the interaction of particle and fluid, inter-particle interaction is also accounted for. The particles can collide using a soft sphere contact model used in discrete element methods. Also, particle-wall contact is included such that bounded problem setups can be investigated. In order to circumvent the differences of gas, liquid, and solid particles when it comes to collisions, the assumption of an immobilized surface of liquid bubbles and gas bubbles in liquid is applied. This is justified because in every real world application small contaminants are ubiquitous in liquids leading to this “freezed” bubble surface. Hence, bubbles behave like solid dispersions. Of course, the special case of clean water (without contaminants) on laboratory test rigs cannot be modeled with the aforementioned assumptions. In order to account for radius changes of the dispersions in bubbly flows, the Rayleigh-Plesset equation can additionally be solved for each particle. This ordinary differential equation governs the radius evolution of the bubble driven by the ambient fluid pressure.

The computational framework to incorporate all the aforementioned features is equipped with a loosely coupled and a strongly coupled solution procedure. Aitken’s Δ^2 method is applied to accelerate convergence of the strongly coupled algorithm. Subcycling is performed between the fields to efficiently consider the relevant time scales. The largest time scale exhibits the fluid, followed by the particle-collision dominated time scales which are usually a factor of $100 \dots 1000$ smaller. The smallest time scales occur in the radius changes of the bubbles which can be several orders of magnitude smaller than the relevant time scales for collisions. The latter is accounted for by an adaptive time stepping procedure to obtain quickly an accurate solution. In contrast, time stepping for the fluid and the particle evolution is performed using constant time step sizes. Linear interpolation of coarse field quantities is applied to obtain the coupling states for the finer time scales. In order to enable large time step sizes for the fluid, the generalized- α time integration scheme is used which is of implicit nature. The particles are time integrated using the explicit central difference time integration scheme.

Special attention is given to the computation of the fluid fraction in the continuous phase. The fluid fraction in the volume averaged Navier-Stokes equations accounts for the displaced volume of the dispersed phase in the fluid domain although the dispersions are treated point-like. A polynomial filtering function is applied at each particle position to project the dispersion's volume onto the fluid. The involved volume integrals over the fluid element comprise the filtering function in the integrand. In order to enable an analytical integration on the unstructured fluid grids, the volume integral is transformed into line integrals by applying divergence theorem twice. A zeroth, a second, and a fourth order polynomial filtering function is investigated.

As the different time scales and potentially large numbers of particles and fluid elements may lead to a high computational effort, an efficient parallelization strategy is crucial. The particles can float around and dynamic reassigning to the processors is applied. When fluid-particle coupling is considered, additionally the fluid domain is distributed among the processors. The fluid is distributed once in the beginning using graph-partitioning leading to an optimal partitioning. The particles are assigned to the processor which owns its underlying fluid element. Hence, the fluid-particle interaction can be evaluated locally without the need for inter-processor communication. An additional layer of ghost or halo particles and fluid elements is necessary at the processor boundaries. The advantage of the chosen parallelization strategy is that no data needs to be provided fully redundant. However, clustering of particles in the fluid-particle coupled case reduces parallel efficiency.

The developed framework is able to perform pure particle simulations, fluid-particle coupled simulations using either the weak or the strong coupling scheme, and finally the fully coupled framework which includes the Rayleigh-Plesset equation to account for particle size changes. The developed framework is investigated using six different test cases which are summarized in the following. A rather small pure particle example is the outflow of 9 k particles through an orifice. This test case is used to verify the implementation of the normal and tangential soft sphere contact model which delivers results that are 20 – 30 % off the findings in literature. The second test case is used to investigate the parallel performance of the developed particle framework. Therefore, the mixing of 571 k particles driven by two paddles is computed. A parallel efficiency of 66 % could be achieved in a strong scaling study using up to 120 processors. Furthermore, the parts in the framework which scale badly are identified to pave the way for improvements.

Next, the fluid-particle framework is investigated using a Taylor-Green vortex test case. The fluid field starts from an initial velocity which describes counter-rotating vortices. 461 k particles are distributed homogeneously within the fluid domain and they are initialized with the underlying fluid velocity. The setup is fully periodic in all three space dimensions. Due to the density ratio of $1/1000$ between particles and fluid, the particles propagate to the center of the vortices. A nearly-linear relationship between the decreasing vorticity and the increasing particle concentration in the vortex center is reported in literature which the developed framework also exhibits. In the Taylor-Green vortex example, particle collisions are neglected in order to enable comparison with literature.

In contrast, in the next test case, a fluidized bed is investigated which includes particle-particle and particle-wall interaction in addition to the fluid-particle coupling. A fluid jet enters from the bottom of the container and the particles are swirled up. The particle to fluid density ratio covers $2505/1$ to $751.5/1$. Due to the density ratio $\gg 1$, the added mass force can be neglected and the weakly coupled approach is applied. Several different regimes are reported in literature of

which four are reproduced with the developed framework. Namely, the fixed bed regime which subsequently is used as starting point for the internal cavity regime, the slugging bed regime, and the jet in fluidized bed regime. Due to the fact, that the chosen drag law is inappropriate, it was necessary to reduce the particle density to obtain the different regimes. Nevertheless, the developed framework is able to reproduce all these regimes.

In the previous setups, the particles feature a constant radius. In contrast, the NACA 0015 test case investigates bubbles with a variable radius. Bubbles are released upstream of the hydrofoil and they undergo size adaption driven by the ambient fluid conditions. On the suction side of the hydrofoil, the bubbles grow up to three times of their initial size whereas they stay almost constant away from the hydrofoil. The strong coupling scheme with Aitken relaxation was necessary to achieve convergence.

The last example is chosen to show that the developed framework can cope with large and complex 3D fluid geometries. The human lung was segmented from patient specific data up to the eighth generation of the bronchial tree. Particles are inserted close to the fluid inflow in the glottis from where they flood into the lung. Due to the small size of the particles, the fluid fraction is omitted in this test case and the weak coupling approach is sufficient. Nevertheless, the contact was evaluated such that the particles could not cross the lung walls.

In summary, a very versatile numerical tool has been developed to investigate Euler-Lagrange settings with a continuous phase that is interpenetrated with a disperse phase each accounted for in its respective frame.

5.2 Outlook

Several issues need to be addressed for future work with the developed framework. A closer look at the drag law applied for the particles is necessary in order to account for the fluid fraction. This is of major importance for dense packings as they occur, e.g. in the fluidized bed application. Several correlations are proposed in literature, cf. Kafui et al. [111], Deen et al. [41], or Lau et al. [130], which may be tested and validated against experimental results. Another crucial issue to be solved are the pressure oscillations within the whole fluid domain induced by bubble size variations as presented with the NACA 0015 test case in Section 4.5.3. Already small changes in bubble size lead to pressure oscillations which are detrimental for detailed analysis using the Rayleigh-Plesset equation. A remedy might be the use of an artificial compressibility approach, see Tamura et al. [202] or Hsiao et al. [96], which weakens the incompressible character of the governing equations.

An Euler-Lagrange framework is limited by an upper ratio of dispersion size to fluid element size, cf. Peng et al. [164]. Hence, an interesting approach might be the combination of the developed disperse fluid-particle framework with, e.g. a level set approach (see Hsiao et al. [96]) or a volume-of-fluid approach (see Vallier [214]) to consider coalescence of the dispersed phase to form larger structures. Therein, the transition will demand for a proper analysis.

Regarding the computational framework, the scaling problems identified while setting up the ghosting need to be addressed. This problem is owed to the fact that the implementation of the developed framework was realized within a finite element solver designed for unstructured grids. The original software tool is optimized for problems including elements and nodes with a static

connectivity throughout the simulation. The particle solver can be improved by exploiting the Cartesian grid aligned bins which are used for the neighborhood search of the dispersions.

While doing so, the load balancing issue for pure particles need to be further investigated. Load balancing based on the number of particles in each bin is implemented but it turned out that the dynamically load balanced simulations took more wall time than without load balancing. This could be traced back to the increased ghosting which was introduced by the additional load balancing steps. Within this work, the parameters could not be tuned such that the savings induced by repeated load balancing dominates the extra cost induced by a disadvantageous large ghosting. The load balancing aspect for fluid-particle coupled problems also needs further investigation. In applications with large subcycling, the cost of particle evaluation usually dominates the overall cost such that it could be beneficial regarding overall simulation time to abandon the optimally distributed fluid domain and focus on a good distribution of the particles while accepting the fluid partitions to be unbalanced.

Another aspect which gives space for improvement is the particle time integration. Using small particles at high velocities lead to a strong limitation in time step size. Implicit time integration for the particles with the respective contact formulations might be beneficial although the risks should not be underestimated. Convergence problems of the discontinuous phenomenon contact are likely to occur and furthermore contact events should not be missed such that efficient searching strategies are necessary to detect such events with the need to correct them appropriately within the Newton iterations. In case, implicit time integration for the particles is available, the next step can be a monolithic framework comprising both, fluid and particles. The monolithic approach might be able to overcome stability issues which cannot be cured by the strong coupling scheme.

So far, the fluid domain is assumed to be fixed in space. An interesting approach is to allow for a moving fluid domain described in an arbitrary Lagrangian Eulerian frame, maybe in a fluid-structure interaction environment. Hence, deformable structures which interact with particles can be investigated. This would be very interesting for the application of cavitation in which the damage of collapsing bubbles is investigated, see Van Terwisga et al. [218] or Dular et al. [53].

Bibliography

- [1] ANSYS CFX, 14.5, *Ansys Reference Manual*, 2013.
- [2] B. J. Alder and T. E. Wainwright, Phase transition for a hard sphere system, *American Institute of Physics* **27**, 1957.
- [3] H. Alehossein and Z. Qin, Numerical analysis of Rayleigh–Plesset equation for cavitating water jets, *International Journal for Numerical Methods in Engineering* **72**, 780–807, 2007.
- [4] M. P. Allen and D. J. Tildesley, *Computer simulation of liquids*, Oxford University Press, New York, 1991.
- [5] T. B. Anderson and R. Jackson, A fluid mechanical description of fluidized beds, *Industrial & Engineering Chemistry Fundamentals* **6**, 527–539, 1967.
- [6] T. Arens, F. Hettlich, C. Karpfinger, U. Kockelkorn, K. Lichtenegger, and H. Stachel, *Mathematik*, Springer-Verlag, 2015.
- [7] M. Astorino, J.-F. Gerbeau, O. Pantz, and K.-F. Traoré, Fluid–structure interaction and multi-body contact: Application to aortic valves, *Computer Methods in Applied Mechanics and Engineering* **198**, 3603–3612, 2009.
- [8] T. R. Auton, The lift force on a spherical body in a rotational flow, *Journal of Fluid Mechanics* **183**, 199–218, 1987.
- [9] B. Avci and P. Wriggers, A DEM-FEM Coupling Approach for the Direct Numerical Simulation of 3D Particulate Flows, *Journal of Applied Mechanics* **79**, 10901, 2012.
- [10] P. C. Babu Salapakkam, *A computational investigation of three turbulent flow problems*, PhD thesis, University of Minnesota, 2007.
- [11] G. K. Batchelor, *An introduction to fluid dynamics*, Cambridge University Press, Cambridge, 1967.
- [12] Y. Bazilevs, V. M. Calo, J. A. Cottrell, T. J. R. Hughes, A. Reali, and G. Scovazzi, Variational multiscale residual-based turbulence modeling for large eddy simulation of incompressible flows, *Computer Methods in Applied Mechanics and Engineering* **197**, 173–201, 2007.
- [13] T. Belytschko, Y. Y. Lu, and L. Gu, Element-free Galerkin Methods, *International Journal for Numerical Methods in Engineering* **37**, 229–256, 1994.

Bibliography

- [14] F. Bertrand, L.-A. Leclaire, and G. Levecque, DEM-based models for the mixing of granular materials, *Chemical Engineering Science* **60**, 2517–2531, 2005.
- [15] W. A. Beverloo, H. A. Leniger, and J. van de Velde, The flow of granular solids through orifices, *Chemical Engineering Science* **15**, 260–269, 1961.
- [16] P. Bochev and R. B. Lehoucq, On the Finite Element solution of the pure Neumann problem, *SIAM Review* **47**, 50–66, 2005.
- [17] P. Bogacki and L. F. Shampine, A 3(2) Pair of Runge-Kutta formulas, *Applied Mathematics Letters* **2**, 321–325, 1989.
- [18] C. M. Boyce, D. J. Holland, S. A. Scott, and J. S. Dennis, Novel fluid grid and voidage calculation techniques for a discrete element model of a 3D cylindrical fluidized bed, *Computers and Chemical Engineering* **65**, 18–27, 2014.
- [19] C. E. Brennen, *Cavitation and bubble dynamics*, Oxford University Press, 1995.
- [20] C. E. Brennen, *Fundamentals of multiphase flows*, Cambridge University Press, 2005.
- [21] M. Breuer, H. T. Baytekin, and E. A. Matida, Prediction of aerosol deposition in 90 degree bends using LES and an efficient Lagrangian tracking method, *Aerosol Science* **37**, 1407–1428, 2006.
- [22] F. Brezzi and M. Fortin, *Mixed and hybrid finite element methods*, Springer, New York, 1991.
- [23] A. N. Brooks and T. J. R. Hughes, Streamline Upwind/Petrov–Galerkin formulations for convection dominated flows with particular emphasis on the incompressible Navier–Stokes equations, *Computer Methods in Applied Mechanics and Engineering* **32**, 199–259, 1982.
- [24] K. A. Buist, L. J. H. Seelen, N. G. Deen, J. T. Padding, and J. A. M. Kuipers, On an efficient hybrid soft and hard sphere collision integration scheme for DEM, *Chemical Engineering Science* **153**, 363–373, 2016.
- [25] B. T. Chao, W. T. Sha, and S. L. Soo, On inertial coupling in dynamic equations of components in a mixture, *International Journal of Multiphase Flow* **4**, 219–223, 1978.
- [26] S. Chen and G. D. Doolen, Lattice Boltzmann Method for Fluid Flows, *Annual Review of Fluid Mechanics* **30**, 329–364, 1998.
- [27] J. Chung and G. M. Hulbert, A time integration algorithm for structural dynamics with improved numerical dissipation: The Generalized- α method, *Journal of Applied Mechanics* **60**, 371, 1993.
- [28] R. Clift, J. R. Grace, and M. E. Weber, *Bubbles, drops and particles*, Academic Press, Inc, 1978.

- [29] A. Comerford, G. Bauer, and W. A. Wall, Nanoparticle transport in a realistic model of the tracheobronchial region, *International Journal for Numerical Methods in Biomedical Engineering* **26**, 904–914, 2010.
- [30] A. Corsini, F. Rispoli, A. G. Sheard, K. Takizawa, T. E. Tezduyar, and P. Venturini, A variational multiscale method for particle-cloud tracking in turbomachinery flows, *Computational Mechanics* **54**, 1191–1202, 2014.
- [31] G.-H. Cottet and P. D. Koumoutsakos, *Vortex Methods: Theory and Practice*, Cambridge University Press, Cambridge, 2000.
- [32] C. T. Crowe, D. E. Stock, and M. P. Sharma, The Particle-Source-In cell (PSI-CELL) Model for Gas-Droplet Flows, *Journal of Fluids Engineering* **99**, 325–332, 1977.
- [33] C. T. Crowe, J. D. Schwarzkopf, M. Sommerfeld, and Y. Tsuji, *Multiphase flows with droplets and particles*, CRC Press, 2012.
- [34] P. A. Cundall and O. D. L. Strack, A discrete numerical model for granular assemblies, *Géotechnique* **29**, 47–65, 1979.
- [35] D. Darmana, N. G. Deen, and J. A. M. Kuipers, Detailed modeling of hydrodynamics, mass transfer and chemical reactions in a bubble column using a discrete bubble model, *Chemical Engineering Science* **60**, 3383–3404, 2005.
- [36] D. Darmana, N. G. Deen, and J. A. M. Kuipers, Parallelization of an Euler-Lagrange model using mixed domain decomposition and a mirror domain technique: Application to dispersed gas-liquid two-phase flow, *Journal of Computational Physics* **220**, 216–248, 2006.
- [37] G. Dasgupta, Integration within Polygonal Finite Elements, *Journal of Aerospace Engineering* **16**, 9–18, 2003.
- [38] T. De Mulder, The role of bulk viscosity in stabilized finite element formulations for incompressible flow: A review, *Computer Methods in Applied Mechanics and Engineering* **163**, 1–10, 1998.
- [39] S. Decker, *Zur Berechnung von gerührten Suspensionen mit dem Euler-Lagrange-Verfahren*, PhD thesis, Martin-Luther-Universität Halle-Wittenberg, 2005.
- [40] N. G. Deen, M. van Sint Annaland, and J. A. M. Kuipers, Multi-scale modeling of dispersed gas–liquid two-phase flow, *Chemical Engineering Science* **59**, 1853–1861, 2004.
- [41] N. G. Deen, M. Van Sint Annaland, M. A. Van Der Hoef, and J. A. M. Kuipers, Review of discrete particle modeling of fluidized beds, *Chemical Engineering Science* **62**, 28–44, 2007.
- [42] E. Delnöij, F. A. Lammers, J. A. M. Kuipers, and W. P. M. van Swaaij, Dynamic simulation of dispersed gas–liquid two-phase flow using a discrete bubble model, *Chemical Engineering Science* **52**, 1429–1458, 1997.

Bibliography

- [43] J. J. Derkens, Numerical Simulation of Solids Suspension in a Stirred Tank, *American Institute of Chemical Engineers Journal* **49**, 2700–2714, 2003.
- [44] M. T. Dhotre, N. G. Deen, B. Niceno, Z. Khan, and J. B. Joshi, Large Eddy Simulation for Dispersed Bubbly Flows: A Review, *International Journal of Chemical Engineering* **2013**, 343276, 2013.
- [45] F. P. Di Maio and A. Di Renzo, Linear and Non-linear Approach, *Chemical Engineering Research and Design* **83**, 1287–1297, 2005.
- [46] A. Di Renzo and F. P. Di Maio, Comparison of contact-force models for the simulation of collisions in DEM-based granular flow codes, *Chemical Engineering Science* **59**, 525–541, 2004.
- [47] A. Di Renzo and F. P. Di Maio, Homogeneous and bubbling fluidization regimes in DEM-CFD simulations: Hydrodynamic stability of gas and liquid fluidized beds, *Chemical Engineering Science* **62**, 116–130, 2007.
- [48] W. Dijkhuizen, I. Roghair, M. Van Sint Annaland, and J. A. M. Kuipers, DNS of gas bubbles behaviour using an improved 3D front tracking model—Drag force on isolated bubbles and comparison with experiments, *Chemical Engineering Science* **65**, 1415–1426, 2010.
- [49] J. Donea and A. Huerta, *Finite element methods for flow problems*, Wiley, 2003.
- [50] O. A. Druzhinin and S. Elghobashi, Direct numerical simulations of bubble- laden turbulent flows using the two-fluid formulation, *Physics of Fluids* **10**, 685–697, 1998.
- [51] C. Duchanoy and T. R. G. Jongen, Efficient simulation of liquid–solid flows with high solids fraction in complex geometries, *Computers & Fluids* **32**, 1453–1471, 2003.
- [52] J. K. Dukowicz, A Particle-Fluid Numerical Model for Liquid Sprays, *Journal of Computational Physics* **35**, 229–253, 1980.
- [53] M. Dular, B. Stoffel, and B. Širok, Development of a cavitation erosion model, *Wear* **261**, 642–655, 2006.
- [54] F. Durst, D. Milojevic, and B. Schönung, Eulerian and Lagrangian predictions of particulate two-phase flows: a numerical study, *Applied Mathematical Modelling* **8**, 101–115, 1984.
- [55] S. Elghobashi, On predicting particle-laden turbulent flows, *Applied Scientific Research* **52**, 309–329, 1994.
- [56] N. Epstein and J. R. Grace (eds.), *Spouted and spout-fluid beds: Fundamentals and applications*, Cambridge University Press, 2011.
- [57] S. Ergun, Fluid flow through packed columns, *Chemical Engineering Progress* **48**, 89–94, 1952.

- [58] E. A. Fadlun, R. Verzicco, P. Orlandi, and J. Mohd-Yusof, Combined Immersed-Boundary Finite-Difference Methods for Three-Dimensional Complex Flow Simulations, *Journal of Computational Physics* **161**, 35–60, 2000.
- [59] C. Farhat, M. Lesoinne, and P. Le Tallec, Load and motion transfer algorithms for fluid/structure interaction problems with non-matching discrete interfaces: Momentum and energy conservation, optimal discretization and application to aeroelasticity, *Computer Methods in Applied Mechanics and Engineering* **157**, 95–114, 1998.
- [60] Y. Feng and C. Kleinstreuer, Micron-particle transport, interactions and deposition in triple lung-airway bifurcations using a novel modeling approach, *Journal of Aerosol Science* **71**, 1–15, 2014.
- [61] A. Ferrante and S. Elghobashi, Reynolds number effect on drag reduction in a microbubble-laden spatially developing turbulent boundary layer, *Journal of Fluid Mechanics* **543**, 93–106, 2005.
- [62] A. Ferrante and S. E. Elghobashi, On the effects of microbubbles on Taylor–Green vortex flow, *Journal of Fluid Mechanics* **572**, 145–177, 2007.
- [63] J. Finn, E. Shams, and S. V. Apte, Modeling and simulation of multiple bubble entrainment and interactions with two dimensional vortical flows, *Physics of Fluids* **23**, 23301, 2011.
- [64] F. Fleissner and P. Eberhard, Parallel load-balanced simulation for short-range interaction particle methods with hierarchical particle grouping based on orthogonal recursive bisection, *International Journal for Numerical Methods in Engineering* **74**, 531–553, 2008.
- [65] B. Freireich, M. Kodam, and C. Wassgren, An exact method for determining local solid fractions in Discrete Element Method simulations, *American Institute of Chemical Engineers Journal* **56**, 3036–3048, 2010.
- [66] D. Fuster and T. Colonius, Modelling bubble clusters in compressible liquids, *Journal of Fluid Mechanics* **688**, 352–389, 2011.
- [67] D. Fuster, G. Agbaglah, C. Josserand, S. Popinet, and S. Zaleski, Numerical simulation of droplets, bubbles and waves: state of the art, *Fluid Dynamics Research* **41**, 65001, 2009.
- [68] P. Gamnitzer, *Residual-based variational multiscale methods for turbulent flows and fluid-structure interaction*, PhD thesis, Technische Universität München, 2010.
- [69] E. Giannadakis, D. Papoulias, M. Gavaises, C. Arcoumanis, C. Soteriou, and W. Tang, Evaluation of the Predictive Capability of Diesel Nozzle Cavitation Models, *SAE Technical Paper Series*, 245–2007, 2007.
- [70] E. Giannadakis, M. Gavaises, and C. Arcoumanis, Modelling of cavitation in diesel injector nozzles, *Journal of Fluid Mechanics* **616**, 153–193, 2008.
- [71] D. Gidaspow, *Multiphase flow and fluidization*, Academic Press, Inc., 1994.

Bibliography

- [72] R. A. Gingold and J. J. Monaghan, Smoothed particle hydrodynamics: theory and application to non-spherical stars, *Monthly Notices of the Royal Astronomical Society* **181**, 375–389, 1977.
- [73] R. Glowinski, T.-W. Pan, T. I. Hesla, and D. D. Joseph, A distributed Lagrange multiplier/fictitious domain method for particulate flows, *International Journal of Multiphase Flow* **25**, 755–794, 1999.
- [74] R. Glowinski, T. W. Pan, T. I. Hesla, D. D. Joseph, and J. Périnaux, A Fictitious Domain Approach to the Direct Numerical Simulation of Incompressible Viscous Flow past Moving Rigid Bodies: Application to Particulate Flow, *Journal of Computational Multiphase Flows* **169**, 363–426, 2001.
- [75] C. Gobert and M. Manhart, Subgrid modelling for particle-LES by Spectrally Optimised Interpolation (SOI), *Journal of Computational Physics* **230**, 7796–7820, 2011.
- [76] D. Goldstein, R. Handler, and L. Sirovich, Modeling a No-Slip Flow Boundary with an External Force Field, *Journal of Computational Physics* **105**, 354–366, 1993.
- [77] V. Gravemeier and W. A. Wall, Residual-based variational multiscale methods for laminar, transitional and turbulent variable-density flow at low Mach number, *International Journal for Numerical Methods in Fluids* **65**, 1260–1278, 2011.
- [78] V. Gravemeier, S. Lenz, and W. A. Wall, Towards a taxonomy for multiscale methods in computational mechanics: building blocks of existing methods, *Computational Mechanics* **41**, 279–291, 2008.
- [79] V. Gravemeier, M. Kronbichler, M. W. Gee, and W. A. Wall, An algebraic variational multiscale-multigrid method for large-eddy simulation: generalized- α time integration, Fourier analysis and application to turbulent flow past a square-section cylinder, *Computational Mechanics* **47**, 217–233, 2011.
- [80] P. M. Gresho and R. L. Sani, *Incompressible flow and the finite element method – Volume one: Advection-Diffusion*, John Wiley & Sons Ltd., Chichester, 2000.
- [81] P. M. Gresho and R. L. Sani, *Incompressible flow and the finite element method – Volume two: Isothermal laminar flow*, John Wiley & Sons Ltd., Chichester, 2000.
- [82] G. M. Guerra, S. Zio, J. J. Camata, F. A. Rochinha, R. N. Elias, P. L. B. Paraizo, and A. L. G. A. Coutinho, Numerical simulation of particle-laden flows by the residual-based variational multiscale method, *International Journal for Numerical Methods in Fluids* **73**, 729–749, 2013.
- [83] P. Gupta, J. Sun, and J. Y. Ooi, DEM-CFD simulation of a dense fluidized bed: Wall boundary and particle size effects, *Powder Technology* **293**, 37–47, 2016.
- [84] C. Gütter, D. Heißelmann, J. Blum, and S. Krijt, Normal collisions of spheres: A literature survey on available experiments, arXiv:1204.0001v2, 2013.

- [85] E. Hairer, S. P. Nørsett, and G. Wanner, *Solving ordinary differential equations I: Nonstiff problems*, Springer, Berlin, Heidelberg, 2nd Edition, 2008.
- [86] G. Hammerl, *Adaptive time stepping for non-linear hyperbolic problems*, Diplomarbeit, Technische Universität München, 2011.
- [87] G. Hammerl and W. A. Wall, A four-way coupled Euler–Lagrange approach using a variational multiscale method for simulating cavitation, *Journal of Physics: Conference Series* **656**, 12125, 2015.
- [88] F. H. Harlow, A Machine Calculation Method for Hydrodynamic Problems, Technical report, Los Alamos Scientific Laboratory, 1955.
- [89] F. H. Harlow and J. E. Welch, Numerical Calculation of Time-Dependent Viscous Incompressible Flow of Fluid with Free Surface, *Physics of Fluids* **8**, 2182–2189, 1965.
- [90] X. He and L.-S. Luo, Theory of the lattice Boltzmann method: From the Boltzmann equation to the lattice Boltzmann equation, *Physical Review E* **56**, 6811–6817, 1997.
- [91] M. A. Heroux, R. A. Bartlett, V. E. Howle, R. J. Hoekstra, J. J. Hu, T. G. Kolda, R. B. Lehoucq, K. R. Long, R. P. Pawlowski, E. T. Phipps, A. G. Salinger, H. K. Thornquist, R. S. Tuminaro, J. M. Willenbring, A. Williams, and K. S. Stanley, An overview of the Trilinos project, *ACM Transactions on Mathematical Software* **31**, 397–423, 2005.
- [92] S. Hicken, N. A. Adams, and J. A. Domaradzki, An adaptive local deconvolution method for implicit LES, *Journal of Computational Physics* **213**, 413–436, 2006.
- [93] C. W. Hirt and B. D. Nichols, Volume of Fluid (VOF) Method for the Dynamics of Free Boundaries, *Journal of Computational Physics* **39**, 201–225, 1981.
- [94] B. P. B. Hoomans, J. A. M. Kuipers, W. J. Briels, and W. P. M. van Swaaij, Discrete particle simulation of bubble and slug formation in a two-dimensional gas-fluidised bed: A hard-sphere approach, *Chemical Engineering Science* **51**, 99–118, 1996.
- [95] C.-T. Hsiao, G. L. Chahine, and H.-L. Liu, Scaling effect on prediction of cavitation inception in a line vortex flow, *Journal of Fluids Engineering* **125**, 53–60, 2003.
- [96] C.-T. Hsiao, J. Ma, and G. L. Chahine, Multi-scale two-phase flow modeling of sheet and cloud cavitation, In *30th Symposium on Naval Hydrodynamics*, 2014.
- [97] H. H. Hu, D. D. Joseph, and M. J. Crochet, Direct Simulation of Fluid Particle Motions, *Theoretical and Computational Fluid Dynamics* **3**, 285–306, 1992.
- [98] H. H. Hu, N. A. Patankar, and M. Y. Zhu, Direct Numerical Simulations of Fluid–Solid Systems Using the Arbitrary Lagrangian–Eulerian Technique, *Journal of Computational Physics* **169**, 427–462, 2001.
- [99] X. Y. Hu, B. C. Khoo, N. A. Adams, and F. L. Huang, A conservative interface method for compressible flows **219**, 553–578, 2006.

Bibliography

- [100] T. J. R. Hughes, Multiscale phenomena: Green's functions, the Dirichlet-to-Neumann formulation, subgrid scale models, bubbles and the origins of stabilized methods, *Computer Methods in Applied Mechanics and Engineering* **127**, 387–401, 1995.
- [101] T. J. R. Hughes, *The finite element method – Linear static and dynamic finite element analysis*, Dover Publications, Inc., Mineola, New York, 2000.
- [102] T. J. R. Hughes and G. N. Wells, Conservation properties for the Galerkin and stabilised forms of the advection-diffusion and incompressible Navier-Stokes equations, *Computer Methods in Applied Mechanics and Engineering* **194**, 1141–1159, 2005.
- [103] T. J. R. Hughes, G. R. Feijóo, L. Mazzei, and J.-B. Quincy, The variational multiscale method—a paradigm for computational mechanics, *Computer Methods in Applied Mechanics and Engineering* **166**, 3–24, 1998.
- [104] S. R. Idelsohn, E. Oñate, and F. Del Pin, The particle finite element method: a powerful tool to solve incompressible flows with free-surfaces and breaking waves, *International Journal for Numerical Methods in Engineering* **61**, 964–989, 2004.
- [105] B. M. Irons and R. C. Tuck, A version of the Aitken accelerator for computer iteration, *International Journal for Numerical Methods in Engineering* **1**, 275–277, 1969.
- [106] M. Ishii, *Thermo-fluid dynamic theory of two-phase flow*, Eyrolles, Paris, 1975.
- [107] M. Ishii, One-dimensional drift-flux model for relative motion between phases in various two-phase flow regimes, ANL-77-47, USA, 1977.
- [108] M. Ishii and K. Mishima, Two-fluid model and hydrodynamic constitutive laws, *Nuclear Engineering and Design* **82**, 107–126, 1984.
- [109] K. E. Jansen, C. H. Whiting, and G. M. Hulbert, A generalized-alpha method for integrating the filtered Navier-Stokes equations with a stabilized finite element method, *Computer Methods in Applied Mechanics and Engineering* **190**, 305–319, 2000.
- [110] S. T. Johansen, N. M. Anderson, and S. R. De Silva, A two-phase model for particle local equilibrium applied to air classification of powers. Power, *Powder Technology* **63**, 121–132, 1990.
- [111] K. D. Kafui, C. Thornton, and M. J. Adams, Discrete particle-continuum fluid modelling of gas-solid fluidised beds, *Chemical Engineering Science* **57**, 2395–2410, 2002.
- [112] S. Kamath, M. Masterov, J. Padding, K. Buist, M. Baltussen, and J. Kuipers, Parallelization of a stochastic euler-lagrange model applied to large scale dense bubbly flows, *Journal of Computational Physics: X* **8**, 100058, 2020.
- [113] T. Kawaguchi, T. Tanaka, and Y. Tsuji, Numerical simulation of two-dimensional fluidized beds using the discrete element method (comparison between the two-and three-dimensional models), *Powder Technology* **96**, 129–138, 1998.

- [114] H. A. Khawaja, S. A. Scott, M. S. Virk, and M. Moatamed, Quantitative analysis of accuracy of voidage computations in CFD-DEM simulations, *The Journal of Computational Multiphase Flows* **4**, 183–192, 2012.
- [115] A. Kitagawa, Y. Murai, and F. Yamamoto, Two-way coupling of Eulerian–Lagrangian model for dispersed multiphase flows using filtering functions, *International Journal of Multiphase Flow* **27**, 2129–2153, 2001.
- [116] C. Kleinstreuer, *Two-Phase flow: Theory and applications*, Taylor & Francis, 2003.
- [117] C. Kloss, C. Goniva, A. Hager, S. Amberger, and S. Pirker, Models, algorithms and validation for opensource DEM and CFD-DEM, *Progress in Computational Fluid Dynamics* **12**, 140–152, 2012.
- [118] D. L. Koch and R. J. Hill, Inertial effects in suspension and porous-media flows, *Annual Review of Fluid Mechanics* **33**, 619–647, 2001.
- [119] S. Koshizuka and Y. Oka, Moving-Particle Semi-Implicit Method for Fragmentation of Incompressible Fluid, *Nuclear Science and Engineering* **123**, 421–434, 1996.
- [120] S. Koshizuka, A. Nobe, and Y. Oka, Numerical analysis of breaking waves using the moving particle semi-implicit method, *International Journal for Numerical Methods in Fluids* **26**, 751–769, 1998.
- [121] P. Koumoutsakos, Multiscale flow simulations using particles, *Annual Review of Fluid Mechanics* **37**, 457–487, 2005.
- [122] A. Kubota, H. Kato, and H. Yamaguchi, A new modelling of cavitating flows: a numerical study of unsteady cavitation on a hydrofoil section, *Journal of Fluid Mechanics* **240**, 59–96, 1992.
- [123] J. G. M. Kuerten, Subgrid modeling in particle-laden channel flow, *Physics of Fluids* **18**, 25108, 2006.
- [124] D. Kunii and O. Levenspiel, *Fluidization engineering: Second edition*, Butterworth-Heinemann, 1991.
- [125] U. Küttler and W. A. Wall, Fixed-point fluid–structure interaction solvers with dynamic relaxation, *Computational Mechanics* **43**, 61–72, 2008.
- [126] S. Laín and M. Sommerfeld, Characterisation of pneumatic conveying systems using the Euler/Lagrange approach, *Powder Technology* **235**, 764–782, 2013.
- [127] S. Laín, D. Bröder, M. Sommerfeld, and M. F. Göz, Modelling hydrodynamics and turbulence in a bubble column using the Euler–Lagrange procedure, *International Journal of Multiphase Flow* **28**, 1381–1407, 2002.
- [128] S. Laín, M. Sommerfeld, and J. Kussin, Experimental studies and modelling of four-way coupling in particle-laden horizontal channel flow, *International Journal of Heat and Fluid Flow* **23**, 647–656, 2002.

Bibliography

- [129] A. R. Lambert, P. O'Shaughnessy, M. H. Tawhai, E. A. Hoffman, and C.-L. Lin, Regional deposition of particles in an image-based airway model: large-eddy simulation and left-right lung ventilation asymmetry, *Aerosol Science and Technology* **45**, 11–25, 2011.
- [130] Y. M. Lau, I. Roghair, N. G. Deen, M. van Sint Annaland, and J. A. M. Kuipers, Numerical investigation of the drag closure for bubbles in bubble swarms, *Chemical Engineering Science* **66**, 3309–3316, 2011.
- [131] B. E. Launder, G. J. Reece, and W. Rodi, Progress in the development of a Reynolds-stress turbulence closure, *Journal of Fluid Mechanics* **68**, 537–566, 1975.
- [132] T. A. Laursen, *Computational contact and impact mechanics*, Springer-Verlag, Berlin, Heidelberg, 2003.
- [133] A. Leonardi, F. K. Wittel, M. Mendoza, R. Vetter, and H. J. Herrmann, Particle-fluid-structure interaction for debris flow impact on flexible barriers, arXiv:1409.8034v1, 2014.
- [134] J. M. Link, L. A. Cuypers, N. G. Deen, and J. A. M. Kuipers, Flow regimes in a spout–fluid bed: A combined experimental and simulation study, *Chemical Engineering Science* **60**, 3425–3442, 2005.
- [135] W. K. Liu, S. Jun, S. Li, J. Adee, and T. Belytschko, Reproducing kernel particle methods, *International Journal for Numerical Methods in Engineering* **38**, 1655–1679, 1995.
- [136] R. Löhner and F. Perazzo, Improvements in speed and scalability of a DEM code, *Mecánica Computacional* **35**, 455–466, 2017.
- [137] R. Löhner, F. Camelli, J. D. Baum, F. Togashi, and O. Soto, On mesh-particle techniques, *Computational Particle Mechanics* **1**, 199–209, 2014.
- [138] S. Lomholt and M. R. Maxey, Force-coupling method for particulate two-phase flow: Stokes flow, *Journal of Computational Physics* **184**, 381–405, 2003.
- [139] O. M. F. R. S. Lord Rayleigh, On the pressure developed in a liquid during the collapse of a spherical cavity, *Philosophical Magazine* **34**, 94–98, 1917.
- [140] S. Luding, Introduction to Discrete Element Methods: Basic of Contact Force Models and How to Perform the Micro-Macro Transition to Continuum Theory, *European Journal of Environmental and Civil Engineering* **12**, 785–826, 2008.
- [141] J. Ma, C.-T. Hsiao, and G. L. Chahine, Euler-Lagrange Simulations of Bubble Cloud Dynamics Near a Wall, *Journal of Fluids Engineering* **137**, 41301, 2015.
- [142] J. Magnaudet and I. Eames, The Motion of High-Reynolds-Number Bubbles in Inhomogeneous Flows, *Annual Review of Fluid Mechanics* **32**, 659–708, 2000.
- [143] M. Manninen and V. Taivassalo, *On the mixture model for multiphase flow*, VTT Publications, Espoo, 1996.

- [144] M. Mattson and K. Mahesh, Towards Numerical Simulation of Cavitating Flows in Complex Geometries, In *Proceedings of 27th Symposium on Naval Hydrodynamics*, 2008.
- [145] M. D. Mattson, *Euler-Lagrangian simulations of turbulent bubbly flow*, PhD thesis, University of Minnesota, 2011.
- [146] M. R. Maxey and B. K. Patel, Localized force representations for particles sedimenting in Stokes flow, *International Journal of Multiphase Flow* **27**, 1603–1626, 2001.
- [147] M. R. Maxey and J. J. Riley, Equation of Motion for a Small Rigid Sphere in a Nonuniform Flow, *Physics of Fluids* **26**, 883–889, 1983.
- [148] I. M. Mazzitelli, D. Lohse, and F. Toschi, The effect of microbubbles on developed turbulence, *Physics of Fluids* **15**, 5–8, 2003.
- [149] M. Menner*, G. Hammerl*, and W. A. Wall, Analytical integration of 0th , 2nd , and 4th order polynomial filtering functions on unstructured grid for dispersed phase fraction computation in an Euler–Lagrange approach, *International Journal of Multiphase Flow* **98**, 147–157, 2018 (*Co-first authorship).
- [150] D. Migdal and V. D. Agosta, A source flow model for continuum gas-particle flow, *Journal of Applied Mechanics* **34**, 860–865, 1967.
- [151] R. Mittal and G. Iaccarino, Immersed boundary methods, *Annual Review of Fluid Mechanics* **37**, 239–261, 2005.
- [152] J. J. Monaghan, Smoothed particle hydrodynamics, *Annual Review of Astronomy and Astrophysics* **30**, 543–574, 1992.
- [153] P. M. Morse and H. Feshbach, *Methods of theoretical physics*, Volume 1 No. 2, New York: McGraw-Hill, 1953.
- [154] W. C. Moss, J. L. Levatin, and A. J. Szeri, A new damping mechanism in strongly collapsing bubbles, *Proceedings of the Royal Society of London A: Mathematical, Physical and Engineering Sciences* **456**, 2983–2994, 2000.
- [155] B. Muth, M.-K. Müller, P. Eberhard, and S. Luding, Collision Detection and Administration Methods for Many Particles with Different Sizes, In *Discrete Element Methods, DEM 07*, pages 1–18, 2007.
- [156] B. Nayroles, G. Touzot, and P. Villon, Generalizing the finite element method: Diffuse approximation and diffuse elements, *Computational Mechanics* **10**, 307–318, 1992.
- [157] R. M. Nedderman, U. Tüzün, S. B. Savage, and G. T. Houlsby, The flow of granular materials—I Discharge rates from hoppers, *Chemical Engineering Science* **37**, 1597–1609, 1982.
- [158] T. M. J. Nijssen, H. A. M. Kuipers, J. van der Stel, A. T. Adema, and K. A. Buist, Complete liquid-solid momentum coupling for unresolved CFD-DEM simulations, *International Journal of Multiphase Flow* **132**, 103425, 2020.

Bibliography

- [159] E. Oñate, S. R. Idelsohn, F. Del Pin, and R. Aubry, The Particle Finite Element Method. An Overview, *International Journal of Computational Methods* **1**, 267–307, 2004.
- [160] E. Oñate, M. A. Celigueta, S. Latorre, G. Casas, R. Rossi, and J. Rojek, Lagrangian Analysis of Multiscale Particulate Flows with Particle Finite Element Method, *Computational Particle Mechanics* **1**, 85–102, 2014.
- [161] S. Osher and J. A. Sethian, Fronts propagating with curvature dependent speed: Algorithms based on Hamilton-Jacobi formulations, *Journal of Computational Physics* **79**, 12–49, 1988.
- [162] C. O’Sullivan and J. D. Bray, Selecting a suitable time step for discrete element simulations that use the central difference time integration scheme, *Engineering Computations* **21**, 278–303, 2004.
- [163] N. A. Patankar, P. Singh, D. D. Joseph, R. Glowinski, and T.-W. Pan, A new formulation of the distributed Lagrange multiplier/fictitious domain method for particulate flows, *International Journal of Multiphase Flow* **26**, 1509–1524, 2000.
- [164] Z. Peng, E. Doroodchi, C. Luo, and B. Moghtaderi, Influence of Void Fraction Calculation on Fidelity of CFD-DEM Simulation of Gas-Solid Bubbling Fluidized Beds, *American Institute of Chemical Engineers Journal* **60**, 2000–2018, 2014.
- [165] K. A. Pericleous and S. N. Drake, An Algebraic Slip Model of PHOENICS for Multi-phase Applications, In N. C. Markatos, M. Cross, D. G. Tatchell, and N. Rhodes (eds.), *Numerical Simulation of Fluid Flow and Heat/Mass Transfer Processes*, Springer, Berlin, Heidelberg, 1986.
- [166] C. S. Peskin, Flow patterns around heart valves: A numerical method, *Journal of Computational Physics* **10**, 252–271, 1972.
- [167] M. S. Plesset, The dynamics of cavitation bubbles, *Journal of Applied Mechanics* **16**, 277–282, 1949.
- [168] S. Plimpton, Fast parallel algorithms for short-range molecular dynamics, *Journal of Computational Physics* **117**, 1–19, 1995.
- [169] S. Popinet and S. Zaleski, Bubble collapse near a solid boundary: a numerical study of the influence of viscosity, *Journal of Fluid Mechanics* **464**, 137–163, 2002.
- [170] A. Popp, *Mortar methods for computational contact mechanics and general interface problems*, PhD thesis, Technische Universität München, 2012.
- [171] T. Pöschel and T. Schwager, *Computational Granular Dynamics*, Springer-Verlag, Berlin, Heidelberg, 2005.
- [172] M. Rastello, J.-L. Marié, and M. Lance, Drag and lift forces on clean spherical and ellipsoidal bubbles in a solid-body rotating flow, *Journal of Fluid Mechanics* **682**, 434–459, 2011.

- [173] U. Rasthofer and V. Gravemeier, Recent Developments in Variational Multiscale Methods for Large-Eddy Simulation of Turbulent Flow, *Archives of Computational Methods in Engineering*, 2017.
- [174] H. T. Rathod and H. S. Govinda Rao, Integration of polynomials over linear polyhedra in Euclidean three-dimensional space, *Computer Methods in Applied Mechanics and Engineering* **126**, 373–392, 1995.
- [175] M. A. Rizk, Mathematical modeling of densely loaded, particle-laden turbulent flows, *Atomization and Sprays* **3**, 1–27, 1993.
- [176] D. Rossinelli, B. Hejazialhosseini, P. Hadjidoukas, C. Bekas, A. Curioni, A. Bertsch, S. Futral, S. J. Schmidt, N. A. Adams, and P. Koumoutsakos, 11 PFLOP/s Simulations of Cloud Cavitation Collapse, In *Proceedings of the International Conference for High Performance Computing, Networking, Storage and Analysis on - SC '13*. ACM Press, 2013.
- [177] C. J. Roth, *Multi-dimensional Coupled Computational Modeling in Respiratory Biomechanics*, PhD thesis, Technische Universität München, 2017.
- [178] P. N. Rowe, Drag Forces in a Hydraulic Model of a Fluidized Bed, Part II, *Transactions of the Institution of Chemical Engineers* **39**, 175–180, 1961.
- [179] E. M. Saiki and S. Biringen, Numerical Simulation of a Cylinder in Uniform Flow: Application of a Virtual Boundary Method, *Journal of Computational Physics* **123**, 450–465, 1996.
- [180] L. Schiller and A. Z. Naumann, Über die grundlegenden Berechnungen bei der Schwerkraftaufbereitung, *Zeitschrift des Vereines Deutscher Ingenieure* **77**, 318–320, 1933.
- [181] D. P. Schmidt, C. J. Rutland, and M. L. Corradini, A fully compressible, two-dimensional model of small, high-speed cavitating nozzles, *Atomization and Sprays* **9**, 255–276, 1999.
- [182] S. Schneiderbauer and S. Pirker, A Coarse-Grained Two-Fluid Model for Gas-Solid Fluidized Beds, *Journal of Computational Multiphase Flows* **6**, 29–47, 2014.
- [183] G. H. Schnerr, I. H. Sezal, and S. J. Schmidt, Numerical investigation of three-dimensional cloud cavitation with special emphasis on collapse induced shock dynamics, *Physics of Fluids* **20**, 40703, 2008.
- [184] J. D. Schwarzkopf, C. T. Crowe, and P. Dutta, A Turbulence Dissipation Model for Particle Laden Flow, *American Institute of Chemical Engineers Journal* **55**, 1416–1425, 2009.
- [185] A. Selle, N. Rasmussen, and R. Fedkiw, A Vortex Particle Method for Smoke, Water and Explosions, *ACM Transactions on Graphics (TOG)* **24**, 910–914, 2005.
- [186] J. A. Sethian and P. Smereka, Level Set Methods for Fluid Interfaces, *Annual Review of Fluid Mechanics* **35**, 341–372, 2003.

Bibliography

- [187] E. Shams, J. Finn, and S. V. Apte, A numerical scheme for Euler–Lagrange simulation of bubbly flows in complex systems, *International Journal for Numerical Methods in Fluids* **67**, 1865–1898, 2011.
- [188] Y. Shan and J. Mostaghimi, Numerical simulation of aerosol droplets desolvation in a radio frequency inductively coupled plasma, *Spectrochimica Acta Part B* **58**, 1959–1977, 2003.
- [189] H. Sigurgeirsson, A. Stuart, and W.-L. Wan, Algorithms for particle-field simulations with collisions, *Journal of Computational Physics* **172**, 766–807, 2001.
- [190] J. C. Simo and T. J. R. Hughes, *Computational inelasticity*, Springer, New York, 1998.
- [191] A. Sokolichin and G. Eigenberger, Gas–liquid flow in bubble columns and loop reactors: Part I. Detailed modelling and numerical simulation, *Chemical Engineering Science* **49**, 5735–5746, 1994.
- [192] A. Sokolichin, G. Eigenberger, A. Lapin, and A. Lübbert, Dynamic numerical simulation of gas–liquid two-phase flows Euler/Euler versus Euler/Lagrange, *Chemical Engineering Science* **52**, 611–626, 1997.
- [193] M. Sommerfeld, Validation of a stochastic Lagrangian modelling approach for inter-particle collisions in homogeneous isotropic turbulence, *International Journal of Multiphase Flow* **27**, 1829–1858, 2001.
- [194] M. Sommerfeld, E. Bourloutski, and D. Bröder, Euler/Lagrange Calculations of Bubbly Flows with Consideration of Bubble Coalescence, *The Canadian Journal of Chemical Engineering* **81**, 508–518, 2003.
- [195] K. D. Squires and O. Simonin, LES–DPS of the effect of wall roughness on dispersed-phase transport in particle-laden turbulent channel flow, *International Journal of Heat and Fluid Flow* **27**, 619–626, 2006.
- [196] G. G. Stokes, On the effect of the internal friction of fluids on the motion of pendulums, *Transactions of the Cambridge Philosophical Society* **9**, 8, 1851.
- [197] S. Subramaniam, Lagrangian–Eulerian methods for multiphase flows, *Progress in Energy and Combustion Science* **39**, 215–245, 2013.
- [198] Y. Sudhakar and W. A. Wall, Quadrature schemes for arbitrary convex/concave volumes and integration of weak form in enriched partition of unity methods, *Computer Methods in Applied Mechanics and Engineering* **258**, 39–54, 2013.
- [199] Y. Sudhakar, J. P. Moitinho de Almeida, and W. A. Wall, An accurate, robust, and easy-to-implement method for integration over arbitrary polyhedra: Application to embedded interface methods, *Journal of Computational Physics* **273**, 393–415, 2014.
- [200] D. Sulsky, Z. Chen, and H. L. Schreyer, A Particle Method for History-Dependent Materials, *Computer Methods in Applied Mechanics and Engineering* **118**, 179–196, 1994.

- [201] R. Sungkorn, J. J. Derksen, and J. G. Khinast, Euler–Lagrange Modeling of a Gas–Liquid Stirred Reactor with Consideration of Bubble Breakage and Coalescence, *American Institute of Chemical Engineers Journal* **58**, 1356–1370, 2012.
- [202] Y. Tamura, K. Sugiyama, and Y. Matsumoto, Physical modeling and solution algorithm for cavitating flow simulations, *AIAA Paper*, 2001–2652.
- [203] C. A. Taylor, T. J. R. Hughes, and C. K. Zarins, Finite element modeling of blood flow in arteries, *Computer Methods in Applied Mechanics and Engineering* **158**, 155–196, 1998.
- [204] G. I. F. R. S. Taylor, On the decay of vortices in a viscous fluid, *Philosophical Magazine* **46**, 671–674, 1923.
- [205] A. Tomiyama, I. Žun, H. Higaki, Y. Makino, and T. Sakaguchi, A three-dimensional particle tracking method for bubbly flow simulation, *Nuclear Engineering and Design* **175**, 77–86, 1997.
- [206] A. Tomiyama, H. Tamai, I. Zun, and S. Hosokawa, Transverse migration of single bubble in simple shear flows, *Chemical Engineering Science* **57**, 1849–1858, 2002.
- [207] G. Tryggvason, R. Scardovelli, and S. Zaleski, *Direct Numerical Simulations of Gas-Liquid Multiphase Flows*, Cambridge University Press, 2011.
- [208] Y. Tsuji, T. Kawaguchi, and T. Tanaka, Discrete particle simulation of two-dimensional fluidized bed, *Powder Technology* **77**, 79–87, 1993.
- [209] R. Tuley, M. Danby, J. Shrimpton, and M. Palmer, On the optimal numerical time integration for Lagrangian DEM within implicit flow solvers, *Computers and Chemical Engineering* **34**, 886–899, 2010.
- [210] M. Uhlmann, Interface-resolved direct numerical simulation of vertical particulate channel flow in the turbulent regime, *Physics of Fluids* **20**, 53305, 2008.
- [211] M. Ungarish, *Hydrodynamics of Suspensions: Fundamentals of centrifugal and gravity separation*, Springer-Verlag, Berlin, Heidelberg, 1993.
- [212] S. O. Unverdi and G. Tryggvason, A Front-Tracking Method for Viscous, Incompressible, Multi-fluid Flows, *Journal of Computational Multiphase Flows* **100**, 25–37, 1992.
- [213] P. Valentini and T. E. Schwartzenruber, A Combined Event-Driven/Time-Driven Molecular Dynamics Algorithm for the Simulation of Shock Waves in Rarefied Gases, *Journal of Computational Physics* **228**, 8766–8778, 2009.
- [214] A. Vallier, *Simulations of cavitation – from the large vapour structures to the small bubble dynamics*, PhD thesis, Lund University, 2013.
- [215] A. Vallier, J. Revstedt, and H. Nilsson, Procedure for the break-up of cavitation sheet, In *Proceedings of 4-th International Meeting on Cavitation and Dynamic Problems in Hydraulic Machinery and Systems*, 2011.

Bibliography

- [216] M. A. van der Hoef, M. van Sint Annaland, N. G. Deen, and J. A. M. Kuipers, Numerical simulation of dense gas-solid fluidized beds: A multiscale modeling strategy, *Annual Review of Fluid Mechanics* **40**, 47–70, 2008.
- [217] A. van Nierop Ernst, S. Luther, J. J. Bluemink, J. Magnaudet, A. Prosperetti, and D. Lohse, Drag and lift forces on bubbles in a rotating flow, *Journal of Fluid Mechanics* **571**, 439–454, 2007.
- [218] T. J. C. Van Terwisga, P. A. Fitzsimmons, L. Ziru, and E. J. Foeth, Cavitation erosion — A review of physical mechanisms and erosion risk models, In *7th International Symposium on Cavitation*, number 41, pages 1–13, 2009.
- [219] B. G. M. van Wachem, J. C. Schouten, C. M. van den Bleek, R. Krishna, and J. L. Sinclair, Comparative analysis of CFD models of dense gas–solid systems, *American Institute of Chemical Engineers Journal* **47**, 1035–1051, 2001.
- [220] B. G. M. van Wachem, J. van der Schaaf, J. C. Schouten, R. Krishna, and C. M. van den Bleek, Experimental validation of Lagrangian–Eulerian simulations of fluidized beds, *Powder Technology* **116**, 155–165, 2001.
- [221] F. Verdugo, C. J. Roth, L. Yoshihara, and W. A. Wall, Efficient solvers for coupled models in respiratory mechanics, *International Journal for Numerical Methods in Biomedical Engineering* **33**, e02795, 2017.
- [222] B. Vreman, B. J. Geurts, N. G. Deen, J. A. M. Kuipers, and J. G. M. Kuerten, Two- and Four-Way Coupled Euler–Lagrangian Large-Eddy Simulation of Turbulent Particle-Laden Channel Flow, *Flow, Turbulence and Combustion* **82**, 47–71, 2009.
- [223] A. Wachs, PeliGRIFF, a parallel DEM-DLM/FD direct numerical simulation tool for 3D particulate flows, *Journal of Engineering Mathematics* **71**, 131–155, 2011.
- [224] A. Wachs, Particle-scale computational approaches to model dry and saturated granular flows of non-Brownian, non-cohesive, and non-spherical rigid bodies, *Acta Mechanica* **230**, 1919–1980, 2019.
- [225] D. Wan and S. Turek, Direct numerical simulation of particulate flow via multigrid FEM techniques and the fictitious boundary method, *International Journal for Numerical Methods in Fluids* **51**, 531–566, 2006.
- [226] M. S. Warren and J. K. Salmon, A Parallel Hashed Oct-Tree N-Body Algorithm, In *Proceedings of Supercomputing '93*, pages 12–21, 1993.
- [227] C. Y. Wen and Y. H. Yu, Mechanics of fluidization, *Chemical Engineering Progress Symposium Series* **62**, 100–111, 1966.
- [228] S. Whitaker, A simple geometrical derivation of the spatial averaging theorem, *Chemical Engineering Education*, 18–21, 50–52, 1985.
- [229] S. Whitaker, *The method of volume averaging*, Kluwer Academic, Dordrecht, 1999.

- [230] C. H. Whiting and K. E. Jansen, A stabilized finite element method for the incompressible Navier-Stokes equations using a hierarchical basis, *International Journal for Numerical Methods in Fluids* **35**, 93–116, 2001.
- [231] B. D. Wood, F. Cherblanc, M. Quintard, and S. Whitaker, Volume averaging for determining the effective dispersion tensor: Closure using periodic unit cells and comparison with ensemble averaging, *Water Resources Research* **39**, 1210, 2003.
- [232] C. L. Wu, J. M. Zhan, Y. S. Li, K. S. Lam, and A. S. Berrouk, Accurate void fraction calculation for three-dimensional discrete particle model on unstructured mesh, *Chemical Engineering Science* **64**, 1260–1266, 2009.
- [233] S. Yakubov, B. Cankurt, M. Abdel-Maksoud, and T. Rung, Hybrid MPI/OpenMP parallelization of an Euler–Lagrange approach to cavitation modelling, *Computers & Fluids* **80**, 365–371, 2013.
- [234] L. Yoshihara, C. J. Roth, and W. A. Wall, Fluid-structure interaction including volumetric coupling with homogenised subdomains for modeling respiratory mechanics, *International Journal for Numerical Methods in Biomedical Engineering* **33**, 2017.
- [235] A. B. Yu and B. H. Xu, Particle-scale modelling of gas–solid flow in fluidisation, *Journal of Chemical Technology and Biotechnology* **78**, 111–121, 2003.
- [236] L. A. Zadeh, Fuzzy sets, *Information and control* **8.3**, 338–353, 1965.
- [237] M. Zeidan, B. H. Xu, X. Jia, and R. A. Williams, Simulation of Aggregate Deformation and Breakup in Simple Shear Flows Using a Combined Continuum and Discrete Model, *Chemical Engineering Research and Design* **85**, 1645–1654, 2007.
- [238] D. Z. Zhang and A. Prosperetti, Averaged equations for inviscid disperse two-phase flow, *Journal of Fluid Mechanics* **267**, 185–219, 1994.
- [239] X. Zhang and G. Ahmadi, Eulerian–Lagrangian simulations of liquid–gas–solid flows in three-phase slurry reactors, *Chemical Engineering Science* **60**, 5089–5104, 2005.
- [240] Z. Zhang, C. Kleinstreuer, and C. S. Kim, Cyclic micron-size particle inhalation and deposition in a triple bifurcation lung airway model, *Aerosol Science* **33**, 257–281, 2002.
- [241] O. C. Zienkiewicz, R. L. Taylor, and J. Z. Zhu, *The finite element method: Its Basis and fundamentals*, Butterworth-Heinemann, 7th Edition, 2013.
- [242] T. I. Zohdi, Computation of strongly coupled multifield interaction in particle–fluid systems, *Computer Methods in Applied Mechanics and Engineering* **196**, 3927–3950, 2007.
- [243] N. Zuber and J. A. Findlay, Average volumetric concentration in two-phase flow systems, *Journal of Heat Transfer* **87**, 453–468, 1965.